Fundamental Understanding of Turbulent Combustion in Droplet-Laden Mixtures Using Direct Numerical Simulations

Gulcan OZEL EROL

School of Engineering

Newcastle University

This dissertation is submitted for the degree of

Doctor of Philosophy

November 2021

To my mother and grandmother
who are my greatest inspirations.

Declaration

I hereby declare that this thesis is my own work and that I have correctly acknowledged the work of others. This submission is in accordance with Newcastle University and the School of Engineering's guidance on good academic conduct. I certify that no part of the material offered has been previously submitted by me for a degree or other qualification in this or any other University. I confirm that the word length is within the prescribed range as advised by my school and faculty. I confirm that this thesis does not contain collaborative work. This thesis contains approximately 60,000 words[1], 102 figures, and 20 tables.

Gulcan OZEL EROL
November 2021

[1] Using LyXProcessor

Acknowledgements

I would like to sincerely express my gratitude to Prof. Nilanjan Chakraborty for his generous support, inspiring guidance, continuous encouragement, and patience throughout this study. I am truly grateful for his limitless support and motivation to present my work in leading international conferences and to meet valuable researchers in the field. Apart from his boundless enthusiasm for combustion science, the collaborative research environment he created in the fluid group office has undoubtedly shaped my future academic career. I would also like to thank my co-supervisor Andrew Aspden for being available to help me when I needed during my PhD.

I am grateful to Dr Osman Turan for providing the first links to start my PhD at Newcastle University. Thanks to Dr Daniel Wacks for introducing numerical spray combustion to me when I first joined the group. I particularly thank Dr Jiawei Lai for teaching me all the tricks he knows about parallel programming. I am deeply grateful to Prof Markus Klein and Dr Josef Hasslberger for their valuable contributions which have played an essential role in my progression during this PhD. I am also thankful to Dr Umair Ahmed and Dr Charles Turquand d'Auzay for all the support and help I recieved during the tough times of my PhD.

I would like to extend a massive thank you to all members of T4 office: Dr Sahin Yigit, Dr Bruno Machado, Dr Chris Stafford, Dr Sam Wood, Bill Papapostolou, Ilias Konstantinou, Fangyu Zhang, Peter Brearley, Arun Varma, Meixi Liu, and Ignas Andriunas for their warm company in T4, leaving memorable moments to me from life in the UK and making me love Newcastle.

I am sincerely grateful to the Republic of Turkey Ministry of National Education not only for their financial support through the course of this PhD but also for making it possible for me to meet lifelong friends Ceren Senturk and Fatih Kerem Boz.

My generous appreciation must go to my partner Ramazan Erol who sacrificed his engineering career for my research, moved to the UK with me, and believed in me more than myself. My dearest son, thank you for being an easy baby in the last months of my writing up period to allow the submission of my thesis within the given deadline. Lastly, special thanks to my parents, grandmother, and brother for their unconditional love and support at every stage of my life.

Abstract

The flame propagation in droplet-laden mixtures is of considerable importance in automotive engines, gas turbines, and accidental explosions. Despite the practical importance of turbulent combustion of droplet-laden mixtures, it remains one of the most challenging topics in thermo-fluid mechanics due to the involvement of complex interactions of evaporation, heat and mass transfer, fluid dynamics, and combustion thermochemistry. Thorough knowledge of these interactions, which occur over a wide range of scales, is necessary for fundamental understanding and modelling of turbulent spray flames. In this thesis, three dimensional compressible Direct Numerical Simulations (DNS) of spherically expanding and V-shaped flames propagating in droplet mists are considered for a fundamental physical understanding of the flame structure and flame speed statistics in turbulent spray flames. Simulations with modified single-step Arrhenius type chemical mechanism have been conducted for a range of different droplet diameters, overall equivalence ratios, and turbulence intensities. The influence of liquid droplets has been investigated by comparing the statistics for spray flames to those for the corresponding gaseous premixed spherically expanding flames with statistically similar initial turbulent flow conditions. It has been found that flame-droplet interaction promotes droplet-induced flame wrinkling for laminar flame kernels, and this strengthens with increasing overall equivalence ratio and droplet diameter. However, the effects of droplet-induced flame wrinkling cannot be readily distinguished from flame wrinkling due to fluid motion for turbulent spherically expanding spray flames. The combustion has been found to take place predominantly under fuel-lean mode in comparison to the overall equivalence ratio for all droplet sizes and this tendency strengthens with increasing droplet diameter due to slow evaporation of large droplets. Furthermore, increasing turbulence intensities enhances the availability of fuel-lean mixture. The statistics of the Surface Density Function (SDF = magnitude of the reaction progress variable gradient) and the strain rates, which affect the behaviour of SDF have been analysed for spherically expanding spray flames. Flame thickening has been observed for large droplets and at high turbulence intensities due to the predominance of fuel-lean combustion. Droplet size and turbulence intensity significantly affect the behaviour of scalar gradients and the infinitesimal distance between non-material surfaces. The flame propagation behaviour in droplet-laden mixtures has been analysed in terms of the statistics of density-weighted dis-

placement and consumption speeds. Flame topologies associated with flame self-interaction events have been discussed along with the small-scale scalar geometries of flame isosurfaces. The presence of droplets, turbulence intensity and droplet diameter have been found to considerably alter the distributions of flame topologies. Additionally, flame-droplet interactions have been investigated in detail based on the source terms associated with two-phase coupling arising from droplet evaporation in various gaseous carrier phase transport equations and the modelling implications of the statistical behaviour of flame-droplet interactions have been addressed. Furthermore, hypothetical inertialess droplet motion is considered to identify the influence of droplet inertia on the combustion characteristics and the evolution of the flame surface area. The number density of droplets within the flame is greater for the inertial droplet cases than the corresponding inertialess droplet cases and this leads to higher availability of obtaining stoichiometric mixture in the flame. Finally, a comparison between the spherically expanding and V-shaped spray flames reveals that flame curvature, density-weighted displacement speed, and consumption speed varies considerably with droplet diameter in the case of spherically expanding spray flame cases, whereas the effects of droplet diameter are relatively weaker in V-flames. Simulations of V-shaped flames propagating in droplet mists for different mean inflow velocities indicate that reacting mixture composition significantly varies with the mean inflow velocity which also plays an important role in determining the flame structure and burning rate statistics.

Publications

Journal Papers

The results provided in this thesis (i.e. Chapters 4-7) have been published as journal articles listed below:

1. **Ozel Erol, G.**, Hasslberger, J., Markus, K., and Chakraborty, N., A direct numerical simulation analysis of spherically expanding turbulent flames in fuel droplet-mists for an overall equivalence ratio of unity. *Phys. Fluids*, 30, 086104, 2018 [1].

2. **Ozel Erol, G.**, Hasslberger, J., Markus, K., and Chakraborty, N., A direct numerical simulation investigation of spherically expanding flames propagating in fuel droplet-mists for different droplet diameters and overall equivalence ratios. *Combust. Sci. and Tech.*, 191(5-6), 833-867, 2019 [2].

3. **Ozel Erol, G.**, Hasslberger, J., Markus, K., and Chakraborty, N., Propagation of spherically expanding turbulent flames into fuel droplet-mists. *Flow Turbulence Combust.,* 103, 913–941, 2019 [3].

4. **Ozel Erol, G.**, Hasslberger, J., Markus, K., and Chakraborty, N., Surface Density Function evolution in spherically expanding flames in globally stoichiometric droplet-laden mixtures. *Combust. Sci. and Tech.,* 2019. Online published: https://doi.org/10.1080/00102202.2019.1678373 [4].

5. **Ozel Erol, G.**, Hasslberger, J., and Chakraborty, N., Statistics of two-phase coupling in turbulent spherically expanding flames in mono-sized fuel-droplet mists. *Combust. Sci. and Tech.*, 2020. Online published: https://doi.org/10.1080/00102202.2020.1769086 [5].

6. **Ozel Erol, G.,** and Chakraborty, N., Inertial effects on globally stoichiometric spherically expanding turbulent flames propagating in droplet-laden mixtures. *Proceedings of the Combustion Institute*, 38(2), 3379-3387, 2020 [6].

7. **Ozel Erol, G.,** Ahmed, U., and Chakraborty, N., Flame self-interactions in globally stoichiometric spherically expanding flames propagating into fuel droplet-mists. *Proceedings of the Combustion Institute*, 38(2), 3351-3359, 2020 [7].

8. **Ozel Erol, G.**, Hasslberger, J., Markus, K., and Chakraborty, N., A Direct Numerical Simulation analysis of turbulent V-shaped flames propagating into droplet-laden mixtures. *International Journal of Multiphase*, 133, 103455, 2020 [8].

9. **Ozel Erol, G.,** and Chakraborty, N., Effects of mean inflow velocity and droplet diameter on the propagation of turbulent V-shaped flames in droplet-laden mixtures. *Fluids*, 6(1), 1, 2020 [9].

Conference Proceedings

Some of the results provided in this thesis (i.e. Chapters 4-7) have been presented at the conferences and symposiums listed below:

1. **Ozel Erol, G.**, Hasslberger J., Klein, M., Chakraborty, N., Spherically expanding turbulent flames in fuel-droplet mists: A Direct Numerical Simulation analysis, *Turbulence, Heat and Mass Transfer 9*, July 10-13, 2018, Rio de Janeiro, Brazil.

2. **Ozel Erol, G.**, Hasslberger, J., Klein, M., Chakraborty, N., Evolution of spherically expanding turbulent flames in droplet-laden mixtures: A Direct Numerical Simulation analysis, *37th International Symposium on Combustion*, July 29-August 2, 2018, Dublin, Ireland.

3. **Ozel Erol, G.**, Hasslberger, J., Klein, M., Chakraborty, N., A Direct Numerical Simulation analysis of turbulent V-flames propagating into droplet-laden mixtures with an overall equivalence ratio of unity, *The 9th European Combustion Meeting*, April 14-17, 2019, Lisbon, Portugal.

4. **Ozel Erol, G.**, Hasslberger, J., Klein, M., Chakraborty, N., Surface Density Function evolution in spherically expanding flames in globally stoichiometric droplet-laden mixtures, *The 11th Mediterranean Combustion Symposium*, June 16-20, 2019, Tenerife, Spain.

5. **Ozel Erol, G.**, Hasslberger, J., Chakraborty, N., Statistics of two-phase coupling in turbulent spherically expanding flames in mono-sized fuel-droplet mists, *The International Colloquium on the Dynamics of Explosions and Reactive Systems (ICDERS*), July 28-August 2, 2019, Beijing, China.

6. **Ozel Erol, G.,** Ahmed, U., and Chakraborty, N., Flame self-interactions in globally stoichiometric spherically expanding flames propagating into fuel droplet-mists, *38th International Symposium on Combustion*, January 24-29, 2021, Adelaide, Australia.

7. **Ozel Erol, G.**, and Chakraborty, N., Inertial effects on globally stoichiometric spherically expanding turbulent flames propagating in droplet-laden mixtures, *38th International Symposium on Combustion*, January 24-29, 2021, Adelaide, Australia.

Contents

List of Figures

List of Tables

Nomenclature

Roman Symbols

$\dot{A}_c$	cross-scalar dissipation term in the reaction progress variable transport equation associated with mixture inhomogeneity
$\dot{S}_\xi$	droplet source term in the mixture fraction transport equation
$\dot{S}_e$	source term in the energy conservation equation due to evaporation of liquid droplets
$\dot{S}_{liq,c}$	source/sink term term in the reaction progress variable transport equation due to droplet evaporation
$\dot{S}_{Y_\alpha}$	source term in the species mass fraction transport equation due to evaporation of liquid droplets
$\dot{w}_\alpha$	reaction rate of species α
$\dot{w}_c$	reaction rate of reaction progress variable
$\hat{T}$	instantaneous temperature
$\overline{c}$	averaged reaction progress variable
$\overrightarrow{N}$	local flame normal vector
$\overrightarrow{r}$	unit radial vector
$\overrightarrow{u}$	velocity vector
$\overrightarrow{u}_d$	velocity of droplet
$\overrightarrow{x}_d$	subgrid position of droplet
$\tilde{c}$	Favre-averaged reaction progress variable

$\tilde{k}$	Favre-averaged turbulent kinetic energy
$\underline{\underline{H}}(c)$	Hessian of the reaction progress variable
A	flame surface area
a	local speed of sound
a_d	droplet diameter
A_m	frequency factor of step m
a_N	flame normal strain rate
a_T	flame tangential strain rate
B	pre-exponential factor
B_d	Spalding mass transfer number
c	reaction progress variable
C_p	heat capacity at constant pressure
$C_{u,d}$	drag correction coefficient
C_v	heat capacity at constant volume
D	mass diffusion coefficient
d	diameter
$d\overrightarrow{n}$	elemental distance in the local flame normal direction
D_c	reaction progress variable diffusivity
Da	Damköhler number
E	stagnation internal energy
$E(\kappa)$	turbulent energy spectrum
E_{ac}	activation energy
G	group number
$H_{(\phi_g)}$	heat release per unit mass of fuel

h_α	enthalpy of species α
h^0_α	enthalpy of formation of species α
k	turbulent kinetic energy
Ka	Karlovitz number
L	domain length
L_i	wave amplitude variation
l_t	integral length scale
l_0	reference length scale
L_{11}	longitudinal integral length scale
L_v	latent heat of vaporization
Le	Lewis number
M	number of steps in reaction mechanism
m	given step in reaction mechanism
m_d	droplet mass
Ma	Mach number
N	number of grid points
N_c	scalar dissipation rate
n_m	temperature exponent of step m
N_p	number of droplets
Nu_c	corrected Nusselt number
P	pressure
P_0	reference pressure
P_∞	static pressure at infinity conditions
P^s_F	partial pressure of the fuel vapor at the droplet surface

Pr	Prandtl number
Q	elementary grid number in the thermal flame thickness
q_k	heat flux vector
R	gas constant of the fuel
r	radius of fully burned gas region
R_0	universal gas constant
Re	Reynolds number
Re_d	droplet Reynolds number
Re_t	turbulent Reynolds number
S	ratio of volume-integrated product formation rate to the flame surface area
s	mass of the oxygen consumed per unit mass of fuel consumption
S_A	rate of flame surface area growth
S_V	rate of growth of the burned gas volume
S_c	consumption speed
S_d	displacement speed
s_d	mean normalised inter-drop distance
S_d^*	density-weighted displacement speed
S_n	normal diffusion component of displacement speed
S_r	reaction component of displacement speed
S_s	component of displacement speed due to droplet evaporation
S_t	tangential diffusion component of displacement speed
S_z	component of displacement speed due to cross-scalar dissipation term
Sc	Schmidt number
Sh_c	corrected Sherwood number

St	Stokes number
T	nondimensional temperature
T_0	unburned gas temperature
t_0	reference time
$T_{ad(\phi_g=1)}$	adiabatic flame temperature for the stoichiometric mixture
t_{chem}	chemical time scale
T_d	temperature of droplet
T_d^s	temperature at the surface of droplet
t_e	turbulent time scale
t_{flow}	flow through time
T_{ref}^s	boiling point of the fuel at the reference pressure
u'	velocity fluctuations
u_i	fluid velocity component in x_i-direction
u_0	reference velocity
u_{mean}	mean inflow velocity
V_b	burned gas volume
$V_{\alpha,k}$	diffusion velocity of species α
W_F	molecular weight of fuel
W_α	molecular weight of species α
W_{air}	molecular weight of air
x_i	Cartesian coordinate
Y_α	mass fraction of the species α
Y_F^s	fuel mass fraction at the surface of the droplet
t	time

Abbreviations

BP	Burned Mixture Pockets
CFD	Computational Fluid Dynamics
DNS	Direct Numerical Simulations
ECBC	Euler Characteristic Boundary Conditions
FAR	Fuel-Air Ratio
FFI	Flame-Flame Interaction
FI	Flame Index
FSD	Flame Surface Density
FSI	Flame Self-Interaction
GP	Gaseous Premixed
HR	Heat Release
IC	Internal Combustion
LES	Large Eddy Simulations
LODI	Local One-Dimensional Inviscid
NSCBC	Navier-Stokes Characteristic Boundary Conditions
PDF	Probability Density Function
RANS	Reynolds Averaged Navier-Stokes
SDF	Surface Density Function
SDR	Scalar Dissipation Rate
SGS	Sub-Grid-Scale
SMD	Sauter Mean Diameter
TC	Tunnel Closure
TF	Tunnel Formation

UP	Unburned Mixture Pocket

Greek Symbols

α	species
α_{hr}	heat release parameter
α_{T0}	thermal diffusivity in the unburned gas
β	Zel'dovich number
δ	characteristic flame thickness
δ_D	diffusive flame thickness
δ_{ki}	Kronecker Symbol
δ_{st}	thermal flame thickness of the unstrained stoichiometric laminar premixed flame
δ_{th}	thermal flame thickness
δ_T	flame brush thickness
δ_z	Zel'dovich flame thickness
η	Kolmogorov length scale
γ	ratio of specific heat
Γ_m	source term in the mass conservation equation due to evaporation of liquid droplets
κ	wave number
κ_m	local flame curvature
λ	thermal conductivity
λ_i	eigenvalues
$\langle \phi_g \rangle$	mean equivalence ratio
μ	dynamic viscosity

ν	kinematic viscosity
ϕ_g	gaseous equivalence ratio
ϕ_{ov}	overall equivalence ratio
ρ	density
ρ_0	unburned gas density
ρ_d	liquid density
ρ_N	droplet number density
Σ_{gen}	generalised Flame Surface Density
τ	heat release parameter
τ_d^p	relaxation timescale for droplet diameter
τ_d^T	relaxation timescale for droplet temperature
τ_d^u	relaxation timescale for droplet velocity
τ_{ki}	viscous stress tensor
θ	V-flame angle
$\tilde{\varepsilon}$	Favre-averaged turbulent dissipation rate
$\triangle U_{slip}$	normalised slip velocity
$\triangle V$	cell volume
$\triangle x$	grid spacing
$\triangle$	filter size
$\upsilon''_{\alpha,m}$	product stochiometric coefficient for step m
$\upsilon'_{\alpha,m}$	reactant stochiometric coefficient for step m
ε	turbulent dissipation rate
Ω_F	volume-integrated fuel reaction rate magnitude
ξ	mixture fraction

v_η	Kolmogorov velocity scale

Superscript

eff	effective
G	gas
L	liquid
+	non-dimensional quantities

Subscripts

F	fuel
O	oxygen
st	stoichiometric

Chapter 1

Introduction

This chapter begins with a brief explanation of the importance of multi-phase combustion. Next, simulation techniques for turbulent combustion are presented, and finally, the research aims and thesis layout are discussed.

1.1 Motivation

Liquid fuels play a pivotal role in the global energy system with the largest consumption share. Major energy consumers, including transportation and industrial sectors, principally use liquid fuels due to their high energy density and storage stability. Despite vigorous debates and concerns on limited fossil fuel resources in the late twentieth century, fossil fuels have survived as the primary contributor to the global energy mix thanks to the advancements in combustion systems. It is also reported that remaining fossil fuel reserves are sufficient to meet the majority of worldwide energy demand in the upcoming decades [10], and demand for liquid fuels is expected to grow as combustion technologies advance [11]. Furthermore, liquid biofuels have emerged as renewable alternative fuels with low carbon content. Combustion of liquid biofuels has received particular attention due to the practical applicability of fossil fuel and biofuel mixtures to generic combustion systems [12–15]. Thus, combustion performance of liquid fuels will be an essential element in achieving a sustainable energy concept in the foreseeable future. Moreover, energy security and global climate change have become major focuses of the world in the context of global energy strategies, so it is essential to improve efficiency and reduce pollutant emission levels for existing systems along with designing novel technologies.

Liquid fuels are generally introduced to combustor as dispersed liquid droplets following an atomisation process. Dispersed liquid droplets evaporate, create gaseous fuel to be mixed with air, and eventually combustion occurs in a turbulent environment as in several engineering

devices such as gas turbines, liquid rocket engines, and internal combustion (IC) engines. Turbulent combustion of sprays involves evaporation of liquid droplets, mixing of fuel vapour with the surrounding air, and interaction of droplets with the flame and flow field, differently from turbulent premixed combustion. The strong coupling of these complex processes needs a detailed understanding of underlying physics to develop energy-efficient and environment-friendly systems.

Efforts to control and use combustion for the benefit of mankind can be dated back over a number of millenniums. Remarkable progress in the combustion field has been made with the development of internal combustion engines in the last century. Furthermore, advanced computational and experimental techniques have been accessible and this has led to the rise in new approaches to solve complex problems. In particular, Computational Fluid Dynamics (CFD) has become a key approach for both industrial applications and academic research which involves the solution of governing equations of fluid motion numerically. CFD methodologies can be useful for the purpose of fundamental understanding of complex fluid flows, including turbulent reacting flows. However, it was stated by Bilger [16] that computational modelling in combustion science requires significant advancement to become comparable to numerical methodologies for other thermal systems. It is apparent that a special attention on combustion modelling needs to be devoted for optimising the performance of energy systems involving combustion.

1.2 Computational Approaches for Turbulent Combustion Analysis

Computational fluid dynamics (CFD) approach was first adopted for aerodynamic applications in the 1960s [17]. As CFD is a promising tool to analyse problems which are either difficult or expensive to investigate experimentally, application of computational simulations expanded in various disciplines ranging from combustion to meteorology. Advances in CFD are strongly linked with the available computational power. Continued progress in computer technology, particularly in execution and storage performance, has strengthened the role of CFD in design and optimisation of engineering flow problems. CFD methods to simulate turbulent flows can be principally classified based on numerical accuracy and complexity as Direct Numerical Simulations (DNS), Large Eddy Simulations (LES) and Reynolds Averaged Navier-Stokes (RANS) simulations.

Turbulent combustion involves a range of different flow and chemical scales. Therefore, it stands as a complicated problem for computational modelling due to its multiscale nonlinear

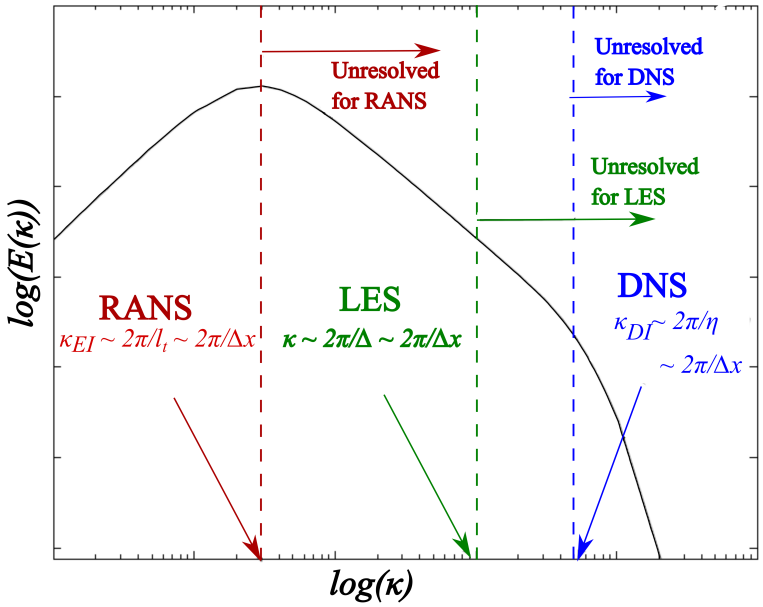

Figure 1.1: A schematic diagram of turbulent energy spectrum $E(\kappa)$ with wave number κ showing the capabilities of different simulation techniques [18].

nature [19] and strong interactions between different processes (e.g. chemical reaction, turbulence, mixing and phase change for multi-phase combustion) [20]. Various simulation methods with abilities to resolve different levels of flow have been developed to overcome these computational challenges. DNS plays a key role in terms of obtaining fundamental physical insight into complex turbulence-chemistry interaction processes and utilises this information for the development of high-fidelity turbulent combustion models. On the other hand, RANS simulation has significantly contributed to analysis of industrial combustion applications for more than the last four decades. Nowadays, LES is gaining popularity in both industry and research for physically and geometrically complex combustion problems with the support of the advancement of computational power. Resolution requirements for different simulation approaches are summarised in Fig. 1.1 based on a schematic diagram of turbulent energy spectrum $E(\kappa)$, where κ is the wave number magnitude, and turbulent kinetic energy is obtained as $k = \int_0^\infty E(\kappa)d\kappa$. It is clear from Fig. 1.1 that the grid size in RANS $\triangle x$ is in the order of integral length scale l_t. This indicates that the entire range of turbulent kinetic energy ($k = \int_0^\infty E(\kappa)d\kappa \approx \int_{2\pi/l}^{\pi/\eta} E(\kappa)d\kappa$ [21]) remains unresolved in the context of RANS simulations and modelling is necessary to approximate the unresolved physics. The grid spacing of LES $\triangle x$ is approximately equal to the filter size of LES $\triangle$ which ranges between integral length scale l_t and Kolmogorov length scale η. LES can capture the contribution of the turbulent large scales, while the effects of smaller scales need to be modelled. The grid size of DNS $\triangle x$ is required to be smaller than Kolmogorov length η which means that almost the whole

range of turbulent kinetic energy ($k = \int_0^\infty E(\kappa)d\kappa \approx \int_0^{\pi/\eta} E(\kappa)d\kappa$ [21]) is resolved but only the viscous dissipation of kinetic energy remains unresolved in DNS.

1.2.1 Direct Numerical Simulations (DNS)

Direct numerical simulation (DNS) is considered as the most accurate approach for simulating turbulent reacting flows as the conservation equations of mass, momentum, energy and species are solved without employing any filtering or averaging operation. DNS can capture micro-scale interactions between fluid dynamics and chemistry while resolving all relevant continuum scales (i.e. flame structures, Kolmogorov length, and time scales) on the grid without closure models for combustion and turbulence [22, 23]. Therefore, DNS can reveal detailed and highly precise information about the reacting flow field with a level of spatial and temporal resolution which can be considerably challenging to extract from an experiment. The fundamental information obtained from DNS database can be used for comprehensive investigation of the underlying physics of turbulent combustion and also for assessing and validating closure models for LES and RANS approaches.

DNS of turbulent combustion is the most demanding method in terms of computational cost due to high temporal and spatial resolution requirements imposed by small time and length scales of flow and flame structures. Computational requirements for DNS of homogeneous non-reacting turbulent flows can be determined based on turbulent Reynolds number as: $N_{DNS} \sim Re_t^{9/4}$, where N is the total number of grid points for a 3D simulation. The range of attainable Reynolds numbers for DNS is limited with the availability of computational power and performing DNS at realistic Reynolds numbers still remains prohibitively expensive. In the case of DNS of turbulent combustion, time and length scales of chemical reaction, which can sometimes be smaller than the Kolmogorov scales, need to be resolved. Additionally, a number of scalar transport equations require to be solved for chemically reacting flows depending on the chemical mechanism adopted for the simulation, and thus DNS of turbulent reacting flows is principally used for the purpose of research and is conducted usually for simple geometries (e.g. planar, spherical and V-shaped flames). The parameter range that can be achieved using DNS was illustrated by Poinsot and Veynante [24] on a combustion regime diagram, as shown in Fig. 1.2. It can be seen from Fig. 1.2 that in spite of high computational cost, DNS can be conducted for a broad range of operating conditions for piston engines and a relatively small range of operating conditions for gas turbines.

Some simplifications and assumptions are often applied to DNS of turbulent combustion flows to optimise the computational cost for a parametric study or to isolate an important component of fundamental physics which is not possible with experiments. Petascale supercomputers have lately become available and enabled the computations of three dimensional

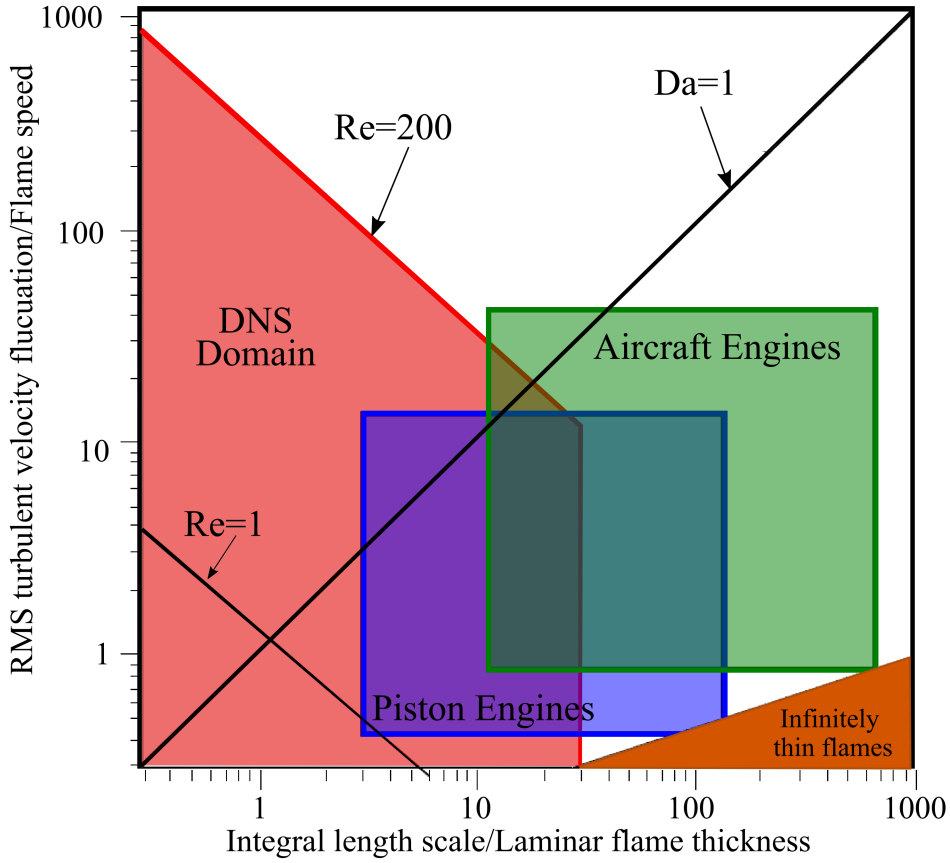

Figure 1.2: Limitations of direct numerical simulation tool for turbulent combustion applications in relation with practical combustion systems by Poinsot and Veynante [24].

DNS at laboratory scales with complex chemical mechanisms [22]. However, such simulations at large physical scales with complex mechanism are still not affordable for extensive parametric studies. Therefore, reduced or single step chemical schemes are typically considered based on the problem being investigated. Similarly, simplified assumptions for the temperature-dependent transport properties such as viscosity, thermal conductivity, and mass diffusivity are commonly made to avoid the added complexity in momentum, heat, and mass transfer mechanisms.

Another important challenge associated with DNS of turbulent combustion is the specification of the appropriate boundary conditions. Derivation of exact boundary conditions which ensure well-posedness is possible for Euler equations, but it remains a difficult task for Navier-Stokes equations due to insufficient theoretical understanding. Hence, boundaries are conventionally treated as periodic or impenetrable walls in the DNS of reacting flows. Nevertheless, inflow and outflow boundary conditions are required to be imposed for practical applications such as bluff body and Bunsen flames. In addition, acoustic and numerical waves interacting

with non-periodic boundaries can cause unphysical flow structures and an accurate control of these waves at open boundaries is of considerable importance for turbulent combustion simulations. Efforts have been devoted to develop precise and stable boundary conditions [25–27] based upon the pioneering study by Poinsot and Lele [28] who proposed the Navier-Stokes Characteristic Boundary Conditions (NSCBC) approach.

1.2.1.1 Dispersed phase treatments in the concept of DNS of turbulent multi-phase combustion

DNS of single phase combustion is established on an Eulerian grid description while in numerical solution of multi-phase combustion, liquid droplets in dispersed phase can either be tracked with a Lagrangian representation or be treated as a continuum by using Eulerian approach.

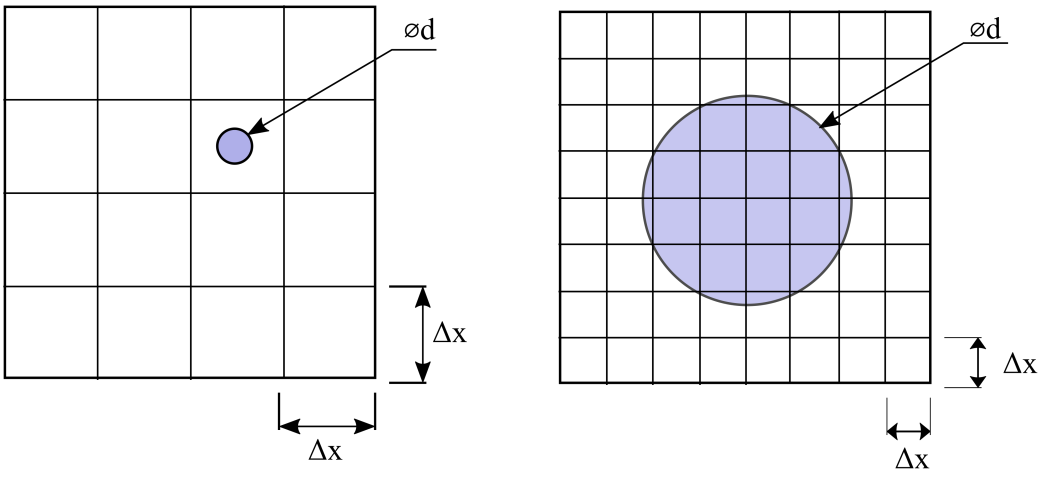

Figure 1.3: Illustration of point-source and resolved-surface approaches [29].

Lagrangian representation of the dispersed phase involves tracing of an individual droplet or a cluster of droplets while they travel in space and time. This flow configuration is referred to as Eulerian-Langrangian formulation in the literature. Lagrangian description of the liquid phase can be conducted with the particle-source approximation or the resolved-surface approach [29]. The particle-source approach is widely employed for the analysis of turbulent spray flames in dilute or very dilute regions which consist of only well-formed small spherical droplets [30]. Each individual droplet is presented as a sub-grid point source without resolving the quantities inside the droplet as shown in Fig. 1.3. Therefore, this approach is appropriate for simulations with droplets smaller than the Kolmogorov length scale (i.e. $d \ll \eta$). The particle-source approach provides an accessible alternative to fully resolved techniques in

terms of computational cost while predicting relevant phenomena with acceptable accuracy. On the other hand, the resolved-surface approach requires a high resolution of the continuous phase flow motion at the vicinity of each droplet which is then numerically coupled to the droplet surface [29]. Droplet position is ultimately advanced by the Lagrangian transport equation based on this momentum interaction. Thus, the grid resolution at the droplet surface needs to be sufficiently fine (i.e. $d \gg \triangle x$) to obtain a detailed stress distribution. The resolved-surface approach remains unfeasible for a large number of droplets due to the high resolution requirement around each droplet which yields a prohibitive computational cost. Point-source and resolved-surface approaches are schematically shown in Fig. 1.3.

Eulerian description of the liquid phase considers the dispersed phase as a continuum, and thus the liquid phase can be discretised using the same numerical scheme with the carrier gaseous phase [30]. This flow structure is reported as the Eulerian-Eulerian approach in the literature. The Eulerian framework can be categorised into mixed-fluid and separated-fluid techniques [29]. In the context of the mixed-fluid approach, liquid concentration is expressed as volume or mass fractions while the local relative velocities and temperature between two phases are assumed negligible. Navier-Stokes equations are solved as a single set for the flow mixture which are inherently two-way coupled. Applicability of the mixed-fluid treatment is limited with sufficiently small droplets which can exactly follow the local gaseous phase velocity [30]. On the other side, in separated-fluid approach, gaseous and liquid phases are assumed as two separate continuum which in turn results the solution of two sets of Navier-Stokes equations for each phase where source/sink terms are used for the coupling between two phases. Since the local relative velocities and temperature are considered, this approach can be performed for the analysis of large droplets. However, it is worth noting that computation of a larger number of conservation equations leads to a higher computational cost for the separated-fluid approach in comparison to the mixed-fluid method.

1.2.2 Large Eddy Simulations (LES)

Practical turbulent flow problems can be solved using Large Eddy Simulation (LES) without the high computational cost associated with DNS but with a higher level of accuracy than that offered by RANS [31]. The underlying concept of LES is based upon the idea that the majority of turbulent kinetic energy is contained in large scale flow structures which are strongly affected by flow and boundary conditions. On the contrary, small scales are considered as flow-independent and nearly universal which enables small scales to be applicable for sub-grid modelling. Hence, the Large Eddy Simulation technique eliminates the necessity to resolve small scale structures of turbulent reacting flows by applying an appropriate filtering in spectral or physical space. The coupling between small flow structures and large scales is provided

by closure models in LES governing equations using relevant sub-grid-scale (SGS) models. As a result of the three-dimensional and unsteady nature of simulations, the LES approach is capable of predicting the flows especially with large-scale unsteadiness (e.g. combustion instabilities and swirling flows [24, 32]) with a higher accuracy than RANS.

Large Eddy Simulations demand less computational resources in comparison to DNS, but still remain computationally expensive compared with RANS. Furthermore, in non-reacting flows, a part of turbulent kinetic energy spectrum is resolved by LES grid, and thus it offers more precise predictions than RANS. Thus, the accuracy of non-reacting flow LES is not strongly dependent on sub-grid turbulence modelling as in the case of RANS. As micro mixing and chemical reaction are associated with small scales, these scales are not resolved in the context of LES of reacting flows. Thus the LES of combustion needs closure models for micro mixing and filtered chemical reaction rate and, therefore, the accuracy of LES for combustion depends strongly on the precision of the model used. Validation of closure models for the filtered reaction rate term is one of the areas of ongoing research and DNS data have contributed significantly to the validation of existing models and the development of advanced new models. Although, simulations of practical combustion systems using LES method remains computationally expensive, recent LES of real engines [33] demonstrate the potential of this method for the analysis of practical combustion devices.

1.2.3 Reynolds Averaged Navier-Stokes (RANS) Simulations

The Reynold averaged Navier-Stokes (RANS) approach is the most popular and the least computationally intensive method for the simulation of turbulent flows. Instantaneous governing equations for mass, momentum, energy, and scalars are averaged using time or ensemble averaging depending on the reacting flow configuration in the context of RANS modelling. Since RANS simulations consider a set of averaged transport equations, all length and time scales of turbulent motion and chemical reaction remain unresolved, and models that can capture the statistical moments of turbulent fluctuations are required.

Modelling of the Reynolds stresses, the mean reaction rate, and the turbulent heat and species fluxes has attracted significant interests in the turbulent reacting flow community. Various versions of the $k-\varepsilon$ model [34] are usually employed to close the Reynolds stresses by solving the additional averaged transport equations for the turbulent kinetic energy k and its dissipation rate ε. It is worth mentioning that the $k-\varepsilon$ model was developed originally for non-reacting flows which poses some limitations for its application in reacting flow problems [24]. Highly non-linear dependency of the mean reaction rate on temperature and mass fractions creates the major challenge for the modelling of this term. Traditional moment closure approaches based on Taylor series expansion can not be employed for modelling the mean reaction term.

Therefore, alternative procedures using geometrical description based on flame surface area and turbulent mixing rates have been developed for modelling reaction rate closures. Furthermore, the classical gradient assumptions, which are extensively used for the modelling of turbulent fluxes of heat and species in non-reacting flows, are reported [35–40] to fail under some conditions in turbulent combustion problems due to counter-gradient turbulent transport.

Simulations of turbulent combustion in practical scales and operating conditions can be achieved using RANS based methods. Furthermore, RANS simulations provide the mean values of quantities with coarser grids relative to LES and DNS which enables the RANS approach to become the cheapest alternative in turbulent combustion simulation techniques. Thus, the RANS method is widely adopted in commercial combustion codes. However, the accuracy in RANS simulations strongly relies on the robustness of the closure models employed.

1.3 Research Aims and Objectives

Numerical analysis of turbulent combustion of droplet-laden mixtures is performed using the direct numerical simulation (DNS) technique with point source assumption for the liquid phase. The DNS method has become a standard tool for the analysis of turbulent reacting flows which involves the solution of Navier-Stokes equations without using any turbulence model. Understanding of fundamental turbulent flame behaviour can be improved with comprehensive and accurate DNS data which also helps to develop high-fidelity models based on physical information extracted from DNS data. Eulerian-Lagrangian formulation is adopted for the treatment of multi-phase flow and this is referred to as the carrier phase DNS in the rest of this thesis. Liquid droplets in the dispersed phase are assumed as sub-grid point sources in the context of the Lagrangian approach. The carrier phase DNS technique has commonly been employed to investigate the complex phenomena in multi-phase combustion [41–48]. Thus, it has reached sufficient maturity for the analysis of the combustion of dilute sprays.

To date, most DNS analyses on flame propagation in droplet-laden mixtures have been conducted for planar or jet flame configurations [41, 42, 47–56]. However, in many applications (e.g., automotive engines, accidental explosions), the flame is initiated as a spherical kernel, and it has been found that the evolution of spherically expanding premixed flames is fundamentally different from statistically planar turbulent premixed flames [57–61]. A similar conclusion was also drawn based on the experimental analysis of turbulent spray flames [62]. DNS of spherically expanding flames in droplet mists is yet to be reported in the existing literature. Therefore, DNS of spherically expanding spray flames propagating into fuel-droplet mists has been conducted in this thesis for a range of different initial droplet diameters, tur-

bulence intensities and for various overall equivalence ratios (i.e. fuel-lean, stoichiometric, fuel-rich). The present study focuses on the following aspects in turbulent droplet-laden mixtures:

- Simulation of turbulent combustion of monodisperse droplet-mist mixtures in spherically expanding flame kernels.

- A detailed parametric analysis to investigate the effects of droplet diameter, overall equivalence ratio (i.e. gaseous+liquid) and root-mean-square of turbulent velocity on the flame structure, evolution of burning rate and flame surface area, flame topologies and flame speeds in turbulent droplet-laden mixtures.

- A comparison between droplet cases and the corresponding premixed gaseous spherically expanding flames to reveal the impact of the presence of liquid fuel droplets on the aforementioned aspects.

- Analysis of the statistical behaviour of the coupling between the Eulerian (i.e. gaseous carrier phase) and Lagrangian (i.e. droplets) phases in the conservation equations of mass, momentum, energy, reaction progress variable and mixture fraction in the gaseous phase for spherically expanding flames propagating into droplet-laden mixtures.

- Investigation of the effects of droplet inertia on the flame evolution and reaction zone structure for spherically expanding spray flames.

- DNS of turbulent V-shaped spray flames to assess the influence of flame configuration on the flame behaviour.

- Discussion of the implications of the above physical information in the context of modelling of turbulent combustion in droplet-laden mixtures.

1.4 Thesis Outline

This PhD thesis will follow the structure summarised in Fig. 1.4. This chapter gives the necessary introduction to the broad area of computational analysis of turbulent reacting flows. Chapter 2 describes the relevant governing equations for liquid and gaseous phases and discusses the necessary assumptions for chemical mechanism and thermophysical properties. This will be followed by Chapter 3 where a brief summary of the findings from existing studies on flame propagation in droplet-laden mixtures and spherically expanding gaseous flame evaluation is presented. In Chapter 4 and 5, the effects of droplet diameter, turbulence intensity and overall equivalence ratio on flame-droplet-turbulence interactions are discussed along with the statistics of burning rate, flame wrinkling and flame speeds. Flame topologies are also introduced in Chapter 4 and statistics of flame topologies are examined. Chapter 6 deals with the impact of droplet inertia on the reaction zone structure in turbulent spray flames, and

focuses on the statistical analysis of two phase coupling. Turbulent V-shaped flames propagating into droplet-laden mixtures are considered to investigate the effects of large-scale flow geometry on flame propagation in droplet-laden mixtures in Chapter 7. Finally, Chapter 8 summarises the main findings of this investigation and identifies avenues of further research.

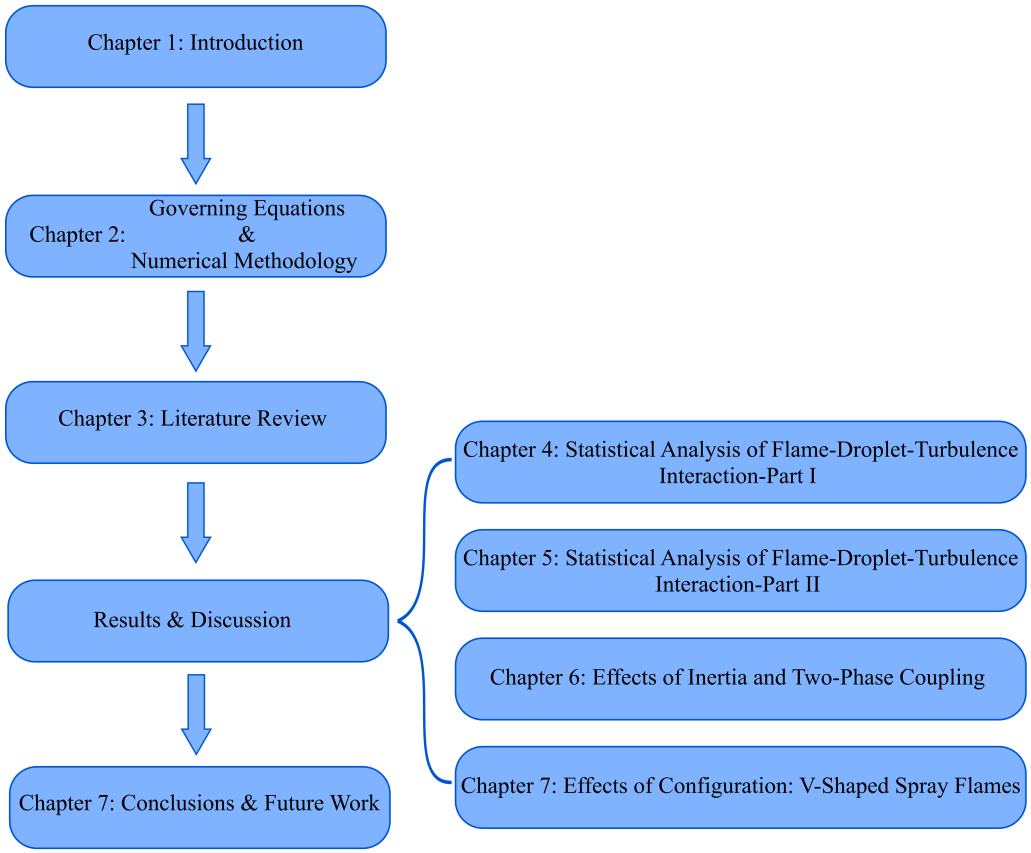

Figure 1.4: A flow chart of the current thesis outline

Chapter 2

Mathematical Background and Numerical Methodology

This chapter provides an overview of the governing equations for analysing the turbulent combustion of droplet-laden mixtures, along with the assumptions that are made for the current analysis. Subsequently, a brief introduction of numerical methodology and initialisation of the turbulent flow fields and reacting scalar fields is presented.

2.1 Mathematical Background

2.1.1 Problem Description

Direct Numerical Simulations of laminar and turbulent n-heptane spray flames are performed in two different configurations and a short description of the corresponding cases is given below. A three-dimensional compressible DNS code SENGA+ [42–44, 46–48] is used to generate the data based on a modified single-step irreversible chemical reaction.

- Spherically expanding flames propagating in fuel droplet-mists: A perfectly spherical kernel flame is allowed to propagate through a fuel droplet-mist from the centre of the cubic domain with partially non reflecting outflow boundaries in all directions as shown in Fig. 2.1.

- V-shaped flames propagating in fuel droplet-mists: Fuel is supplied in the form of liquid droplets at the inlet boundary which is placed on the left-hand side of the domain as illustrated in Fig. 2.1. Boundary conditions in the stream-wise direction (x−direction) are considered to be inflow and outflow whereas the remaining (i.e. y and z) directions

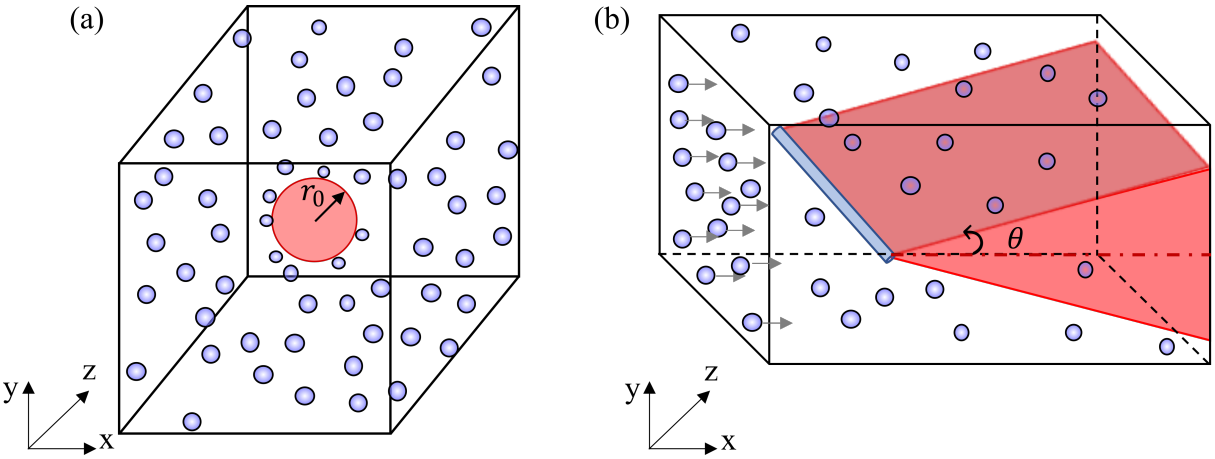

Figure 2.1: Description of computational domain (a) Spherically expanding spray flame (b) V-shaped spray flame

are assumed to be periodic. A flame holder is placed a certain distance from the inlet boundary following the previous study by Dunstan et al. [63, 64].

2.1.2 Governing Equations

2.1.2.1 Gaseous phase governing equations

Standard compressible Navier-Stokes equations for reactive flows are solved in an Eulerian frame of reference for the carrier gaseous phase, and these equations for mass, momentum, energy and species can be expressed in Cartesian tensor notation in the following manner:

$$\frac{\partial}{\partial t}\rho + \frac{\partial}{\partial x_k}\rho u_k = \Gamma_m \tag{2.1a}$$

$$\frac{\partial}{\partial t}\rho u_i + \frac{\partial}{\partial x_k}\rho u_k u_i = -\frac{\partial}{\partial x_i}P + \frac{\partial}{\partial x_k}\tau_{ki} + \dot{S}_{u_k} \tag{2.1b}$$

$$\frac{\partial}{\partial t}\rho E + \frac{\partial}{\partial x_k}\rho u_k E = -\frac{\partial}{\partial x_k}P u_k + \frac{\partial}{\partial x_k}\tau_{ki}u_i - \frac{\partial}{\partial x_k}q_k + \dot{S}_e \tag{2.1c}$$

$$\frac{\partial}{\partial t}\rho Y_\alpha + \frac{\partial}{\partial x_k}\rho u_k Y_\alpha = \dot{w}_\alpha - \frac{\partial}{\partial x_k}\rho V_{\alpha,k} Y_\alpha + \dot{S}_{Y_\alpha}, \text{ where } \alpha = 1,2,...,N \tag{2.1d}$$

In the above equations, ρ denotes gas density, u_j indicates the j^{th} component of fluid velocity. $\Gamma_m = -(1/\triangle V)\sum_d dm_d/dt$ is the source term in the mass conservation equation due to evap-

oration of liquid droplets, while $\triangle V$ is the cell volume and $m_d = (1/6)\rho_d \pi a_d^3$ is the droplet mass, with ρ_d and a_d being liquid density and droplet diameter, respectively. Additionally, P is pressure, E indicates the stagnation internal energy, Y_α is the mass fraction of species α in reacting mixture which contains N number of species in total with a reaction rate $\dot{w}_\alpha$. τ_{ki} is the viscous stress tensor defined by:

$$\tau_{ki} = \mu \left(\frac{\partial u_k}{\partial x_i} + \frac{\partial u_i}{\partial x_k} \right) - \frac{2}{3} \mu \frac{\partial u_j}{\partial x_j} \delta_{ki} \tag{2.2}$$

where μ is the dynamic viscosity and δ_{ki} is the Kronecker Symbol ($\delta_{ki} = 1$ for $k = i$, otherwise $\delta_{ki} = 0$). Pressure can be expressed following a perfect gas equation of state:

$$P = \rho R_0 \hat{T} \sum_{\alpha=1}^{N} \frac{Y_\alpha}{W_\alpha} \tag{2.3}$$

where R_0 is the universal gas constant, $\hat{T}$ is the temperature and W_α is the molecular weight of species α. The compatibility condition of the species mass fraction is $\sum_{\alpha=1}^{N} Y_\alpha$=1. The caloric equation of state is defined as:

$$E = C_v \hat{T} + \frac{1}{2} u_k u_k + \sum_{\alpha=1}^{N} h_\alpha^0 Y_\alpha \tag{2.4}$$

where C_v is the mixture heat capacity at constant volume and h_α^0 is the enthalpy of formation of species α. The heat flux vector q_k is defined as:

$$q_k = -\lambda \frac{\partial \hat{T}}{\partial x_k} + \rho \sum_{\alpha=1}^{N} h_\alpha V_{\alpha,k} Y_\alpha \tag{2.5}$$

where $h_\alpha = \int_{T_0}^{T} C_{p,\alpha} d\hat{T} + h_\alpha^0$ is the enthalpy of species α with $C_{p,\alpha}$ being the mass heat capacity at constant pressure of species α and $V_{\alpha,k}$ is the k^{th} component of the diffusion velocity V_α of species α. The compatibility condition of the diffusion velocity is given as: $\sum_{\alpha=1}^{N} \rho V_{\alpha,k} Y_\alpha = 0$. The chemical reaction rate $\dot{w}$ of species α for a reaction mechanism with N species and M step is given as:

$$\dot{w}_\alpha = W_\alpha \sum_{m=1}^{M} \left[(\upsilon''_{\alpha,m} - \upsilon'_{\alpha,m}) A_m \hat{T}^{n_m} \exp\left(-\frac{E_{ac,m}}{R_0 \hat{T}} \right) \prod_{\beta=1}^{N} \left(\frac{\rho Y_\beta}{W_\beta} \right)^{\upsilon'_{\beta,m}} \right] \tag{2.6}$$

In the above expression, for a given step m, stoichiometric coefficients corresponding to reactant and product are denoted by $\upsilon'_{\alpha,m}$ and $\upsilon''_{\alpha,m}$, respectively, n_m is the temperature exponent,

the frequency factor is represented by A_m, while $E_{ac,m}$ indicates the activation energy. Lastly, the coupling between liquid and gaseous phases is provided by additional source terms in the gaseous phase transport equations which are tri-linearly interpolated from the droplet's sub-grid position $\vec{x_d}$, to the eight surrounding nodes. The droplet source terms for momentum, energy and species mass fraction transport equations are expressed as:

$$\dot{S}_{u_k} = -\left(\frac{1}{\triangle V}\right)\sum_d \frac{d(m_d u_{k,d})}{dt} \tag{2.7a}$$

$$\dot{S}_e = -\left(\frac{1}{\triangle V}\right)\sum_d \frac{d(m_d E)}{dt} \tag{2.7b}$$

$$\dot{S}_{Y_\alpha} = -\left(\frac{1}{\triangle V}\right)\sum_d \frac{d(m_d Y_\alpha)}{dt} \tag{2.7c}$$

2.1.2.2 Liquid phase governing equations

A Lagrangian approach is adopted to simulate droplets dispersed within the carrier gaseous phase which is described using an Eulerian formulation to solve compressible Navier–Stokes equations as explained in the previous section. Fluid movement and temperature gradient inside the droplets are neglected, and droplet collision, agglomeration and microexplosion effects are assumed small [65]. Thus, only drag force drives the droplet momentum. The transport equations of position $\vec{x_d}$, velocity, $\vec{u_d}$, diameter, a_d and temperature, T_d of the individual droplet d are given following the approach proposed by Reveillon and Vervisch [51]:

$$\frac{d\vec{x_d}}{dt} = \vec{u_d} \tag{2.8a}$$

$$\frac{d\vec{u_d}}{dt} = \frac{\vec{u}(\vec{x_d},t) - \vec{u_d}}{\tau_d^u} \tag{2.8b}$$

$$\frac{da_d^2}{dt} = \frac{-a_d^2}{\tau_d^p} \tag{2.8c}$$

$$\frac{dT_d}{dt} = \frac{\hat{T}(\vec{x_d},t) - T_d - B_d L_v / C_p^G}{\tau_d^T} \tag{2.8d}$$

where L_v is the latent heat of vaporisation, and τ_d^u, τ_d^p and τ_d^T are relaxation timescales for droplet velocity, diameter and temperature, respectively, which can be expressed as [43, 44, 47, 48, 51]:

$$\tau_d^u = \frac{\rho_d a_d^2}{18 C_u \mu} \tag{2.9}$$

$$\tau_d^p = \frac{\rho_d a_d^2}{4\mu} \frac{Sc}{Sh_c ln(1+B_d)} \tag{2.10}$$

$$\tau_d^T = \frac{\rho_d a_d^2}{6\mu} \frac{Pr}{Nu_c ln(1+B_d)} \frac{C_p^L}{C_p^G} \tag{2.11}$$

where Sc is the Schmidt number, Pr is the Prandtl number, C_p^L is the specific heat for the liquid phase, $C_{u,d} = 1 + Re_d^{2/3}/6$ [66] is corrected drag coefficient. Here Re_d is the droplet Reynolds number, B_d is the Spalding mass transfer number, Sh_c and Nu_c are the corrected Sherwood and Nusselt numbers, which are defined as [43, 44, 47, 48, 51]:

$$Re_d = \frac{\rho \mid \vec{u}(\vec{x_d},t) - \vec{u_d} \mid a_d}{\mu} \tag{2.12}$$

$$B_d = \frac{Y_{F,d}^s - Y_F(\vec{x_d},t)}{1 - Y_{F,d}^s} \tag{2.13}$$

$$Sh_c = Nu_c = 2 + \frac{0.555 Re_d Sc}{(1.232 + Re_d Sc^{4/3})^{1/2}} \tag{2.14}$$

where $\vec{u}(\vec{x_d},t)$ indicates the gaseous phase velocity at droplet position and Y_F^s represents the fuel mass fraction Y_F at the surface of the droplet, is given by:

$$Y_{F,d}^s = \left(1 + \frac{W_{air}}{W_F}\left[\frac{P(\vec{x_d},t)}{P_F^s} - 1\right]\right)^{-1} \tag{2.15}$$

Here, W_{air} and W_F are respectively the molecular weight of air and fuel, $P(\vec{x_d},t)$ denotes the gas pressure at the droplet position and the partial pressure of the fuel vapor at the droplet surface P_F^s is obtained by the Clausius–Clapeyron equation as:

$$P_{F,d}^s = P_{ref} exp\left(\frac{L_v}{R}\left[\frac{1}{T_{ref}^s} - \frac{1}{T_d^s}\right]\right) \tag{2.16}$$

where T^s_{ref} is the boiling point of the fuel at pressure P_{ref}, R is the gas constant of the fuel and T^s_d is assumed to be T_d.

For the current study, a drag correction coefficient ($C_{u,d} = 1 + Re_d^{2/3}/6$) is used for large values of the droplet Reynolds number (i.e., $Re_d \gg 1$). The same procedure was employed in many previous analyses for spray combustion simulations [51, 53–55, 67]. Here, the droplet Reynolds number Re_d remains either of the order of unity or smaller than unity (i.e., $Re_d \leq 1$) in most (95%) locations (especially in the vicinity of the flame), and therefore, the exact nature of the corrections to the drag coefficient is not expected to have a significant influence on the simulation results. Accordingly, a simple drag coefficient correction has been considered in this analysis. Alternative empirical drag coefficients, including the blowing velocity at the droplet surface, were preferred in some previous analyses [49, 52, 68–70], but the nature of empiricism is likely to have higher order effects for small values of Re_d when DNS is carried out for the carrier phase and the droplets are considered as sub-grid point sources.

2.1.3 Boundary Conditions

Specification of appropriate boundary conditions is of significant importance for the DNS of unsteady compressible reacting flows due to the numerical and acoustic waves involved to the solution [71]. The coupling between acoustic waves and combustion can influence the behaviour of the flame front. Furthermore, numerical waves introduced by the discretisation scheme employed at the boundaries can cause unphysical oscillations. The methodology known as Navier-Stokes Characteristic Boundary Conditions (NSCBC) offers well-posed boundary conditions aiming to suppress numerical instabilities and artificial wave reflections at the boundary [28]. The NSCBC technique is discussed in detail by Poinsot and Lele [28] and a brief description of the methodology is provided here.

Poinsot and Lele [28] classified the boundary conditions into two categories in order to apply the NSCBC formulation to reacting flow problems. *Physical boundary conditions* involves the imposition of the desired physical behaviour of one or more of the dependent variables at the boundaries. Fixed outlet pressure specification at subsonic outflow boundaries can be given as an example for the application of physical boundary conditions. However, for most cases, the number of physical boundary conditions imposed to solve the problem remains less than the number of primitive variables. Hence, the variables which can not be explicitly specified by using physical boundary conditions requires the numerical solution of conservation equations at the boundaries. This approach is called as *numerical (soft) boundary condition*s. The NSCBC method principally extends the Euler Characteristic Boundary Conditions (ECBC) to the Navier-Stokes equations. Thus, the NSCBC approach adopts the well-posed ECBC procedure for the description of physical boundary conditions in a manner

that the Euler conditions (i.e. inviscid conditions) are imposed for the relevant variables, then additional expressions (i.e. viscous conditions) are supplied for the mechanisms which are specific to Navier-Stokes equations such as viscous dissipation and thermal diffusion. The numerical boundary conditions are established based on a local one-dimensional inviscid (LODI) approximation for the wave crossing the boundary in either direction.

In the context of LODI analysis, a locally one-dimensional conservative equation system can be written in the following generic form:

$$\frac{\partial \psi^*}{\partial t} + \frac{\partial F_i}{\partial x} + C_i'' = 0 \quad \text{where } i = 1 \text{ to } n \tag{2.17}$$

where $\psi^* = \{\rho, \rho u_k, \rho E, \rho Y_\alpha\}^T$ represents the conservative variable vector, F_i indicates the representative flux vector and C_i'' is a non-homogeneous term without derivatives. Eq. 2.17 can be recast based on the dependent variables ψ_i to obtain:

$$\frac{\partial \psi_i}{\partial t} + A_{ij}\frac{\partial \psi_j}{\partial x} + C_i = 0 \tag{2.18}$$

The relation between Eqs. 2.17 and 2.18 yields the expressions below:

$$\frac{\partial \psi^*}{\partial t} = P_{ij}\frac{\partial \psi_j}{\partial t} \quad \text{where} \quad P_{ij} = \frac{\partial \psi_i^*}{\partial \psi_j} \tag{2.19}$$

$$\frac{\partial F_i}{\partial t} = Q_{ij}\frac{\partial \psi_j}{\partial t} \text{ where } Q_{ij} = \frac{\partial F_i}{\partial \psi_j} \tag{2.20}$$

where $A_{ij} = P_{ij}^{-1}Q_{kj}$ and $C_i = P_{ik}^{-1}C_k''$, while A_{ij}, P_{ij} and Q_{ij} being the components of the $n \times n$ matrices. The matrix A_{ij} has n linearly independent eigenvectors which yield to the following relation $S_{ik}A_{kp}S_{pj} = \Lambda_{ij}$ where S_{ij} is eigenvector matrix and Λ_{ij} is diagonal matrix with $\Lambda_{ij=i}$ being equal to the eigenvalues λ_i. Considering the eigenvector matrix Λ_{ij}, Eq. 2.18 can be rearranged as:

$$S_{ij}\frac{\partial \psi_j}{\partial t} + \Lambda_{ik}S_{kj}\frac{\partial \psi_j}{\partial x} + S_{ij}C_j = 0 \tag{2.21}$$

Following this, a new vector $\overrightarrow{\varsigma}$ can be constructed such that:

$$d\varsigma_i = S_{ij}d\psi_j + S_{ij}C_j dt \tag{2.22}$$

which leads to further recast Eq. 2.21 in the following forms:

$$\frac{\partial \varsigma_i}{\partial t} + \Lambda_{ik}\frac{\partial \psi_k}{\partial x} = 0 \quad \text{and} \quad \frac{\partial \varsigma_i}{\partial t} + \lambda_i\frac{\partial \psi_i}{\partial x} = 0 \tag{2.23}$$

Eq. 2.23 indicates a set of wave equations with a characteristic velocity λ_i and a wave amp-

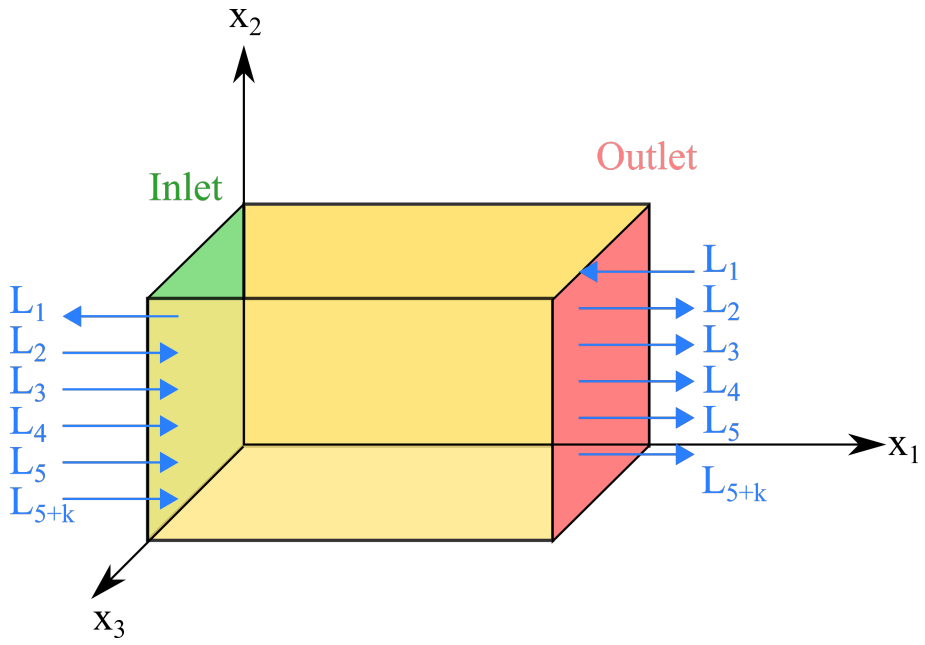

Figure 2.2: Schematic of the wave amplitude variations L_i interacting with the inflow and outflow boundaries.

litude variation $L_i = \Lambda_{ik} S_{kj} (\partial \psi_j / \partial x)$. The LODI scheme not only ensures the well-posedness of the problem by imposing the numerical boundary conditions but also provides the derivatives normal to the boundary. The NSCBC approach uses the equivalent formulations of L_i in place of such derivatives. These L_i expressions represent the different characteristic physical waves which interact with the boundary under inviscid flow conditions. The L_i formulations can be obtained by carrying out a characteristic analysis of three dimensional extension of Eqs. 2.17-2.23 [72]. The wave amplitude variations crossing the inlet and outlet boundaries are schematically illustrated in Fig. 2.2.

Following the procedure briefly presented earlier, the LODI system can be obtained in terms of primitive variables:

$$\frac{\partial}{\partial t}\begin{bmatrix} \rho \\ P \\ u_1 \\ u_2 \\ u_3 \\ Y_\alpha \end{bmatrix} + \begin{bmatrix} \left[L_2 + \frac{1}{2}(L_5 + L_1)\right]/a^2 \\ (L_5 + L_1)/2 \\ (L_5 - L_1)/2\rho a \\ L_3 \\ L_4 \\ L_{5+\alpha} \quad \text{for} \quad \alpha = 1, N \end{bmatrix} = \begin{bmatrix} 0 \\ 0 \\ 0 \\ 0 \\ 0 \\ 0 \end{bmatrix} \tag{2.24}$$

Furthermore, the wave amplitude variations L_i $(1 \leq i \leq 5+N)$ which corresponds to the temporal rate of change of the amplitudes of the different acoustic, convective, or entropy waves

can be expressed considering the x_1- direction normal to the boundary [24, 72]:

$$L = \begin{bmatrix} L_1 \\ L_2 \\ L_3 \\ L_4 \\ L_5 \\ L_{5+i} \end{bmatrix} = \begin{bmatrix} \lambda_1 \left(\frac{\partial P}{\partial x_1} - \rho a \frac{\partial u_1}{\partial x_1} \right) \\ \lambda_2 \left(a^2 \frac{\partial \rho}{\partial x_1} - \frac{\partial P}{\partial x_1} \right) \\ \lambda_3 \frac{\partial u_2}{\partial x_1} \\ \lambda_4 \frac{\partial u_3}{\partial x_1} \\ \lambda_5 \left(\frac{\partial P}{\partial x_1} + \rho a \frac{\partial u_1}{\partial x_1} \right) \\ \lambda_{5+\alpha} \frac{\partial Y_\alpha}{\partial x_1} \quad \text{for} \quad \alpha = 1, N \end{bmatrix} \tag{2.25}$$

In the above equation, the characteristic wave velocities λ_i can be written in the following manner:

$$\lambda_1 = u - a, \quad \lambda_2 = \lambda_3 = \lambda_4 = \lambda_{5+i} = u, \quad \lambda_5 = u + a \tag{2.26}$$

where the velocities of sound waves travelling in the negative and positive directions x_1- direction are represented by λ_1 and λ_5, the velocity of entropy advection is denoted with λ_2, the velocities that correspond to the advection in the x_2- and x_3- directions are given by λ_3 and λ_4, respectively, while λ_{5+i} is the velocity for the species advection. Lastly, a is the local speed of sound defined by $a^2 = \gamma P/\rho$ with $\gamma = C_p^G/C_v^G$ being the ratio of specific heat.

The NSCBC procedure can be carried out to implement a broad range of different boundary conditions. However, the boundary conditions only adopted in the current thesis will be briefly explained in the following sections for the sake of brevity.

2.1.3.1 Inlet boundary condition

In the present thesis, an inlet boundary condition is specified on the left side of the streamwise direction for the simulations of V-shaped flames propagating in fuel droplet-mists, while the other end of the streamwise direction being outlet and the rest is taken to be periodic. Unsteady velocity signals are introduced at the inlet plane to maintain the turbulence in the domain throughout the simulation time following the methodology discussed by Chakraborty and Cant [73]. For this purpose, a three-dimensional incompressible velocity field is generated using the Batchelor-Townsend energy spectrum, as described later in this chapter. This velocity field is then scanned by a plane in order to apply the velocity fluctuations to the inlet face of the domain. At the inlet plane, density ρ, mass fractions of species Y_α and all components of the turbulent flow fluctuations u_i are imposed following the LODI procedure as explained in the previous section. The wave amplitude variations specified at the inlet boundary are given as

below:

$$L_1 = (u_1 - a)\left(\frac{\partial P}{\partial x_1} - \rho a \frac{\partial u_1}{\partial x_1}\right) \tag{2.27}$$

$$L_3 = -\frac{\partial u_2}{\partial t} \tag{2.28}$$

$$L_4 = -\frac{\partial u_3}{\partial t} \tag{2.29}$$

$$L_5 = L_1 - 2\rho a \frac{\partial u_1}{\partial t} \tag{2.30}$$

$$L_{5+\alpha} = -\frac{\partial Y_\alpha}{\partial t} \tag{2.31}$$

$$L_2 = -\frac{1}{2}(L_1 + L_5) - a^2 \frac{\partial \rho}{\partial t} \tag{2.32}$$

2.1.3.2 Partial non-reflecting outlet boundary condition

In the current thesis, all sides of the cubic domain in which computing spherically expanding turbulent flames in droplet-mists are assumed as partial non-reflecting outlet boundaries. Employing the perfectly reflecting outlet boundaries for the simulations of compressible flows can lead to inaccurate results, on the contrary drifting of the mean pressure can be observed by using the perfectly non-reflecting outlet boundaries. Therefore, partially non-reflecting boundary conditions is adopted which provide the controlled acoustic wave reflections which conveys the pressure information from the outside flow through the outlet.

Characteristic waves with the wave amplitudes L_2, L_3, L_4, L_5 and $L_{5+\alpha}$ leave the domain at the partially non-reflecting boundary whereas the wave with L_1 reaches the boundary from outside of the domain. Thus, it is appropriate to control the mean pressure over the wave amplitude L_1 to sustain well-posedness of the simulation. Hence, the local pressure value at the outlet can be maintained to a value close to P_∞ by the reflected waves, if this pressure value deviates from P_∞. The amplitude of entering wave L_1 can be expressed in the following manner:

$$L_1 = K(P - P_\infty) \tag{2.33}$$

Here, K is a constant which is defined by Rudy and Strikwerda [74] as below:

$$K = \sigma(1 - Ma_{max}^2)a/L \tag{2.34}$$

where Ma_{max} is the maximum Mach number in the flow and σ is the relaxation parameter. Setting the relaxation parameter σ to zero leads the amplitude of incoming waves to 0, which indicates a perfectly non-reflecting condition. On the other side, a large value of σ allows the strong reflections from the outlet boundary. In the current analysis, the relaxation parameter σ is chosen as 0.25. In addition to this, viscous conditions should be specified for the analysis of turbulent reacting flows as:

$$\text{Derivatives of the tangential viscous stresses:} \quad \frac{\partial \tau_{12}}{\partial x_1} = 0, \quad \frac{\partial \tau_{13}}{\partial x_1} = 0 \tag{2.35}$$

$$\text{Derivatives of the normal heat flux (i.e. } q_1 = -\lambda \partial \hat{T}/\partial x_1) : \quad \frac{\partial q_1}{\partial x_1} = 0 \tag{2.36}$$

$$\text{Derivatives of the scalar fluxes (i.e. } M_{\alpha 1} = -\rho D_\alpha \partial Y_\alpha / \partial x_1) : \quad \frac{\partial M_{\alpha 1}}{\partial x_1} = 0 \tag{2.37}$$

2.1.4 Chemical Mechanism

A modified single-step Arrhenius-type irreversible chemical reaction [75] is used for the current analysis for the purpose of a detailed parametric analysis:

$$1 \text{ unit mass of } Fuel + s \text{ unit mass of } Ozidiser \rightarrow (1+s) \text{ unit mass of } Products \tag{2.38}$$

where s is the mass of the oxygen consumed per unit mass of fuel consumption. Based on the modified Arrhenius-type chemical mechanism, the fuel reaction rate can be expressed as:

$$\dot{w}_F = -\rho B^* Y_F Y_O exp\left(-\frac{\beta(1-T)}{1-\alpha_{hr}(1-T)}\right) \tag{2.39}$$

where Y_O is the oxygen mass fractions. The heat release parameter α_{hr}, the normalised pre-exponential factor B^*, the nondimensional temperature T and the Zel'dovich number β, can be given as follows:

$$\alpha_{hr} = \frac{\tau}{\tau + 1} \tag{2.40}$$

$$B^* = B.exp\left(-\frac{\beta}{\alpha_{hr}}\right) \tag{2.41}$$

$$T = \frac{\hat{T} - T_0}{T_{ad(\phi_g=1)} - T_0} \tag{2.42}$$

$$\beta = \frac{E_{ac}(T_{ad(\phi_g=1)} - T_0)}{R_0 T^2_{ad(\phi_g=1)}} \tag{2.43}$$

Here, $\tau = (T_{ad(\phi_g=1)} - T_0)/T_0$ is a heat release parameter, T_0 is the unburned gas temperature, $T_{ad(\phi_g=1)}$ is the adiabatic flame temperature for the stoichiometric mixture. According to the model of Fernández-Tarrazo et al. [75], the activation energy E_{ac} and the heat of combustion can be calculated based on the gaseous equivalence ratio $\phi_g = FAR/(FAR)_{st}$ where FAR and $(FAR)_{st}$ are the actual and stoichiometric fuel-air ratios in the gaseous mixture, respectively. The Zel'dovich number β, is defined as $\beta = 6f(\phi_g)$, where $f(\phi_g)$ is a function of gaseous phase equivalence ratio ϕ_g:

$$f(\phi_g) = \begin{cases} 1.0 + 8.250(\phi_g - 0.64)^2, & \phi_g \leq 0.64 \\ 1.0, & 0.64 < \phi_g \leq 1.07 \\ 1.0 + 1.443(\phi_g - 1.07)^2, & \phi_g \geq 1.07 \end{cases} \tag{2.44}$$

The heat release per unit mass of fuel $H_{(\phi_g)} = \left[\left(T_{ad(\phi_g)} - T_0\right) C_p^G\right] / \left[Y_{F,0(\phi_g)} - Y_{F,b(\phi_g)}\right]$ is given by $H_{(\phi_g)}/H_{(\phi_g=1)} = 1$ for $\phi_g \leq 1$ and $H_{(\phi_g)}/H_{(\phi_g=1)} = 1 - \alpha_H(\phi_g - 1)$ for $\phi_g > 1$, while $\alpha_H = 0.18$, $Y_{F,0(\phi_g)}$ and $Y_{F,b(\phi_g)}$ are the fuel mass fractions in the unburned and burned gases, respectively, for a premixed flame of equivalence ratio ϕ_g [75].

The modified single-step Arrhenius-type irreversible chemical reaction is adopted for the current study for the purpose of computational economy because three-dimensional DNS simulations with detailed chemistry are extremely expensive for a parametric analysis involving three initial droplet diameters, three different overall equivalence ratios, three different flow conditions and two different flame configurations as carried out in this study. The modified single-step chemical mechanism used for this analysis provides realistic equivalence ratio dependence of unstrained laminar burning velocity, especially for fuel-rich mixtures involving hydrocarbon fuels. It has been shown in Fig. 1 in Tarrazo et al. [75] that the mechanism compares favourably with both experiments and detailed chemistry simulations for all hydrocarbon-air flames. It has been demonstrated by Swaminathan and Bray [76] based on experimental data that the normalised laminar burning velocity $S_{b(\phi_g)} / \left[S_{b(\phi_g)}\right]_{max}$ dependence of equivalence ratio ϕ_g is not sensitive to the choice of fuel for hydrocarbon-air mixtures. For

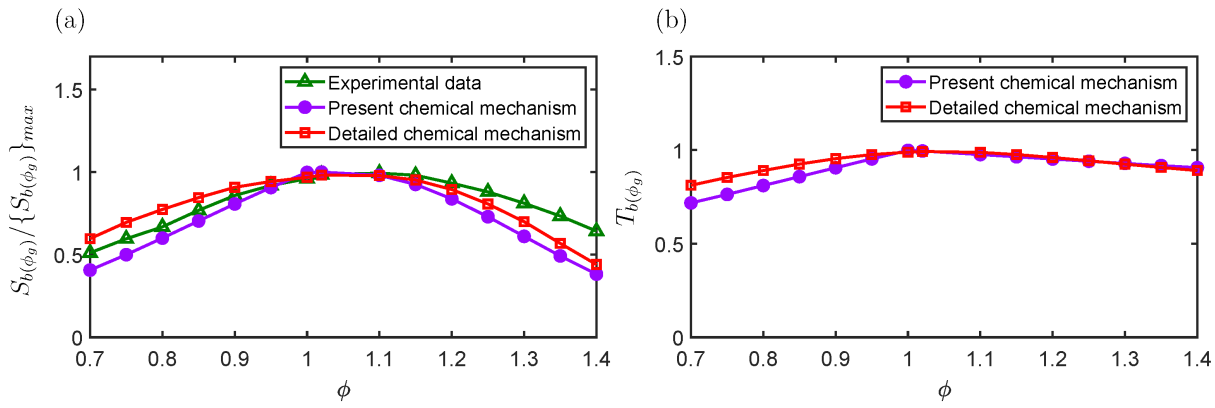

Figure 2.3: Variations of the (a) normalised laminar burning velocity $S_{b(\phi_g)}/\left[S_{b(\phi_g)}\right]_{max}$ and (b) normalised adiabatic flame temperature $T_{b(\phi_g)} = (T_{ad(\phi_g)} - T_0)/(T_{ad(\phi_g=1)} - T_0)$ with equivalence ratio ϕ_g for n-heptane obtained from modified single step chemistry [75], detailed chemical mechanism [79] and experimental [78] data.

further information on this behaviour in hydrocarbon-air flames, the interested readers are directed to Malkeson and Chakraborty [77].

Comparisons between the laminar burning velocity $S_{b(\phi_g)}$ of n-heptane from experiments [78], simulations with detailed chemical mechanism [79] and modified single step chemistry used in this study are presented in Fig. 2.3a. It is shown that the modified single-step chemistry by Tarrazo et al. [75] captures the realistic variation of laminar burning velocity with a gaseous equivalence ratio ϕ_g in the context of the thermo-chemistry used in this study. Moreover, the dependence of adiabatic flame temperature $T_{b(\phi_g)}$ to gaseous equivalence ratio ϕ_g for a detailed chemical mechanism and the modified single-step mechanism is given in Fig. 2.3b. Similarly, there is no significant difference between the profiles obtained from the modified single step and multi-step detailed chemical mechanisms [79]. The small differences between the variations of $S_{b(\phi_g)}/\left[S_{b(\phi_g)}\right]_{max}$ and $T_{b(\phi_g)}$ between the different chemical mechanisms and experimental data [78] arise due to the differences in the treatments of molecular transport characteristics.

Previous simple chemistry DNS analyses [57, 59, 80–83] have been found to capture correctly the flame propagation statistics extracted from detailed chemistry DNS data [84–89] for turbulent premixed flames and this holds true in particular for curvature effects. Nevertheless, the present findings based on moderate turbulence intensity and simple chemical mechanism need to be validated further for higher values of turbulent Reynolds number (and consequently different Da and Ka) in the presence of detailed chemistry and transport.

2.1.5 Non-Dimensional Numbers

Non-dimensional forms of gaseous governing equations are solved in the context of the current DNS study by using reference values of principal variables (i.e. u_0, l_0, t_0, ρ_0 and T_0) which are presented below:

- The unstrained laminar burning velocity of the stoichiometric mixture $S_{b(\phi_g=1)}$ is considered as reference velocity u_0.
- The reference length scale l_0 is taken to be a function of the thermal flame thickness of the stoichiometric mixture δ_{st} (see Eq. 2.45).
- Reference time t_0 can be obtained with l_0/u_0.
- Unburned gas density ρ_0 is considered as reference density.
- Unburned gas temperature T_0 is considered as reference temperature.

The thermal flame thickness of the unstrained stoichiometric laminar premixed flame is estimated by:

$$\delta_{st} = \frac{T_{ad(\phi_g=1)} - T_0}{max \mid \nabla \hat{T} \mid_L} \tag{2.45}$$

The reference pressure P_0 is assumed as $P_0 = \rho_0 u_0^2$ which represents dynamic rather than thermo-chemical effects. Further reference values for the transport quantities involving dynamic viscosity μ, thermal conductivity λ, the density-weighted mass diffusivity ρD and the gaseous specific heats at constant pressure and volume C_p^G and C_v^G are taken to be constant and independent of temperature for the current study. Soret and Dufour effects are neglected for the present analysis. In addition, non-dimensional parameters employed in this study are listed as follows:

- $Re = (\rho_0 u_0 l_0)/\mu$, Reynolds number describes the ratio of inertial force to viscous force.
- $Pr = (\mu C_p^G)/\lambda$, Prandtl number represents the relative importance of momentum diffusion to thermal diffusion.
- $Sc = \mu/(\rho D)$, Schmidt number compares momentum diffusion versus mass diffusion, with D being the mass diffusion coefficient.
- $Ma = u_0/a_0$, Mach number provides the ratio of fluid velocity to the speed of sound in the same fluid.

- $Le = \lambda/(\rho C_p^G D)$, Lewis number describes the ratio of thermal diffusivity to mass diffusivity.

Following the aforementioned non-dimensionalisation operations, governing equations for the carrier phase can be rewritten in non-dimensional form in the following manner:

$$\frac{\partial}{\partial t^+}\rho^+ + \frac{\partial}{\partial x_k^+}\rho^+ u_k^+ = \Gamma_m^+ \tag{2.46a}$$

$$\frac{\partial}{\partial t^+}\rho^+ u_i^+ + \frac{\partial}{\partial x_k^+}\rho^+ u_k^+ u_i^+ = -\frac{\partial}{\partial x_i^+}P^+ + \frac{1}{Re}\frac{\partial}{\partial x_k^+}\tau_{ki}^+ + \dot{S}_{u_k}^+ \tag{2.46b}$$

$$\frac{\partial}{\partial t^+}\rho^+ E^+ + \frac{\partial}{\partial x_k^+}\rho^+ u_k^+ E^+ = -(\gamma-1)Ma^2\frac{\partial}{\partial x_k^+}P^+ u_k^+ + \frac{1}{Re}(\gamma-1)Ma^2\frac{\partial}{\partial x_k^+}\tau_{ki}^+ u_i^+ + \frac{\tau}{RePr}\frac{\partial}{\partial x_k^+}\left[\frac{\partial T}{\partial x_k^+}\right] + \dot{S}_e^+ \tag{2.46c}$$

$$\frac{\partial}{\partial t^+}\rho^+ Y_\alpha + \frac{\partial}{\partial x_k^+}\rho^+ u_k^+ Y_\alpha = \dot{w}_\alpha^+ - \frac{1}{ReSc}\frac{\partial}{\partial x_k^+}\left[\rho D\frac{\partial Y_\alpha}{\partial x_k^+}\right] + \dot{S}_{Y_\alpha}^+, \text{ where } \alpha = 1,2,...,N \tag{2.46d}$$

where the non-dimensional quantities can be given by:

$$\rho^+ = \frac{\rho}{\rho_0},\quad u_j^+ = \frac{u_j}{u_0},\quad P^+ = \frac{1}{\gamma Ma^2}\rho^+(1+\tau T),\quad E^+ = \frac{1}{\gamma}(1+\tau T) + \frac{1}{2}(\gamma-1)Ma^2 u_j^+ u_j^+ \tag{2.47a}$$

$$\Gamma_m^+ = \frac{\Gamma l_0}{\rho_0 u_0},\quad \dot{S}_{u_k}^+ = \frac{\dot{S}_{u_k} l_0}{\rho_0 u_0^2};\quad \dot{S}_e^+ = \frac{\dot{S}_e l_0}{\rho_0 C_p^G T_0 u_0};\quad \dot{S}_{Y_\alpha}^+ = \frac{\dot{S}_{Y_\alpha} l_0}{\rho_0 u_0} \tag{2.47b}$$

2.1.6 Reacting Mixture Variables

The evaporation process of dispersed liquid droplets in air yields an inhomogeneous reacting mixture ahead of the flame front. Coexistence of premixed and diffusion combustion in spray flames [51, 90] enhances the complexity in understanding and modelling of combustion of droplet-laden mixtures. The variables such as mixture fraction, flame index and reaction progress variable are useful for describing combustion process in droplet-laden mixtures.

2.1.6.1 Mixture fraction

The mixing between fuel vapour and oxidiser is obtained by molecular diffusion and dispersion induced by turbulent motion following the liquid droplet evaporation. The local mixture composition can be quantified using the mixture fraction which can be expressed in terms of the local mass fractions of the fuel Y_F and the oxidiser Y_O as [91, 92]:

$$\xi = \frac{Y_F - Y_O/s + Y_{O\infty}/s}{Y_{F\infty} + Y_{O\infty}/s} \tag{2.48}$$

where $Y_{O\infty}$ is the oxygen mass fraction in air and $Y_{F\infty}$ is the fuel mass fraction in the pure fuel stream. Equivalence ratio ϕ can be rewritten based on the mixture fraction ξ [93]:

$$\phi = \frac{\xi}{1-\xi}\frac{(1-\xi_{st})}{\xi_{st}} \quad \text{while} \quad \xi_{st} = \frac{Y_{O\infty}}{sY_{F\infty}+Y_{O\infty}} \tag{2.49}$$

This indicates that the mixture fraction can be expressed as a normalised form of equivalence ratio.

2.1.6.2 Flame index

The mode of combustion can be characterised by the flame index which distinguishes premixed and diffusion modes of combustion [70, 94–96]. In this thesis, a normalised flame index FI is used following the definition by Yamashita et al. [94]:

$$FI = \frac{(\nabla Y_F \cdot \nabla Y_O)}{(|Y_F||Y_O|)} \tag{2.50}$$

The FI takes a positive value for a premixed mode of combustion while FI is negative for non-premixed combustion mode, as depicted in Fig.2.4.

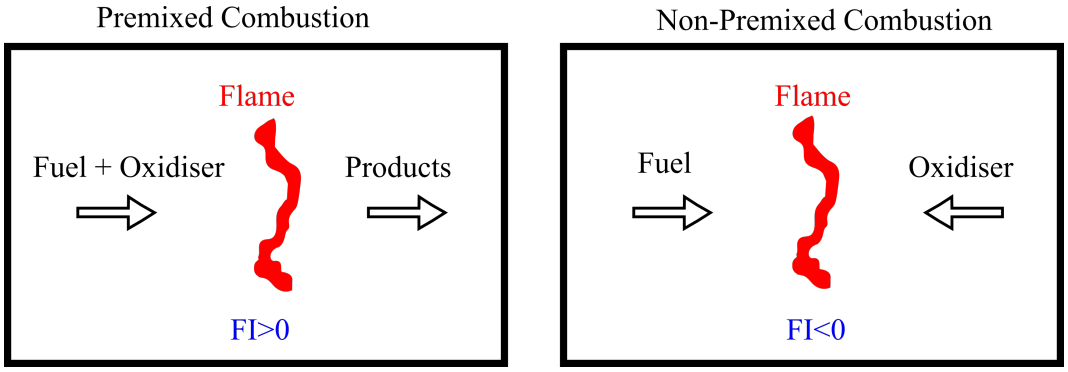

Figure 2.4: Premixed and non-premixed combustion modes

2.1.6.3 Reaction progress variable

It is useful to define a reaction progress variable c, based on oxygen mass fraction Y_O and mixture fraction ξ in the following manner in order to identify the reaction zone for turbulent combustion of droplet laden mixtures [43–45, 47, 48]:

$$c = \frac{(1-\xi)Y_{O\infty} - Y_O}{(1-\xi)Y_{O\infty} - \max\left(0, \frac{[\xi_{st}-\xi]}{\xi_{st}}\right) Y_{O\infty}} \tag{2.51}$$

The reaction progress variable increases monotonically from zero in unburned reactants to unity in burned products, while allowing an appropriate tracking for the position where the chemical reaction takes place.

The transport equation of the reaction progress variable, c can be obtained by using the transport equations for oxidiser mass fraction Y_O and mixture fraction ξ as [47, 48]:

$$\frac{\partial(c\rho)}{\partial t} + \nabla\cdot(\rho\overrightarrow{u}c) = \nabla\cdot(\rho D\nabla c) + \dot{w}_c + \dot{A}_c + \dot{S}_c^* \tag{2.52}$$

where $\dot{w}_c$ represents the reaction rate of reaction progress variable, $\dot{A}_c$ is the cross-scalar dissipation term associated with mixture inhomogeneity and $\dot{S}_c^* = \dot{S}_{liq,c} + \Gamma_m c$ indicates the source/sink term arising due to droplet evaporation.

The reaction rate of the reaction progress variable $\dot{w}_c$ can be expressed as [47, 48]:

$$\dot{w}_c = \begin{cases} -\frac{\xi_{st}\dot{w}_O}{Y_{O\infty}\xi(1-\xi_{st})}, & \xi \le \xi_{st} \\ -\frac{\dot{w}_O}{Y_{O\infty}(1-\xi)}, & \xi > \xi_{st} \end{cases} \tag{2.53}$$

where $\dot{w}_O$ denotes the reaction rate of oxidiser. The terms associated with mixture inhomogeneity $\dot{A}_c$ and droplet evaporation $\dot{S}_{liq,c}$ are given as [47, 48]:

$$\dot{S}_{liq,c} = \begin{cases} -\frac{\xi_{st}}{Y_{O\infty}\xi^2(1-\xi_{st})}\left[\xi\dot{S}_O + (Y_{O\infty}-Y_O)\dot{S}_\xi\right], & \xi \le \xi_{st} \\ -\frac{1}{Y_{O\infty}(1-\xi)^2}\left[(1-\xi)\dot{S}_O + Y_O\dot{S}_\xi\right], & \xi > \xi_{st} \end{cases} \tag{2.54}$$

$$\dot{A}_c = \begin{cases} \frac{2\rho D}{\xi}\nabla c\cdot\nabla\xi, & \xi \le \xi_{st} \\ \frac{-2\rho D}{(1-\xi)}\nabla c\cdot\nabla\xi, & \xi > \xi_{st} \end{cases} \tag{2.55}$$

In Equation 2.54, $\dot{S}_\xi^* = \dot{S}_\xi + \Gamma_m\xi$ is the droplet source term in the mixture fraction transport equation given by:

$$\frac{\partial(\xi\rho)}{\partial t} + \nabla\cdot(\rho\overrightarrow{u}\xi) = \nabla\cdot(\rho D\nabla\xi) + \dot{S}_\xi^* \tag{2.56}$$

where $\dot{S}_\xi$ is expressed as: $\dot{S}_\xi = (\dot{S}_F - \dot{S}_O/s)/(Y_{F\infty} + Y_{O\infty}/s)$ while $\dot{S}_F = \Gamma_m(1-Y_F)$ and $\dot{S}_O = -\Gamma_m Y_O$ being the droplet source/sink terms in the mass fraction transport equations for fuel and oxygen, respectively.

2.1.7 Flame Speed Definitions

Propagation mechanism of the flame surface is an essential component of combustion theory. Therefore, various concepts have been adopted to define and quantify flame propagation rates in terms of different flame speeds. The definitions of flame speed presented here are limited only for those utilised in the context of the current study.

The laminar burning velocity $S_{b(\phi_g)}$ is the velocity at which a premixed flame front propagates with respect to the unburned gas mixture in the direction normal to the flame surface [24, 93]. Considering a one dimensional steady state planar laminar premixed flame configuration, $S_{b(\phi_g)}$ can be quantified with the integration of the fuel reaction rate from the unburned gas mixture (i.e. $x \to -\infty$) to burned gas mixture (i.e. $x \to +\infty$) as follows [24]:

$$S_{b(\phi_g)} = -\frac{1}{\rho_0(Y_{F,0} - Y_{F,b})} \int_{-\infty}^{+\infty} \dot{w}_F dx \tag{2.57}$$

The displacement speed S_d measures the movement of a chosen scalar isosurface (e.g. temperature, fuel mass fraction or reaction progress variable) normal to itself with respect to an initially coincident material surface [86, 97, 98]. An expression for S_d can be derived utilising the kinematic form of reaction progress variable transport equation:

$$\frac{\partial c}{\partial t} + u_j \frac{\partial c}{\partial x_j} = S_d \mid \nabla c \mid \tag{2.58}$$

$$S_d = \frac{\left[\nabla \cdot (\rho D \nabla c) + \dot{w}_c + \dot{A}_c + \dot{S}_{liq,c}\right]}{\rho \mid \nabla c \mid} = S_n + S_t + S_r + S_z + S_s \tag{2.59}$$

where S_n, S_t and S_r are the normal diffusion, tangential diffusion, reaction components, and S_z and S_s are the contributions due to cross-scalar dissipation term and droplet evaporation, respectively, which are defined as:

$$S_n = \frac{\vec{N}\cdot\nabla(\rho D \vec{N}\cdot\nabla c)}{\rho|\nabla c|}; \quad S_t = -2D\kappa_m; \quad S_r = \frac{\dot{w}_c}{\rho|\nabla c|}; \quad S_r = \frac{\dot{A}_c}{\rho|\nabla c|}; \quad S_s = \frac{\dot{S}_{liq,c}}{\rho|\nabla c|} \tag{2.60}$$

where $\vec{N} = -\vec{\nabla} c/|\nabla c|$ is the local flame normal vector pointing toward reactants as an element of flame surface and $\kappa_m = \nabla \cdot \vec{N}/2$ is the local flame curvature. It can be seen from Eqs. 2.60 that a change in density ρ can affect the displacement speed S_d and its components

(i.e. S_n, S_t, S_r, S_z, S_s). Thus, it is worthwhile to consider density-weighted displacement speed $S_d^* = \rho S_d/\rho_0$ and its components: $S_r^* = \rho S_r/\rho_0$, $S_n^* = \rho S_n/\rho_0$, $S_t^* = \rho S_t/\rho_0$, $S_z^* = \rho S_z/\rho_0$, and $S_s^* = \rho S_s/\rho_0$.

The consumption speed determines the speed at which the flame burns the reactants based on the reaction rate of reaction progress variable:

$$S_c = \frac{1}{\rho_0}\int \dot{w}_c d\overrightarrow{n} \tag{2.61}$$

where $d\overrightarrow{n}$ is the elemental distance in the local flame normal direction.

2.2 Numerical Implementation

Simulations have been conducted using a three-dimensional compressible DNS code SENGA+ [42–44, 46, 99, 100], which solves the standard conservation equations of mass, momentum, energy and species of the gaseous phase in non-dimensional form. A uniform Cartesian grid is used for the purpose of spatial discretisation. The spatial differentiation is performed using a 10^{th} order central difference scheme for the internal grid points, but the order of differentiation gradually decreases to a one-sided 2^{nd}order scheme at the non-periodic boundaries. An explicit low-storage 3^{rd} order Runge-Kutta scheme is [101] employed to calculate the time advancement. For spherically expanding flames propagating into droplet-laden mixtures, partially non-reflecting outflow boundary condition is assumed according to the Navier-Stokes Characteristic Boundary Conditions (NSCBC) technique which is described in detail by Poinsot and Veynante [24]. For V-shaped flames propagating into droplet-laden mixtures, inflow and outflow boundary conditions are specified in the stream-wise direction ($x-$direction) whereas the remaining (i.e. y and z) directions are assumed to be periodic.

2.2.1 Resolution of Scales

Computation of turbulent flames propagating into droplet-laden mixtures using carrier phase DNS must fulfil the fundamental requirements listed below:

- The domain length L should be chosen sufficiently large which ensures containment of enough large scales for the purpose of statistically converged results ($L > 5l_t$)
- The grid size $\triangle x$ should be fine enough to allow the resolution of the smallest flow scale ($\triangle x \leq \eta$)

- The grid size $\triangle x$ should be chosen sufficiently fine which ensures the resolution of the inner structure of the flame ($\triangle x \ll \delta_{th}$)
- The droplet diameter a_d should be chosen well below the smallest flow scale to allow the point source assumption treatment for the liquid phase ($a_d \ll \eta$)

Here $\delta_{th} = (T_{ad} - T_0)/max \mid \nabla \hat{T} \mid_L$ denotes thermal flame thickness. The basic resolution conditions of the largest and smallest flow scales yield a typical grid size $\triangle x = L/(N-1)$ for a cubic computational domain with the length of L (or the shortest length in a rectangular domain) on which has N grid points.

The smallest length scale of the turbulence (i.e. Kolmogorov scale) requires to be captured in the context of DNS of non-reacting turbulent flows. Velocity fluctuation u' and integral length scale l_t can be used to describe the turbulent flow. Based on the above considerations, the length of the domain should meet at least of the order of l_t ($L = (N-1) \triangle x \geq l_t$) and the grid size should remain smaller or equal to the Kolmogorov length scale $\triangle x \leq \eta$. Thus, the number of grid points required in one direction can be linked to turbulent Reynolds number Re_t based on the Kolmogorov cascade approach (i.e. $\eta \sim Re_t^{3/4}$) as: $N - 1 > Re_t^{3/4}$. This suggests that turbulent Reynolds number Re_t is a crucial feature for non-reacting turbulent flows on determining the computational cost of DNS.

Besides the resolution of flow scales, inner flame structure needs to be resolved on the grid for DNS of turbulent combustion. Resolution practice for the chemical scales is strongly dependent on the chemical reaction mechanism employed in the DNS. A single step modified irreversible Arrhenius mechanism, which requires at least ten grid points in the thermal flame thickness δ_{th}, is adopted for generation of the DNS database used in the this thesis. The length of the domain L can be rephrased in terms of the thermal flame thickness δ_{th} as follows:

$$L \approx \frac{(N-1)}{Q} \delta_{th} \tag{2.62}$$

where Q denotes the elementary grid number in the thermal flame thickness ($Q \approx 10$). Applying the criteria that the integral length scale l_t should be smaller than the length of the domain L leads an upper limit for l_t:

$$\frac{l_t}{\delta_{th}} < \frac{L}{\delta_{th}} < \frac{N-1}{Q} \tag{2.63}$$

Alternatively, Eq. 2.63 can be rearranged by using the diffusive flame thickness $\delta_D \sim \nu / S_b$ and the product of the Re_t and Da:

$$Re_t Da \sim \frac{l_t^2 S_b}{\nu \delta_D} \sim \left(\frac{l_t}{\delta_D} \right)^2 < \left(\frac{N-1}{Q} \right)^2 \tag{2.64}$$

where ν is kinematic viscosity and $Da = l_t S_b / u' \delta_{th}$ indicates the Damköhler number which relates the flow time scale l_t/u' to the chemical time scale δ_{th}/S_b.

2.2.2 Initialisation of Turbulent Flow Field

The turbulence initialisation procedure in DNS intends to develop a good approximation of the solutions of Navier-Stokes equations, which in turn, avoids strong initial transients and excessive time spent to generate a precise turbulent solution. It is an appropriate approach to establish a numerical initial approximation when the closed form of a Navier-Stokes solution, or sufficiently detailed experimental data are unattainable [102]. Therefore, a homogeneous, isotropic, incompressible, turbulent and periodic velocity field with a specified energy spectrum is used for the purpose of turbulent flow field initialisation in the present analysis.

The Fourier space formulation is employed to generate the velocity field $\hat{u}$ which is then inverse Fourier transformed into real space [102]. Furthermore, this numerical approximation follows a pseudo-spectral scheme according to the methodology proposed by Rogallo [103]. The continuity condition for incompressible flow:

$$\nabla \cdot \overrightarrow{u} = 0 \tag{2.65}$$

can be rewritten in Fourier space as:

$$\overrightarrow{\kappa} \cdot \hat{u} = 0 \tag{2.66}$$

where $\overrightarrow{\kappa}$ is the linear wave number vector and $\hat{u}$ is the Fourier transform of the real-space velocity vector $\overrightarrow{u}$. Equation 2.66 clearly states that $\hat{u}$ is orthogonal to $\overrightarrow{\kappa}$ and the Fourier-space velocity vector $\hat{u}$ does not have a component in the direction of the wavenumber vector. Therefore, $\hat{u}$ can be expressed as:

$$\hat{u} = \alpha(\kappa)\overrightarrow{e}_1 + \beta(\kappa)\overrightarrow{e}_2 \tag{2.67}$$

where κ denotes the magnitude of the linear wave number vector $\overrightarrow{\kappa}$, the system of unit basis vectors are indicated by $\overrightarrow{e}_1$, $\overrightarrow{e}_2$ and $\overrightarrow{e}_3$, while $\overrightarrow{e}_3$ being aligned with $\overrightarrow{\kappa}$ and $\overrightarrow{e}_1$ is chosen arbitrarily in such a manner that it is normal to $\overrightarrow{e}_3$. In addition, the complex functions $\alpha(\kappa)$ and $\beta(\kappa)$ are calculated using the random phase, such that their magnitudes at each Fourier mode are considered to be adjusted with the average energy described by the energy spectrum $E(\kappa)$. Accordingly, α and β can be expressed as follows:

$$\alpha(\kappa) = \sqrt{\frac{E(\kappa)}{2\pi\kappa^2}} e^{i\theta_1} cos\varphi \tag{2.68a}$$

$$B(\kappa) = \sqrt{\frac{E(\kappa)}{2\pi\kappa^2}} e^{i\theta_2} sin\varphi \tag{2.68b}$$

Here, θ_1, θ_2 and φ are uniformly-distributed random angles. For the analyses in the current thesis, the $E(\kappa)$ is considered to follow a commonly used procedure in DNS proposed by Batchelor and Townsend [104] which is indicative of decaying isotropic turbulence:

$$E(\kappa) = c_0 \frac{\kappa^4}{\kappa_0^5} e^{-2(\kappa/\kappa_0)} \tag{2.69}$$

where c_0 denotes a multiplier and κ_0 is the wavenumber associated with the peak energy. Here, the term κ^4 represents strictly the incompressible limit for low wavenumbers, whereas Gaussian tail causes a rapid roll-off of the energy at high wavenumbers [104]. Quantities of interest, such as turbulent kinetic energy $k = \langle u_i' u_i'/2 \rangle$ and its dissipation rate $\varepsilon = \langle \nu(\partial u_i'/\partial x_j)(\partial u_i'/\partial x_j) \rangle$ can be expressed in the framework of the Batchelor and Townsend spectrum:

(i) turbulent kinetic energy over the entire domain of initialisation:

$$k\frac{3}{2}u'^2 = \frac{3}{32}\sqrt{\frac{\pi}{2}} c_0 \tag{2.70}$$

(ii) dissipation rate of turbulent kinetic energy over the entire domain of initialisation:

$$\varepsilon = \frac{15}{16}\sqrt{\frac{\pi}{2}} \pi^2 \nu c_0 \kappa_0^2 \tag{2.71}$$

Here, $\langle \cdots \rangle$ indicates the averaging operation over the entire domain of initialisation and u' is the root-mean square (rms) of the velocity fluctuations. Based on Eqs. 2.70 and 2.71, the different length scales can be obtained as follow :

Longitudinal integral length scale:

$$L_{11} = \frac{1}{\sqrt{2\pi}\kappa_0} \tag{2.72}$$

Taylor length scale:

$$\lambda = \sqrt{\frac{10\nu k}{\varepsilon}} = \sqrt{\frac{1}{2\pi^2\kappa_0^2}} \tag{2.73}$$

Kolmogorov length scale:

$$\eta = \left[\frac{\nu^2}{\frac{15}{16}\sqrt{\frac{\pi}{2}}\pi^2 c_0 \kappa_0^2} \right]^{1/4} \tag{2.74}$$

In this thesis, an incompressible, homogeneous and isotropic turbulence flow field is used to simulate turbulent flames propagating in droplet-laden mixtures. This approximation for the turbulent flow field implies the invariance of all statistics under translations, rotations and reflections of the coordinate system. The homogeneous and isotropic turbulence concept has been widely adopted by the turbulent combustion community due to its practicality and validity over a wide range of applications [42, 54, 105–107]. Thus, the homogeneous and isotropic turbulent flow assumption has provided a considerable understanding of turbulence-flame interaction.

The initial turbulent flow field is generated by using a Fourier spectral method following the procedures described by Orszag [108] and Rogallo [103] with the Batchelor–Townsend spectrum [104]. A single realisation of the turbulent flow field is obtained by assigning the random phase angles given in Eq. 2.56. Therefore, employing a different value for a phase angle from the previous analysis provides a turbulence flow field that is statistically identical but locally different from the previous initial flow field. In this study, for the purpose of turbulent flow initialisation, a single value has been defined for a random phase angle for all cases. However, a different realisation of initial turbulent velocity is not expected to cause a significant change in statistics of flame propagation presented in this study, as the initial turbulence flow field remains statistically identical (i.e., the same L_{11} and u'). It is worth mentioning that studies by Papapostolou et al. [109] and Turquand d'Auzay et al. [110], which demonstrated that the flame propagation statistics in both premixed and droplet-laden mixtures are not qualitatively affected by the realisation of the initial turbulence flow field, but the outcome of the ignition phenomenon depends on the turbulent flow realisation due to its stochastic nature. However, the analysis presented in this thesis does not deal with the ignition phenomenon and focuses principally on flame propagation statistics, and therefore, a choice of different initial turbulent flow realisation is unlikely to affect the qualitative nature of the findings reported in this thesis. Moreover, it is not computationally practical to carry out a large parametric analysis conducted in this thesis for more than one turbulent flow realisation using DNS. This approach was adopted in several analyses by several authors [64, 111–113] in the past.

2.2.3 Initialisation of Reacting Gaseous and Liquid Phases

2.2.3.1 Spherically expanding flames propagating in fuel droplet-mists

Simulations of the spherically expanding turbulent spray and premixed flames have been conducted within a cubic box with $L_x = L_y = L_z = 84.5\delta_z$ ($119\delta_z$ only for the cases with initial $u'/S_{b(\phi_g=1)} = 10$) in each direction where $\delta_z = \alpha_{T0}/S_{b(\phi_g=1)}$ is the Zel'dovich flame thickness with α_{T0} being the thermal diffusivity in the unburned gas. The domain is discretised using a uniform Cartesian grid of 512^3 (720^3 only for the cases with initial $u'/S_{b(\phi_g=1)} = 10$) which ensures about 10 grid points within the unstrained laminar thermal flame thickness δ_{st} of the stoichiometric mixture. The partially non-reflecting boundary conditions are specified for all faces of the simulation domain using the Navier-Stokes Characteristic Boundary Conditions (NSCBC) technique [28].

For the purpose of initialisation, 1D steady-state laminar spray flame solutions are generated for three different initial values of droplet diameter a_d (i.e. $a_d/\delta_{st} = 0.04, 0.05$ and 0.06) and for overall equivalence ratios ϕ_{ov} (i.e. $\phi_{ov} = 0.8, 1.0$ and 1.2) using COSILAB [114] following Neophytou and Mastorakos [115]. These 1D steady state solutions are then specified in the radial direction from the centre of the domain. These initialised scalar fields are allowed to evolve in such a manner in a quiescent environment so that the spherical flame can evolve and adjust itself. This phase has been continued until the radius of fully burned gas region (i.e. the region corresponding to reaction progress variable c value greater than 0.99) r_0 reaches $2\delta_{st}$ (i.e. $r_0/\delta_{st} = 2.0$). It is recognised that the energy content for a stoichiometric premixed spherical flame with radius $r_0 = 2\delta_{st}$ is different from a spherical droplet flame. However, for the purpose of comparison, the initial burned gas (i.e., $c \geq 0.99$) radius for all cases considered here is taken to be $r_0/\delta_{st} = 2.0$. Standard values have been considered for the ratio of specific heats ($\gamma = C_p^G/C_v^G = 1.4$) and Prandtl number ($Pr = \mu C_p^G/\lambda = 0.7$). The unburned gas temperature T_0 is taken to be $300K$ which implies a heat release parameter $\tau = (T_{(ad(\phi_g=1)} - T_0)/T_0$ of 6.54 and an atmospheric pressure condition is considered for this analysis.

For turbulent simulations, the turbulent velocity field is superimposed on the laminar spherical flames with $r_0/\delta_{st} = 2.0$. A standard pseudo-spectral method, as described in the previous section (see section 2.2.2) [103], has been used to initialise turbulent velocity fluctuations by an incompressible homogeneous isotropic velocity field. The turbulent flame simulations are performed for initial values of normalised root-mean-square (rms) turbulent velocities $u'/S_{b(\phi_g=1)} = 4.0, 8.0$ and 10.0 with a non-dimensional longitudinal integral length-scale of $L_{11}/\delta_{st} = 2.5$ and have been continued for at least 2.1 chemical time scale (i.e. $2.1t_{chem} = 2.1\alpha_{T0}/S^2_{b(\phi_g=1)}$, which corresponds to about 2.0, 4.0 and 5.0 initial eddy turnover

times (i.e. $L_{11}/\sqrt{k}$) for $u'/S_{b(\phi_g=1)} = 4.0, 8.0,$ and 10.0 cases, respectively. By this time u' has decayed by about 40,50 and 54 for initial $u'/S_{b(\phi_g=1)} = 4.0, 8.0$ and 10.0 cases, respectively, and at that stage turbulent kinetic energy and its dissipation rate no longer change significantly with time. The simulation time used in this analysis remains comparable to a number of recent DNS analyses [43–46, 57, 59–61, 99, 100], which significantly contributed to the fundamental understanding of turbulent combustion. The initial turbulent Reynolds number $Re_t = \rho_0 k^2/\mu_0\varepsilon$ based on turbulent kinetic energy k and its dissipation rate ε for the turbulent cases considered here remains about 68, 135 and 170 for $u'/S_{b(\phi_g=1)} = 4.0, 8.0$ and 10.0 cases, respectively.

The initial droplet number density ρ_N varies between $1.38 \leq (\rho_N)^{1/3}\delta_{st} \leq 2.34$ in the unburned gas depending on the value of droplet diameters considered here, and the liquid volume fraction remains well below 0.01%, which ensures the dilute spray regime as described later in Chapter 3, section 3.1. The droplet diameter remains smaller than the Kolmogorov length scale η for all cases and a_d/η ranges between 0.15 and 0.45. The Stokes number $St = \tau_d^u\sqrt{k}/L_{11} = \rho_d a_d^2\sqrt{k}/(18C_u\mu L_{11})$ (where $\tau_d^u = \rho_d a_d^2/18C_u\mu$ is the particle time scale and $L_{11}/\sqrt{k}$ is the turbulent time scale) for the largest droplet remains smaller than 0.18 in the turbulent cases considered here. Alternatively, the Stokes number $St' = \tau_d^u S^2_{b(\phi_g=1)}/\alpha_{T0} = \rho_d a_d^2 S^2_{b(\phi_g=1)}/(18C_u\mu\alpha_{T0})$ can be calculated based on chemical time scale $\alpha_{T0}/S^2_{b(\phi_g=1)}$ and the maximum value of St' remains smaller than 0.3 for the largest droplets considered in this analysis. The mean normalised inter-droplet distance s_d/η varies between 2.47 and 6.53.

2.2.3.2 V-shaped flames propagating in fuel droplet-mists

The computational domain for the V-shaped flames propagating in droplet-laden mixtures is taken to be a cube of $L_x = L_y = L_z = 30\delta_{st}$ and is discretised by a uniform Cartesian grid of 384^3, which ensures about 10 grid points within δ_{st}. Boundary conditions in the stream-wise direction (x−direction) are assumed to be inflow and outflow according to the NSCBC technique [28], whereas the remaining (i.e. y and z) directions are taken to be periodic. COSILAB [114] is utilised to obtain 1D laminar steady state spray flame solutions, which in turn have been used to initialise the reacting flow field for three different initial values of droplet diameter a_d (i.e. $a_d/\delta_{st} = 0.04, 0.05$ and 0.06) for an overall equivalence ratio ϕ_{ov} of unity (i.e. $\phi_{ov} = 1.0$). The flame holder with a radius of $0.3\delta_{st}$ is placed at approximately $10\delta_{st}$ from the inlet plane. The reactant mass fractions (i.e. Y_F and Y_O) and the non-dimensional temperature of gaseous phase T are imposed using a Gaussian weighting function $g(r) = Aexp[-r^2/2\varsigma^2]$ at the flame holder following Dunstan et al. [63, 64] where A and ς are adjustable constants to obtain the desired flame holder radius (i.e. $r = 0.3\delta_{st}$). The ratio of specific heats ($\gamma = 1.4$) and Prandtl number ($Pr = 0.7$) are taken to have standard values. The statistics are

presented at three different axial distances (i.e. position A, B and C) from the flame holder (i.e. $9\delta_{st}, 13\delta_{st}$ and $17\delta_{st}$) after $2.0t_{flow}$, where $t_{flow} = L_x/u_{mean}$ is the flow through time.

The V-flame is subjected to a moderate level of inlet turbulence (i.e. $u'/S_{b(\phi_g=1)} = 2.0$), with two different mean inlet velocities of $u_{mean}/S_{b(\phi_g=1)} = 5.0$ and 10 and a normalised longitudinal integral length scale of $L_{11}/\delta_{st} = 2.5$. A plane is scanned through a frozen field of homogeneous isotropic turbulence to specify turbulent velocity fluctuations at the inlet plane with the help of Taylor's hypothesis. Interested readers are referred to Chakraborty and Cant [73] and Dunstan et al. [63, 64], for further discussion on inlet boundary condition specification. The turbulent Reynolds number Re_t for the flames considered here is about 35.0. It is admitted that the value of Re_t remains small but comparable to experiments by Vena et al. [116, 117] (where u' at the inlet varied from $0.19m/s$ to $0.33m/s$, the hydraulic diameter of the burner exit is $0.024m$, the integral length scale can be estimated as 7% of the hydraulic diameter, and the kinematic viscosity is given by $1.8 \times 10^{-5}m^2/s$). Moreover, the turbulent Reynolds number Re_t value of these simulations remains comparable to turbulent premixed V-flame simulations of Dunstan et al. [63, 64]. However, these V-shaped spray flame simulations are considerably more expensive than turbulent premixed V-flame DNS [63, 64] because individual droplets are tracked in addition to accounting for gaseous phase combustion. A small value of $u'/S_{b(\phi_g=1)}$ is considered in this study because the analysis of the flame-droplet interaction is one of the focal points of this study and the flame-droplet interaction (e.g. curvature) induced by droplets is eclipsed by flame-turbulence interaction for large values of $u'/S_{b(\phi_g=1)}$ [118, 119].

Fuel is supplied in the form of liquid droplets at the inlet which is placed on the left-hand side of the domain. Liquid fuel droplets, distributed randomly but statistically uniform in space at the inlet plane, are introduced with a temperature of $T_0 = 300K$. The mass flux of liquid fuel at the inlet plane is estimated based on the values of u_{mean} and ϕ_{ov}. The initial droplet number density ρ_N ranges between $1.23 \leq (\rho_N)^{1/3}\delta_{st} \leq 1.85$ in the unburned gas depending on the value of droplet diameters considered here, and the liquid fuel spray is assumed in the dilute spray regime with a liquid volume fraction less than 0.01%. As the resolution requirements restrict the application of the point source assumption for large droplets, the ratio of initial droplet diameter to the Kolmogorov length scale is $a_d/\eta = 0.09, 0.11$ and 0.13 for the cases of $a_d/\delta_{st} = 0.04, 0.05$ and 0.06, respectively for the inlet turbulence intensity (i.e. $u'/S_{b(\phi_g=1)} = 2.0$) considered here. The Stokes number St and the alternative Stokes number are obtained as smaller than 0.13 and 0.27, respectively. The mean normalised inter-droplet distance s_d/η remains in the range of $1.64 \leq s_d/\eta \leq 2.47$ for the inlet turbulence intensity considered here.

For both configurations, a group number $G = 3(1 + 0.276Re_d^{1/2}Sc^{1/3})LeN^{2/3}(a_d/s_d)$ can

be used to distinguish between individually burning droplets ($G \ll 1.0$) and external sheath combustion ($G \gg 1.0$). All droplet cases considered in the current study come under the category of external sheath combustion (i.e. G remains much greater than unity). In the case of the small value of G, pyrolysis takes place at the fuel-rich core due to extremely high temperature, whereas the temperature values in the external sheath combustion are usually not high enough to give rise to a significant amount of pyrolysis [92]. For the present study, the burned gas temperature remains either comparable or smaller than the adiabatic flame temperature of the stoichiometric mixture, and thus the effects of pyrolysis are expected to be minimal. Moreover, thermochemistry for the present analysis involves a modified single-step Arrhenius-type chemical mechanism for the computational economy, and this chemical mechanism is not adequate for the analysis of the pyrolysis process. A similar assumption was made in several previous analyses [42–46, 54, 56, 67] and the same approach has been adopted here. A recent DNS analysis by Zhou et al. [120] demonstrated, with the help of the Kerstein-Law parameter, that either group combustion or individual burning is unlikely to occur under conditions which are comparable to the conditions analysed here.

For the purpose of simplicity, the Lewis numbers ($Le_i = \alpha_i/D_i$ for the species i) of all species are considered to be unity in simulations of both spherically expanding and V-shaped spray flame configurations and all species in the gaseous phase are assumed to be perfect gases following several previous studies [42–44, 51, 67]. In principle, it is not necessary to consider the unity Lewis number for these simulations although most previous analyses made this assumption. The DNS code used for this analysis was used several times for non-unity Lewis number turbulent premixed flames and interested readers are referred to Alqallaf et al. [121] and references therein for the relevant information. However, the initialisation of spherical flames with non-unity Lewis number is computationally expensive. The spherical flames with $Le < 1$ expand rapidly due to thermo-diffusive instabilities, so keeping the flame within the computational domain for a meaningful timespan becomes extremely computationally expensive. Moreover, a non-unity Lewis number complicates the expression used for the corrected Sherwood number Sh_c which is used for dispersed phase modelling. Furthermore, the thermo-diffusive effects induced by non-unity Lewis number significantly affect the burning rate and flame wrinkling statistics, and thus it becomes difficult to isolate the effects of flame wrinkling induced by droplets and fluid turbulence from the ones due to differential diffusion of heat and mass. Thus, all the species are considered to be of unity Lewis number for this analysis for the purpose of simplicity so that the effects of droplet-induced flame wrinkling effects can be analysed in absence of the additional complexities induced by differential diffusion of heat and mass. In spite of the unity Lewis number assumption, the present thermo-chemistry captures the variations of normalised unstrained laminar burning velocity $S_{b(\phi_g)} / \left[S_{b(\phi_g)}\right]_{max}$ and

adiabatic flame temperature $T_{b(\phi_g)} = (T_{ad(\phi_g)} - T_0)/(T_{ad(\phi_g=1)} - T_0)$ with gaseous equivalence ratio ϕ_g reasonably accurate when compared to detailed chemistry calculations [79] and experimental data [78], as shown in Fig. 2.3. The small differences between the variations of $S_{b(\phi_g)}/\left[S_{b(\phi_g)}\right]_{max}$ and $T_{b(\phi_g)}$ between the different chemical mechanisms and experimental data arise due to the differences in the treatments of molecular transport characteristics.

Due to the high volatility of n-heptane, the size of droplets decreases significantly ($\geq 50\%$) by the time they reach the reaction zone. As a result, the flame interacts with the droplets, which are much smaller in reality than the initial size of the droplets. Thus, the assumption of sub-grid evaporation is not expected to affect the statistics of flame-droplet interaction, which is the subject of this analysis. It is worth noting that a recent analysis by Haruki et al. [122] demonstrated that the point source assumption accurately captures the evaporation characteristics obtained from fully resolved multiphase simulations for droplets with sizes smaller than the Kolmogorov length scale. The Eulerian approaches, which resolve both gaseous and liquid phases, also have some limitations (e.g., capturing polydispersity and droplet crossing). de Chaisemartin et al. [123] compared the combustion of polydisperse droplets in a two dimensional free jet using carrier phase DNS with point source and fully Eulerian phase DNS. The results by de Chaisemartin et al. [123] showed a good agreement between gaseous fuel mass fraction fields obtained from these two approaches. These authors also reported that simulations with the full Eulerian approach were 10 times more expensive than those with the point source approach and a huge parallelisation capability for 3D simulations is needed for the Eulerian phase DNS for sprays. Moreover, combustion simulations involving the fully resolved dispersed phase are currently in a primitive stage and need further validation to be used on a routine basis. Thus, a point source assumption for the dispersed phase (i.e., droplets) has been considered in this analysis.

The primary resolution requirements for the carrier phase DNS of turbulent spray flames are explained in Section 2.2.1 earlier in this chapter. In accordance with the requirements for reacting flow DNS, the domain length of spherically expanding flame configuration contains around 16 longitudinal integral length scales (i.e. $L_x = L_y = L_z = 16L_{11}$) whereas V-shaped flame configuration has a domain length of $L_x = L_y = L_z = 12L_{11}$. Furthermore, the grid spacing $\triangle x$ remains smaller than the Kolmogorov length scale for both spherically expanding (i.e. $\eta > 1.25\triangle x$) and V-shaped (i.e. $\eta > 4\triangle x$) flame configurations. Simulations have been carried out for different initial droplet diameters which are chosen smaller than the Kolmogorov length scale so that the point source approximation can be safely applied. Therefore, the ratio of initial droplet diameter to the Kolmogorov length scale remains smaller than 0.45 for the spherically expanding flame configuration, and 0.13 for the V-shaped flame configuration. Inner flame structures are resolved by ensuring around 14 elementary grid points (i.e., $Q = 14$)

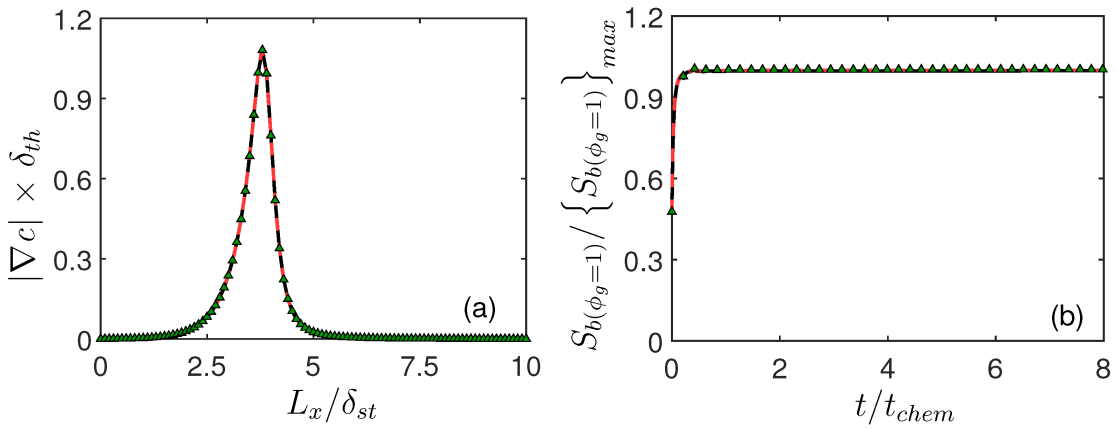

Figure 2.5: (a) $|\nabla c| \times \delta_{th}$ and (b) $S_{b(\phi_g=1)}/\{S_{b(\phi_g=1)}\}_{max}$ for the one-dimensional unstrained stoichiometric premixed planar flame with $\delta_{th} = 10\triangle x$ (solid black line), $\delta_{th} = 13\triangle x$ (dashed red line) and $\delta_{th} = 20\triangle x$ (green triangle)

in the thermal flame thickness δ_{th}. However, a grid-independence test has been performed for a one-dimensional unstained stoichiometric premixed planar flame case in order to be sure that statistics of flame propagation are not sensitive to the change in grid spacing. Figure 2.5 shows the distribution of $|\nabla c| \times \delta_{th}$ across the one-dimensional domain after simulations reach a steady-state for the cases with $Q = 11, 14$ and 21. The quantity $|\nabla c|$ plays an important role in the evaluation of the flame propagation and it is clear from Fig. 2.5 that grid-independence is obtained with the chosen grid spacing. Moreover, Fig. 2.5 shows that the evolution of laminar flame speed in time exhibits nearly the same trend for the cases with different grid spacing. An increase in the grid points across the thermal flame thickness from 11 to 21 leads to a 0.5% change in laminar flame speed.

Chapter 3

Literature Review

This chapter is devoted to an extensive review of the investigations on turbulent spray combustion while presenting findings of pioneering studies along with the on-going researches in the field. The present chapter will focus on the analysis of turbulent spray flames in line with the scope of the current thesis, and thus the studies on non-reacting droplets are excluded from the discussion.

3.1 Fundamental Concepts in Spray Combustion

Liquid fuels are mostly utilised as sprayed liquid droplet-mists into a combustion chamber in order to enhance the surface area, thereby augmenting heat and mass transfer rates which affect the evaporation process and subsequently the combustion characteristics. The simulation and modelling of turbulent flames propagating into droplet-mists is a challenging task because spray combustion involves a wide range of different phenomena, which are strongly coupled, including atomisation, collision, phase change, mixing, heat transfer, turbulence and chemical reaction. In the DNS of turbulent combustion, atomisation and droplet collision are generally neglected due to their highly complex nature and droplets are initially assumed atomised. Understanding the fundamental physics on the interactions between flame, droplets and turbulence is essential to establish a framework for the challenges and complexities in turbulent spray combustion. The diagram in Fig. 3.1 summarises some major interactions in turbulent spray flames following Jenny et al. [30]. In gaseous combustion, turbulent flow gives rise to dispersion at large scales (macro-mixing), and this is followed by mixing at small scales and eventually mixing occurs at the molecular level (micro-mixing). Moreover, heat release due to combustion and thermal expansion alter the underlying turbulence flow field. In the context of spray flame, droplet and surrounding gas motions have an impact on each other due to momentum exchange between liquid and gaseous phases. A local velocity differ-

ence between liquid and gaseous phases develops due to the differences in inertia between the droplet and carrier phase and this relative velocity plays a key role on the evaporation characteristics of droplets. Additionally, evaporation rate and turbulence are linked through macro- and micro-mixing. The flame structure in spray flames is strongly affected by the evaporation rate and micro-mixing. Furthermore, a high temperature region close to the flame promotes a faster evaporation rate which is coupled with micro-mixing in the gaseous phase. The general features of processes involved in turbulent spray flames can briefly be discussed based on the review by Jenny et al. [30].

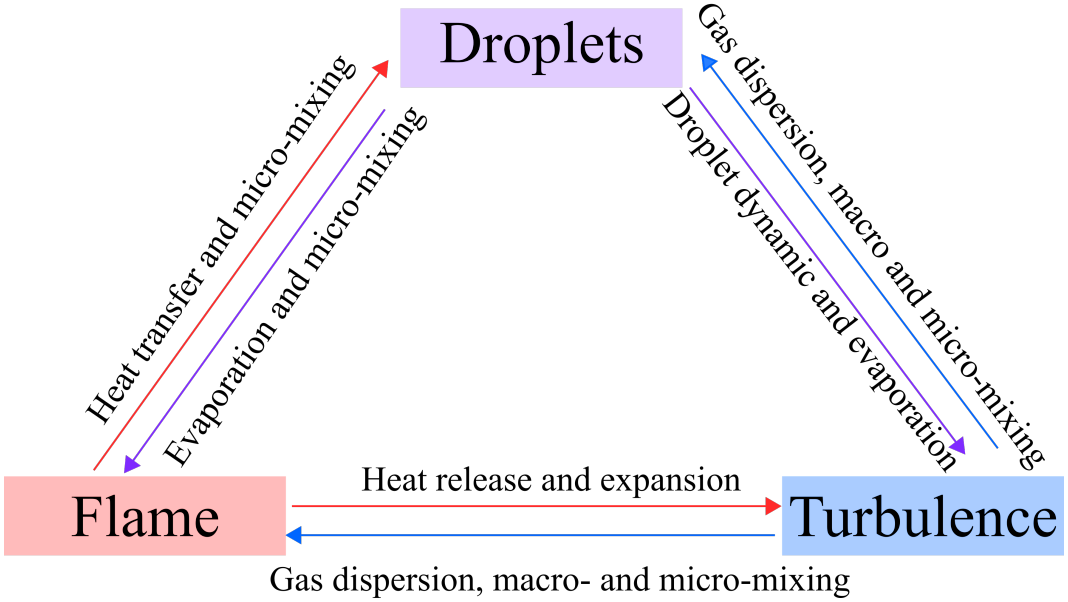

Figure 3.1: Schematic diagram of flame droplet turbulence interaction. Reproduced from Jenny et al. [30]

Liquid atomisation refers to the process of generating a fine spray which includes the disintegration of injected liquid fuel into small droplets. The atomisation characteristic controls the droplet size and distribution and plays a crucial role for spray combustion [124]. The droplet break-up behaviour is related to aerodynamic parameters and capillary forces due to surface tension [125]. The spray formation process can be evaluated into two major phases: primary and secondary atomisation, as shown in Fig. 3.2. Primary atomisation involves the initial break-up to ligaments and large blobs of the continuous liquid body. The shear rate between gas and liquid phases are dominant in the primary breakup region which is governed by Kelvin-Helmholtz instabilities. Small droplets are formed in the secondary breakup region as a result of Rayleigh-Taylor instability which occurs due to density differences between two fluids [126]. The transition of ligaments to different secondary breakup modes is characterised by the nondimensional numbers known as Weber (i.e. the ratio of the hydrodynamic forces

to the surface tension) and Ohnesorge (i.e. the ratio of liquid viscous forces to the surface tension) [127, 128].

Flow regimes can be divided into three categories based on the volume fraction of the dispersed phase, as illustrated in Fig. 3.2. A dispersed phase volume fraction greater than 10^{-3} represents the dense regime where droplet collision and coalescence can reach considerable frequecy. Dilute regime is described by dispersed phase volume fraction within the range of 10^{-6} and 10^{-3} and droplet collision can be neglected. In the very dilute regime, dispersed phase volume fraction is below 10^{-6} and the effects of gaseous phase turbulence dominates over those of the liquid phase [30].

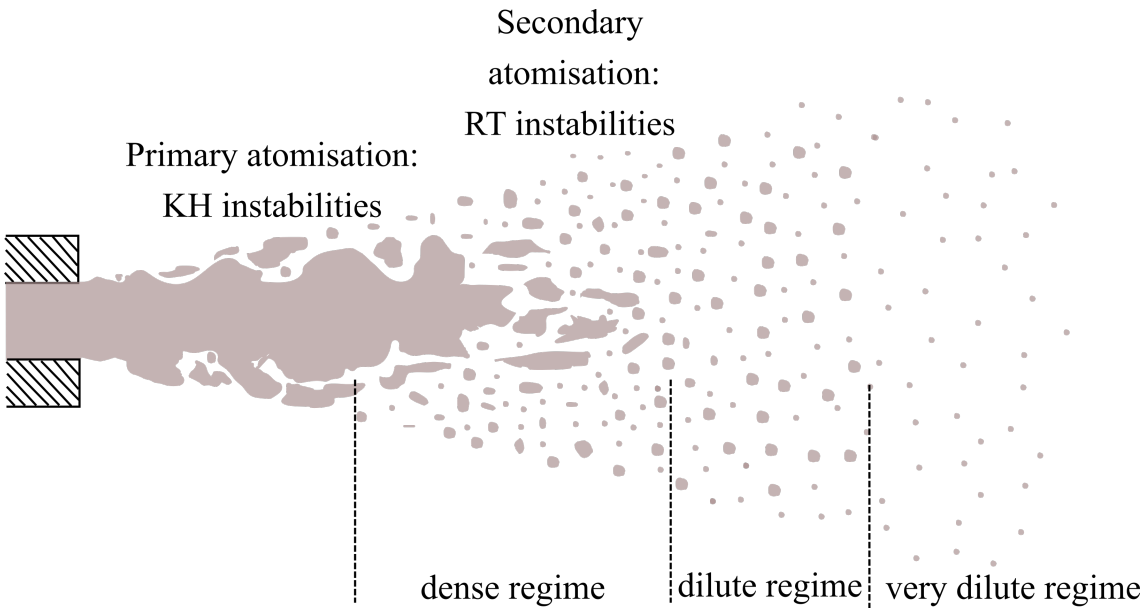

Figure 3.2: Structure of flow regimes and spray atomisation. Adapted from Jenny et al. [30] and Gutheil [129].

Dispersion of droplets in a stream of turbulent gaseous medium takes place due to two way momentum coupling. Moreover, the gaseous turbulence field is influenced by the presence of the dispersed liquid phase. Turbulence modulation and preferential droplet concentration are essential aspects to understand the dynamic interactions between the carrier and dispersed phase turbulence [130]. In the context of turbulence modulation, coupling of different mechanisms is possible [131]: (i) enhanced dissipation associated with large liquid droplets, (ii) transport of kinetic energy to the carrier phase from liquid droplets and (iii) formation of wakes and vortex shedding behind the particles. These mechanisms occur over a broad range of length scale and liquid droplets can simultaneously augment and suppress the turbulence intensity of the carrier phase [132]. Furthermore, carrier phase turbulence can drag liquid droplets into the zones which are away from the centre of vortices. This phenomenon is called

preferential droplet concentration and leads to a high concentration of liquid droplets at convergence zones between multiple vortices [133]. Stokes number *St,* expresses the ratio of characteristic particle timescale to turbulent timescale, and is a critical parameter in preferential droplet concentration. Droplets with $St \ll 1$ can entirely respond to carrier phase turbulence motion whereas for the case of $St \gg 1$, droplets exhibit a slow response to turbulent eddies. At moderate values of Stokes number (i.e. $St \approx 1$), liquid droplets tend to be drawn away from the core of turbulence eddies, which indicates the development of preferential droplet concentration.

Evaporation and micro-mixing determine the character of reacting gaseous mixture for spray combustion. Reacting mixture composition ahead of the flame consequently affects reaction rate and flame propagation rate, and thus, evaporation and micro-mixing should be precisely represented for the accurate prediction of spray flame behaviour. The evaporation pattern for droplets under different scenarios was described by Reveillon and Demoulion [53] as given in Fig. 3.3. Liquid droplets rapidly evaporate in the fist scenario, as they are distributed in a region with low fuel vapor. At scenario 2, however, droplets with smaller inter-droplet spacing have a lower evaporation rate due to the richer vapor concentration in the vicinity of droplets in comparison to the first case. Lastly, droplets subjected to turbulence flow travel from high vapor concentration region to a place where vapor concentration is low [30, 53].

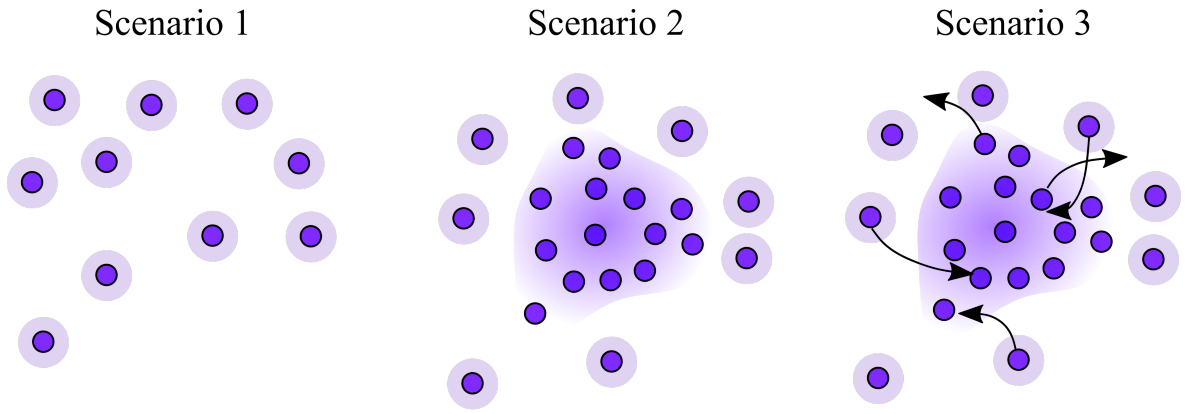

Figure 3.3: Schematic illustration of liquid droplet evaporation for different scenarios [30]

Combustion in droplet laden mixtures is reviewed in the following sections based on the previous studies on spray flame structure.

3.2 A Basic Droplet Combustion Model: Single Droplet Combustion

The endeavours to understand spray combustion in practical engineering devices have started with the modelling of a single droplet burning in an oxidising atmosphere. The single droplet combustion model provides a basis for the analysis of complex spray combustion problems. In the context of single droplet combustion, a spherical cold liquid fuel drop is suspended in a hot quiescent oxidant medium as illustrated in Fig. 3.4. Heat is conducted from the hot ambient gas to the liquid droplet which leads to heating up the droplet and its evaporation. Fuel vapour diffuses from the droplet surface to its surrounding due to the concentration gradient between ambient and droplet surface. The evaporation rate is controlled by heat and mass transfer mechanisms, and initially remains slow for the cold droplet, but increases, as the droplet heats up. Droplet ignition (by forced or auto-ignition) creates a spherical diffusion flame around the liquid droplet as shown in Fig. 3.4. It is worth noting that a non-spherical flame can be formed in the case of a relative velocity between the droplet and surrounding gas (i.e. convection effect). Chemical reaction occurs at locations where the stoichiometric mixture is obtained where the outwardly-diffusing fuel vapour and inwardly-diffusing oxidiser is achieved. Infinitely very thin flame sheet divides the flow field into two regions. The heat released during the combustion is transferred to these two regions and also into the liquid fuel droplet. It is assumed that a stable diffusion flame is established following the ignition and the temperature distribution within the droplet is uniform with a constant surface temperature.

Godsave [136] described the linear relation between the square of the droplet diameter and evaporation time considering the quasi-steady assumption with constant transport properties and a Lewis number of unity. This simplest possible model for droplet evaporation and combustion is named as d^2 law:

$$d^2 = d_0^2 - K_e t \tag{3.1}$$

where d_0 is the initial droplet diameter, d is the droplet diameter after the evaporation time t and K_e denotes the evaporation coefficient. The validity, limitations and possible modifications of d^2 law based on the experimental studies were extensively discussed and reviewed by Williams [137], Faeth [138] and Law [134]. Furthermore, Spalding [139] introduced a mass transfer number to estimate the evaporation rate based on the single droplet combustion approach. It is also referred to as Spalding number and defined as:

$$B_d = \frac{Y_F^s - Y_{F,\infty}}{1 - Y_F^s} \tag{3.2}$$

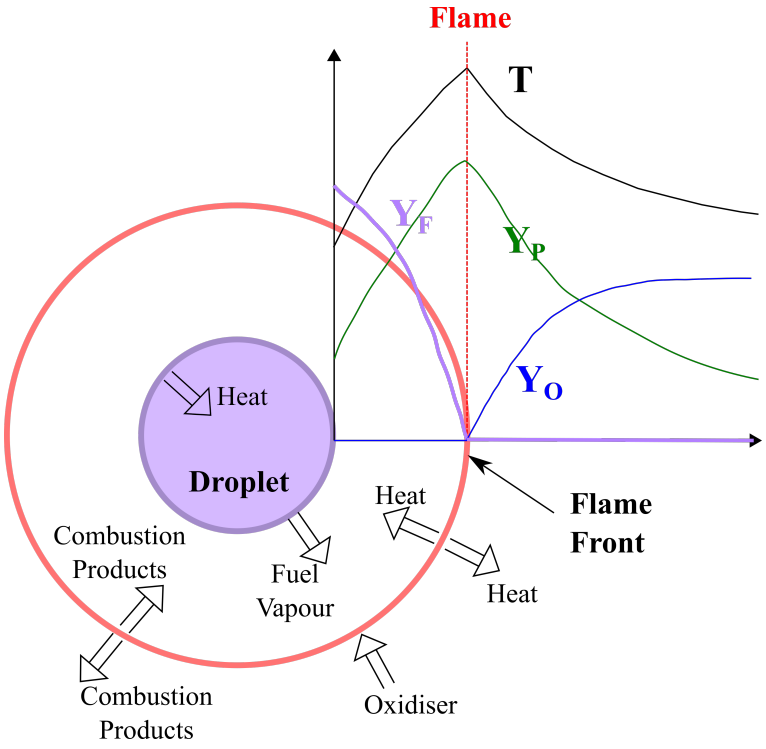

Figure 3.4: Schematic description of single droplet combustion model [134, 135].

where $Y_{F,\infty}$ represent the fuel mass fraction in the ambient gas.

3.3 Combustion Regimes

3.3.1 The Regimes of Premixed Turbulent Combustion

In general, a premixed flame can be characterised by three distinct zones called the preheat zone, reaction zone and equilibration zone. The preheat zone contains unburned mixture in which the temperature increases due to thermal diffusion from the reaction zone. A chemical reaction occurs at a negligible level as the temperature of reactants remains too low in comparison to the activation temperature of the chemical reaction [140]. The reaction zone is a very thin region with the temperature high enough to overcome the activation energy of the reaction, and thus, the chemical reaction mainly takes place in this region. Finally, the temperature reaches the highest level in the equilibration zone as a result of the large amount of heat release. In the equilibration zone, chemical equilibrium is achieved whereas the reaction is much slower compared to the reaction zone [140].

Chemical reaction in turbulent premixed combustion often occurs much faster than fluid-dynamic processes, and this originates from the existence of the shorter chemical time scales

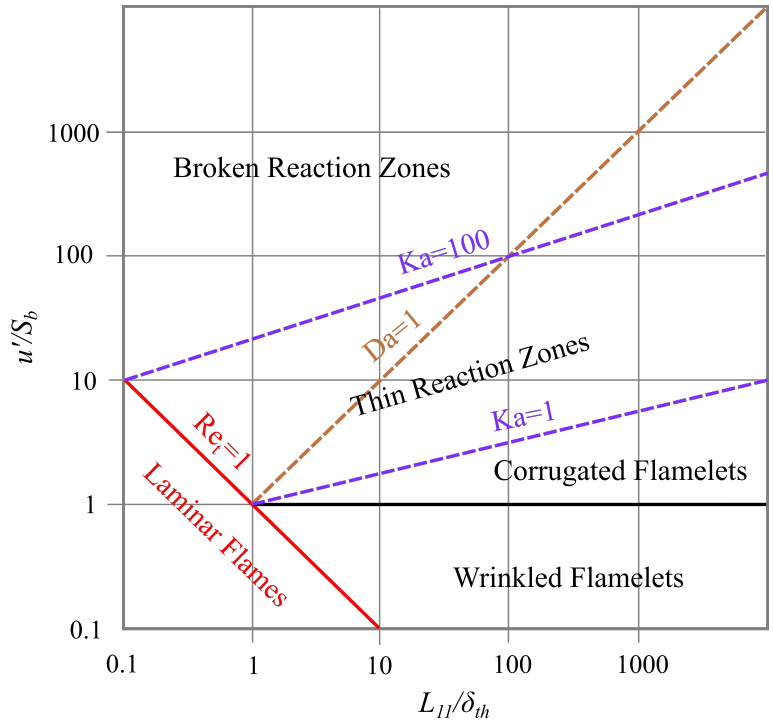

Figure 3.5: A regime diagram for turbulent premixed combustion [93].

than the turbulence time scales [18]. In such conditions, the chemical reaction is assumed to take place in a thin layer, namely the flamelet, which separates the unburned mixture from that of fully burned products. The flamelet concept is an essential element of formulating the turbulent premixed combustion and this assumption enables the entire turbulent combustion analysis to be modelled as a two-fluid problem. Furthermore, this approach suggests the description of the flow properties in the fresh and burnt gases in terms of burning rate and flame surface. Additional simplifications are possible with the consideration that the flamelets retain the local structure of a strained and curved laminar flame. This allows a practical approximation of the reactant consumption rate in turbulent premixed flames to that of strained laminar flames. Hence, the analysis of the chemical reaction can be decoupled from the turbulence flow field calculations. However, further separate laminar flame calculations are required in order to capture the variations in local flame speed due to the chemical effects [141]. Turbulent motions give rise to the straining and wrinkling of laminar flamelets. As strong assumptions are considered for the application of the flamelet approach, it is instructive to frame the validity and the limitations of flamelet concept on a regime diagram. Flame structures are mapped onto two-dimensional diagrams based on the normalised velocity (i.e. u'/S_b) and length (i.e. L_{11}/δ_{th}) scales (or Damköhler and Reynolds numbers). These diagrams are also called Borghi diagrams [142] and a typical regime diagram proposed by Peters [93] is illustrated in Fig. 3.5.

Figure 3.5 presents the boundaries of different combustion regimes based on the non-dimensional numbers: the turbulent Reynolds number Re_t, turbulent Damköhler number Da and the Karlovitz number Ka. Here, the turbulent Damköhler number is the ratio of turbulent time scale $t_e = l_t/u'$ to the chemical time scale $t_{chem} = D/S_b^2$ and can be given as:

$$Da = \frac{t_e}{t_{chem}} = \frac{(l_t/u')}{(D/S_b^2)} \tag{3.3}$$

Karlovitz number Ka provides the ratio of the chemical time scale t_{chem} to the Kolmogorov time scale $t_\eta = (\nu/\varepsilon)^{1/2}$, and the assumptions of equal diffusivity for all reactive scalars and unity Schmidt number (i.e. $Sc = \nu/D = 1$) lead to the following expression:

$$Ka = \frac{t_{chem}}{t_\eta} \sim \frac{\delta_{th}^2}{\eta^2} \sim \frac{v_\eta^2}{S_b^2} \tag{3.4}$$

where $v_\eta = (\nu\varepsilon)^{1/4}$ is the Kolmogorov velocity scale. The Kolmogorov length scale η can be written based on the overall turbulent kinetic energy dissipation rate ε and kinematic viscosity ν by the following equation:

$$\eta = \left(\frac{\nu^3}{\varepsilon}\right)^{1/4} \tag{3.5}$$

where the turbulent kinetic energy dissipation rate ε can be scaled as $\varepsilon \sim u'^3/l_t$ under the assumption of local equilibrium. Lastly, the turbulent Reynolds number Re_t can be related with non-dimensonal numbers Da and Ka as:

$$Re_t = Da^2 Ka^2 \tag{3.6}$$

According to the regime diagram shown in Fig. 3.5, *laminar flame regime* is bordered by the line of unity turbulent Reynolds number. *Wrinkled flame regime* is identified with low turbulence intensities (i.e. $u' < S_b$) and Karlovitz numbers (i.e. $Ka < 1$). Under these conditions, the turbulent flame exhibits a thin quasi-laminar flame front, which is moderately wrinkled by the turbulent motions. When the turbulence intensity becomes higher (i.e. $u' > S_b$) while Karlovitz numbers remain under unity, flame front is severely wrinkled. Large-scale interactions of flame fronts can lead to the formation of reactant and product pockets, and therefore, this type of flames is also described as *wrinkled flames with pockets.* Furthermore, the criterion of $Ka < 1$ presents a laminar flame thickness δ_{th} smaller than the all turbulence length scales, including the Kolmogorov scale η (i.e. $\delta_{th} < \eta$) which indicates that the inner structure of the flame is not disturbed by the turbulence field. Alternatively, $Ka = 1$ line introduces a limit for the Klimov–Williams criterion which determines whether a laminar flamelet can occur in

a premixed turbulent combustion. If the Karlovitz number reaches values above unity (i.e. $Ka > 1$), the Kolmogorov length scale η becomes small enough in comparison to the flame thickness (i.e. $\eta < \delta_{th}$) to penetrate the inner flame structures. Peters [143] introduced another characteristic thickness for the reaction zone (i.e. δ_r) in order to identify the level of penetration of small eddies into flame. Thus, an alternative Karlovitz number Ka_r can be defined assuming the reaction zone thickness being typically one tenth of the overall thermal thickness (i.e. $\delta_r \sim \delta_{th}/10$), and which relates two Karlovitz numbers as $Ka_r/Ka \sim 1/100$. Hence, *thin reaction zone* is specified based on the inequalities of $1 < Ka < 100$ and $Re_t > 1$. In the thin reaction zone, the flame is subjected to thickening by unsteady fluctuations due to penetration of energetic turbulent eddies to the preheat zone. However, the reaction zone is still smaller than the Kolmogorov length scale (i.e. $\delta_r < \eta$), and thus, the reaction zone remains unbroken by turbulent motions. For the reaction zone Karlovitz numbers greater than unity $Ka_r > 1$ and $Re_t > 1$, combustion occurs in the *broken reaction zones regime* where both preheat and reaction zone are perturbed by turbulent eddies. Turbulent motion can cause thickening, stretching and extinction in the broken reaction zones regime [19].

3.3.2 The Regimes of Spray Combustion

Classification of spray combustion is a complex task as several characteristic parameters, such as droplet size, number density of droplets, inter droplet spacing, flame structure and flow features are involved in the process. Particular attention has been given for the description of spray flames using the combustion regime diagrams. The earliest attempt to create an extensive spray combustion regime diagram was made by Chiu and co-workers [144, 145]. The concept of group combustion of droplet clusters which is notably related to practical combustion systems was proposed. A spherical liquid droplet cloud dispersed in hot oxidiser was considered to investigate the spray flame propagation behaviour. Flame location in the droplet cloud was used to distinguish the different spray flame morphologies and a combustion regime diagram was introduced based on the group combustion number G as shown in Fig. 3.6.

The group combustion number G describes the relation between the characteristic speed of evaporation and the molecular diffusion speed [145] and it can be given by:

$$G = 3(1 + 0.276 Re_d^{1/2} Sc^{1/3}) Le N_p^{2/3} (a_d/s_d) \tag{3.7}$$

where N_p is the total number of droplets in the cloud and s_d is the average inter droplet spacing. At very low group combustion number values (i.e. $G < 10^{-2}$), droplets are dispersed dilute enough so that preheated oxidiser can reach around each droplet, and thus all droplets are

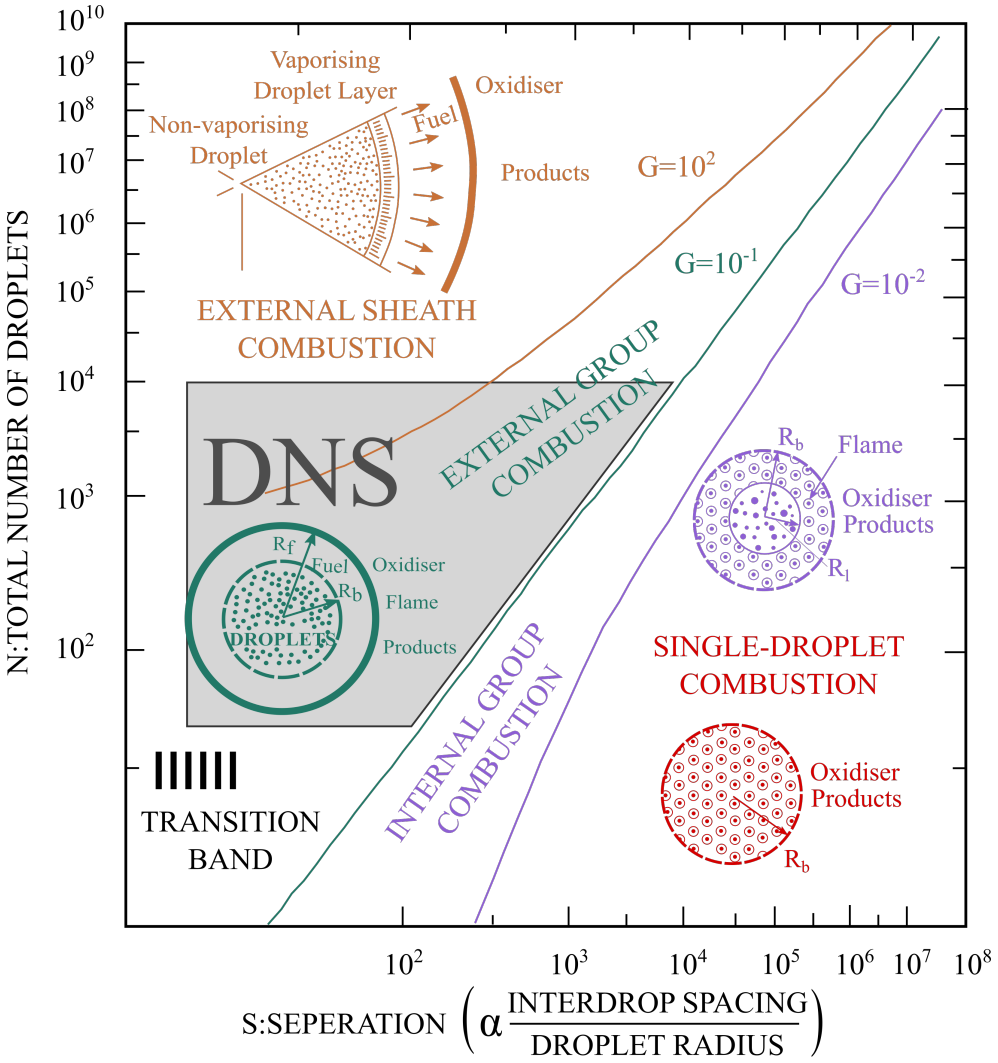

Figure 3.6: Group combustion modes depicted on spray combustion regime diagram [92, 145, 146]

surrounded by a separate flame. This is called *the single droplet combustion regime*. The region corresponding for $10^{-2} < G < 1$ is named *the internal group combustion regime* where a diffusion flame encloses the droplets located in the core. This main flame is developed at the layer where evaporated fuel in the centre of the cloud meets with the oxidiser diffusing inwardly. Beyond the main flame, droplets outside of the core burn individually. If G further enhances, the main flame location moves outwards and eventually the flame envelops the entire droplet cloud with a certain stand off distance. This region in the diagram (i.e. $1 < G < 10^2$) is known as *the external group combustion regime.* For large values of the group combustion number (i.e. $G > 10^2$), densely packed droplets form the non-evaporating core at the centre of the droplet cloud due to the lack of heat diffusion into the centre. In this case, only a thin layer

of droplets at the outer edge of the cloud evaporates and the flame is established at a stand of distance from the periphery of the droplet cloud. This type of spray flames are classified into *external sheath combustion regime*.

Alternatively, Borghi [147, 148] categorised spray flames by including the two characteristic parameters τ_v/τ_f (i.e. the ratio of evaporation time τ_v to flame time τ_f) and s_d/δ_{th} (i.e. the ratio of inter droplet spacing s_d to flame thickness δ_{th}) to the analysis. Borghi considered laminar combustion of homogeneously distributed polydisperse droplets and the regime diagram proposed by Borghi can be seen in Fig. 3.7. In the case of a smaller evaporation time than flame time (i.e. $\tau_v/\tau_f < 1$), droplets complete their evaporation before reaching the reaction zone. Thus, a propagating premixed flame is formed due to the locally premixed mixture ahead of the reaction zone. This type of combustion mode is called *prevaporised flames*. Some droplets can penetrate to the reaction zone if the evaporation rate is sufficiently slow for the flames with a thickness larger than inter droplet distance (i.e. $\delta_{th} > s_d$). Interaction of droplets with the reaction zone leads to a *thick flame.* Droplets which survive beyond the primary partially premixed flame front can create a secondary reaction zone there. Flame morphology of this secondary reaction zone is classified pocket, percolation and group combustion regimes according to the separation number $S{=}s_d/r_f$, where r_f is a characteristic diffusion flame radius, as illustrated in Fig. 3.7.

Reveillon and Vervisch [51] considered the global liquid equivalence ratio as a key parameter in addition to those used in Borghi's analysis. It is stated that the global liquid fuel/air mass ratio can affect the local flame structure through the local mixture composition. Spray combustion regimes were investigated in three main categories as *external combustion*, *group combustion* and *hybrid combustion* using carrier phase DNS [51]. Figure 3.8 shows the characteristic flame structures identified by Reveillon and Vervisch [51]. The *external combustion* regime consists of a single (*closed external*) or two (*open external*) continuous flames which engulf the droplets and the evaporated gaseous fuel. Flames in the external combustion regime exhibit predominantly premixed behaviour. In the context of *group combustion*, droplets burn in clusters enveloped by separate flames. Rich premixed and diffusion flames can be formed together in the corresponding regime. External and group combustion modes are combined in the *hybrid combustion* regime so that premixed flames develop around the droplet clusters while the rest of the droplets form a continuous diffusion flame.

3.4 Flame Propagation in Droplet-Laden Mixtures

Over the past decades, a series of experimental [62, 118, 119, 132, 149–154], analytical [155–157] and also numerical [41–52, 54–56, 67, 68] studies have focused on turbulent spray com-

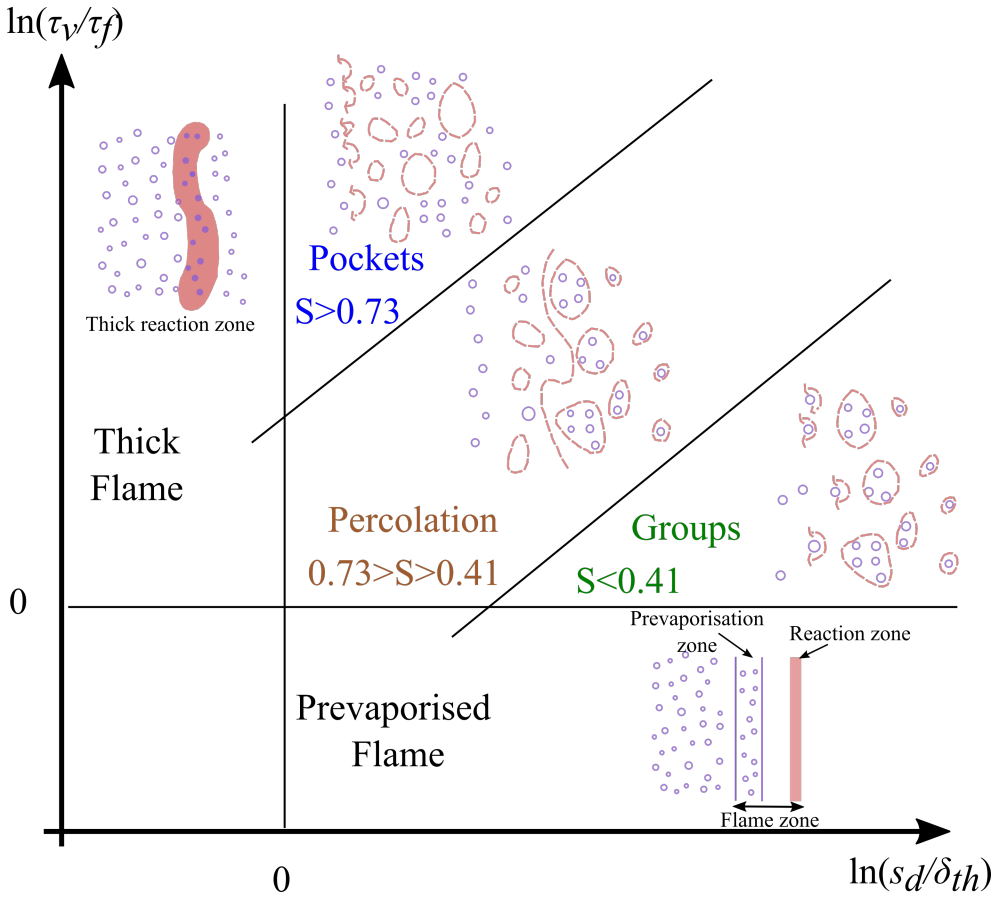

Figure 3.7: Borghi's regime diagram for laminar spray flames where S represents the separation number [147].

bustion. However, relatively limited effort [43, 46, 62, 118, 119] has been directed to the analysis of spherical flame propagation into turbulent droplet-laden mixtures.

The pioneering experimental analysis by Burgoyne and Cohen [149] indicated that the burning velocity and flammability limits of tetralin aerosols depend strongly on the droplet diameter. Suspensions of small droplets (diameter of 10 μm and below) behave similar to a gaseous mixture, whereas large droplets (with diameter of 40 μm and above) burn individually and can ignite other droplets around them. Ballal and Lefebvre [151] experimentally demonstrated that the burning velocities of iso-octane droplet-mist with overall fuel-lean and stoichiometric mixture composition increase with decreasing droplet diameters. It was also reported that the evaporation rate influences the flame propagation rate in the case of large droplets higher than those of small droplets. Hayashi et al. [118] experimentally observed that small droplet sizes of about 7 μm diameter create a smooth and continuous flame front but for the large droplet sizes of about 20 μm diameter, the flame front is rugged, undulated and thickened because of the locally heterogeneous mixture composition and burning rate. It

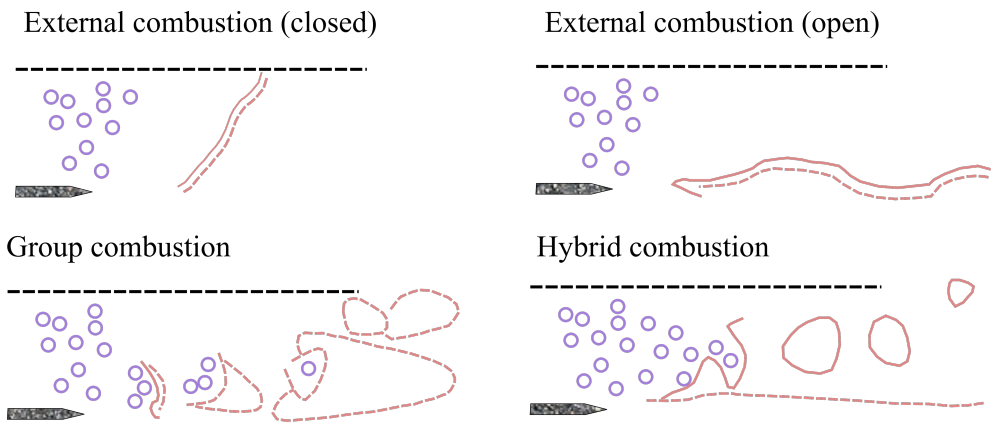

Figure 3.8: Spray combustion modes proposed by Reveillon and Vervisch [51] where solid lines represent the premixed burning and dashed lines indicate diffusion burning.

was suggested that the large fuel droplets of n-octane can augment the burning velocity under some conditions and these effects are negligible for small droplet sizes. The evaporation characteristics of the large propane droplets with a wide range of sizes ($400-1000\,\mu m$ diameter) was investigated as a function of mass fraction by Szekely and Faeth [153] and Faeth [132] in a turbulent environment. Mizutani and co-workers [62, 150] indicated that in spherically expanding flames, droplets may affect the rate of burning differently from the open burner flames. Lawes and Saat [119] carried out a series of experiments to reveal the difference in the flame structure and burning rates between iso-octane spray and premixed combustion. It was observed by Lawes and Saat [119] that the spray flame is more wrinkled than the gaseous flame under low turbulence intensity but no significant difference between gaseous and spray flame structure have been found under high turbulence intensity. All the aforementioned experimental investigations have revealed that the flame speed of spray flames depends on the complex interaction of droplet diameter, equivalence ratio and turbulence intensity.

The flame-droplet interaction was also analytically addressed by Polymeropoulos [155] who found that the burning velocity assumes a maximum value at a certain droplet diameter. Silverman et al. [157] developed an expression for laminar burning velocity of premixed polydisperse spray flames by analysing the combustion structure in a number of distinct zones. Figure 3.9 [115, 157] illustrates different zones of laminar freely propagating premixed spray flame on the temperature profile. It is stated that droplets evaporate in the first two region of the flame ahead of *the homogeneous reaction zone*. Evaporation occurs at constant temperature conditions in *the primary evaporation zone* whereas temperature increases in *the heating zone* due to the heat release from the flame. An effective equivalence ratio is defined to deduce the local composition of gaseous mixture which burns at *the homogeneous reaction zone.* Although the overall equivalence ratio, which is calculated based on the total gaseous and

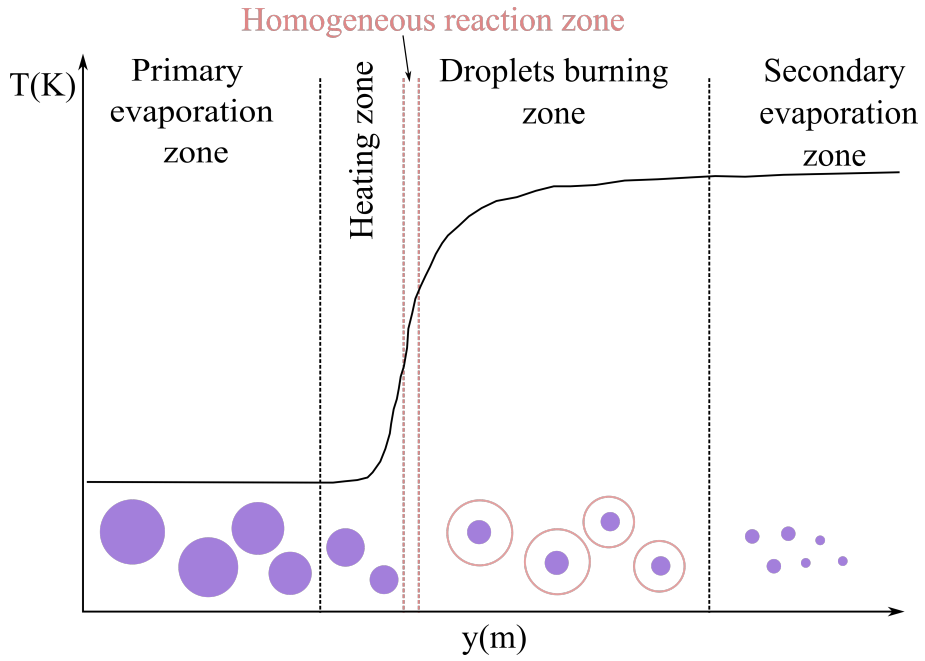

Figure 3.9: Schematic representation of different flame zones of one dimensional laminar premixed spray flame on the temperature profile [115, 157]

liquid fuel mass, is fuel-rich ($\phi_{ov} > 1$), the effective equivalence ratio can be fuel-lean ($\phi_{eff} < 1$) due to the slow evaporation rate of droplets with large diameter or low volatility. These liquid droplets with a slow evaporation rate can continue their evaporation in the *droplets burning zone* and can burn here individually (or in clusters) if the effective equivalence ratio is sufficiently lean in the homogeneous reaction zone so that the post flame zone contains enough hot oxidiser for burning. After consuming all oxidiser in the the post flame zone, surviving droplets continue to evaporate in *the secondary evaporation zone*. They also observed that initial Sauter mean diameter (SMD) is not enough to characterise polydisperse sprays because flames in different initial distributions with the same SMD behave differently. Greenberg et al. [156] proposed an analytical model in order to capture the enhancement of burning velocity due to the distortion created by droplets on the flame front. Flame stretch was modelled for spherically expanding polydisperse spray flames for the first time by Greenberg and Kalma [158] who also accounted for the effects of finite-rate evaporation and droplet drag [159]. It was indicated that droplet evaporation rate plays an important role on the flame extinction.

With the advancement of high-performance computing, several researchers have used the carrier phase DNS to investigate the combustion of spray flames [41–48, 50–52, 54–56, 67, 68]. Miller and Bellan [49] carried out DNS to investigate a three-dimensional planar gas mixing layer growth and development for different initial liquid mass loading ratios, initial Stokes numbers and initial droplet temperatures. It was proposed that the initial Stokes

number has no significant influence on the evolution of the mixing layer and an increase in the mass loading ratio of the droplets leads to an attenuation of the growth rate of the mixing layer. Wang and Rutland [67] and Schroll et al. [42] analysed the autoignition of n-heptane fuel droplets using DNS and the ignition delay has been found to increase with increasing equivalence ratio. Reveillon and Vervisch [50], Reveillon and Demoulin [53], Sreedhara and Huh [54], and Luo et al. [41] used the carrier phase DNS to explore the interactions between turbulent motion and spray combustion, which was subsequently used for different aspects of modelling turbulent spray flames. Wandel et al. [43], Wandel [44], Neophytou et al. [45, 46] and Papapostolou [109] applied DNS to analyse forced ignition in turbulent droplet-laden mixing layers and confirmed previous experimental observations by Ballal and Lefebvre [151] that large droplet diameters adversely affect the chance of successful ignition due to the lack of available gaseous fuel arising from a slow evaporation rate. A comprehensive DNS investigation of the influences of equivalence ratio, fuel droplet size and radiation on jet spray flames has been conducted by Fujita et al. [56]. It was found that the high temperature region moves from the jet centre to the outer jet edges as the equivalence ratio increases, and an increase in droplet diameter leads to a decrease in the gas temperature in the central downstream region (shown in Fig. 3.10).

Wandel [44] performed a three-dimensional DNS based analysis of localised forced ignition of n-heptane liquid fuel droplets and suggested that the dissipation rate of reaction progress variable c can be a quantitative indicator to determine whether a flame will globally extinguish after being ignited by the spark. Neophytou et al. [46] demonstrated that the structure of spray kernel flames obtained after spark ignition of n-heptane droplet-laden mixtures can be significantly different from that of a pure gaseous flame. Recently, Wacks and coworkers [47, 48] have analysed the effects of initial droplet diameter, overall equivalence ratio and turbulence intensity on statistically planar turbulent flame propagation into fuel-droplet mists. It has been shown that the gaseous phase combustion takes place predominantly under fuel-lean mode, even for fuel-rich overall equivalence ratios, and this trend strengthens with increasing droplet diameter because of the high evaporation time scale of large droplets. Flame propagation in spray combustion has been analysed in terms of displacement speed statistics in Refs. [47] and [48] and it was indicated that the mean density-weighted displacement speed of turbulent spray flames remains smaller than the unstrained laminar burning velocity of a stoichiometric mixture due to the predominance of the fuel–lean mode of combustion [47]. Furthermore, spray flames under turbulent conditions show a thicker flame structure than the corresponding turbulent stoichiometric premixed flames and this tendency strengthens with increasing droplet diameter [48].

Edge flame is an essential concept for partially premixed conditions. Edge flame structure

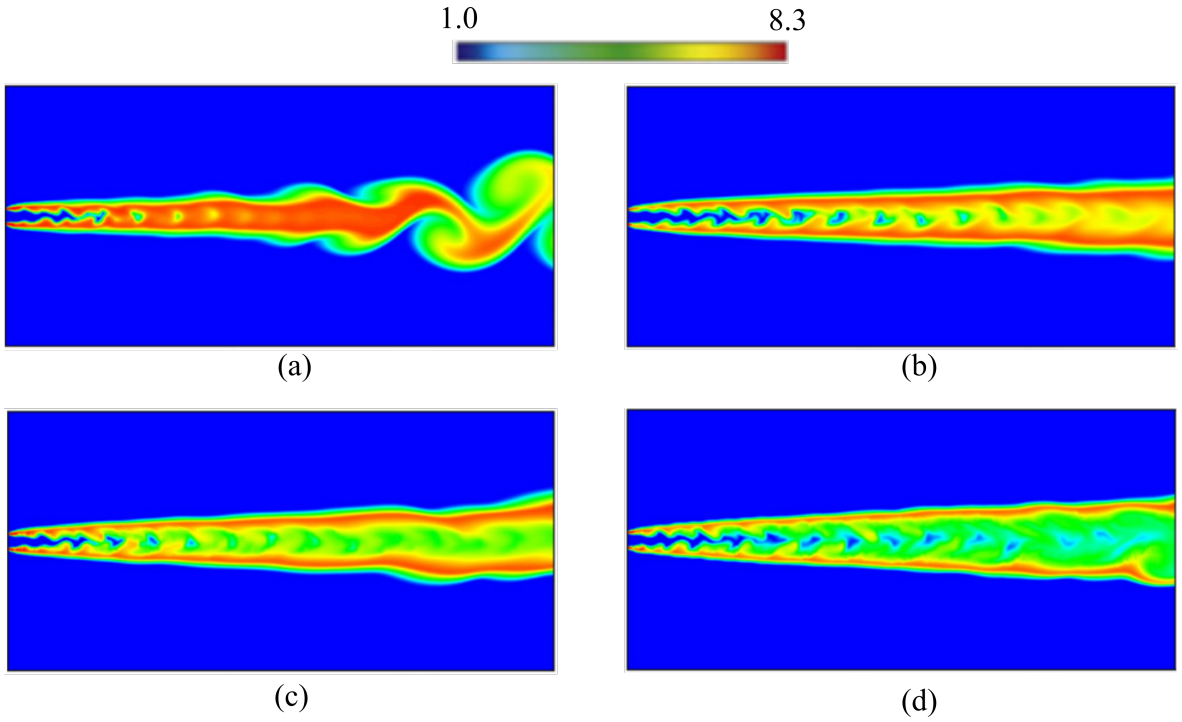

Figure 3.10: Distributions of instantaneous gas temperature for jet spray flames for (a) $\phi = 0.6$, (b) $\phi = 2.0$ with smaller droplet size, (c) $\phi = 2.0$ with larger droplet size and (d) $\phi = 10.0$ [56].

is being associated with the ignition, extinction and stabilisation of diffusion flames [92] and there has been a particular attempt for understanding the edge flame formation in these fundamental combustion phenomena [160–164]. The importance of the edge flame propagation for the ignition of mono-disperse liquid droplets has been highlighted in a recent study by Papapostolou et al. [164]. It was revealed that droplet size and overall equivalence ratio affect the propagation of edge flame through the inhomogeneous mixture created in the gaseous phase.

All the aforementioned studies on turbulent combustion in droplet-laden mixture revealed the complex interactions between droplets, flame and flow field. Equivalence ratio, droplet diameter and turbulence intensity play key roles on combustion characteristics and are not straightforwardly understandable, and need to more investigation for a fundamental understanding.

3.5 Spherically Expanding Gaseous Premixed Flame Propagation

A brief background for the evolution of gaseous spherical flames is provided in this section in order to gain fundamental physical insights into the impact of presence of liquid fuel droplets on the flame propagation. Gaining awareness about the physical parameters affecting the propagation of gaseous spherical kernels would be helpful to compare the behaviour of spherically expanding spray and gaseous premixed flames.

Laminar burning velocities of spherically expanding flames were measured by Bradley et al. [165] for a various range of initial pressure and temperature. Experiments for iso-octane–air and iso-octane–n-heptane–air mixtures showed that burning velocity decreases with increasing pressure and increases with temperature. It was also observed that flames at higher pressure and temperatures are more likely to develop a cellular structure which leads to an increase in flame speed. Thermo-diffusive instabilities arising from non-unity Lewis number (i.e. differential diffusion of heat and mass) were experimentally shown to enhance burning rate in spherically expanding turbulent premixed flames [166–168]. Three-dimensional DNS analysis was carried out by Thevenin et al. [169] to investigate the evolution of premixed methane/air flame kernels under homogeneous isotropic turbulence flow conditions. Considerable differences between two- and three- dimensional simulations identified and qualified for the statistical behaviour of flame surface area, stretch rate and flame front curvature. Jenkins and Cant [170] observed that large turbulence intensity leads to severe wrinkling on premixed kernel flame. For large turbulence intensities, flame kernel gets strongly distorted from its spherical shape. Discontinuities can appear in the flame surface and local flame separations can be observed.

DNS of flame kernels with detailed chemical mechanism were performed to investigate the structure of the flame front [171, 172]. The growth rate of the flame surface area and the global flame stretch rate were found to be larger at higher Reynolds number [172]. Although the mean values of flame curvature remain comparable for different turbulence intensities, the spread of flame curvature was observed to be affected by variations of Reynolds number [172]. Furthermore, flame stretch and curvature were used to predict local burning velocities of spherically expanding turbulent premixed flames in the corrugated flamelet regime [171]. On the other side, Hult et al. [173] and Gashi et al. [174] focussed on the evolution of the premixed flame kernels and obtained qualitatively good agreement between the DNS data based on simple chemical mechanism and the experimental measurements. The flame curvature influences the displacement speed of a flame through the tangential diffusion component. Klein et al. [57, 58] revealed that the initial radius of the kernel flame is closely linked with the minimum ignition

energy and quantified a critical initial radius exists for self-sustained propagation of turbulent premixed flame kernels. Flame locally propagates in the opposite direction to the local flame normal and ultimately quenches when it has a smaller radius value than critical radius (see Fig. 3.11). Moreover this critical kernel radius has been reported to increase with turbulent intensity. A spectral regime diagram based on flame-vortex interactions enables characterising fundamental mechanisms that control the coupling between turbulence and combustion. As turbulence interacts with a curved and stretched flame in the case of spherically expanding flame configuration, Echekki and Kolera-Gokula [175] developed a spectral regime diagram for kernel-vortex interactions. Important differences between the characteristics of planar and kernel flames were highlighted due to the strong influence of flame curvature on the interactions between flame and turbulence.

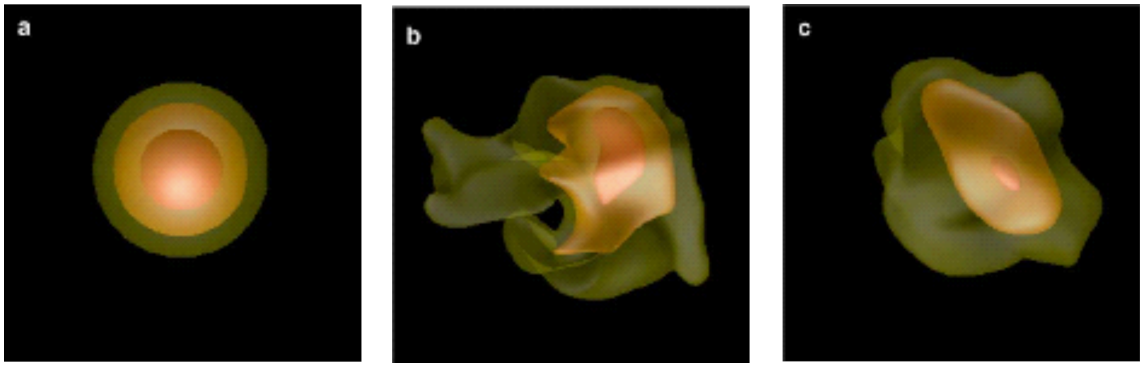

Figure 3.11: Isosurfaces of reaction progress variable $c = 0.9$ (red), 0.3 (orange), 0.1 (beige) after (a) 0.0 (b) 1.0 and (c) 2.0 eddy turnover times [58]

Dunstan and Jenkins [176] related the global flame growth to the evolution of global flame surface area of the kernel flames. The global fuel consumption rate was reported to diminish with increasing turbulence intensity although there was an enhancement in flame surface area. It was noted that global burning rate reduces due to the greater heat transfer away from the reaction zone by turbulent diffusion. Flame propagation statistics of spherical flames were compared with those of corresponding planar flames under the same flow and thermochemical conditions [177]. The planar flames were observed to reach a steady propagation while spherical flames exhibit a continuous acceleration of propagation.

Chapter 4

Statistical Analysis of Flame-Droplet-Turbulence Interaction-Part I: Effects of Turbulence Intensity

This chapter attempts to reveal physical fundamental insight into the flame propagation over a wide range of parameters, including droplet diameter and turbulence intensity. Flame propagation characteristics in spherically expanding spray flames are discussed based on flame wrinkling, reaction zone structure, and burning rate. Particular attention is given to the statistics of the reactive scalar gradient and flame-flame interaction which play important roles on flame propagation behaviour and its modelling.

4.1 Flame-Turbulence Interaction

Three dimensional DNS of spherically expanding n-heptane spray flames with a modified single step Arrhenius chemical mechanism are performed to investigate the influence of turbulence intensity on flame-droplet-turbulence interactions. A detailed description of initial simulation parameters is provided in Chapter 2. However, the simulation parameters used in Sections 4.1-4.5 have also been summarised in Table 4.1 for the sake of clarity in the results chapters.

The instantaneous non-dimensional temperature T, normalised gaseous fuel mass fraction, Y_F/Y_{Fst} and reaction progress variable c fields at the central $x-y$ mid-plane at $t = 2.1t_{chem}$ are shown in Figs. 4.1-4.3 for both laminar and turbulent flow conditions, respectively. It can be

Table 4.1: Simulation parameters considered in Section 4.1.

Parameter	Value
a_d/δ_{st}	0.04, 0.05 and 0.06
ϕ_{ov}	1.0
$u'/S_{b(\phi_g=1)}$	0.0, 4.0 and 8.0
L_{11}/δ_{st}	2.5
Pr	0.7
Le	1.0
$\gamma = C_p^G/C_v^G$	1.4

seen from Fig. 4.1 that the contours of c remain perfect circles for the laminar stoichiometric premixed flame case, indicating that the flame grows as a perfect sphere. By contrast, the contours of c for laminar droplet kernels are not perfectly circular because these flames do not remain perfectly spherical due to flame-droplet interaction. The above observations are consistent with the previous experimental findings of Hayashi et al. [118] and Lawes and Saat [119]. Figures 4.2 and 4.3 show that the droplet-induced flame wrinkling cannot be distinguished from turbulence-induced flame deformation for both premixed and droplet cases.

In both laminar and turbulent cases, the droplets reduce in size due to evaporation as they approach the flame and eventually disappear as a result of complete evaporation (examples are shown in the insets of Figs. 4.1-4.3, see 1^{st}column and 2^{nd} row). During the evaporation process, droplets extract latent heat from the surrounding gaseous phase and this contributes to the local reduction in the temperature of the burned gas region in the droplet cases in comparison to the corresponding gaseous premixed flame cases, and this effect is prominent for large droplets (see 1^{st} column of Figs. 4.1-4.3). However, the evaporation rate was not sufficient to provide stoichiometric mixture ahead of the flame in all the droplet cases considered here (see 2^{nd} column of Figs. 4.1-4.3), and thus, the combustion of predominantly fuel-lean mixture ($Y_F/Y_{Fst} < 1.0$) also acts to bring down the burned gas temperature in comparison to that in the stoichiometric premixed flame. For the initial $a_d/\delta_{st} = 0.04$ case, the evaporation rate is greater than in the other droplet cases, and thus droplets evaporate either mostly ahead of or within the flame in this case but for the initial $a_d/\delta_{st} = 0.05$ and 0.06 cases droplets penetrate the flame and continue to evaporate in the burned gas region and unburned fuel pockets can be found within the burned gas kernel in these cases (significantly fuel-rich pockets in the burned gas can be discerned in the $a_d/\delta_{st} = 0.06$ case in Figs. 4.1-4.3).

Under high turbulence intensity, the flames become severely wrinkled and move away from the centre of the domain and the out of plane movement leads to broken contours of T, Y_F/Y_{Fst} and c in Fig. 4.3 for both premixed and droplet cases. The strong turbulent motion also carries the droplets across the flame and increases the availability of droplets in the burned

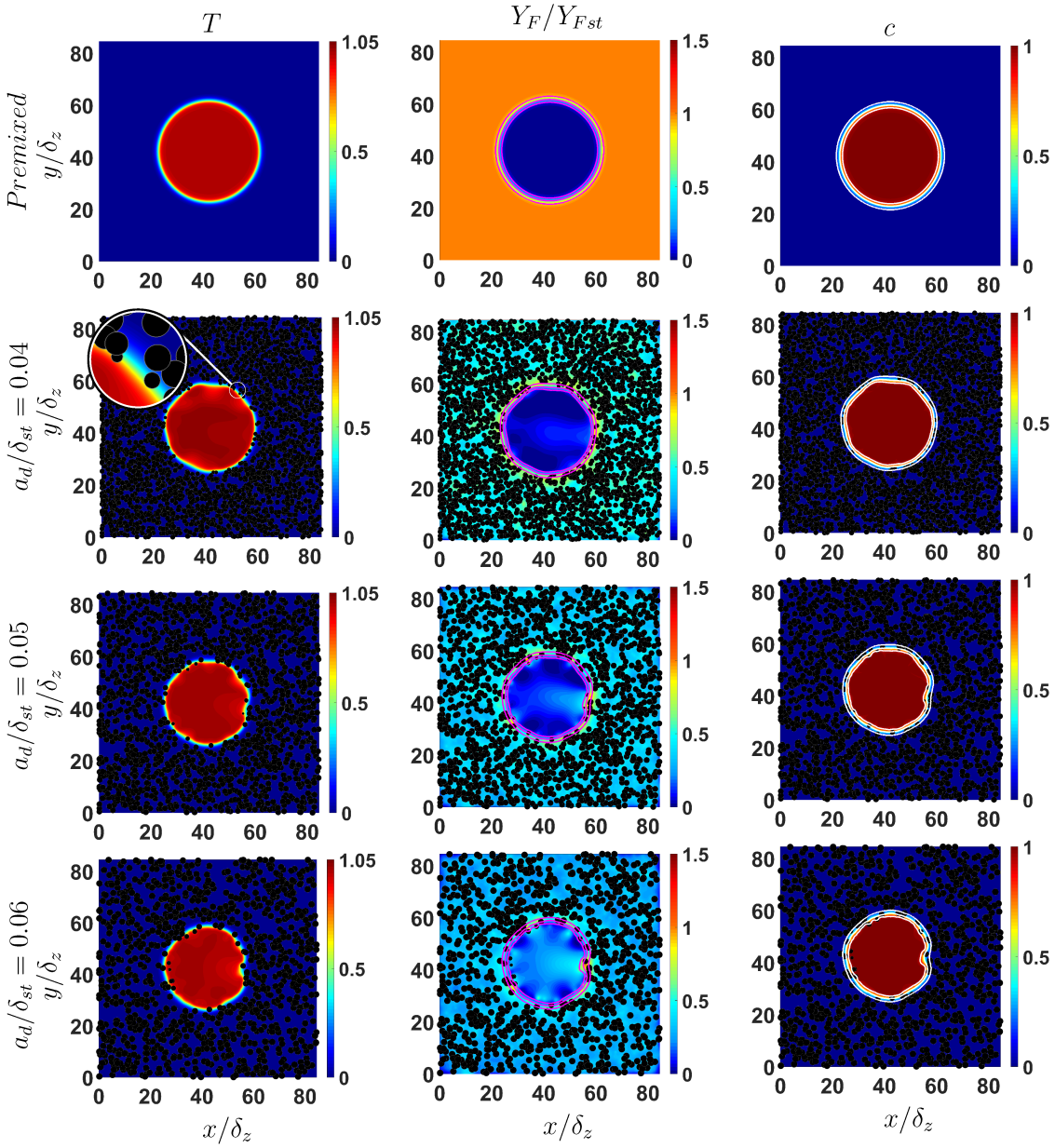

Figure 4.1: (Left to right) Distribution of T, Y_F/Y_{Fst} (magenta lines show $c = 0.1, 0.5, 0.9$ contours from outer to inner periphery) and c (white lines show $c = 0.1, 0.5, 0.9$ contours from outer to inner periphery) on the central $x-y$ mid-plane for laminar flames. Black dots show the droplets residing on the plane (not to scale). All figures correspond to $t = 2.1t_{chem}$.

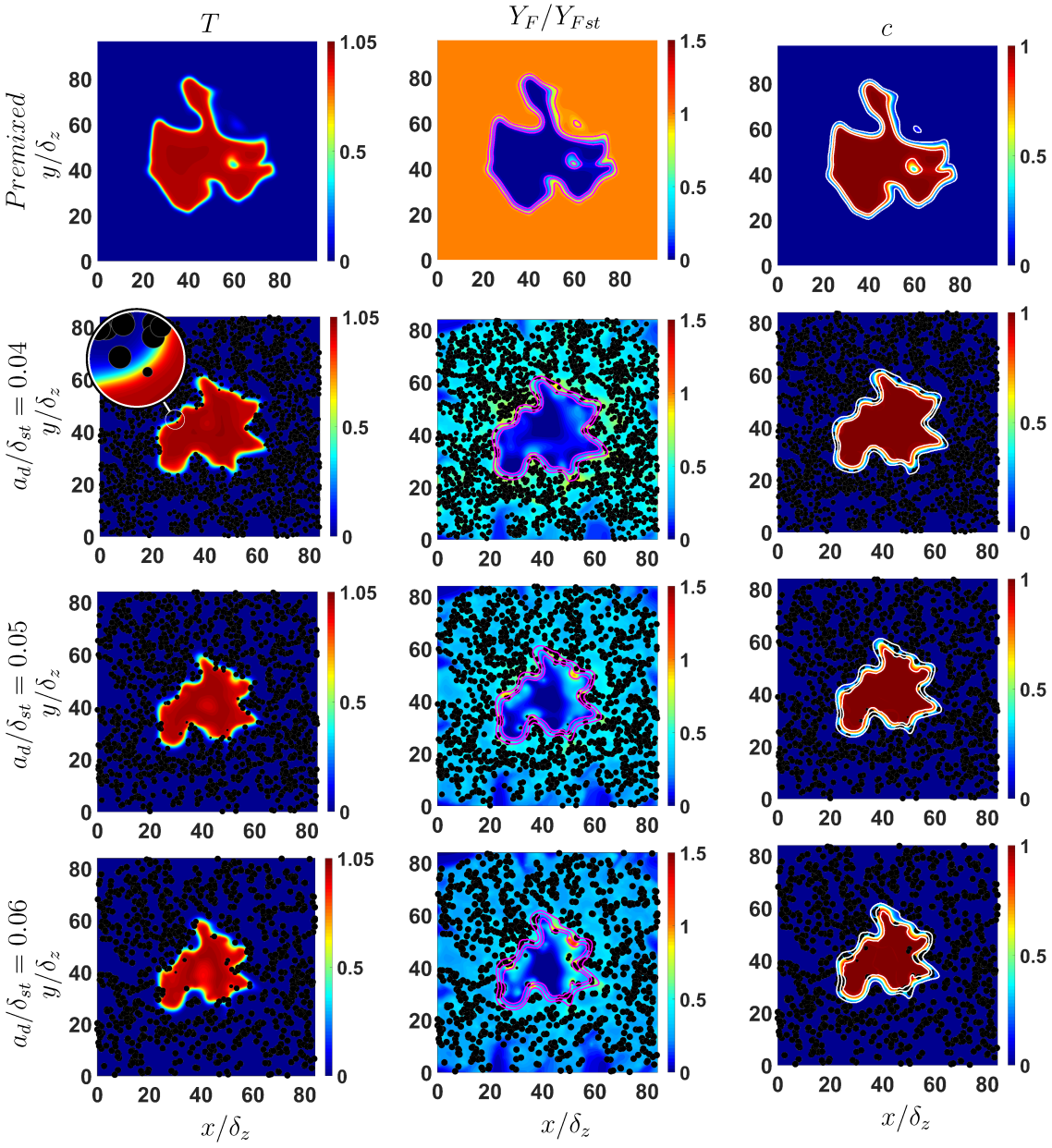

Figure 4.2: (Left to right) Distribution of T, Y_F/Y_{Fst} (magenta lines show $c = 0.1, 0.5, 0.9$ contours from outer to inner periphery) and c (white lines show $c = 0.1, 0.5, 0.9$ contours from outer to inner periphery) on the central $x-y$ mid-plane for turbulent flames with initial $u'/S_{b(\phi_g=1)} = 4.0$ at $t = 2.1t_{chem}$. Black dots show the droplets residing on the plane (not to scale).

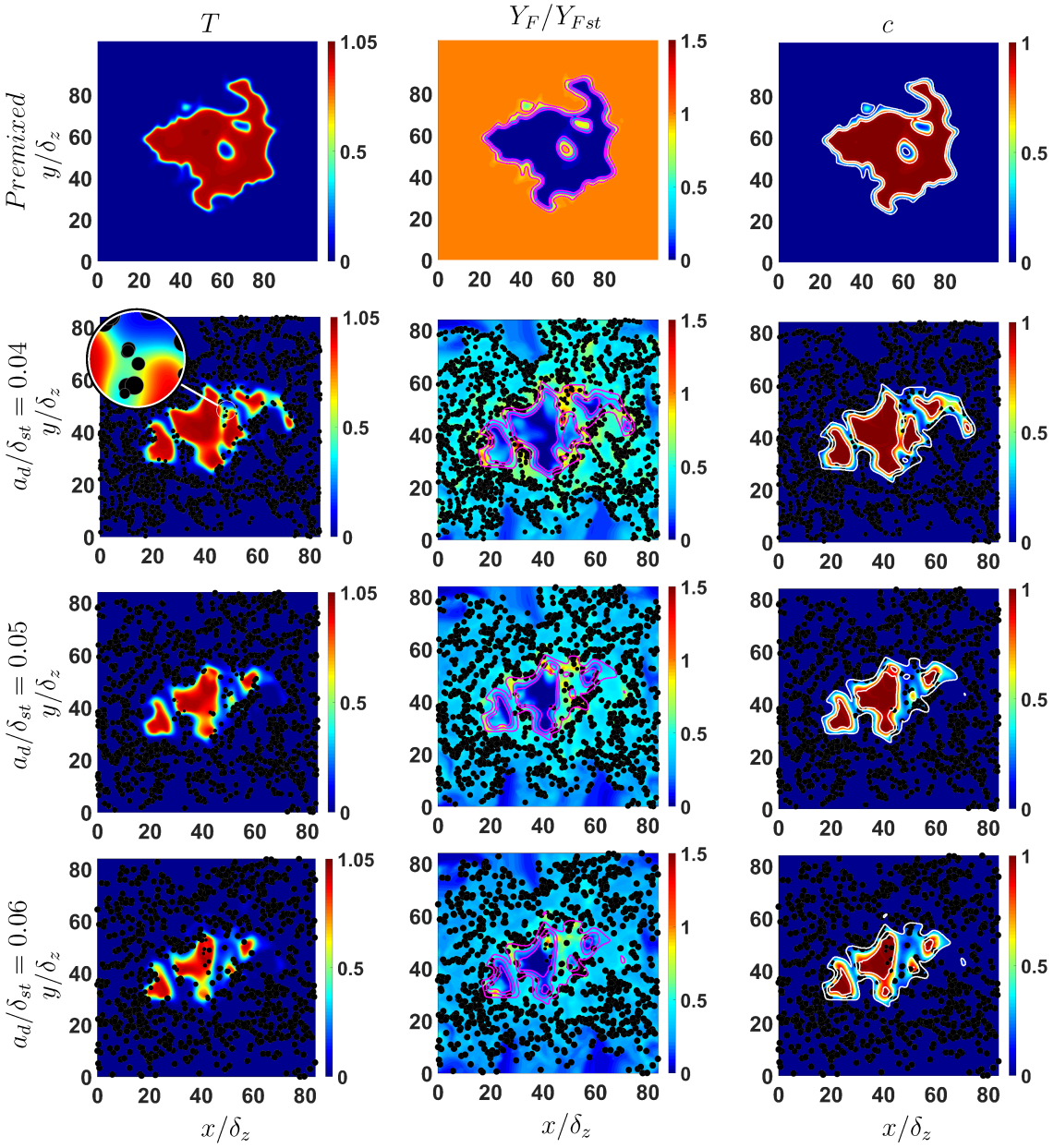

Figure 4.3: (Left to right) Distribution of T, Y_F/Y_{Fst} (magenta lines show $c = 0.1, 0.5, 0.9$ contours from outer to inner periphery) and c (white lines show $c = 0.1, 0.5, 0.9$ contours from outer to inner periphery) on the central $x-y$ mid-plane for turbulent flames with initial $u'/S_{b(\phi_g=1)} = 8.0$ at $t = 2.1t_{chem}$. Black dots show the droplets residing on the plane (not to scale).

gas side. This tendency is particularly dominant for large droplet cases. The effects of droplets on c-contour lines (see 3^{rd} column of Figs. 4.1-4.3) are evident for both laminar and turbulent cases and the flames exhibit instances of local flame thickening for large droplet cases. This tendency is particularly evident under high turbulence intensity cases.

The initial values of Damköhler and Karlovitz numbers (i.e. $Da_{(\phi_g=1)} = L_{11}S^2_{b(\phi_g=1)}/u'\alpha_{T0}$ and $Ka_{(\phi_g=1)} = (u'/S_{b(\phi_g=1)})^{1.5}/(L_{11}S_{b(\phi_g=1)}/\alpha_{T0})^{-0.5}$) for the premixed case with initial $u'/S_{b(\phi_g=1)} = 4.0$ are 1.31 and 3.49 respectively. The values of $Da_{(\phi_g=1)}$ and $Ka_{(\phi_g=1)}$ are 0.65 and 9.88 respectively for the premixed case with initial $u'/S_{b(\phi_g=1)} = 8.0$. The value of Damköhler (Karlovitz) number for the droplet cases is likely to be smaller (greater) than the corresponding premixed flame cases because of predominantly fuel-lean burning (which implies that the chemical time scale is likely to be larger than $\alpha_{T0}/S^2_{b(\phi_g=1)}$ because of smaller burning velocity). These Damköhler and Karlovitz number values are representative of the distributed burning regime, and thus all the cases exhibit local flame thickening and these tendencies are particularly strong for droplet cases due to small (large) values of Da (Ka).

4.2 Flame Wrinkling

The influences of the droplets on the flame surface are evident from Fig. 4.4 where the instantaneous $c = 0.5$ isosurfaces are coloured by local values of flame curvature $\kappa_m \times \delta_{st}$. The local curvature κ_m is defined as $\kappa_m = \nabla \cdot \overrightarrow{N}/2$ where $\overrightarrow{N} = -\nabla c/|\nabla c|$ is the local flame normal vector. According to these definitions, the flame normal vector points towards the reactants and an element of flame surface, which is convex (concave) to the reactants, has a positive (negative) curvature. Fig. 4.4 shows dimples (i.e. droplet-induced curvatures) on $c = 0.5$ isosurfaces in both laminar (1^{st} row) and turbulent (2^{nd} and 3^{rd} rows) droplet cases, which are completely absent in the laminar premixed flame.

The droplet-induced flame deformation can be quantified with the help of the Probability Density Functions (PDFs) of κ_m shown in Fig. 4.5 for $c = 0.1, 0.5$ and 0.9 isosurfaces. The curvature PDFs of the laminar droplet cases show a spread of curvature values due to flame-droplet interaction, whereas the PDF of κ_m is a delta function for the laminar premixed flame, owing to its perfect spherical shape. The PDFs in the turbulent cases show higher probability of finding positive values (i.e. flame surface convex to the reactants) than obtaining negative curvatures (i.e. flame surface concave to the reactants) but the droplet cases exhibit wider κ_m distributions than the premixed case because of the droplet-induced curvatures. The widening of curvature PDFs is particularly prominent for larger droplets, especially in the burned gas region for both laminar and turbulent flames. The large droplets can survive longer than others due to their slow evaporation and as a result they can interact with the flame towards the burned

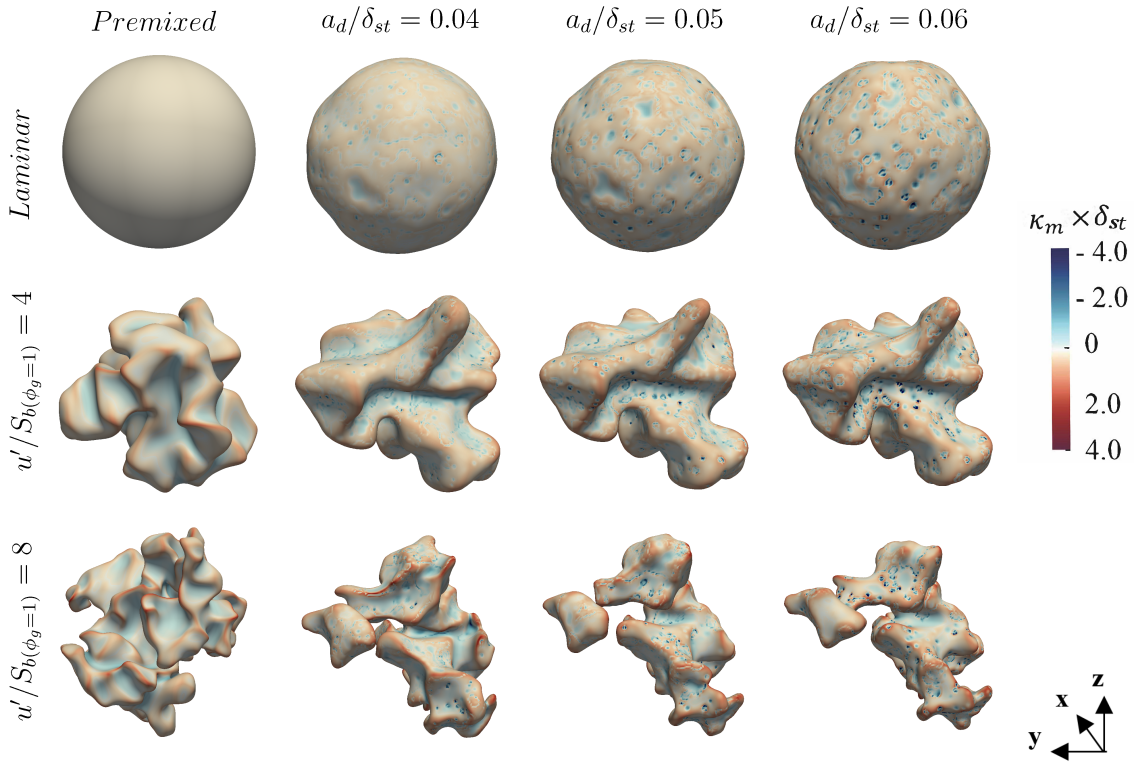

Figure 4.4: Instantaneous view of $c = 0.5$ isosurface coloured with local values of $\kappa_m \times \delta_{st}$ for laminar (1^{st} row) and turbulent (2^{nd} and 3^{rd} rows) flames at $t = 2.1t_{chem}$.

gas side of the flame front. The same tendency was also experimentally observed [118, 119], but these effects were more magnified in Lawes and Saat [119] due to the presence of thermo-diffusive and hydro-dynamic instabilities.

The magnitude of the inner product of the local flame normal $\overrightarrow{N}$ and the unit radial vector $\overrightarrow{r}$ from the centre of the mass of the flame kernel can be used to quantify the extent of flame wrinkling. The angle between these two unit vectors ($\overrightarrow{N}$ and $\overrightarrow{r}$) is equal to zero (or the projection $|\overrightarrow{N} \cdot \overrightarrow{r}|$ equals to $|cos\theta| = |\overrightarrow{N} \cdot \overrightarrow{r}| = 1.0$) for a perfectly spherical flame. A greater extent of flame wrinkling leads to a higher extent of deviation of the projection $|\overrightarrow{N} \cdot \overrightarrow{r}|$ from 1.0. The PDFs of $|\overrightarrow{N} \cdot \overrightarrow{r}|$ are shown for $c = 0.1, 0.5$ and 0.9 isosurfaces in Fig. 4.6. It can be seen from Figs. 4.6a-c that PDFs of $|\overrightarrow{N} \cdot \overrightarrow{r}|$ become a delta function at $|\overrightarrow{N} \cdot \overrightarrow{r}| = 1.0$ for the laminar premixed flame case due to its perfect spherical shape. The PDFs of $|\overrightarrow{N} \cdot \overrightarrow{r}|$ for the laminar droplet flames assume peak value at 1.0 but they also show finite probability of having $|\overrightarrow{N} \cdot \overrightarrow{r}| < 1.0$, indicating imperfect spherical shape as apparent from Fig. 4.4 due to droplet-induced flame wrinkling. A careful examination of the PDFs of $|\overrightarrow{N} \cdot \overrightarrow{r}|$ for laminar cases reveals that the extent of deviation of $|\overrightarrow{N} \cdot \overrightarrow{r}|$ from 1.0 is the highest for $a_d/\delta_{st} = 0.06$ amongst all the droplet cases considered here. However, there is no significant

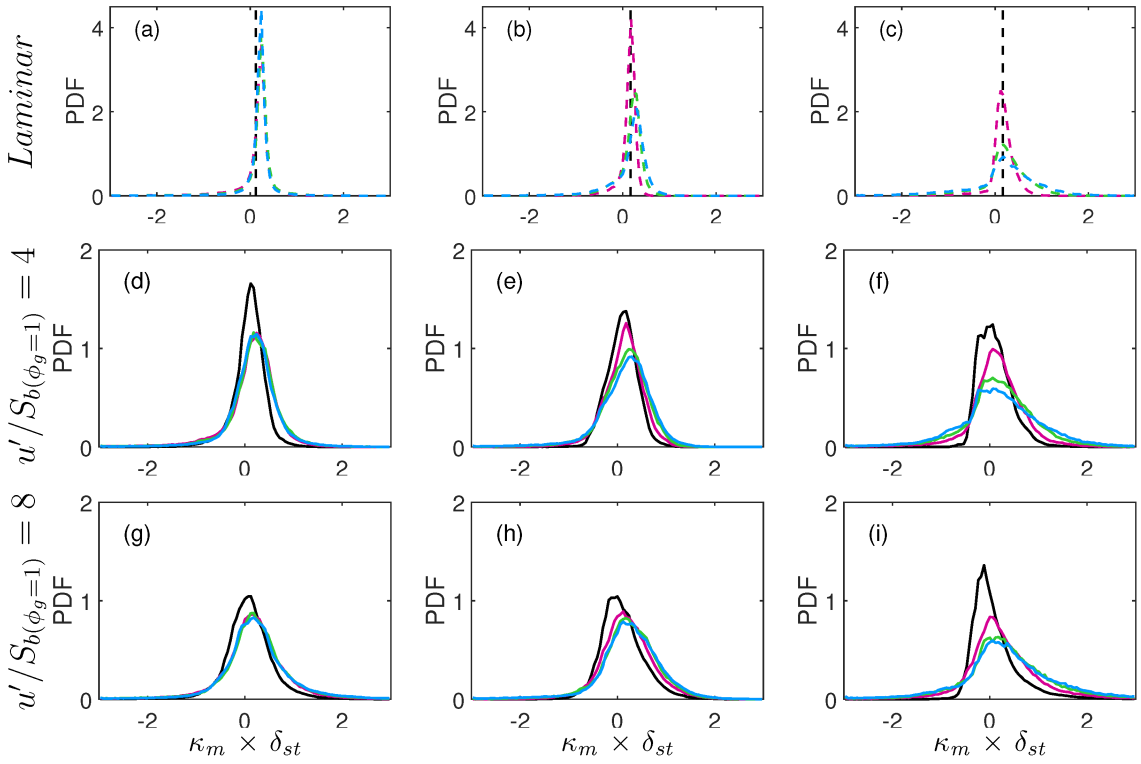

Figure 4.5: PDFs of $\kappa_m \times \delta_{st}$ for c= (a,d,g) 0.1, (b,e,h) 0.5 and (c,f,i) 0.9 isosurfaces for the premixed stoichiometric flame (——) and for all droplet cases with initial $a_d/\delta_{st} = 0.04$ (——), 0.05 (——), 0.06 (——) for laminar (dashed line) and turbulent (solid lines). Same colour keys are used in Figs. 4.6-4.8,4.11-4.13,4.15 and 4.16.

difference between the extent of flame wrinkling of the premixed and droplet turbulent flames with the initial $u'/S_{b(\phi_g=1)} = 4.0$ where the wrinkling by turbulence eclipses the wrinkling due to the flame-droplet interaction, which is consistent with previous experimental findings [118, 119]. Additionally, increasing turbulence intensity leads to a significant increase in the extent of wrinkling for premixed flame, and this is reflected in the greater extent of deviation of $|\overrightarrow{N} \cdot \overrightarrow{r}|$ from 1.0 for the premixed case than the droplet cases at high values of $u'/S_{b(\phi_g=1)}$. This behaviour originates due to the differences in flame surface area between the premixed and droplet flame cases.

The extent of flame wrinkling plays a key role in determining the growth rate of flame surface area in expanding flame kernels, and the temporal evolutions of flame area normalised by its initial value A/A_0 (where A is evaluated by the volume-integral $A = \int_V |\nabla c| dV$) for all cases considered here are shown in Figs. 4.7a-c, which reveal that laminar droplet cases have higher A/A_0 than the laminar stoichiometric premixed flame. Flame surface area A, of small droplets under laminar conditions reaches nearly eightfold of its initial flame surface area and

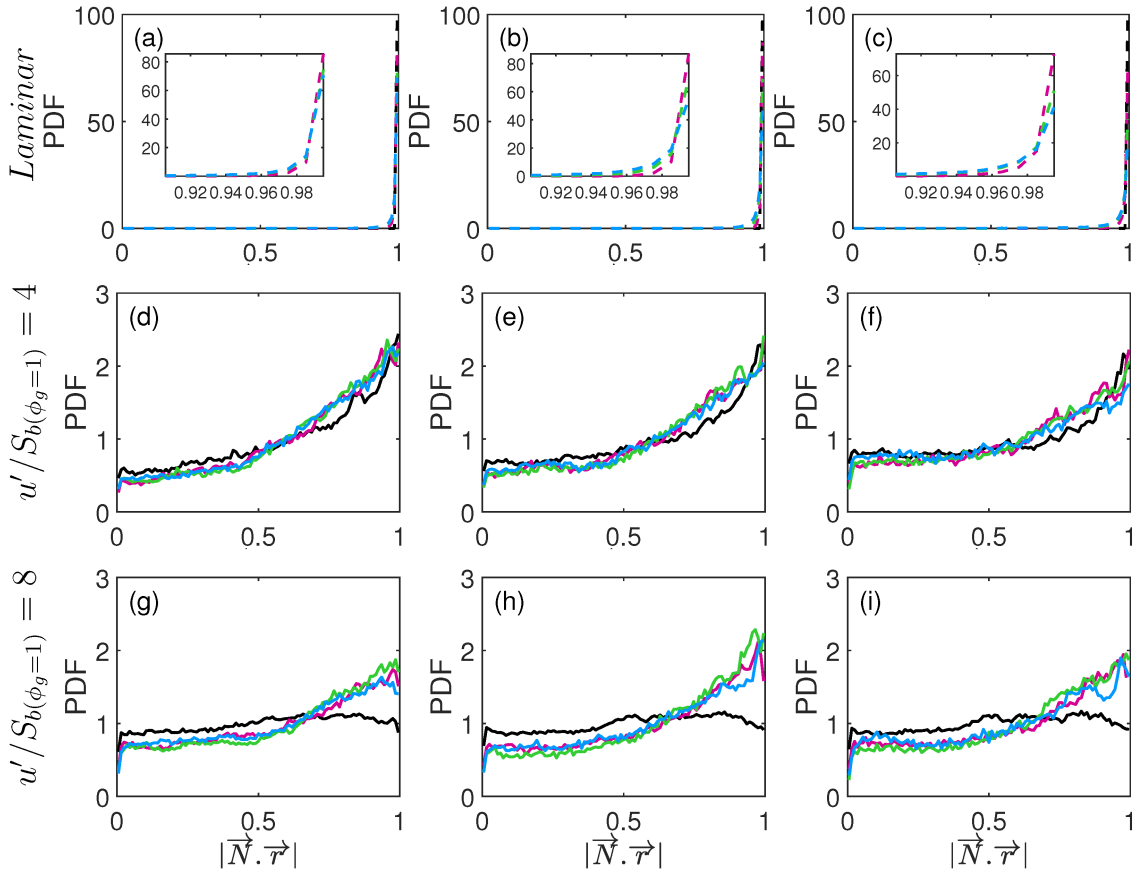

Figure 4.6: PDFs of $|\overrightarrow{N} \cdot \overrightarrow{r}|$ on $c = 0.1$ (a,d,g), 0.5 (b,e,h) and 0.9 (c,f,i) isosurfaces. See Fig. 4.5 caption for the colour keys.

this ratio is around 5 for laminar premixed flame. However, the turbulent droplet case with initial $a_d/\delta_{st} = 0.04$ and $u'/S_{b(\phi_g=1)} = 4.0$ (see Fig. 4.7b) shows a marginally higher value of A/A_0 than the turbulent stoichiometric premixed flame, whereas turbulent droplet cases with initial $a_d/\delta_{st} = 0.05$ and 0.06 exhibit A/A_0 values smaller than the corresponding premixed flame case for $u'/S_{b(\phi_g=1)} = 4.0$. The value of A/A_0 in the premixed flame is greater than all droplet cases for initial turbulence intensity of $u'/S_{b(\phi_g=1)} = 8.0$ (see Fig. 4.7c). Moreover, A/A_0 decreases with increasing droplet diameter for both laminar and turbulent cases. However, it is worth noting that A_0 values are different for the cases considered here and A_0 (i.e. flame surface area $A = \int_V |\nabla c| dV$ of a spherical laminar flame of initial burned gas radius $r_0 = 2\delta_{st}$) for $a_d/\delta_{st} = 0.04, 0.05$ and 0.06 cases have been found to be 0.53, 0.57, 0.66 times the value for the stoichiometric laminar premixed flame $A_{(0,pre)}$, respectively. The temporal evolution of $A/A_{(0,pre)}$ for all the laminar and turbulent cases are shown in Figs. 4.7d-f, which indicate that $A/A_{(0,pre)}$ in droplet cases remains smaller than the stoichiometric premixed flame case for both laminar and turbulent conditions. In order to explain this difference in $A/A_{(0,pre)}$ val-

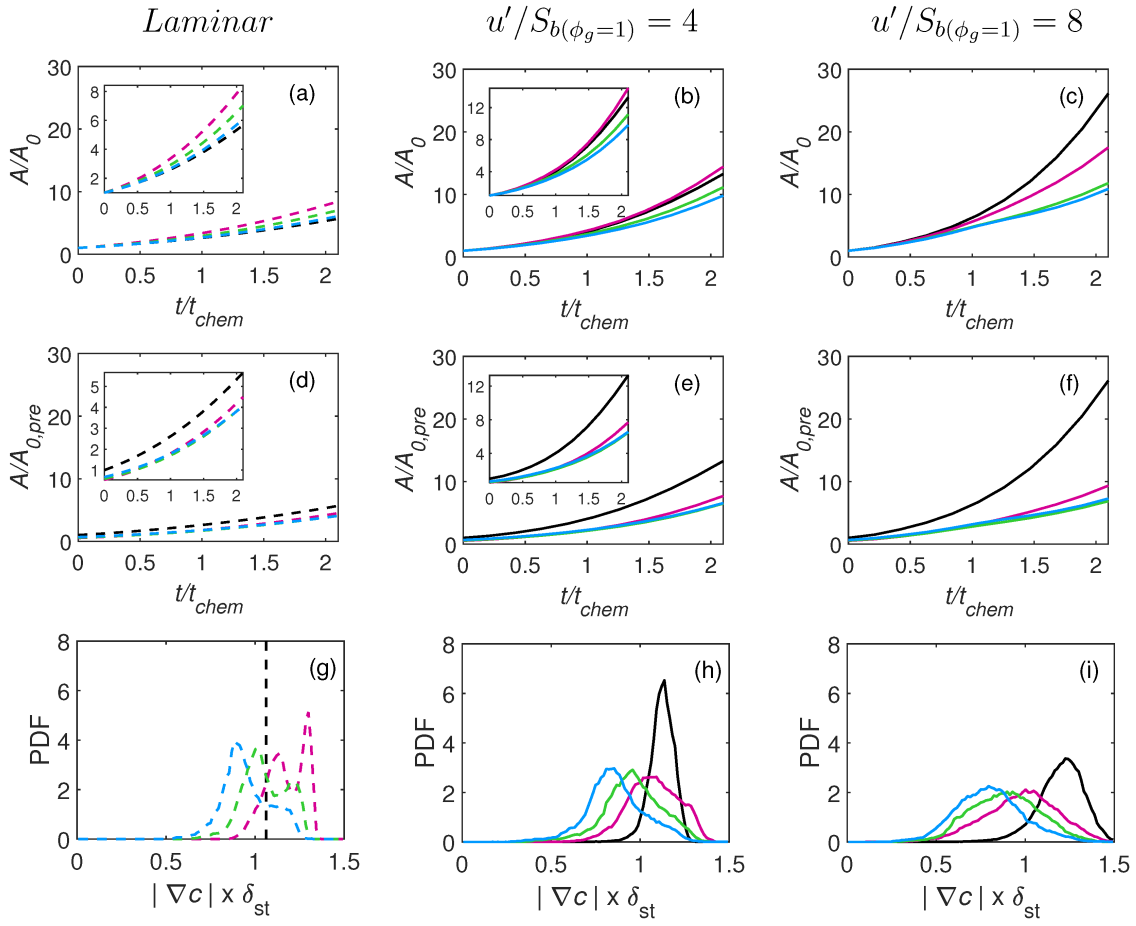

Figure 4.7: (a-c) Temporal evolution of normalised flame surface area A/A_0; (d-f) Temporal evolution of flame surface area normalised by initial value of premixed flame $A/A_{0,pre}$; (g-i) PDF of $|\nabla c| \times \delta_{st}$ on $c = 0.5$. See Fig. 4.5 caption for the colour keys.

ues between the cases considered here, the PDFs of $|\nabla c| \times \delta_{st}$ are exemplarily shown in Fig. 4.7g-i for $c = 0.5$ isosurface (same qualitative trend is observed for other c isosurfaces) for all cases considered here. Figures 4.7g-i show that the droplet cases exhibit greater probability of finding small values of $|\nabla c|$ than the corresponding premixed flame cases except for the laminar case with $a_d/\delta_{st} = 0.04$, and the probability of finding smaller values of $|\nabla c|$ is greater for $a_d/\delta_{st} = 0.06$ cases than in $a_d/\delta_{st} = 0.05$ cases. This along with smaller volume over which $|\nabla c|$ assumes non-zero values (see Fig. 4.1 for the region with $0.01 \leq c \leq 0.99$) gives rise to smaller $A/A_{(0,pre)}$ in the droplet cases with $a_d/\delta_{st} = 0.05$ and 0.06 in comparison to the corresponding premixed case. It is worth noting that the volume over which $|\nabla c|$ assumes non-zero values is smaller in the laminar droplet flame with $a_d/\delta_{st} = 0.04$ than in the corresponding laminar premixed flame. This leads to smaller values of $A/A_{(0,pre)}$ and A_0 in the laminar droplet flame with $a_d/\delta_{st} = 0.04$ than in the corresponding laminar premixed

Table 4.2: Normalised flame speed $S_A/S_{b(\phi_g=1)}$, which quantifies the growth rate of flame surface area A.

	Laminar	$u^{'}/S_{b(\phi_g=1)}=4$	$u^{'}/S_{b(\phi_g=1)}=8$
$a_d/\delta_{st}=0.04$	5.460	7.956	9.154
$a_d/\delta_{st}=0.05$	4.871	6.928	7.228
$a_d/\delta_{st}=0.06$	4.687	6.777	7.312
Premixed	5.423	10.445	16.000

flame despite exhibiting greater probability of obtaining higher $|\nabla c|$ value in comparison to the premixed laminar flame. The integral that yields A_0 value is influenced by the magnitude of $|\nabla c|$ and the volume over which $|\nabla c|$ assumes non-zero values. The smaller magnitudes of $|\nabla c|$ in laminar droplet cases with initial $a_d/\delta_{st}=0.05$ and 0.06 in comparison to those in the corresponding premixed case are principally responsible for yielding smaller values of A_0 than $A_{(0,pre)}$ despite all cases having same initial burned gas radius $r_0=2\delta_{st}$. Thicker flame (i.e. larger flame volume) in the laminar droplet cases with initial $a_d/\delta_{st}=0.05$ and 0.06, in comparison to the corresponding droplet case with initial $a_d/\delta_{st}=0.04$ gives rise to greater values of A_0 than the corresponding value in the $a_d/\delta_{st}=0.04$ case despite exhibiting higher probability of showing smaller values of $|\nabla c|$ and identical values of r_0. The probability of finding local high values of $|\nabla c|$ is greater in turbulent cases than in the corresponding laminar case for both droplet and premixed flames, which is consistent with higher values of $A/A_{(0,pre)}$ under turbulent conditions in Figs. 4.7d-f.

The rate of flame surface area growth can be estimated by a flame speed S_A, which is defined as $S_A=dr_A/dt$ where $r_A=\sqrt{(A/4\pi)}$ is an equivalent radius based on flame surface area. The value of S_A is estimated by using the slope of the linear part of temporal evolution of r_A and this slope remains unchanged since halfway through the simulation. The evaluated values of S_A are summarised in Table 4.2, which indicates that the laminar droplet case with initial $a_d/\delta_{st}=0.04$ grows slightly faster than the spherically expanding stoichiometric laminar premixed flame but S_A for laminar droplet cases with initial $a_d/\delta_{st}=0.05$ and 0.06 are found to be smaller than that in the premixed case. However, turbulent stoichiometric premixed cases exhibit greater values of S_A than the droplet cases. The value of S_A tends to decrease with increasing a_d/δ_{st} for droplet cases. Furthermore, S_A increases with increasing $u'/S_{b(\phi_g=1)}$. All the above conclusions are consistent with the observations made from Figs. 4.7a-c, but Table 4.2 provides quantifications of the effects of droplet size and turbulence intensity on the growth rate of flame surface area.

A comparison between Y_F/Y_{Fst} fields in Fig. 4.1-4.3 (2^{nd} column) reveals that combustion predominantly takes place under fuel-lean mode (i.e. $Y_F/Y_{Fst}<1$) for all laminar and turbu-

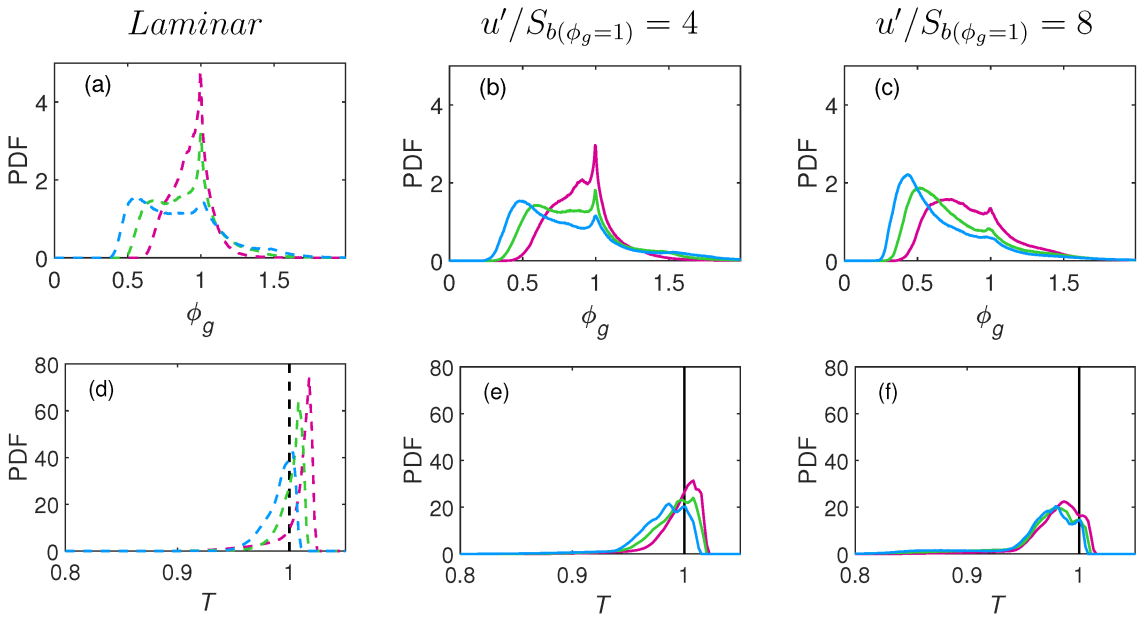

Figure 4.8: (a-c) PDF of ϕ_g in the region corresponding to $0.01 \leq c \leq 0.99$; (d-f) PDF of non-dimensional temperature T in the region corresponding to $c \geq 0.99$. See Fig. 4.5 caption for the colour keys.

lent droplet cases in spite of having an overall equivalence ratio of $\phi_{ov} = 1.0$. The PDFs of gaseous phase equivalence ratio ϕ_g for $0.01 \leq c \leq 0.99$ are shown in Fig. 4.8a-c, which shows a considerable variation of ϕ_g within the flame. Although the PDF of ϕ_g in Fig. 4.8b peaks at 1.0 for the $a_d/\delta_{st} = 0.04$ case under turbulence conditions with initial $u'/S_{b(\phi_g=1)} = 4.0$, the probability of finding a fuel-lean (i.e. $\phi_g < 1$) mixture overwhelms the availability of $\phi_g \geq 1$ mixtures. This tendency strengthens further for the $a_d/\delta_{st} = 0.05$ and 0.06 cases. Moreover, it is evident from Fig. 4.8c that an increase in turbulence intensity enhances the likelihood of finding fuel-lean mixtures. The turbulent mixing strengthens with increasing u' which enables turbulent transport of gaseous fuel from the evaporation sites to distant locations which would have not been possible for either laminar or smaller values of u'. This reduces the probability of finding localised fuel-rich pockets and increases the possibility of obtaining fuel-lean mixtures in the droplet cases for an initial turbulence intensity of $u'/S_{b(\phi_g=1)} = 8.0$ in comparison to the corresponding laminar and $u'/S_{b(\phi_g=1)} = 4.0$ droplet cases. The predominant fuel-lean mode of combustion and the extraction of latent heat by droplets reaching the burned gas act to reduce the burned gas temperature, and this can be substantiated from the PDFs of T, shown for the region corresponding to $c \geq 0.99$ in Fig. 4.8d-f, which indicate that there is a considerable probability of finding $T < 1.0$ in the burned gas for the droplet cases whereas the corresponding PDF for the stoichiometric premixed flames (both laminar and turbulent) is a delta function at $T = 1.0$. However, the non-dimensional burned gas temperature for the

droplet cases also shows small finite probabilities of obtaining $T \geq 1.0$ even when the peak value of the gaseous equivalence ratio PDF is obtained at $\phi_g < 1$ (e.g. see $a_d/\delta_{st} = 0.05$ and 0.06 cases under turbulent conditions in Fig. 4.8a-c). In order to explain this behaviour, it is necessary to understand the reaction zone structure in the spherically expanding droplet flames.

4.3 Reaction Zone Structure

The mode of combustion can be distinguished with the help of the flame index FI, which is defined as $FI = (\nabla Y_F \cdot \nabla Y_O)/(|\nabla Y_F||\nabla Y_F|)$ [94]. The flame index FI assumes positive (negative) values for premixed (non-premixed) mode of combustion. The percentages of heat release rate arising from premixed and non-premixed modes of combustion are shown in Fig. 4.9 for laminar and turbulent droplet cases. The total heat release rate is calculated with $HR_{total} = \int_V H_\phi |\dot{w}_F| dV$ [47] where H_ϕ indicates the heat release per unit mass of fuel (see section 2.1.4) and is defined using the approach developed by Tarrazo et al. [75].

It is evident from Fig. 4.9 that the cases with small droplets show that heat release predominantly arises from the premixed mode of combustion. The contribution of premixed (non-premixed) mode of combustion to the overall heat release rate decreases (increases) with increasing droplet diameter due to slow evaporation rates. Furthermore, turbulent cases show a higher contribution of non-premixed combustion mode to total heat release rate than the corresponding laminar droplet cases. Turbulence not only mixes the gaseous fuel with the surrounding air but also transports droplets. As evident from Figs. 4.2 and 4.3, more droplets can penetrate towards the burned gas side of the flame under turbulent conditions than in the corresponding laminar cases and this effect is particularly prevalent for large droplets. These droplets evaporate and release gaseous fuel in the burned side and some of that fuel diffuses back to the unburned gas side to form local diffusion (i.e. non-premixed) flames, which also contribute to the overall heat release. This trend can be seen from the c isosurfaces coloured by FI for $a_d/\delta_{st} = 0.06$ under laminar and high turbulence intensity conditions in Fig. 4.10. For $c = 0.5$ and 0.9 isosurfaces, the flame index FI predominantly assumes positive values, indicating the dominance of premixed mode but local islands of non-premixed mode ($FI < 0$) can also be discerned. However, this behaviour is reversed on the unburned gas side (e.g. $c = 0.1$) of the flame front. In this configuration, the fuel in the gaseous phase originates from the evaporation of droplets and the evaporated fuel mixes with air as it burns on the unburned gas side of the flame front, and thus the flame index FI assumes predominantly negative values.

For a detailed investigation on flame index and reaction rate of c across the flame, the mean values of FI and the normalised reaction rate of progress variable $\dot{w}_c \times \delta_{st}/\rho_0 S_{b(\phi_g=1)}$

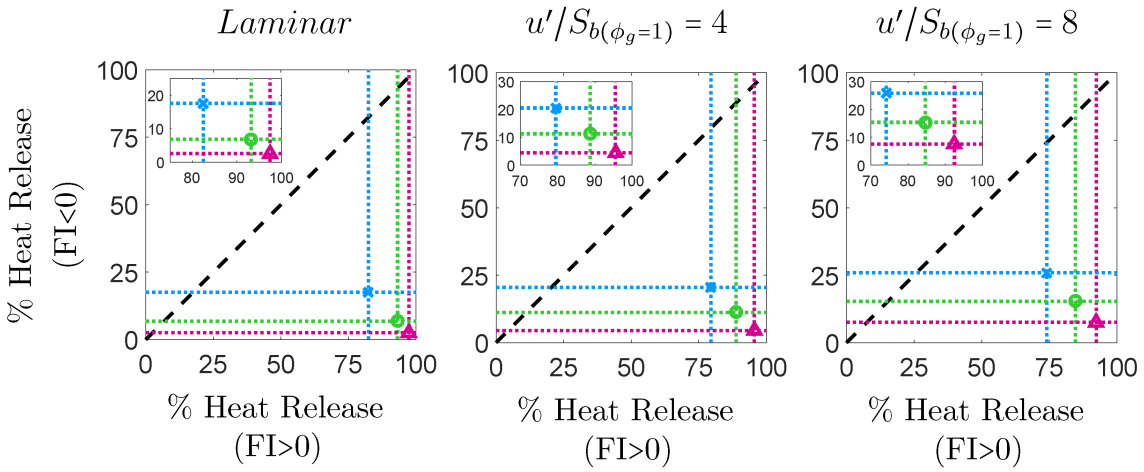

Figure 4.9: Percentage of heat release arising from premixed ($FI > 0$) and non-premixed ($FI < 0$) modes of combustion for all droplet cases with initial $a_d/\delta_{st} = 0.04$ (△), 0.05 (◯), 0.06 (×).

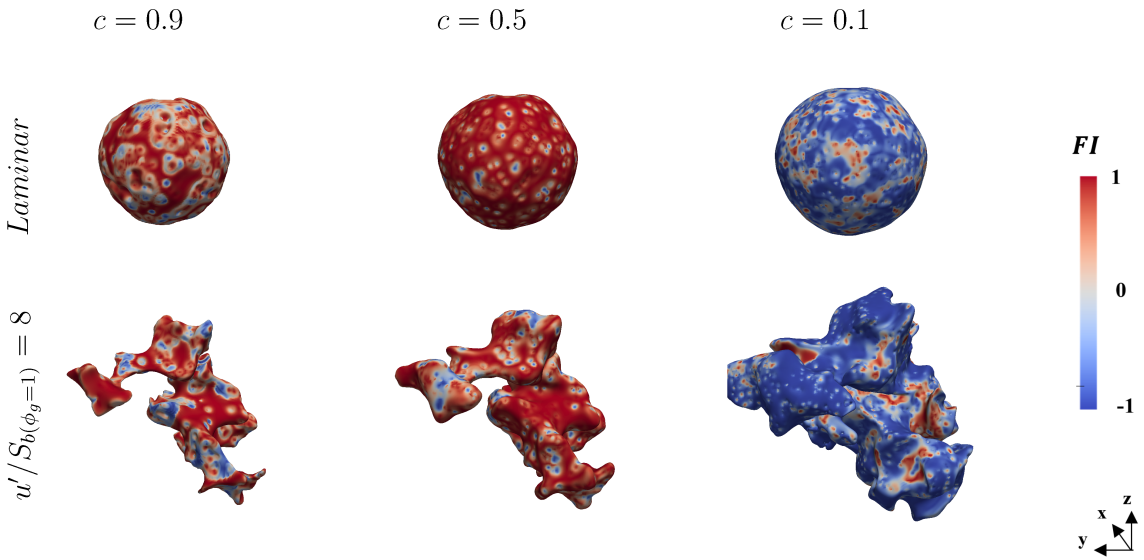

Figure 4.10: Distribution of flame index (FI) on different c isosurfaces ($c = 0.9, 0.5$ and 0.1 left to right) for $a_d/\delta_{st} = 0.06$ case for laminar flow and initial $u'/S_{b(\phi_g=1)} = 8.0$ conditions.

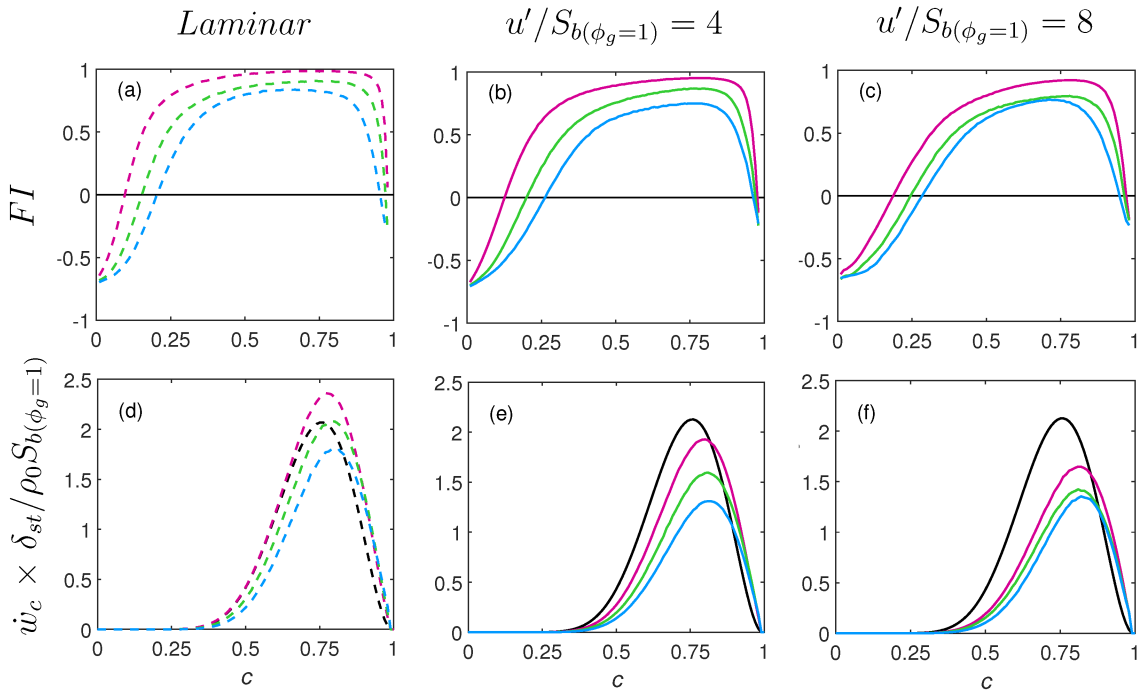

Figure 4.11: Variations of the mean values of flame index FI and normalised reaction rate of reaction progress variable $\dot{w}_c \times \delta_{st}/\rho_0 S_{b(\phi_g=1)}$ conditional upon c. See Fig. 4.5 caption for the colour keys.

conditional on c are shown in Fig. 4.11, where $\dot{w}_c$ is defined earlier in Chapter 2 with Eq. 2.53. It is evident from Figs. 4.11a-c that low values of c are associated with negative values of FI, whereas the flame index is predominantly positive for $c \geq 0.3$. However, the mode of combustion becomes predominantly non-premixed ($FI < 0$) around $c \approx 1.0$. This non-premixed mode of combustion originates from the diffusion of oxidiser from the unburned gas side and diffusion of gaseous fuel from post-flame evaporation for the droplets which escape through the flame on the burned gas side. The transport and mixing of evaporated fuel from the droplet sites to the surrounding gaseous mixture strengthens with increasing turbulence intensity, and thus the extent of non-premixed combustion increases with increasing $u'/S_{b(\phi_g=1)}$. A comparison between FI and $\dot{w}_c$ distributions in Fig. 4.12 indicates that the premixed mode of combustion (i.e. $FI > 0$) is obtained in the reaction zone where the mean value of $\dot{w}_c$ conditional upon c assumes large values.

The probability of obtaining fuel-lean mixture increases for increasing a_d/δ_{st} due to decreasing evaporation rates (see Fig. 4.8). This leads to decreases in the peak mean value of $\dot{w}_c$ conditional upon c with increasing droplet size for both laminar and turbulent cases. The mean value of $\dot{w}_c$ conditional upon c peaks approximately at $c = 0.75$ for all premixed cases but this location for droplet cases moves towards the burned gas side for all droplet cases with increas-

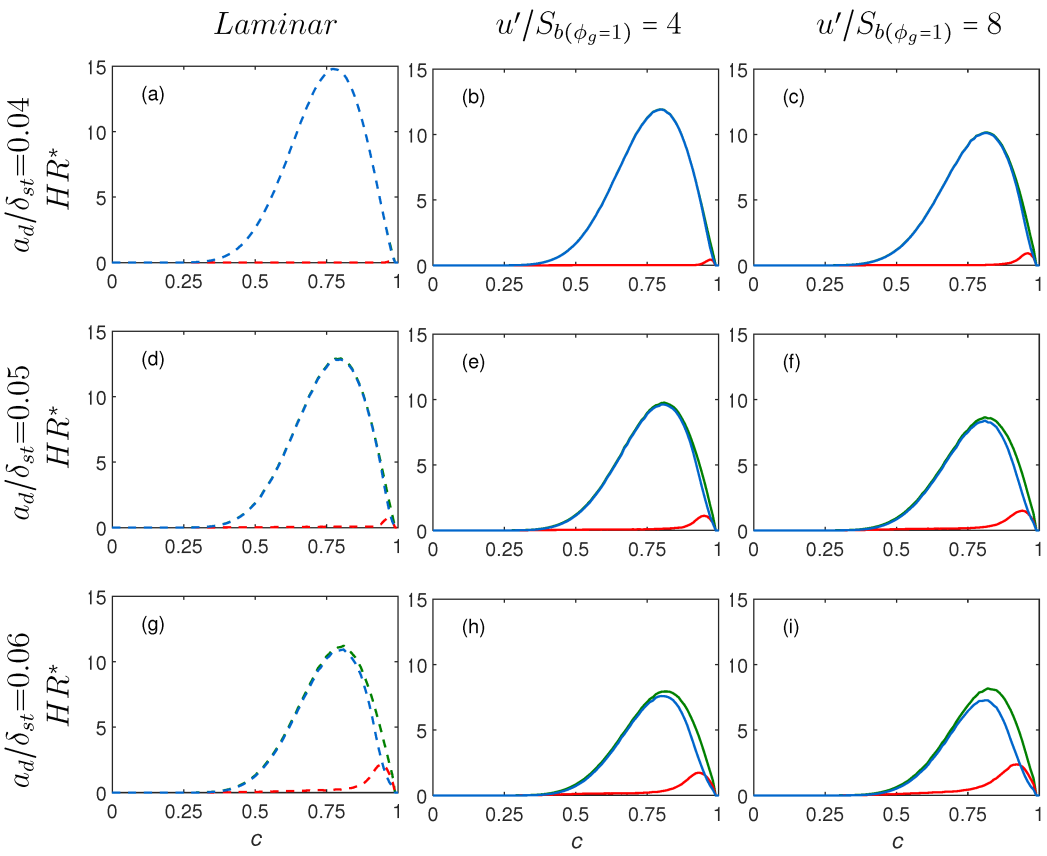

Figure 4.12: Variation of normalised mean heat release, $HR^* = H_\phi|\dot{w}_F| \times \delta_{st}/(C_p^G T_0 \rho_0 S_{b(\phi_g=1)})$ with c for droplet cases. Total mean heat release (——), mean heat release arising from premixed ($FI > 0$) combustion mode (——) and non-premixed ($FI < 0$) combustion mode (——).

ing turbulence intensity and the peak value decreases with increasing droplet diameter. For the present thermo-chemistry, the activation energy (or Zel'dovich number β, see Eq. 2.43) does not change and remains the same as the stoichiometric mixture for fuel-rich mixtures in the equivalence ratio range of $1 < \phi_g < 1.07$ (see eq. 2.44) [75]. Thus, the considerable availability of fuel-rich mixture with $1 < \phi_g < 1.07$ in the laminar droplet case with initial $a_d/\delta_{st} = 0.04$ (see Fig. 4.8) leads to a higher peak mean value of $\dot{w}_c$ conditional upon c than in the stoichiometric laminar premixed flame case. However, the probability of finding less reactive mixtures corresponding to $\phi_g < 1.0$ and $\phi_g > 1.07$ increases with increasing $u'/S_{b(\phi_g)}$. This leads to a decrease in the peak mean value of $\dot{w}_c$ conditional upon c in the turbulent droplet cases in comparison to that in the corresponding turbulent stoichiometric spherical premixed flame.

It can be seen from Fig. 4.11d-f that the peak mean value of $\dot{w}_c$ for the droplet cases decreases with increasing $u'/S_{b(\phi_g=1)}$. This behaviour can be explained with the help of the

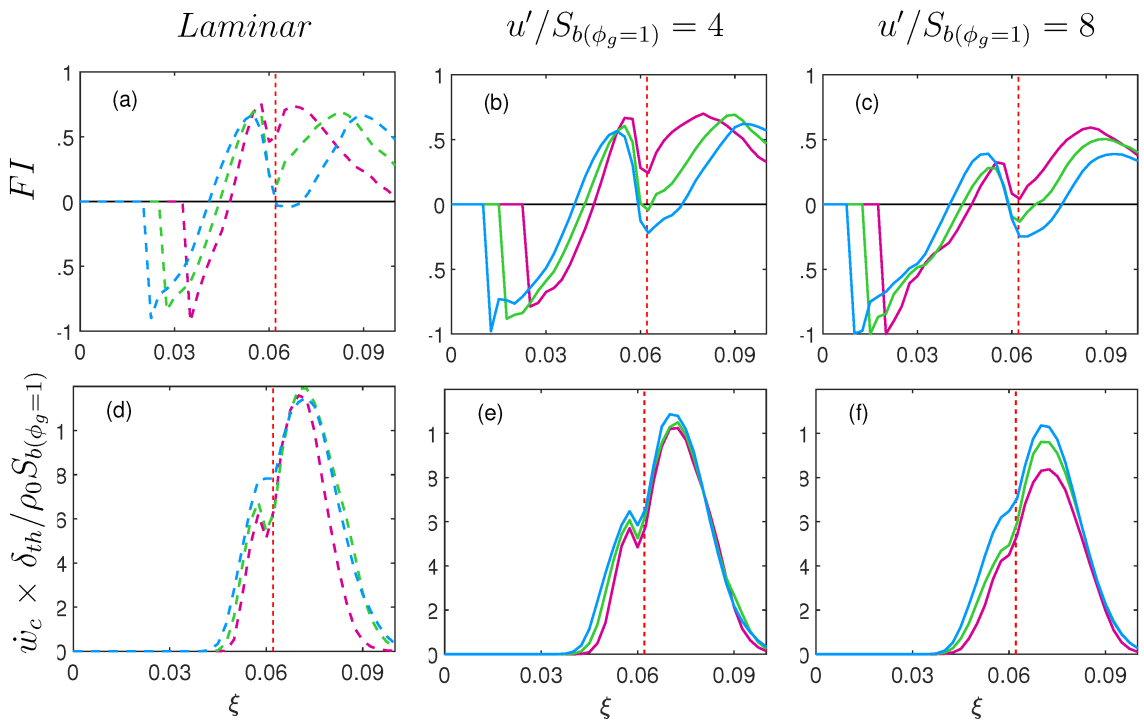

Figure 4.13: Variation of mean flame index FI and normalised reaction rate of reaction progress variable $\dot{w}_c \times \delta_{st}/\rho_0 S_{b(\phi_g=1)}$ conditional upon mixture fraction ξ in the region corresponding to $0.01 \leq c \leq 0.99$. The red dashed line shows the value of the stoichiometric mixture fraction.

variations of the mean normalised heat release rate $HR^* = H_\phi |\dot{w}_F| \times \delta_{st}/(C_p^G T_0 \rho_0 S_{b(\phi_g=1)})$ conditional upon c for the droplet cases, which are shown in Fig. 4.12. It can be seen from Fig. 4.12 that the mean value of HR^* arising from the premixed mode of combustion remains greater than that from the non-premixed mode of combustion for all droplet cases and this tendency is particularly strong for the cases with small droplet diameter. This is consistent with the observations made earlier from Fig. 4.9. The peak mean value of HR^* for the premixed mode of combustion takes place close to $c = 0.75$, whereas the peak mean value of HR^* for the non-premixed mode of combustion takes place towards the burned gas side of the flame. The maximum heat release for non-premixed combustion takes place at the stoichiometric mixture (i.e. $\xi = \xi_{st}$) which occurs for a reaction progress variable value close to unity (i.e. $c \approx 1.0$), which is consistent with previous findings by Wacks et al. [47]. The value of the reaction progress variable, where the peak location of HR^* is obtained, changes depending on the contribution of the non-premixed mode of combustion to the total HR^*.

Figure 4.13 shows the variation of mean values of flame index FI and reaction rate $\dot{w}_c$ conditional on mixture fraction ξ in the region corresponding to $0.01 \leq c \leq 0.99$. It can be seen from Fig. 4.13a-c that FI is predominantly negative for $\xi < \xi_{st}$. In this configuration,

the fuel in gaseous form is obtained only upon the evaporation of the droplets. Thus, the bulk of the fuel-lean mixture is obtained when fuel vapour diffuses to the surrounding air from evaporation sites. The evaporation rate is high for small droplets and there are more evaporation sites for small values of a_d for a given value of ϕ_{ov}. The combination of these effects leads to an increased probability of having positive values of FI for small droplet cases in the gaseous mixture where some fuel is already present. Accordingly, mean FI values remain positive for $\xi > 0.05$ in the case of $a_d/\delta_{st} = 0.04$ irrespective of flow conditions. A similar behaviour has been observed for the laminar droplet case with $a_d/\delta_{st} = 0.05$. However, the mean value of FI assumes negative value close to $\xi \approx \xi_{st}$ for the laminar case with $a_d/\delta_{st} = 0.06$ and also for the turbulent cases considered here for $a_d/\delta_{st} = 0.05$ and 0.06 because of the diffusion flame formed at the stoichiometric mixture. The signature of the diffusion flame at $\xi = \xi_{st}$ can be seen as a kink at $\xi = \xi_{st}$ in the profiles of the mean values of $\dot{w}_c$ conditional upon ξ, which are presented in Figs. 4.12d-f. A comparison between Figs. 4.13a-c with Figs. 4.13d-f reveals that high mean values of $\dot{w}_c$ conditional on ξ originate due to the rich premixed mode of combustion. It has been found that the maximum mean value of $\dot{w}_c$ conditional on ξ is obtained at around $\xi \approx 0.07$ for all flow conditions. It is worth noting that $\xi \approx 0.07$ corresponds to a gaseous phase equivalence ratio $\phi_g = \xi(1-\xi_{st})/[(1-\xi)\xi_{st}] \approx 1.07$ for which the highest laminar burning velocity $S_{b(\phi_g)}$ is obtained for this thermo-chemistry [75]. A decrease in droplet size for a given ϕ_{ov} gives rise to an increase in the number of droplets and these small droplets evaporate more readily than large droplets owing to their high surface to volume ratio. The extraction of latent heat at the evaporation sites tends to reduce the gas temperature, which in turn acts to increase the number of samples with small values of c for a given mixture fraction ξ value with decreasing a_d/δ_{st} (not shown here but the mean value of c conditional upon ξ decreases with decreasing a_d/δ_{st}), and this leads to a reduction of mean value of $\dot{w}_c$ conditional upon ξ. This effect is more prominent for large values of $u'/S_{b(\phi_g=1)}$ (e.g. initial $u'/S_{b(\phi_g=1)} = 8.0$ case) because the enhanced mixing of fuel from the evaporation sites increases the Spalding number B_d, which in turn increases evaporation rate of droplets. It is worth noting that the profile of the mean value of HR^* conditional on ξ is qualitatively similar to the variation of mean reaction rate $\dot{w}_c$ conditional on mixture fraction and thus is not shown here for the sake of conciseness. A comparison between Figs. 4.12 and 4.13d-f confirms that non-premixed mode of combustion occurs at $c \approx 1.0$ where mixture fraction is close to its stoichiometric value $\xi \approx \xi_{st}$.

For a diffusion flame formed at $\phi_g \approx 1.0$ (i.e. $\xi \approx \xi_{st}$), the corresponding burned gas temperature is expected to be $T \approx 1.0$ under globally adiabatic condition with unity Lewis number for all species. Moreover, the premixed mode of combustion also takes place for $\phi_g \approx 1.0$, which yields a burned gas temperature corresponding to $T \approx 1.0$. It can be seen

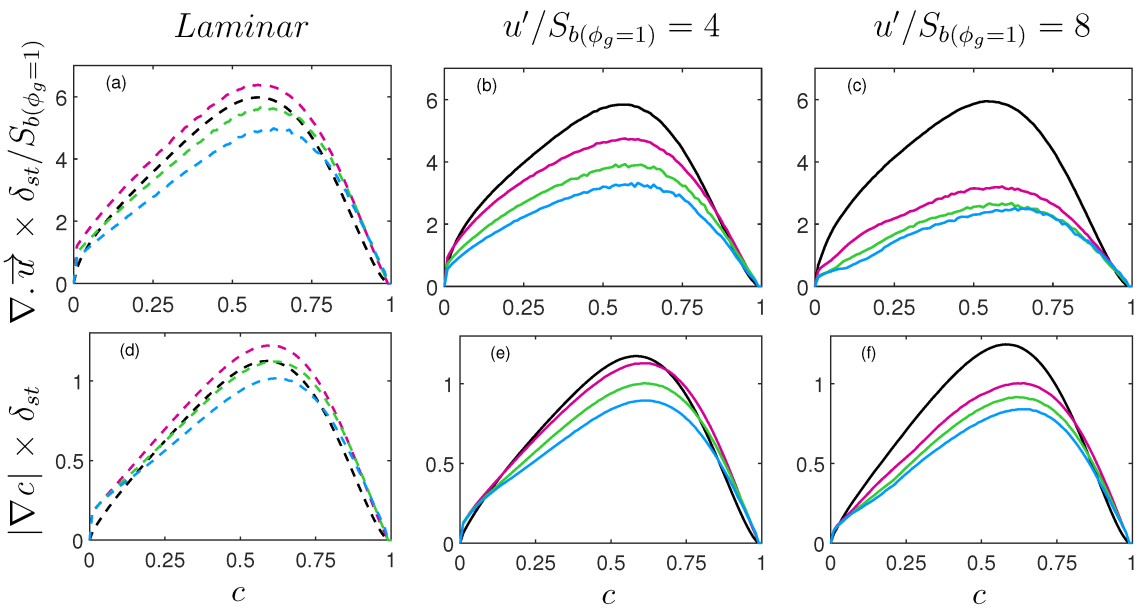

Figure 4.14: Variations of mean values of (a-c) $\nabla \overrightarrow{u} \times \delta_{st}/S_{b(\phi_g=1)}$ and (d-f) $|\nabla c| \times \delta_{st}$ conditional upon c at $t = 2.1 t_{chem}$.

from Figs. 4.1-4.3 that some droplets penetrate the flame front, evaporate at the burned gas side, and generate locally fuel-rich pockets, whereas the unused oxidiser diffuses from the unburned gas side to the burned gas side from the fuel-lean zones. Instances of heat transfer to the gaseous phase from high temperature droplets give rise to a small probability of obtaining $T \geq 1.0$ upon completion of combustion of the evaporated fuel.

The reaction rate and heat release variations have implications on the statistical behaviours of the magnitude of gradient of reaction progress variable $|\nabla c|$ and also on thermal expansion due to heat release which can be quantified in terms of dilatation rate $\nabla \cdot \overrightarrow{u}$. It can be seen from Fig. 4.14 that both $\nabla \cdot \overrightarrow{u} \times \delta_{st}/S_{b(\phi_g=1)}$ (see Figs. 4.14a-c) and $|\nabla c| \times \delta_{st}$ (see Figs. 4.14d-f) conditional upon c show a decreasing trend with increasing droplet size, which is qualitatively consistent with the variations of mean value of $\dot{w}_c$ conditional upon c (see Fig. 4.11). For the premixed flame cases, there is no considerable effect of turbulence intensity on mean values of $\nabla \cdot \overrightarrow{u} \times \delta_{st}/S_{b(\phi_g=1)}$ conditional upon c. However, normalised mean dilatation rate $\nabla \cdot \overrightarrow{u} \times \delta_{st}/S_{b(\phi_g=1)}$ in the droplet cases decreases with increasing turbulence intensity and droplet diameter because of the reduction in heat release rate (see Fig. 4.12 and 4.13d-f) as a result of predominant fuel-lean burning. The mean value of $\nabla \cdot \overrightarrow{u} \times \delta_{st}/S_{b(\phi_g=1)}$ for turbulent premixed flames remains greater than those for turbulent droplet cases and the same trend has been observed for laminar droplet cases with initial $a_d/\delta_{st} = 0.05$ and 0.06. However, the laminar droplet case with initial $a_d/\delta_{st} = 0.04$ shows higher peak mean value of $\nabla \cdot \overrightarrow{u} \times \delta_{st}/S_{b(\phi_g=1)}$ than in the premixed flame, which is consistent with the higher mean value of $\dot{w}_c$

conditional upon c for this droplet case (see Fig. 4.11).

The variation of the mean value $|\nabla c| \times \delta_{st}$ conditional upon c exhibits a peak value close to $c \approx 0.6$ for premixed cases, whereas its location shifts to $c \approx 0.65$ for droplet cases. The peak mean value of $|\nabla c| \times \delta_{st}$ for the premixed flames increases with increasing turbulence intensity. The peak mean value of $|\nabla c|$ can be taken as a measure of the inverse of flame thickness (i.e. $\delta \sim 1/max|\nabla c|$) [77, 178–180], and thus, Figs. 4.14d-f indicate a thinning in flame thickness with increasing turbulence intensity for premixed flame cases. This is consistent with findings from several previous analyses and interested readers are referred to Sandeep et al. [179] and Chakraborty et al. [180] for further discussion in this regard. However, the peak mean value of $|\nabla c| \times \delta_{st}$ decreases with increasing a_d/δ_{st} and $u'/S_{b(\phi_g=1)}$ in turbulent droplet cases, which suggests that the flame tends to be thicker as turbulence intensity and droplet size are enhanced. This is consistent with the predominance of fuel-lean combustion for large values of turbulence intensity and droplet size, and thus the flame thickness is expected to increase with decreasing ϕ_g in fuel-lean gaseous mixtures. The flame thickening in droplet cases in comparison to the corresponding stoichiometric premixed flame is obtained for all turbulent cases, and also for laminar flames with initial $a_d/\delta_{st} = 0.05$ and 0.06. However, the laminar droplet case with initial $a_d/\delta_{st} = 0.04$ shows higher peak mean value of $|\nabla c| \times \delta_{st}$ than in the premixed flame, which is consistent with the higher mean value of $\dot{w}_c$ conditional upon c for this droplet case (see Fig. 4.11) due to the considerable availability of $1 < \phi_g < 1.07$, as discussed earlier. For this thermo-chemistry, the laminar burning velocity $S_{b(\phi_g)}$ and the characteristic flame thickness $\delta \sim \alpha_{T0}/S_{b(\phi_g)}$ attain their maximum and minimum values respectively for $\phi_g \approx 1.07$ [75]. Thus, the significant presence of $1 < \phi_g < 1.07$ in the flame in the laminar droplet case with initial $a_d/\delta_{st} = 0.04$ gives rise to the thinner flame than in the stoichiometric premixed spherical laminar flame. This has implications on the overall flame area $A = \int_V |\nabla c| dV$ and volume of the burned gas (i.e. volume of gas with $c \geq 0.99$) as it gives rise to smaller values of A in the droplet flame with initial $a_d/\delta_{st} = 0.04$ than in the corresponding stoichiometric premixed spherical flame even though the mean value of $|\nabla c| \times \delta_{st}$ is greater in this droplet case (see Fig. 4.14). This arises because the volume over which $|\nabla c|$ assumes significant values in this droplet case (i.e. $a_d/\delta_{st} = 0.04$) is smaller than the corresponding volume in the premixed flame case. The same reason is responsible for yielding smaller value of A_0 in the droplet case with initial $a_d/\delta_{st} = 0.04$ than in the laminar stoichiometric premixed spherical flame even though the burned gas radius is the same (i.e. $r_0 = 2\delta_{st}$) for both cases.

4.4 Extent of Burning

A combination of fuel-lean combustion and the predominant probability of obtaining reduced burned gas temperature adversely affects the growth rate of spherically expanding flames. This can be verified from Fig. 4.15a-c which show temporal evolution of the volume-integrated fuel reaction rate magnitude $\Omega_F = \int_V |\dot{w}_F| dV$ normalised by its initial value (i.e. $\Omega_F/\Omega_{F0} = \int_V |\dot{w}_F| dV / [\int_V |\dot{w}_F| dV]_{t=0}$).

Figures 4.15a-c show that Ω_F/Ω_{F0} increases rapidly with time for all cases, but under turbulent environment, the growth rate is the highest for the premixed case and Ω_F/Ω_{F0} decreases with increasing droplet diameter under both laminar and turbulent conditions. However, Ω_F/Ω_{F0} in the laminar droplet cases is found to be greater than in the laminar stoichiometric premixed flame. The growth rate of Ω_F/Ω_{F0} is found to be qualitatively consistent with the evolution of A/A_0, as shown in Fig. 4.7a-c. However, it is worth noting that Ω_{F0} values (i.e. Ω_F of a spherical laminar flame of initial radius $r_0 = 2\delta_{st}$) are not the same as shown in Fig. 4.15d-f and Ω_{F0} for $a_d/\delta_{st} = 0.04, 0.05$ and 0.06 cases have been found to be 0.564, 0.567, 0.57 times the Ω_{F0} value (i.e. $\Omega_{F0,pre}$) for the stoichiometric laminar premixed flame, respectively. Thus, $\Omega_F/\Omega_{F0,pre}$ in the droplet cases remains smaller than the stoichiometric premixed flame, and it decreases with increasing a_d under both laminar and turbulent conditions. It is worth mentioning that the temporal evolution of $\Omega_c = \int_V \dot{w}_c dV$ and Ω_c/Ω_{c0} are qualitatively similar to Ω_F and Ω_F/Ω_{F0}, respectively. The temporal evolutions of $S = \left[\rho_0 S_{b(\phi_g=1)}\right]^{-1} \int_V \dot{w}_c dV / \int_V |\nabla c| dV$ are shown in Fig. 4.16a-c, which shows that S remains close to unity in the premixed flame under both laminar and turbulent conditions. The departure of S from a unity value (i.e. $S < 1$) for spherical stoichiometric premixed flames takes place due to the non-zero stretch rate effects induced by non-zero mean flame curvature. This behaviour is consistent with previous findings by Klein et al. [57] for statistically spherical turbulent premixed flames and detailed explanations for this behaviour have been provided in Refs. [57, 59–61] and thus are not repeated here. Figures 4.16a-b show that the values of S for the initial $a_d/\delta_{st} = 0.04$ cases remain comparable to the stoichiometric premixed flame but S decreases with increasing initial droplet size, which is qualitatively consistent with the experimental findings of Lawes and Saat [119]. Under high turbulence intensity (e.g. initial $u'/S_{b(\phi_g=1)} = 8.0$ case), S for the droplet case (Fig. 4.16c) diminishes and stays at considerably lower values compared with other flow conditions (i.e. the initial $u'/S_{b(\phi_g=1)} = 0.0$ and 4.0). The product formation rate per unit flame surface area in the large droplet cases is smaller than that in the stoichiometric premixed flame case. This can be verified from Figs. 4.16d-f, which show a reduction of the volume of the gas with $c \geq 0.99$ (i.e. V_b) with increasing droplet size and the highest V_b is obtained for the gaseous premixed flame. It is evident from Figs. 4.16d-f

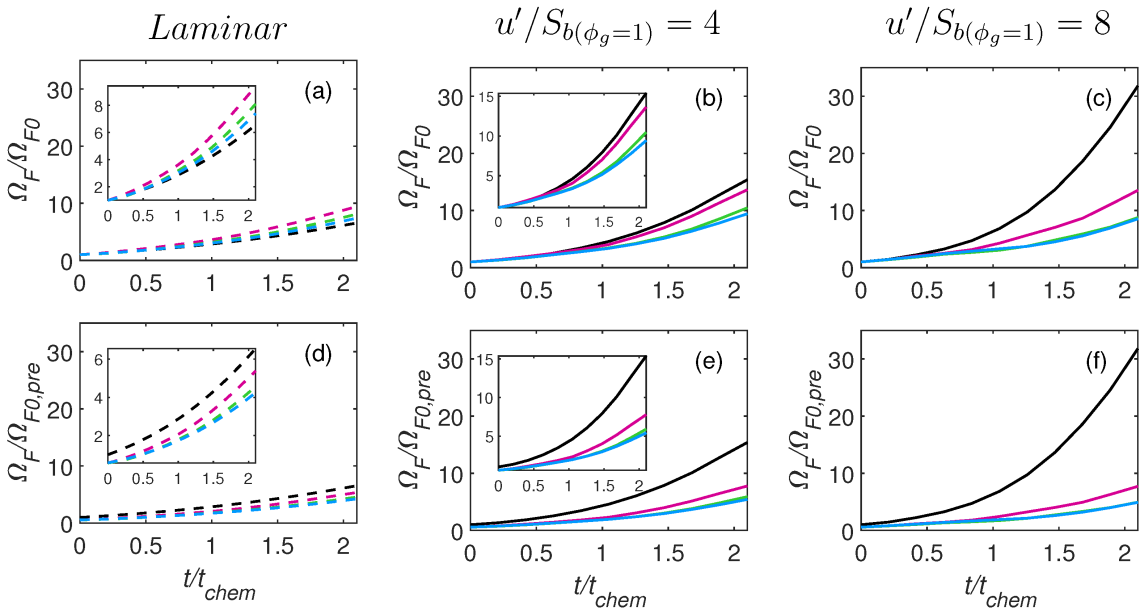

Figure 4.15: Temporal evolutions of (a-c) volume integrated fuel reaction rate magnitude normalised by its initial value Ω_F/Ω_{F0}; (d-f) volume integrated fuel reaction rate magnitude normalised by Ω_{F0} value (i.e. $\Omega_{F0,pre}$) for the stoichiometric laminar premixed flame.

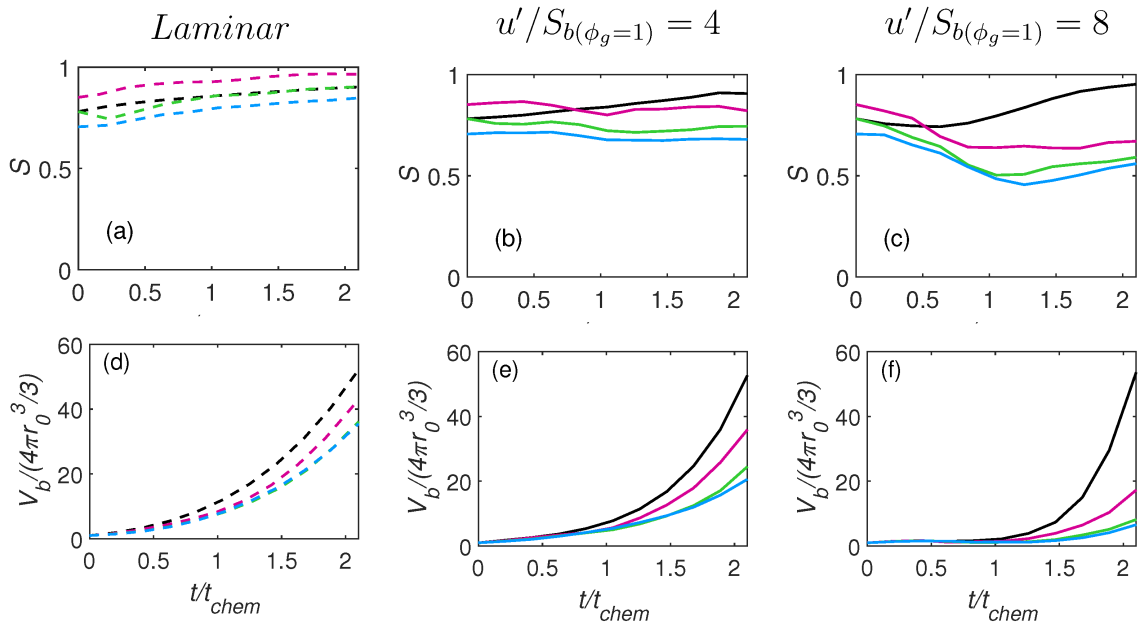

Figure 4.16: Temporal evolutions of (a-c) the ratio of volume-integrated product formation rate to the flame surface area S; (d-e) volume $V_b/(4\pi r_0^3/3)$ of the region with $c \geq 0.99$.

Table 4.3: Normalised flame speed $S_B/S_{b(\phi_g=1)}$, which quantifies the growth rate of the burned gas volume V_b.

	Laminar	$u^{'}/S_{b(\phi_g=1)}=4$	$u^{'}/S_{b(\phi_g=1)}=8$
$a_d/\delta_{st}=0.04$	5.336	5.703	5.770
$a_d/\delta_{st}=0.05$	4.899	4.338	4.589
$a_d/\delta_{st}=0.06$	4.906	3.733	4.077
Premixed	5.496	6.626	9.951

that the difference of V_b between premixed and spray flame widens with increasing turbulence intensity and this difference for high turbulence intensity (e.g. initial $u'/S_{b(\phi_g=1)}=8.0$ case) originates due to the smaller S in droplet flames than in the corresponding stoichiometric turbulent premixed case.

The rate of growth of the burned gas volume can be estimated by a flame speed S_V, which is defined as $S_V=dr_V/dt$ where $r_V=(3V_b/4\pi)^{(1/3)}$ is an equivalent radius based on burned gas volume. The value of S_V is estimated by using the slope of the linear part of temporal evolution of r_V and this slope remains unchanged since halfway through the simulation. The evaluated values of S_V are summarised in Table 4.3, which reveals that the growth of burned gas volume for the stoichiometric premixed flame and the droplet case with initial $a_d/\delta_{st}=0.04$ increases with increasing turbulence intensity. However, the values of $S_V/S_{b(\phi_g=1)}$ for the droplet cases with initial $a_d/\delta_{st}=0.05$ and 0.06 remain smaller than the corresponding laminar case values for initial $u'/S_{b(\phi_g=1)}=4.0$, whereas $S_V/S_{b(\phi_g=1)}$ under initial $u'/S_{b(\phi_g=1)}=8.0$ in these droplet cases assumes values comparable to that under the laminar condition. Although the ratio of volume-integrated product formation rate to the flame surface area S decreases with increasing $u'/S_{b(\phi_g=1)}$ for the $a_d/\delta_{st}=0.05$ and 0.06 (see Figs. 4.16a-c), this effect is countered by the higher growth rate of flame surface area (see Table 4.2) with increasing $u'/S_{b(\phi_g=1)}$. These two counter-acting effects lead to a non-monotonic variation of S_V with increasing $u'/S_{b(\phi_g=1)}$ for the droplet cases with initial $a_d/\delta_{st}=0.05$ and 0.06.

4.5 Statistics of Reactive Scalar Gradient

The statistics of the reactive scalar gradient play a significant role in the analysis and modelling of flame-turbulence interaction. The magnitude of the reaction progress variable gradient $|\nabla c|$ is alternatively known as the Surface Density Function (SDF) [181, 182], and its transport equation takes the following forms [47, 180, 183–190]:

$$\frac{\partial|\nabla c|}{\partial t}+v_j\frac{\partial|\nabla c|}{\partial x_j}=-\left(a_N+N_j\frac{\partial S_d}{\partial x_j}\right)|\nabla c| \tag{4.1}$$

$$\frac{\partial|\nabla c|}{\partial t}+\frac{\partial(v_j|\nabla c|)}{\partial x_j}=-\left(a_T+2S_d\kappa_m\right)|\nabla c| \tag{4.2}$$

where the j^{th} component of the flame propagation velocity is given by $v_j = u_j + S_d N_j$ and the flame normal strain rate is stated as $a_N = N_i N_j \partial u_i / \partial x_j$. The fractional temporal changes of the infinitesimal normal distance between two neighbouring c isosurfaces $(1/\Delta x_N)(d\Delta x_N/dt)$ and the surface area element $(1/A)(dA/dt)$ are related to the flame normal strain rate, a_N and tangential strain rate, $a_T = \nabla \cdot \overrightarrow{u} - a_N = (\delta_{ij} - N_i N_j)\partial u_i/\partial x_j$ as [183, 184, 186, 187]:

$$(1/\Delta x_N)(d\Delta x_N/dt) = a_N + \partial S_d/\partial x_N = a_N^{eff} \tag{4.3}$$

$$(1/A)(dA/dt) = a_T + 2S_d\kappa_m = a_T^{eff} \tag{4.4}$$

where $\nabla \cdot \overrightarrow{u}$ is dilatation rate, and $d(\,)/dt = \partial(\,)/\partial t + v_j \partial(\,)/\partial x_j$ is the total derivative based on $v_j = u_j + S_d N_j$. In Eqs. 4.3-4.4, a_T^{eff} and a_N^{eff} represent the effective tangential strain rate (alternatively stretch rate [183, 184]) and normal strain rate, respectively [47, 179, 180, 186–190].

The SDF and its evolution are of fundamental importance because of its close relation to the generalised Flame Surface Density (FSD) $\Sigma_{gen} = \overline{|\nabla c|}$ [191] (with overbar representing Reynolds averaging/filtering operation, as appropriate) and Scalar Dissipation Rate (SDR) $N_c = D_c|\nabla c|^2$ [192] (where D_c is the reaction progress variable diffusivity). Moreover, the SDF plays a key role in the analysis of pocket formation [182] and the inverse of the peak value of the SDF can be taken as a measure of flame thickness [180, 189, 193]. The statistical behaviour of the SDF and different terms of its transport equation have been extensively studied for turbulent premixed flames from various viewpoints [89, 179, 185, 190, 193–197]. In comparison to purely gaseous premixed turbulent flames, relatively limited effort has been directed to the similar analyses for turbulent flame propagation in droplet-laden mixtures [47] in spite of its relevance in compression ignition and direct injection engines. The evolution of the SDF in droplet-laden mixtures is more complex than in turbulent premixed flames due to the simultaneous interactions of turbulence, flame and droplets. A recent analysis by Wacks et al. [47] focussed on the SDF evolution for statistically planar flames propagating into droplet-laden mixtures for different turbulence intensities, droplet sizes and overall (liquid+gaseous phases) equivalence ratios and important differences between gaseous premixed and droplet-laden cases were reported. Moreover, most of the aforementioned analyses on the statistical behaviours of the SDF and its transport characteristics have been carried out for statistically planar flames but the SDF statistics in spherically expanding turbulent premixed flames can be different from those in statistically planar flames [59–61]. Mizutani and Nishimoto [62]

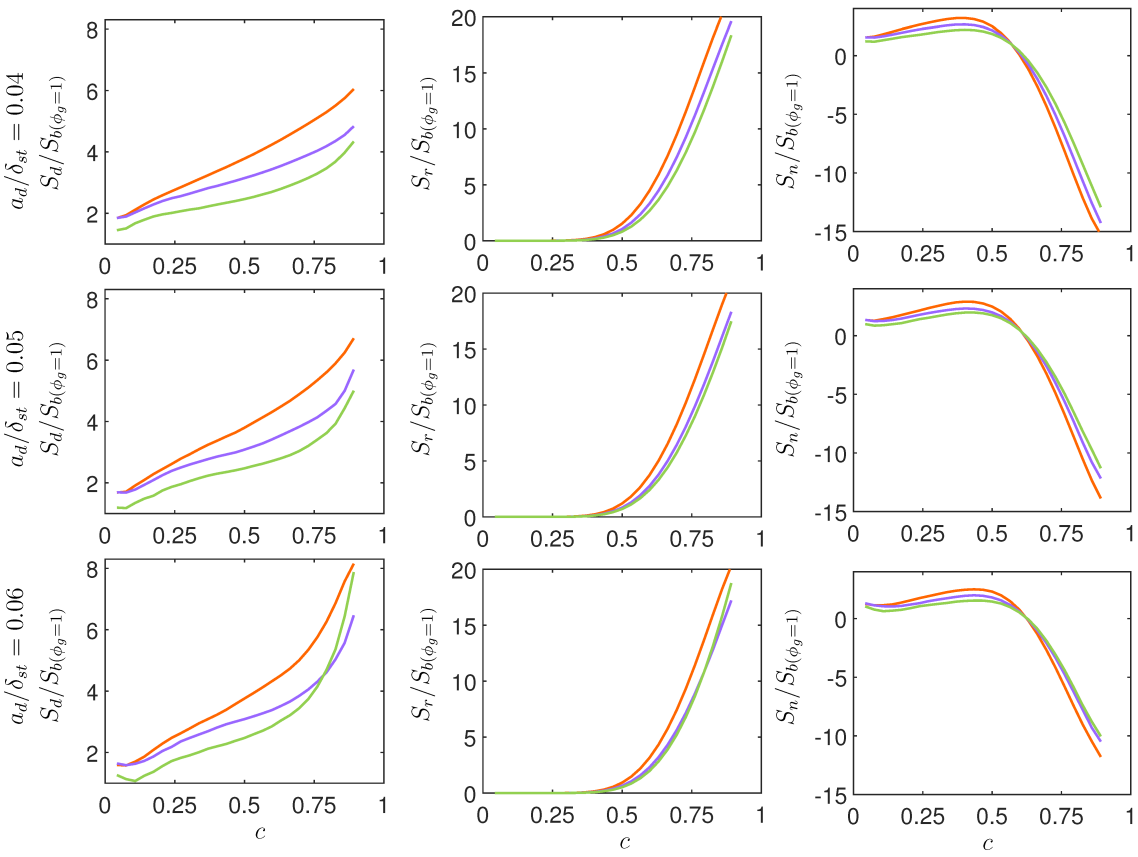

Figure 4.17: Profiles of mean values of $S_i/S_{b(\phi_g=1)}$ (where $i = d,r,n$) conditional upon c for initial $a_d/\delta_{st} = 0.04, 0.05$ and 0.06 (1^{st} -3^{rd} rows), for laminar (——), initial $u'/S_{b(\phi_g=1)} = 4.0$ (——) and 8.0 (——) cases.

demonstrated that the burning characteristics of spherically expanding droplet-laden flames could be significantly different to the corresponding planar flames. However, the statistics of the SDF and the strain rates, which affect the SDF evolution, are yet to be analysed for turbulent spherically expanding flames in droplet-laden mixtures. The current analysis addresses the aforementioned gap in the existing literature by analysing the statistical behaviours of the SDF and different strain rates, which affect its evolution. For this purpose, spherically expanding flames propagating into mono-sized fuel-droplets for a range of different initial droplet diameters (i.e. $a_d/\delta_{st} = 0.04, 0.05, 0.06$) and turbulence intensities (i.e. $u'/S_{b(\phi_g=1)} = 0.0, 4.0, 8.0$) at an overall equivalence ratio of unity has been considered. Thus, the main objectives of this section are: (a) to demonstrate and explain the effects of turbulence intensity and droplet diameter on the strain rates, which affect the evolution of the SDF in turbulent spherically expanding flames in droplet-mists, (b) to indicate the implications of the above physical information in the context of modelling of turbulent combustion in droplet-laden mixtures.

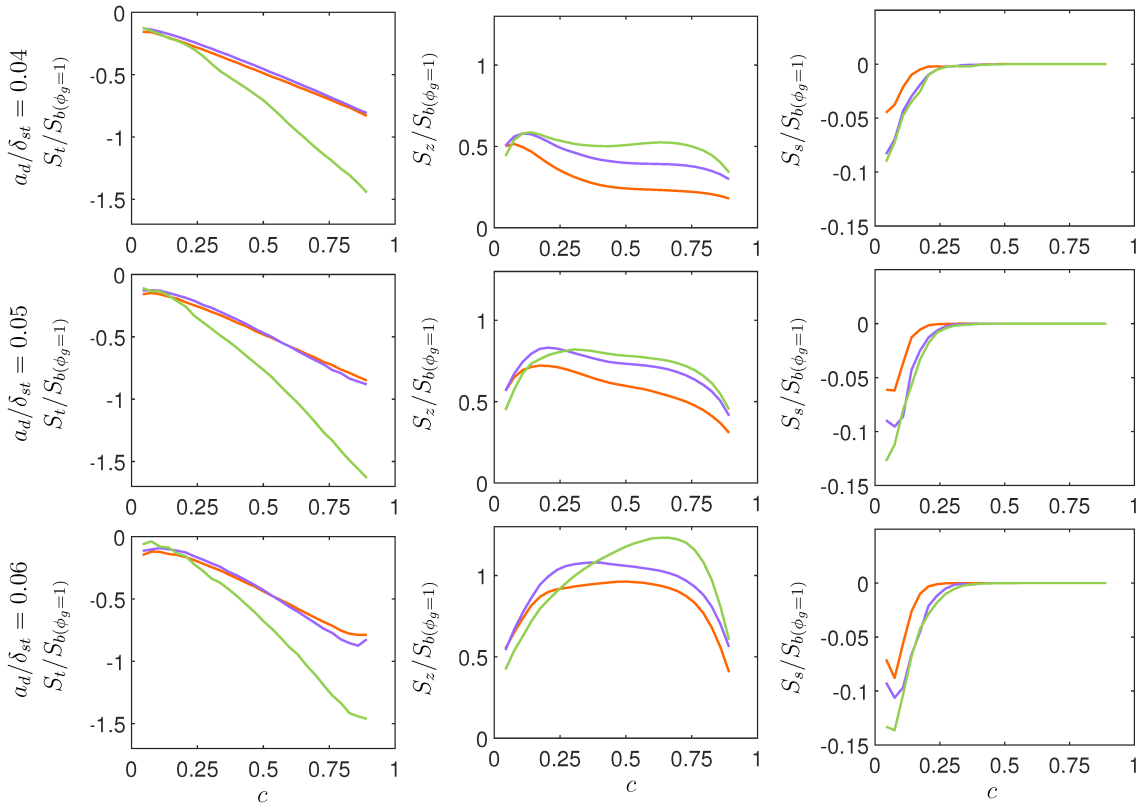

Figure 4.18: Profiles of mean values of $S_i/S_{b(\phi_g=1)}$ (where $i = t,z,s$) conditional upon c for initial $a_d/\delta_{st} = 0.04, 0.05$ and 0.06 (1^{st}-3^{rd} rows). See Fig. 4.17 caption for the colour keys.

Equations 2.60,4.1-4.4 indicate that the flame curvature affects the displacement speed behaviour, which in turn influences the evolution of $|\nabla c|$. The variations of the mean values of normalised displacement speed and its components $S_i/S_{b(\phi_g=1)}$ (where $i = d,r,n,t,z,s$) conditional upon c are shown in Fig. 4.17 and Fig 4.18, respectively, which reveal that $S_d/S_{b(\phi_g=1)}$ increases from the unburned to the burned gas side due to density drop as a result of thermal expansion. Figure 4.17 further shows that the mean value of the reaction component $S_r/S_{b(\phi_g=1)}$ remains positive but its magnitude increases from the unburned to the burned gas side of the flame, whereas the mean normal diffusion component $S_n/S_{b(\phi_g=1)}$ assumes small positive and large negative values towards the unburned and burned gas sides of the flame front respectively. The mean contributions of S_z and S_s remain smaller in magnitude than those of S_r and S_n. The mean contribution of tangential diffusion component of displacement speed $S_t/S_{b(\phi_g=1)} = -2D\kappa_m/S_{b(\phi_g=1)}$ remains negative throughout the flame due to predominantly positive values of curvature κ_m and the magnitude of the mean negative value increases with decreasing mean radius of the flame kernel. The magnitude of negative mean value of $S_t/S_{b(\phi_g=1)}$ for the initial $a_d/\delta_{st} = 0.06$ case remains considerably greater than

in the corresponding cases with initial $a_d/\delta_{st} = 0.04$ and 0.05 cases because of the smaller mean flame radius. The statistics of S_d and its components influence the statistical behaviours of $N_j\partial S_d/\partial x_j$ and $2S_d\kappa_m$.

The mean values of $\{\nabla\cdot\overrightarrow{u}, a_N, a_T = \nabla\cdot\overrightarrow{u} - a_N\}\times\delta_{st}/S_{b(\phi_g=1)}$ conditional upon c are shown in Fig. 4.19, which shows that the mean value of $\nabla\cdot\overrightarrow{u}$ remains positive and the mean value decreases with increasing a_d and $u'/S_{b(\phi_g=1)}$. It has already been shown in Fig. 4.8 that the probability of fuel-lean combustion increases with increasing a_d and $u'/S_{b(\phi_g=1)}$. This reduces the strength of thermal expansion in the large droplet cases, and this effect is further augmented for high values of $u'/S_{b(\phi_g=1)}$, and this is reflected in the reduced magnitude of dilatation rate $\nabla\cdot\overrightarrow{u}$. The normal strain rate a_N can be expressed as: $a_N = (e_\alpha cos^2\theta_\alpha + e_\beta cos^2\theta_\beta + e_\gamma cos^2\theta_\gamma)$ where e_α, e_β and e_γ are the most extensive, intermediate, and most compressive principal strain rates, and $\theta_\alpha, \theta_\beta$ and θ_γ are the angles between ∇c and the eigenvectors corresponding to e_α, e_β and e_γ, respectively [179, 180, 189, 190, 194]. The reactive scalar gradient ∇c aligns with the eigenvector associated with e_α (i.e. $cos^2\theta_\alpha \approx 1$) when the strain rate induced by flame normal acceleration dominates over turbulent straining [61, 194, 195]. By contrast, ∇c aligns with the eigenvector associated with e_γ (i.e. $cos^2\theta_\gamma \approx 1$) when turbulent straining overwhelms the strain rate due to flame normal acceleration [61, 194, 195]. As combustion takes place increasingly in fuel-lean mode with increasing a_d, the flame normal acceleration weakens with increasing droplet size, which also decreases the extent of collinear alignment between ∇c and the eigenvector associated with e_α. However, in all cases, ∇c aligns with the eigenvector associated with e_α in the reaction zone where the effects of heat release are strong, and thus a_N assumes positive values in this region. However, the extent of collinear alignment with the eigenvector associated with e_α decreases with increasing droplet size and turbulence intensity. Thus, ∇c aligns with the eigenvector associated with e_γ on both unburned and burned gas sides of the flame for the cases with high turbulence intensities and accordingly a_N assumes negative values in these regions. The relative magnitudes of $\nabla\cdot\overrightarrow{u}$ and a_N determine the variation of $a_T = \nabla\cdot\overrightarrow{u} - a_N$ across the flame. In the laminar flames, a_T decreases from the unburned to the burned gas side of the flame, whereas this behaviour is less prominent for the turbulent cases and the mean value of a_T increases with increasing turbulence intensity because of small mean values of a_N for large $u'/S_{b(\phi_g=1)}$ values.

The profiles of the normalised mean values of the normal strain rate induced by displacement speed and its components $\partial S_i^+/\partial n = N_j\partial S_i/\partial x_j \times \delta_{st}/S_{b(\phi_g=1)}$ (where $i = d, r, n, t+z+s$) conditional upon c are shown in Fig. 4.20. The mean value $N_j\partial S_r/\partial x_j \times \delta_{st}/S_{b(\phi_g=1)}$ assumes negative values throughout the flame because S_r predominantly increases from the unburned to the burned gas side of the flame. By contrast, $N_j\partial S_n/\partial x_j \times \delta_{st}/S_{b(\phi_g=1)}$ assumes positive values towards the burned gas side, which is consistent with the behaviour of S_n across the

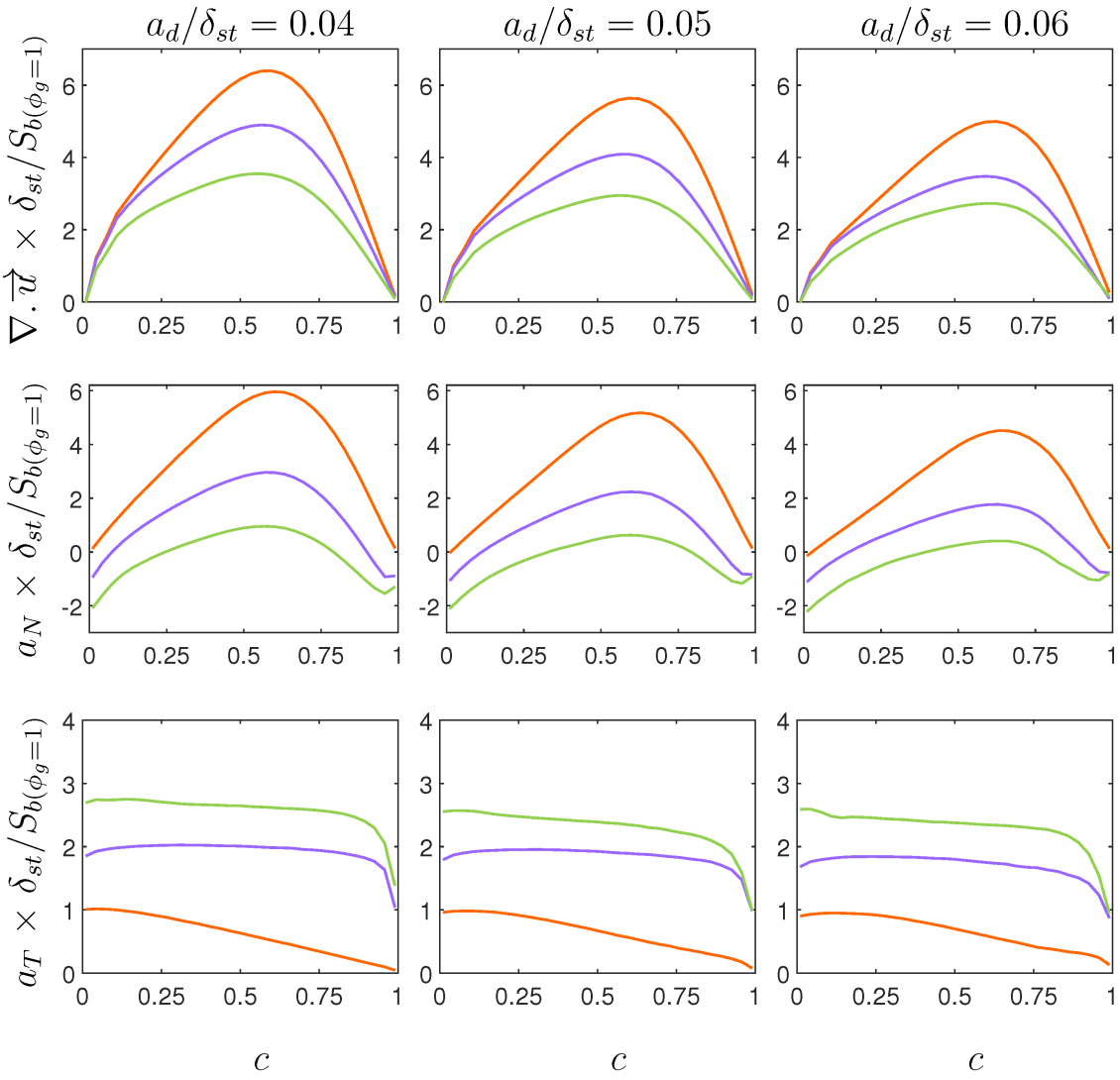

Figure 4.19: Profiles of mean values of $\nabla \cdot \overrightarrow{u}, a_N, a_T = \nabla \cdot \overrightarrow{u} - a_N \times \delta_{st}/S_{b(\phi_g=1)}$ conditional upon c for initial $a_d/\delta_{st} = 0.04, 0.05$ and 0.06. See Fig. 4.17 caption for the colour keys.

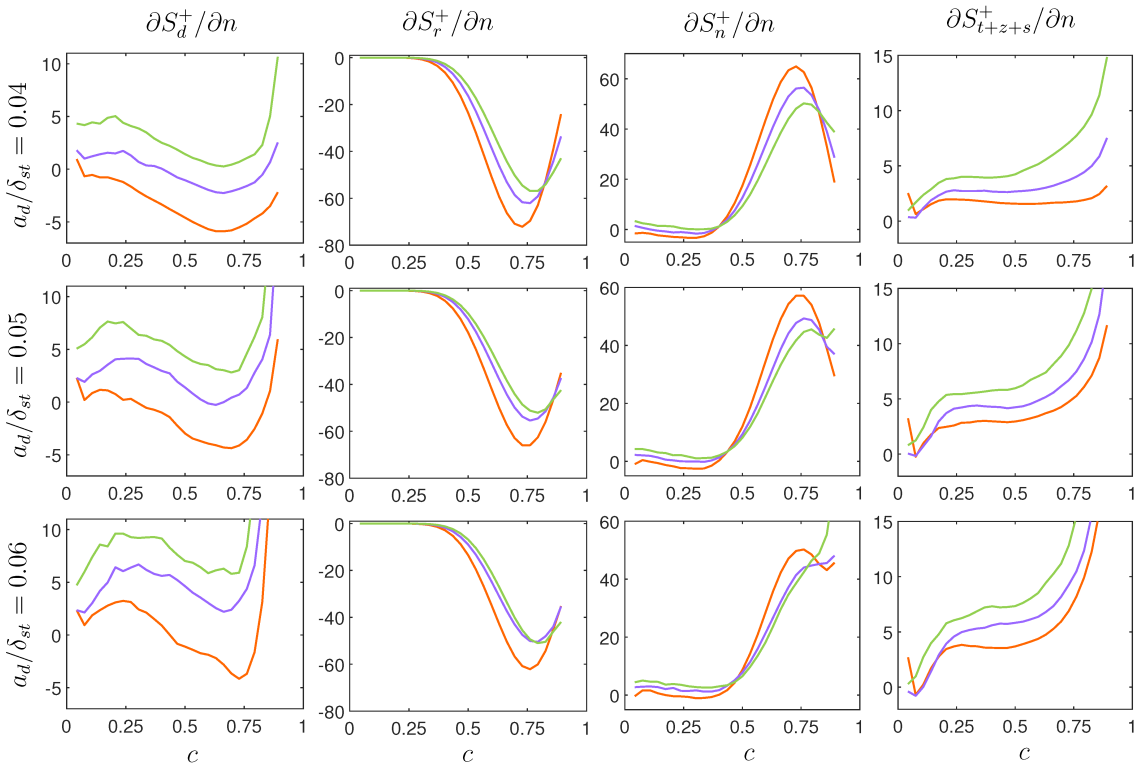

Figure 4.20: Profiles of mean values of $N_j\partial S_i/\partial x_j \times \delta_{st}/S_{b(\phi_g=1)}$ (where $i = d,r,n,t+z+s$) conditional upon c for initial $a_d/\delta_{st} = 0.04, 0.05$ and 0.06. See Fig. 4.17 caption for the colour keys.

flame (see Fig. 4.17). The magnitudes of mean values of $N_j\partial S_r/\partial x_j$ and $N_j\partial S_n/\partial x_j$ remain much greater than the mean contribution of $N_j\partial S_{(t+z+s)}/\partial x_j$. For the laminar case, negative contributions of $N_j\partial S_r/\partial x_j$ dominate over positive contributions of $N_j\partial S_n/\partial x_j$ to yield predominantly negative mean values of $N_j\partial S_d/\partial x_j$ within the reaction zone but positive values can be discerned on both unburned and burned gas sides. However, an opposite behaviour is observed for turbulent cases and the mean contribution of $N_j\partial S_d/\partial x_j$ assumes higher positive values for greater values of $u'/S_{b(\phi_g=1)}$.

The variations of the normalised mean values of the tangential strain rate induced by displacement speed (or curvature stretch rate) $(2S_i\kappa_m)^+ = 2S_i\kappa_m \times \delta_{st}/S_{b(\phi_g=1)}$ (where $i = d,r+n+z+s,t$) conditioned upon c are shown in Fig. 4.21. It has been found that the mean value of $2S_d\kappa_m \times \delta_{st}/S_{b(\phi_g=1)}$ assumes mostly negative values throughout the flame except for the laminar case with initial droplet size of $a_d/\delta_{st} = 0.04$. Figure 4.21 further shows that the mean values of $2S_t\kappa_m \times \delta_{st}/S_{b(\phi_g=1)} = -4D\kappa_m^2 \times \delta_{st}/S_{b(\phi_g=1)}$ dominate over the mean values of $2S_{r+n+z+s}\kappa_m \times \delta_{st}/S_{b(\phi_g=1)}$ to yield negative mean value of $2S_d\kappa_m \times \delta_{st}/S_{b(\phi_g=1)}$ for all cases except for the laminar case with initial droplet size of $a_d/\delta_{st} = 0.04$. Small droplets in

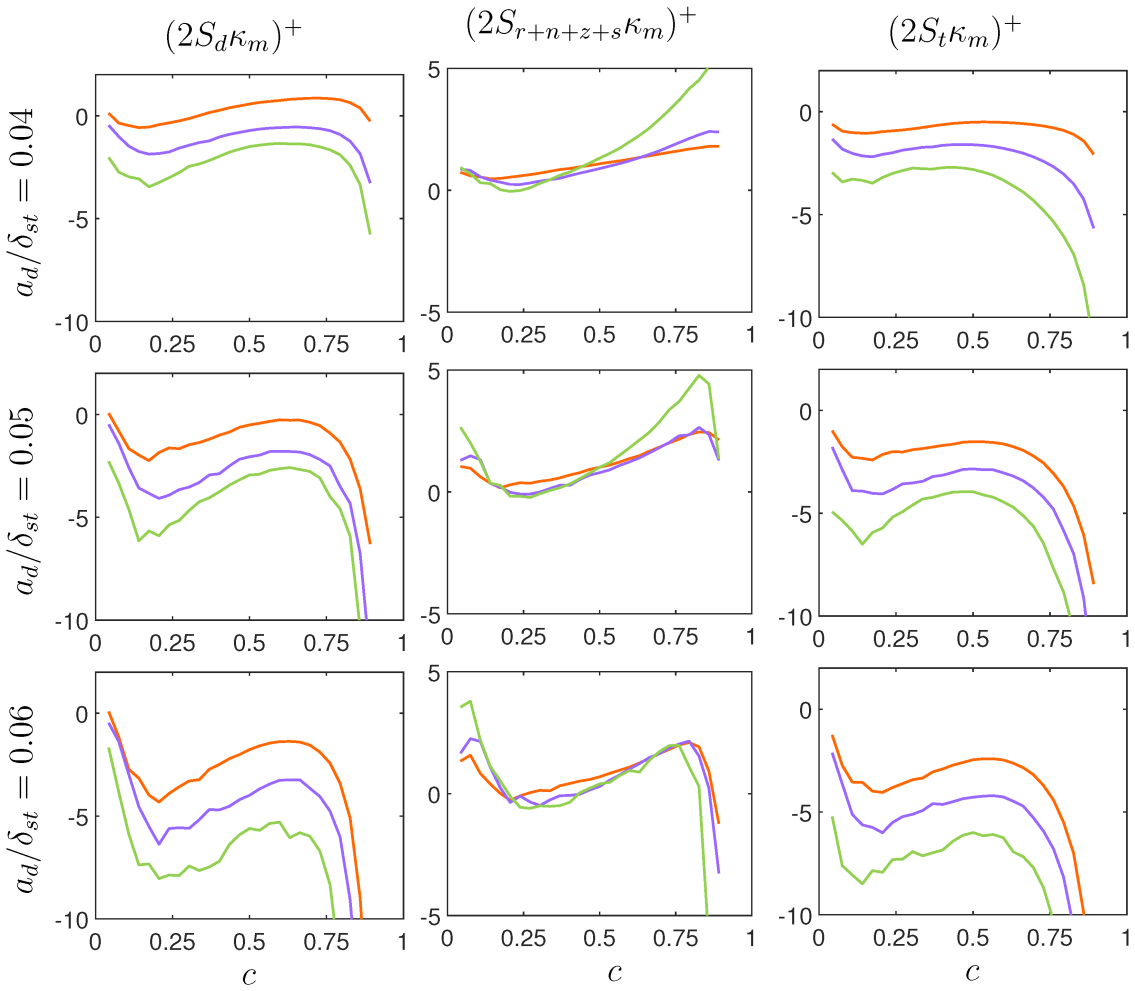

Figure 4.21: Profiles of mean values of $2S_i\kappa_m \times \delta_{st}/S_{b(\phi_g=1)}$ (where $i = d, r+n+z+s, t$) conditional upon c for initial $a_d/\delta_{st} = 0.04, 0.05$ and 0.06. See Fig. 4.17 caption for the colour keys.

the initial $a_d/\delta_{st} = 0.04$ laminar case evaporate rapidly and do not impart much influence on flame wrinkling. The droplets in the initial $a_d/\delta_{st} = 0.05$ and 0.06 cases induce considerable flame wrinkling due to flame droplet interaction under laminar conditions (see Figs. 4.4-4.7). Furthermore, it has been shown in the previous section (see the discussion regarding Tables 4.2 and 4.3) that the flame radius decreases with increasing droplet size for the cases considered here. For the above reasons, the contribution of $2S_t\kappa_m = -4D\kappa_m^2$ remains small for the droplet cases with initial droplet size of $a_d/\delta_{st} = 0.04$, whereas this contribution plays a more significant role in the laminar droplet cases with initial $a_d/\delta_{st} = 0.05$ and 0.06 because of the smaller flame radii and larger extent of flame wrinkling in these cases. Thus, the mean curvature stretch remains predominantly positive due to spherical positive curvature in the

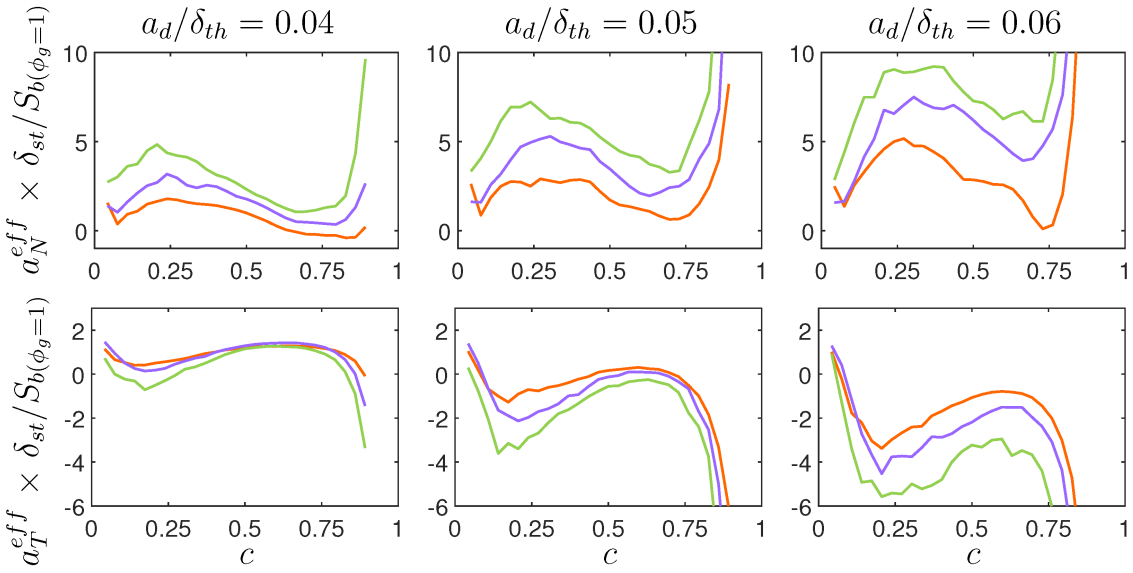

Figure 4.22: Profiles of mean values of $\left\{a_N^{eff}, a_T^{eff}\right\} \times \delta_{st}/S_{b(\phi_g=1)}$ conditional upon c for initial $a_d/\delta_{st} = 0.04, 0.05$ and 0.06. See Fig. 4.17 caption for the colour keys.

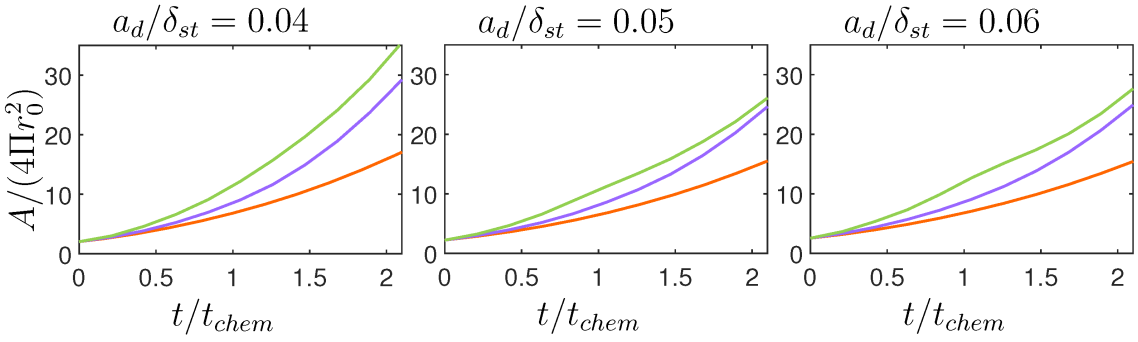

Figure 4.23: Temporal evolution of normalised flame surface area $A/(4\pi r_0^2)$ for initial $a_d/\delta_{st} = 0.04, 0.05$ and 0.06. See Fig. 4.17 caption for the colour keys.

laminar case with initial $a_d/\delta_{st} = 0.04$, whereas it assumes negative values for the laminar cases with initial $a_d/\delta_{st} = 0.05$ and 0.06. The extent of flame wrinkling increases with increasing $u'/S_{b(\phi_g=1)}$, which widens the range of curvature κ_m values and increases the mean values of κ_m^2 and $2S_t\kappa_m = -4D\kappa_m^2$.

The mean values of normalised effective normal and tangential strain rates (i.e. $\left\{a_N^{eff}, a_T^{eff}\right\} \times \delta_{st}/S_{b(\phi_g=1)}$) conditioned on c are shown in Fig. 4.22, which indicates that the mean values of a_N^{eff} show an increasing trend with turbulence intensities for all initial values of a_d considered here. Moreover, the mean value of a_N^{eff} remains positive in turbulent cases, which suggests that a_N^{eff} promotes thickening of the flame in a mean sense, which is consistent with the observations made from Fig. 4.7. The mean value of a_T^{eff} remains mostly negative for all the cases except for the laminar case corresponding to initial $a_d/\delta_{st} = 0.04$. In the initial $a_d/\delta_{st} = 0.04$ case, predominantly positive mean values of $2S_d\kappa_m$ along with positive mean values of a_T give rise to the net positive mean value of a_T^{eff}, but for other cases, the negative mean values of $2S_d\kappa_m$ dominate over positive mean values of a_T to yield negative mean values of a_T^{eff}. The negative mean values of a_T^{eff} due to predominantly negative mean values of $2S_d\kappa_m$ indicate smoothening of the wrinkled flame front due to flame propagation. The decreasing trend of a_T^{eff} with increasing droplet size is consistent with the evolution of the normalised flame surface area $A = \int_V |\nabla c| dV/(4\pi r_0^2)$ (where $r_0 = 2.0\delta_{st}$) shown in Fig. 4.23, which suggests that the normalised flame area $A/(4\pi r_0^2)$ drops with an increase in a_d. Further discussion of the effects of droplet size and turbulence intensity on flame surface area and overall burning rate for the cases considered here can be found in Sections 4.2 and 4.4 and thus is not repeated here.

4.6 Flame-Flame Interactions in Spherically Expanding Turbulent Spray Flames

The concept of local flame structures based on the scalar fields, such as reaction progress variable, is pivotal to the fundamental understanding of flame propagation statistics due to its role in flame surface generation and overall burning rate. The relationship between geometrical structures and the gradient of scalar fields in turbulent flows was considered in the pioneering analysis by Gibson [97]. Moffatt [198] described the topological structures using the critical points as elliptic or hyperbolic according to the signature of the eigenvalues of the scalar Hessian tensor. The flat and tile-like topologies have been found to be predominant structures for both passive scalar mixing [199] and turbulent premixed combustion [170, 200, 201].

The flame topologies play a key role in characterising the flame-flame interaction (FFI)

Table 4.4: Simulation parameters considered in Section 4.6.

Parameter	Value
a_d/δ_{st}	0.04, 0.05 and 0.06
ϕ_{ov}	1.0
$u'/S_{b(\phi_g=1)}$	4.0, 8.0 and 10.0
L_{11}/δ_{st}	2.5
Pr	0.7
Le	1.0
$\gamma = C_p^G/C_v^G$	1.4

events in turbulent combustion processes [111, 202–208]. Several different approaches have been used in the literature to identify FFI, including critical point theory (e.g. [111, 202, 203]), automatic feature extraction technique based on complex wavelet transform (e.g. [204, 205]) and Minkowski functional (e.g. [206, 207]) based techniques. A recent experimental investigation [208] focussed on the influences of flow features on the FFI events for turbulent premixed flames in dual Bunsen burner configuration. In comparison to the existing body of literature on FFI in turbulent premixed combustion, relatively limited information is available on this topic for turbulent flames propagating into droplet-laden mixtures. It has already been reported both experimentally and numerically that in addition to flame-turbulence interaction, the complex interaction of flame and droplets induces wrinkling on the flame surface in turbulent spray combustion. This section aims to broaden the current knowledge of flame self-interactions (FSI) by focusing on turbulent flames propagating into droplet mists. In the current analysis, the critical point theory approach adopted in Griffiths et al. [202] and Trivedi et al. [111, 203], has been used. The main objectives of this section are to analyse the influences of turbulence intensity and droplet diameter on the behaviour of the FSI events in turbulent spherically expanding flames propagating into droplet-mists and compare these statistics with corresponding spherically expanding turbulent premixed flames. Simulation parameters used in Section 4.6 are listed in Table 4.4.

As the gradient of c vanishes at the critical points in the flame, the Taylor series expansion around a critical point can be written as [202, 203]:

$$c(\mathbf{a}+\mathbf{x}) = c(\mathbf{a}) + (\mathbf{x}^T/2)\underline{\underline{H}}(c(\mathbf{a}))\mathbf{x} + ... \tag{4.5}$$

The topologies can be obtained with the eigenvalues of the Hessian $\underline{\underline{H}}(c)$. The shape factors θ and φ can be defined based on the eigenvalues ($\lambda_1 > \lambda_2 > \lambda_3$) of the Hessian $\underline{\underline{H}}(c)$ as

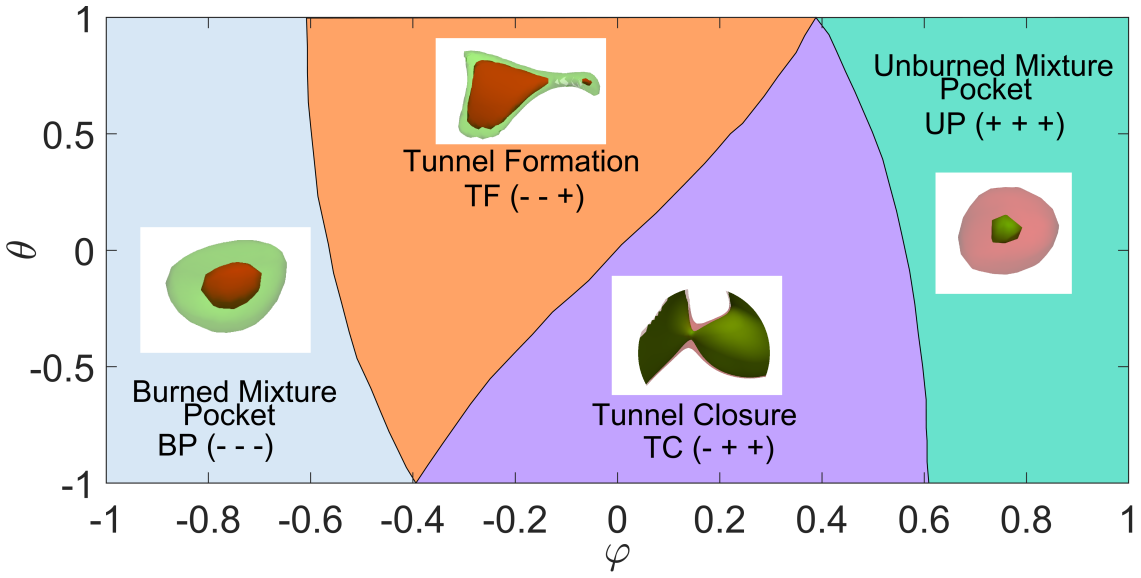

Figure 4.24: Various types of FSI topologies characterised by shape factors. The sign of eigenvalues of $\underline{\underline{H}}(c)$ is shown in each quadrant with the black line indicating the change in the sign of eigenvalues. The examples (where c increases from green to red) FSI events are taken from the droplet case with initial $u'/S_{b(\phi_g=1)} = 4.0$ and $a_d/\delta_{st} = 0.06$.

[202, 203]:

$$\theta = \frac{6}{\pi} arctan\left(\frac{(\lambda_1 - 2\lambda_2 + \lambda_3)/6^{1/2}}{(\lambda_1 - \lambda_3)/2^{1/2}}\right) \tag{4.6}$$

$$\varphi = \frac{2}{\pi} arctan\left(\frac{(\lambda_1 + \lambda_2 + \lambda_3)cos(\theta\pi/6)/3^{1/2}}{(\lambda_1 - \lambda_3)/2^{1/2}}\right) \tag{4.7}$$

The FSI topologies in $\theta - \varphi$ space are shown in Fig. 4.24 where the sign of eigenvalues of $\underline{\underline{H}}(c)$ changes from $(---)$ to $(--+)$ to $(-++)$ and to $(+++)$, moving from left to right with the black line indicating the change in the sign of the eigenvalues. Eigenvalues with the sign of $(---)$ correspond to burned mixture pockets (BPs) (see the LHS of Fig. 4.24) whereas eigenvalues with the sign of $(+++)$ show unburned mixture pockets (UPs) (see the RHS of Fig. 4.24). Tunnel formation (TF) and tunnel closure (TC) topologies are represented by eigenvalues with the sign of $(--+)$ and $(-++)$, respectively. TF grows cylindrically outward, whereas TC is a cylindrical flame topology and propagates inwards (see Fig. 4.24). The examples shown in Fig. 4.24 are taken from the droplet cases considered in this analysis. The singular points have been identified using the methodology used in Ref. [202] and thus is not repeated here. The statistics of FSI are conditioned on the reaction progress variable range given by $0.01 \leq c \leq 0.99$; therefore, the identification of FSI topologies is restricted in

a manner where combustion takes place.

It is clear from instantaneous fields of c given in Figs. 4.1-4.3, that the interaction between the flame and the turbulence leads to strongly wrinkled c isosurfaces for all cases, and the extent of wrinkling increases with increasing u' for both premixed and droplet cases. It has been shown in Section 4.3 that the heat release rate for these flames takes place predominantly in premixed mode but non-negligible contribution is also obtained from the diffusion mode of burning, and such cases have previously been referred to as premixed sprays by several authors [150, 156, 157]. This diffusion burning mode in these cases are captured in the region given by $0.01 \leq c \leq 0.99$ (see Section 4.3) and the definition of c used here can be applied to edge flames [164]. Therefore, the topologies of FSI in these flames can be identified based on the geometric properties of c isosurfaces. As the FSI is the focus of this study, the deformation of c isosurfaces in Figs. 4.1-4.3 should be distinguished from the FSI events, which creates either a UP/BP or TF/TC topology.

Figure 4.25 shows the frequency of the FSI topologies for different values of c. The topologies associated with the FSI events have predominantly been found close to the burned gas region corresponding to $0.975 \leq c \leq 0.99$ for all turbulent premixed flames considered here. Figure 4.25 shows that TF has the highest frequency in all turbulent premixed gaseous cases, whereas the occurrence of UPs is rare in these cases. This behaviour is consistent with previous investigations on the FSI events in turbulent premixed gaseous flames [111, 202] in which a rapid consumption of UPs was provided as the reason for the lack or low occurrence of UPs at the time when the statistics were extracted.

The presence of liquid droplets leads to significant changes in the distribution of the FSI topologies across the flame. In the initial $u'/S_{b(\phi_g=1)} = 4.0$ case, the FSI events start to become visible towards the reaction zone (i.e. $c = 0.8$ where the maximum heat release is obtained for this thermo-chemistry) and this tendency is particularly prevalent for large droplets (e.g. initial $a_d/\delta_{st} = 0.06$). Slower evaporation rate for larger droplets enhances the frequency of flame-droplet interactions, which leads to more wrinkled flame surfaces on the burned gas side of flame front for low turbulence intensities. It has been discussed earlier in Section 4.2 that large droplet cases exhibit a wider distribution of flame curvature on the burned gas side. However, under high turbulence intensities (e.g. initial $u'/S_{b(\phi_g=1)} = 8.0$ and 10.0 cases), the FSI events occur predominantly in the preheat zone corresponding to $c \leq 0.5$.

The initial values of Damköhler and Karlovitz numbers for the premixed case with initial $u'/S_{b(\phi_g=1)} = 4.0$ are 1.31 and 3.49, respectively. The values of $Da_{(\phi_g=1)}$ and $Ka_{(\phi_g=1)}$ are 0.65 and 9.88 (0.52 and 13.88) respectively for the premixed case with initial $u'/S_{b(\phi_g=1)} = 8.0$ ($u'/S_{b(\phi_g=1)} = 10.0$). As discussed earlier in section 4.1, all the cases considered here represent the thickened flame regime, hence the contours of c representing the preheat zone (i.e. $c < 0.5$)

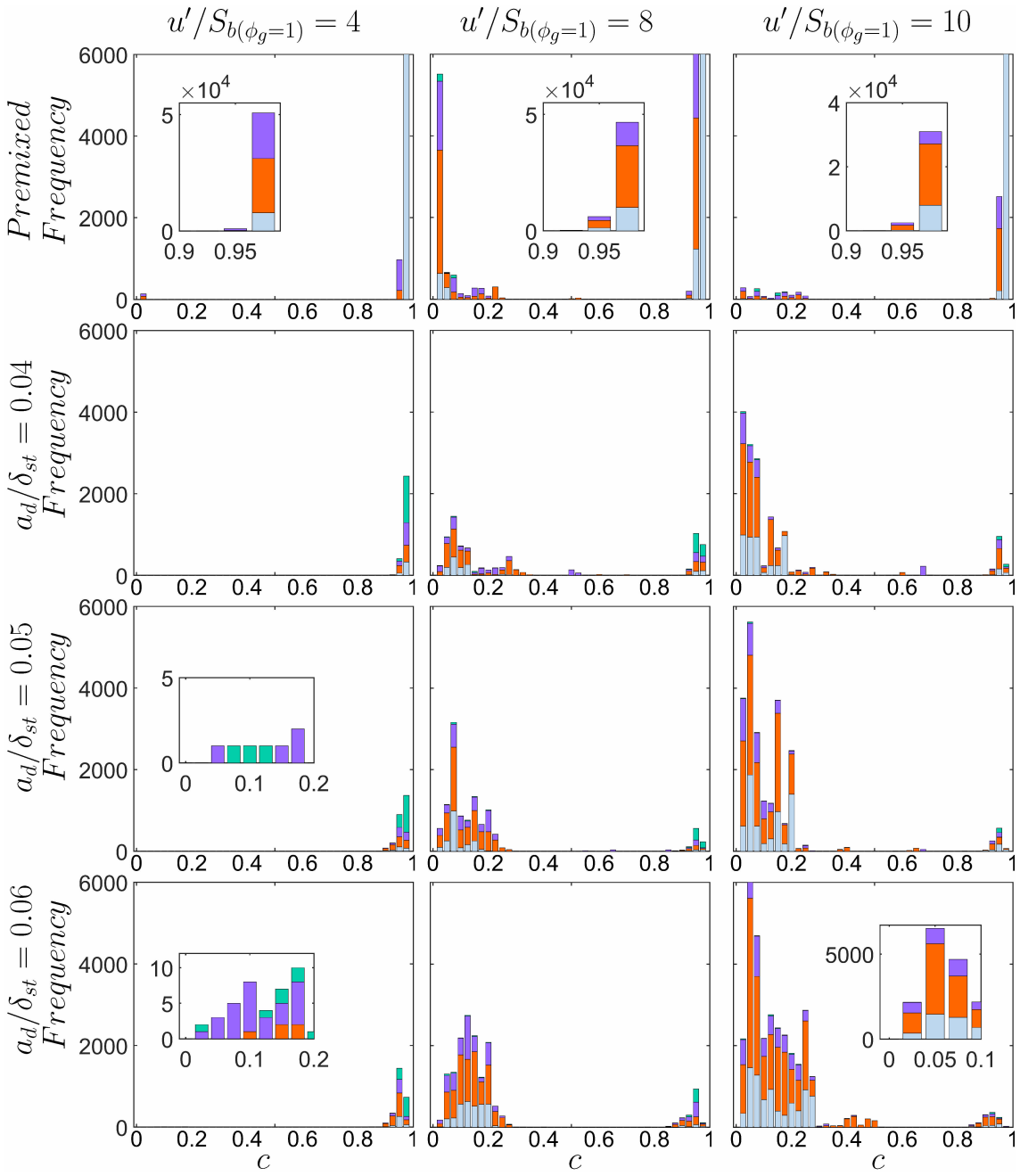

Figure 4.25: Histograms of the number of samples of four FSI topologies: burned mixture pocket (BP (- - -)), tunnel formation (TF (- - +)), tunnel closure (TC (- + +)) and unburned mixture pocket (UP (+ + +)) for different values of c.

are found to be more deformed than the ones representing the reaction zone (i.e. $0.7 < c < 0.9$) in the cases shown in Figs. 4.1-4.3, where this behaviour is particularly prevalent for turbulent droplet cases. This tendency strengthens with increasing u' due to an increase in the Karlovitz number. The flame deformation is compounded by the wrinkling induced by droplets and their latent heat extraction from the flame surface. As a result of the combination of the aforementioned mechanisms, the FSI events in the droplet cases have been observed over a larger range of c than in the corresponding premixed turbulent flames (see Figs. 4.1-4.3). Figures 4.1-4.3 further show that TF/TC topologies have the largest frequency for all droplet cases except for the initial $u'/S_{b(\phi_g=1)} = 4.0$ case, where UPs are predominantly observed.

The local flame surface geometries can be categorised based on the local mean curvature $\kappa_m = (\kappa_1 + \kappa_2)/2$ and Gauss curvature $\kappa_g = \kappa_1 \kappa_2$ [199, 200], where κ_1 and κ_2 are the two principal curvatures. The region given by $\kappa_g > \kappa_1 \kappa_2$ is unrealisable because it leads to complex principal curvatures. In the above definitions, positive values of κ_g imply elliptic cup-like topologies while negative κ_g values represent hyperbolic saddle geometries. A negative (positive) value of κ_m indicates the flame surface in question remains concave (convex) to the reactants. The locations where κ_g vanishes exhibit tile convex (concave) geometries for $\kappa_m > 0$ ($\kappa_m < 0$) or flat topologies for $\kappa_m = 0$. The scatters of the different FSI events in the region corresponding to $0.01 \leq c \leq 0.99$ in the $\kappa_m - \kappa_g$ plane are shown in Fig. 4.26 for all cases considered here. Note that the UPs (e.g. geometries propagating inwards) are associated with concave cup-like topologies, whereas BPs (i.e geometries propagating outwards) are representative of convex cup-like topologies. Furthermore, Fig. 4.26 shows that TF/TC topologies are associated with hyperbolic saddle geometries. The distribution of the FSI events in Fig. 4.26 reveals that the UPs are predominantly obtained for turbulent droplet cases with initial $u'/S_{b(\phi_g=1)} = 4.0$. By contrast, TF/TC events are predominantly obtained for turbulent droplet cases with high turbulence intensities (e.g. initial $u'/S_{b(\phi_g=1)} = 8.0$ and 10.0). It has been shown earlier in Section 4.3 that the contribution to overall heat release rate due to non-premixed combustion increases with increasing $u'/S_{b(\phi_g=1)}$ for the droplet cases considered here and the high burning rate of the stoichiometric mixture (where the non-premixed combustion is obtained) makes the occurrence of UPs less likely for high u'.

A comparison between the droplet cases with the corresponding gaseous premixed cases in Figs. 4.25 and 4.26 reveals important differences in the topology distributions for FSI. Most of the FSI events for the gaseous premixed flames occur towards the burned gas side, although the frequency of finding these events on the unburned gas side increases with decreasing (increasing) Da (Ka), which is consistent with previous findings [111, 202]. However, the TF events towards the burned gas side remain the major FSI topology for all the premixed cases considered here, and this behaviour is found to be consistent with previous findings for tur-

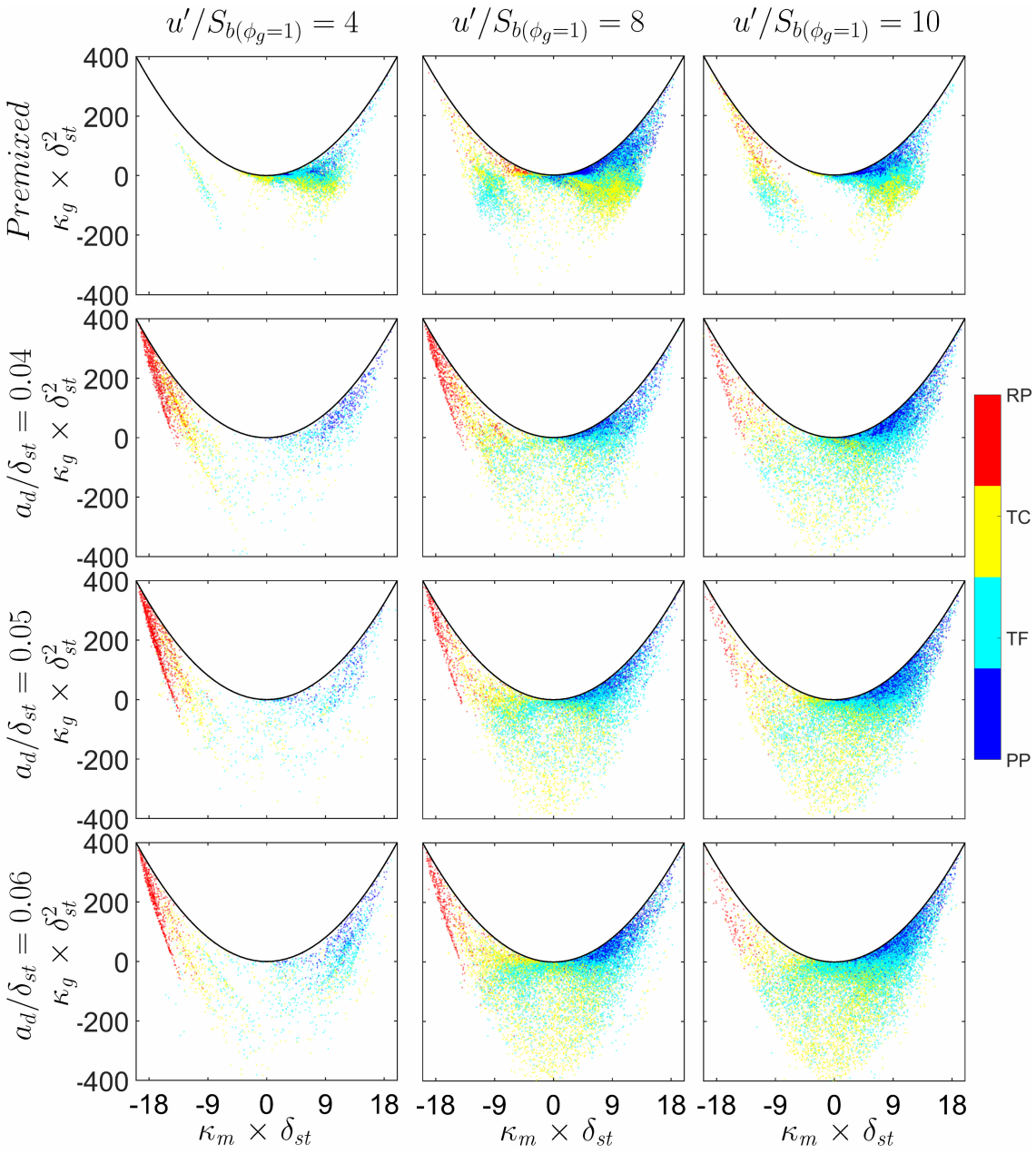

Figure 4.26: Scatter of $\kappa_g \times \delta_{st}^2$ with $\kappa_m \times \delta_{st}$ in the region $0.01 \leq c \leq 0.99$ for turbulent premixed gaseous and droplet cases with initial $u'/S_{b(\phi_g=1)} = 4.0, 8.0, 10.0$. Scatter is coloured by the different types of topologies associated with the FSI events.

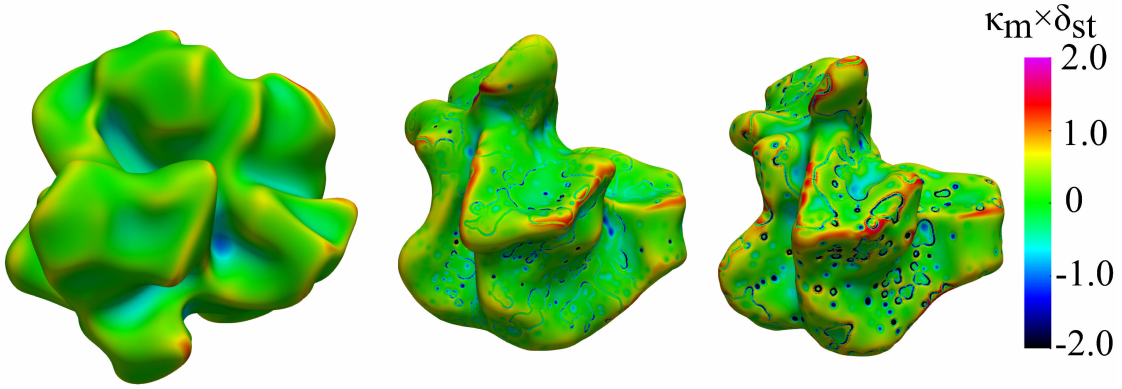

Figure 4.27: Instantaneous view of $c = 0.5$ isosurface coloured with $\kappa_m \times \delta_{st}$ for turbulent premixed (1^{st} column) and droplet cases with initial $a_d/\delta_{st} = 0.04$ (2^{nd} column) and 0.06 (3^{rd} column) for initial $u'/S_{b(\phi_g=1)} = 4.0$.

bulent premixed gaseous flames [111, 202]. Although most FSI events occur on the product side of the flame front in the laminar (not shown here) and turbulent droplet cases with small turbulence intensity (e.g. initial $u'/S_{b(\phi_g=1)} = 4.0$ case), these FSI events are predominantly representative of UPs in contrast to TF/TC topologies in the premixed cases. In order to explain this behaviour, it is useful to consider instantaneous views of c isosurfaces coloured by local values of $\kappa_m \times \delta_{st}$, which are exemplarily shown for $c = 0.5$ in Fig. 4.27 for the premixed flames and droplet cases with initial $a_d/\delta_{st} = 0.04$ and 0.06 and $u'/S_{b(\phi_g=1)} = 4.0$. Figure 4.27 shows that dimples with large negative values of $\kappa_m \times \delta_{st}$ (note that UPs are associated with negative values of κ_m, see Fig. 4.26) appear on $c = 0.5$ isosurfaces in turbulent droplet cases, which are completely absent in the corresponding premixed flames. The evaporation of small droplets is mostly completed in the preheat zone (e.g. $c < 0.5$) of the flame but large droplets can survive longer within the flame (i.e. $0.01 \leq c \leq 0.99$) and interact with the flame surface, giving rise to flame deformation while releasing fuel vapour as a result of evaporation. This leads to dimples on the flame surface under laminar and low turbulence intensity (e.g. initial $u'/S_{b(\phi_g=1)} = 4.0$ cases) conditions, which may give rise to UPs on c isosurfaces.

These dimples may cause the occurrence of UP type FSI events for the droplet cases, especially under laminar and low turbulence intensity (e.g. initial $u'/S_{b(\phi_g=1)} = 4.0$ cases) conditions. Moreover, the frequency of finding dimples increases with increasing droplet diameter, as large droplets survive longer within the flame because of their slower evaporation rate and bigger size. The mean flame displacement speed in droplet cases is smaller than the corresponding premixed flames due to the predominantly fuel-lean mode of combustion in droplet cases (see Section 5.5). Thus, the UPs in droplet cases are also relatively slowly consumed in comparison to the corresponding premixed gaseous flames. Consequently, the UPs in droplet

cases are more stable than in the corresponding premixed flame cases. Figure 4.26 shows that the frequency of finding UPs increases with increasing a_d/δ_{st} for initial $u'/S_{b(\phi_g=1)} = 4.0$ cases. However, the FSI topologies associated with TF/TC and BPs, which are characteristic of flame-turbulence interaction in premixed turbulent flames [111, 202], increasingly play important roles with increasing $u'/S_{b(\phi_g=1)}$ for the droplet cases. Accordingly, the frequency of finding UPs decreases with increasing $u'/S_{b(\phi_g=1)}$ for the droplet cases. However, the distribution of the FSI events across the flame front in the droplet cases remains significantly different to the corresponding turbulent premixed flames. Unlike premixed flames, these events in the droplet cases occur towards the unburned gas side of the flame for high turbulence intensities (e.g. initial $u'/S_{b(\phi_g=1)} = 8.0$ and 10.0 cases) because the droplets penetrate into the flame due to turbulent fluid motion and induce FSI events but they eventually evaporate as the burned gas side is approached. As the large droplets evaporate slowly, they exhibit high frequency of the FSI events on the unburned gas side for the droplet cases under high turbulence intensities (e.g. initial $u'/S_{b(\phi_g=1)} = 8.0$ and 10.0 cases). It has been previously reported [111, 202] that the likelihood of obtaining FSI on the unburned gas side of the flame increases with decreasing (increasing) Da (Ka) for premixed turbulent flames. The characteristic value of Da (Ka) decreases (increases) significantly with increasing $u'/S_{b(\phi_g=1)}$ and this effect is particularly strong in the droplet cases because of the greater likelihood of fuel-lean gaseous phase combustion (see Fig. 4.8). Thus, the increased frequency of finding the FSI events towards the unburned gas side in the droplet cases for large turbulence intensities could be linked with the small (large) values of characteristic Da (Ka) in these cases.

The differences in the topology distributions for the FSI events between droplet and premixed flames have several important implications. The differences in frequency and distribution of the FSI events in the droplet cases in comparison to the premixed flames suggest that the flame surface area annihilation due to FSI is likely to be different in droplet cases when compared to the corresponding gaseous premixed flames. This may lead to a different variation of flame surface area with increasing u' in the droplet cases than in the corresponding gaseous premixed flame cases, which has been demonstrated earlier in Section 4.2. Furthermore, the qualitative differences in flame topology distributions for the FSI events between spray and premixed flames suggest that the existing closures (e.g. Flame Surface Density methodology [184, 209]), which depend on the flame surface topology, may need significant modifications to make them applicable for flames propagating into droplet-laden mixtures. Moreover, any such attempt to extend the flame surface based modelling methodology for spray flames needs to include the effects of ϕ_g and a_d.

4.7 Summary of Key Findings

Effects of turbulence intensity on flame-droplet-turbulence interactions have been investigated for spherically expanding n-heptane spray flames based on three-dimensional DNS simulations. Some important results are listed below:

- Having higher surface to volume ratio, small droplets evaporate quicker compared to large droplets. Hence small droplets with initial $a_d/\delta_{st} = 0.04$ mostly complete their evaporation ahead of the reaction zone. On the contrary, large droplets with initial $a_d/\delta_{st} = 0.05$ and 0.06 can survive longer in the flame and continue to evaporate across the flame. Thus, unburned fuel pockets can be formed in the burned gas region and the temperature of the burned gas region drops locally due to the latent heat of evaporation.

- The flame-droplet interaction gives rise to dimples on the flame surface for both laminar and turbulent droplet cases whereas premixed gaseous flames have a smooth surface. Although the droplet-induced flame wrinkling is partially masked by the flow-induced flame wrinkling at increasing turbulence intensities, wider distributions of curvature PDFs for droplet cases provide a clear indication of droplet induced flame deformation. Furthermore, the growth rate of flame surface area is found to diminish with increasing droplet diameter while higher turbulence intensities enhance the flame surface area generation.

- Premixed mode of combustion is responsible for the significant part of overall heat release rate and the contribution of premixed mode of combustion to overall heat release rate decreases with increasing droplet diameter and turbulence intensity. Additionally, mean heat release associated with premixed combustion attains its maximum value at around $c = 0.75$ where the peak value of reaction rate of progress variable is found. The maximum mean heat release arising from non-premixed combustion is obtained close to the burned gas region (i.e. $c \approx 1.0$) at the stoichiometric mixture.

- The gaseous mixture composition in the flame is found to be principally fuel-lean and this tendency strengthens with increasing droplet diameter and turbulence intensities. Thus, burned gas volume and the product formation rate per unit flame surface area decreases with increasing droplet diameter and turbulence intensity.

- Spray flames becomes thicker for the cases with large droplet diameters and high turbulence intensities due to the greater extent of fuel-lean combustion. The mean displacement speed assumes positive values across the flame for all droplet cases. The mean

behaviour of displacement speed is primarily governed by reaction, normal and tangential diffusion components, while the mean values of the contributions due to cross-scalar dissipation term and droplet evaporation remain weak in comparison to other components.

- As thermal expansion declines due to predominantly fuel-lean burning of reacting mixture, dilatation rate diminishes with increasing droplet diameters and turbulence intensities. Moreover, the mean tangential strain rate takes positive values which originate the relative magnitude of dilatation rate and normal strain rate. The positive mean values of normalised effective normal strain rate in turbulent droplet cases indicate flame thickening, while the negative mean values of normalised effective tangential strain rate, which originates predominantly negative mean values of $2S_d\kappa_m$, implies smoothening of the wrinkled flame front due to flame propagation.

- The flame self interaction events mainly occur close to the burned gas region for turbulent premixed flames and droplet cases with initial $u'/S_{b(\phi_g=1)} = 4.0$. Tunnel formation is the most commonly observed flame self interaction event in turbulent premixed flames whereas flame-droplet interactions lead to frequent occurrence of unburned mixture pockets in the droplet cases with small turbulence intensities. However, the flame self interaction events are predominantly observed in the preheat zone for the droplet cases with high turbulence intensities.

Chapter 5

Statistical Analysis of Flame-Droplet-Turbulence Interaction-Part II: Effects of Overall Equivalence Ratio

This chapter mainly focuses on the effects of overall equivalence ratio on the flame structure and combustion characteristics. The statistical behaviour of spherically expanding turbulent spray flames is analysed along with flame wrinkling, flame surface area, and volume of the burned gas. Furthermore, flame propagation statistics are characterised in terms of displacement and consumption speeds. The flame surface topologies and the statistical characteristics of various flame speeds for different droplet diameters and overall equivalence ratios are discussed in detail later in this chapter.

5.1 Flame-Turbulence Interaction

Laminar and turbulent spherically expanding n-heptane flames in mono-sized fuel droplet-mists have been simulated for a range of different overall equivalence ratios and droplet diameters using three-dimensional DNS. Parameters used for the simulations in this chapter are provided in Table 5.1. Figures 5.1-5.3 show the instantaneous distributions of reaction progress variable c, normalised gaseous fuel mass fraction Y_F/Y_{Fst}, and non-dimensional temperature T fields, respectively, at the central $x-y$ mid-plane at $t = 2.52\alpha_{T0}/S^2_{b(\phi_g=1)}$ under laminar and turbulent flow conditions (with initial $u'/S_{b(\phi_g=1)} = 4.0$) and for overall equivalence ratios $\phi_{ov} = 0.8$,1.0, and 1.2. The droplets residing on the $x-y$ mid-plane are shown by

Table 5.1: Simulation parameters considered in Chapter 5.

Parameter	Value
a_d/δ_{st}	0.04, 0.05 and 0.06
ϕ_{ov}	0.8, 1.0 and 1.2
$u'/S_{b(\phi_g=1)}$	0.0 and 4.0
L_{11}/δ_{st}	2.5
Pr	0.7
Le	1.0
$\gamma = C_p^G/C_v^G$	1.4

black dots in Figs. 5.1-5.3. It is worth noting that these droplets are individually tracked in a Lagrangian manner and they are not meant to indicate individual droplet burning. For globally stoichiometric (i.e. $\phi_{ov} = 1.0$) droplet cases, unburned fuel pockets can appear in the burned gas region notably for large droplets. However, these unburned fuel pockets are obtained for all droplet sizes for $\phi_{ov} = 1.2$ under both laminar and turbulent conditions. Unburned fuel is mostly found ahead of the flame for the droplet cases with $\phi_{ov} = 0.8$ due to small number density of droplets. The latent heat of evaporation induces local temperature drop in the burned gas region for $\phi_{ov} = 1.0$ and $\phi_{ov} = 1.2$ (see Figs. 5.1 and 5.3) and this tendency is particularly prominent for large droplets (e.g. $a_d/\delta_{st} = 0.06$). However, the burned gas temperature increases with increasing droplet diameter for $\phi_{ov} = 0.8$ and the burned gas temperature for the initial $a_d/\delta_{st} = 0.04$ case is found to be similar to that in the corresponding fuel-lean premixed case under both laminar and turbulent flow conditions. It can be seen from Fig. 5.3 that the burned gas temperature for $\phi_{ov} = 0.8$ cases is smaller than that in the corresponding $\phi_{ov} = 1.0$ cases due to predominantly fuel-lean combustion. The burned gas temperature for $\phi_{ov} = 1.2$ cases is also found to be marginally smaller than but comparable to that in the corresponding $\phi_{ov} = 1.0$ cases. This can be explained from the Burke-Schumann relation for the burned gas temperature, which indicates that the drop of the burned gas temperature for $\phi_g = 0.8$ is expected to be greater than that in case of $\phi_g = 1.2$. A comparison between Figs. 5.1 and 5.2 reveals that the fuel mass fraction in the unburned gas remains smaller than the corresponding value in the premixed flame case, which indicates that the evaporation of droplets is not sufficient to supply as much fuel in the gaseous phase as in the corresponding premixed flame case. Thus, the gaseous phase combustion in droplet cases takes place mostly under leaner conditions than in the corresponding premixed flame cases.

It can further be seen from Figs. 5.1-5.3 that the laminar premixed flames remain perfectly spherical but laminar spray flames exhibit weakly wrinkled c isosurfaces especially for large droplets (i.e. $a_d/\delta_{st} = 0.06$). This tendency strengthens with increasing ϕ_{ov}. For laminar globally stoichiometric (i.e. $\phi_{ov} = 1.0$) spray flames, flame-droplet interaction can be seen

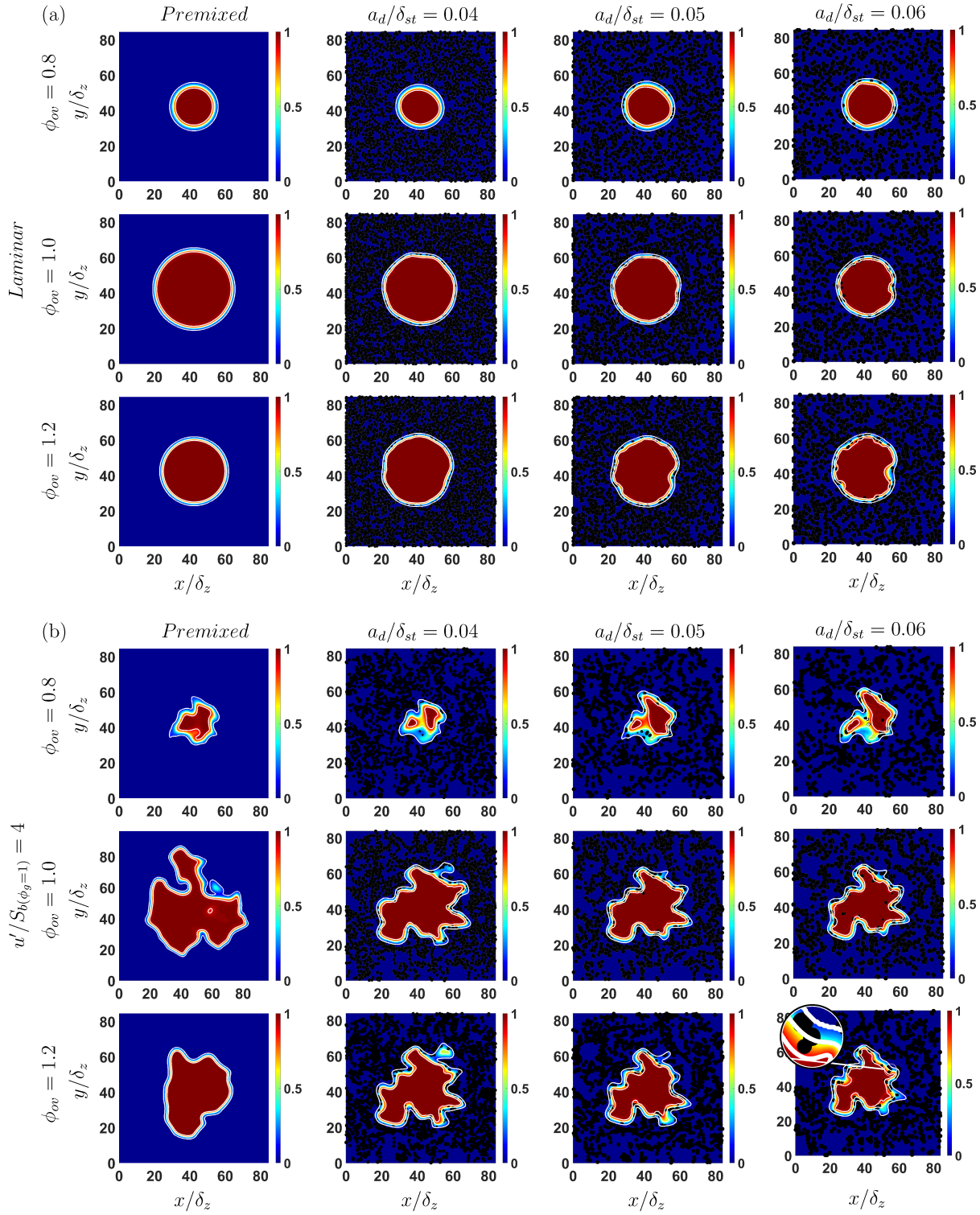

Figure 5.1: Distribution of c (white lines show $c = 0.1, 0.5, 0.9$ contours from outer to inner periphery) on the central $x-y$ mid-plane for laminar (a) and turbulent (b) flames with $\phi_{ov} =$ 0.8, 1.0 and 1.2. Black dots show the droplets residing on the plane (not to scale). All figures correspond to $t = 2.52\alpha_{T_o}/S^2_{b(\phi_g=1)}$.

from imperfectly spherical c isosurfaces. This is prominently evident in the cases with $\phi_{ov} = 1.2$ because of the availability of larger number of droplets. Moreover, it can be discerned from the c contours in Figs. 5.1 and 5.2 that all cases exhibit instances of local flame thickening and this tendency is particularly prevalent for droplet cases especially for $\phi_{ov} = 0.8$. The initial values of Damköhler number for the premixed flames with $\phi_g = 0.8$, 1.0, and 1.2 with initial $u'/S_{b(\phi_g=1)} = 4.0$ are 0.473, 1.31, and 0.93, respectively. The corresponding values of the Karlovitz number are 9.70, 3.50, and 4.85 for $\phi_g = 0.8$, 1.0, and 1.2, respectively. According to the Damköhler and Karlovitz number values for the premixed gaseous flames, combustion take places in the distributed burning regime for all cases considered in this section, and thus they exhibit local flame thickening and these tendencies are particularly strong for droplet cases due to small (large) values of Da (Ka).

5.2 Flame Wrinkling

The flame-droplet interaction can be discerned from Fig. 5.4 where the instantaneous $c = 0.5$ isosurfaces are coloured by local values of flame curvature $\kappa_m \times \delta_{st}$ for the cases considered here. Dimples can be seen from Fig. 5.4 for $a_d/\delta_{st} = 0.05$ and 0.06 droplet cases under laminar conditions for $\phi_{ov} = 0.8$, whereas the $c = 0.5$ isosurface is a smooth sphere in the corresponding premixed flame case. However, the $c = 0.5$ isosurface for the laminar droplet case with initial $a_d/\delta_{st} = 0.04$ for $\phi_{ov} = 0.8$ does not show dimples but also does not remain spherical. A similar qualitative trend is observed for the turbulent droplet cases for $\phi_{ov} = 0.8$ where the droplet-induced flame wrinkling increases with increasing droplet diameter. For $\phi_{ov} = 1.0$ and 1.2, dimples on the $c = 0.5$ isosurface due to flame-droplet interaction can be seen for both laminar and turbulent cases. A comparison between laminar $\phi_{ov} = 1.0$ and $\phi_{ov} = 1.2$ cases reveals that evaporation of clustered droplets creates large distributed dimples for the $\phi_{ov} = 1.2$ cases in contrast to small densely packed dimples in the $\phi_{ov} = 1.0$ cases. This difference is eclipsed by the flow-induced flame wrinkling in turbulent $\phi_{ov} = 1.0$ and 1.2 cases. The droplet-induced flame wrinkling can be quantified in terms of the PDFs of κ_m which are given in Fig. 5.5 for $c = 0.1$,0.5, and 0.9 isosurfaces for all cases considered here. The perfect spherical shape of laminar premixed flames leads to delta functions for the curvature PDFs but laminar droplet cases exhibit a distribution of curvature values, which is indicative of droplet-induced flame wrinkling. The extent of droplet-induced flame wrinkling is the smallest (largest) for the initial droplet size of $a_d/\delta_{st} = 0.04$ ($a_d/\delta_{st} = 0.06$) for $\phi_{ov} = 0.8$ ($\phi_{ov} = 1.2$). The combination of small number density of droplets and rapid evaporation of small droplets gives rise to a weak laminar flame front deformation for $a_d/\delta_{st} = 0.04$ in the case of $\phi_{ov} = 0.8$. The number density of droplets increases with increasing ϕ_{ov} for a given

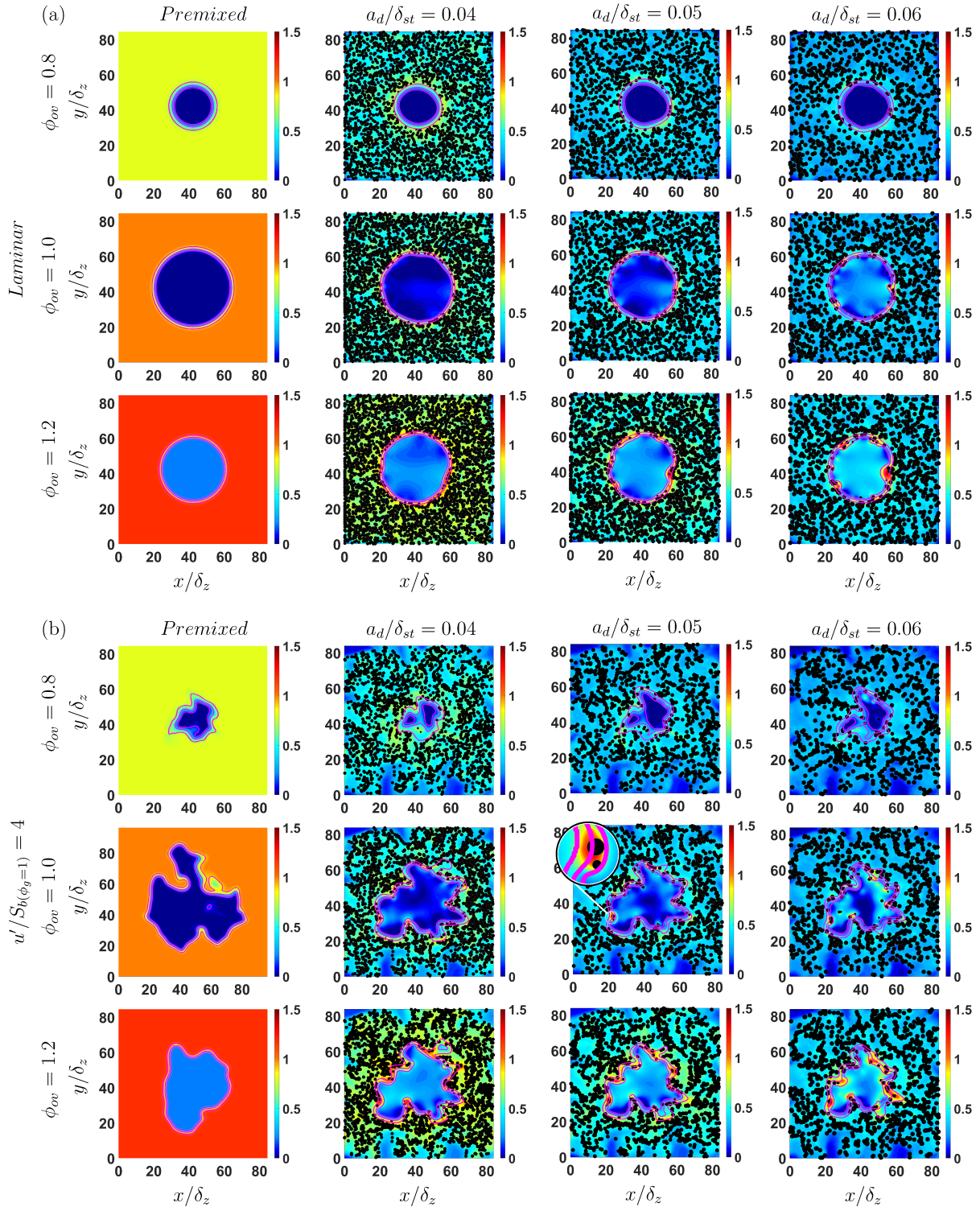

Figure 5.2: Distribution of Y_F/Y_{Fst} (magenta lines show $c = 0.1, 0.5, 0.9$ contours from outer to inner periphery) on the central $x-y$ mid-plane for laminar (a) and turbulent (b) flames with $\phi_{ov} = 0.8$, 1.0 and 1.2. Black dots show the droplets residing on the plane (not to scale). All figures correspond to $t = 2.52\alpha_{T_o}/S^2_{b(\phi_g=1)}$.

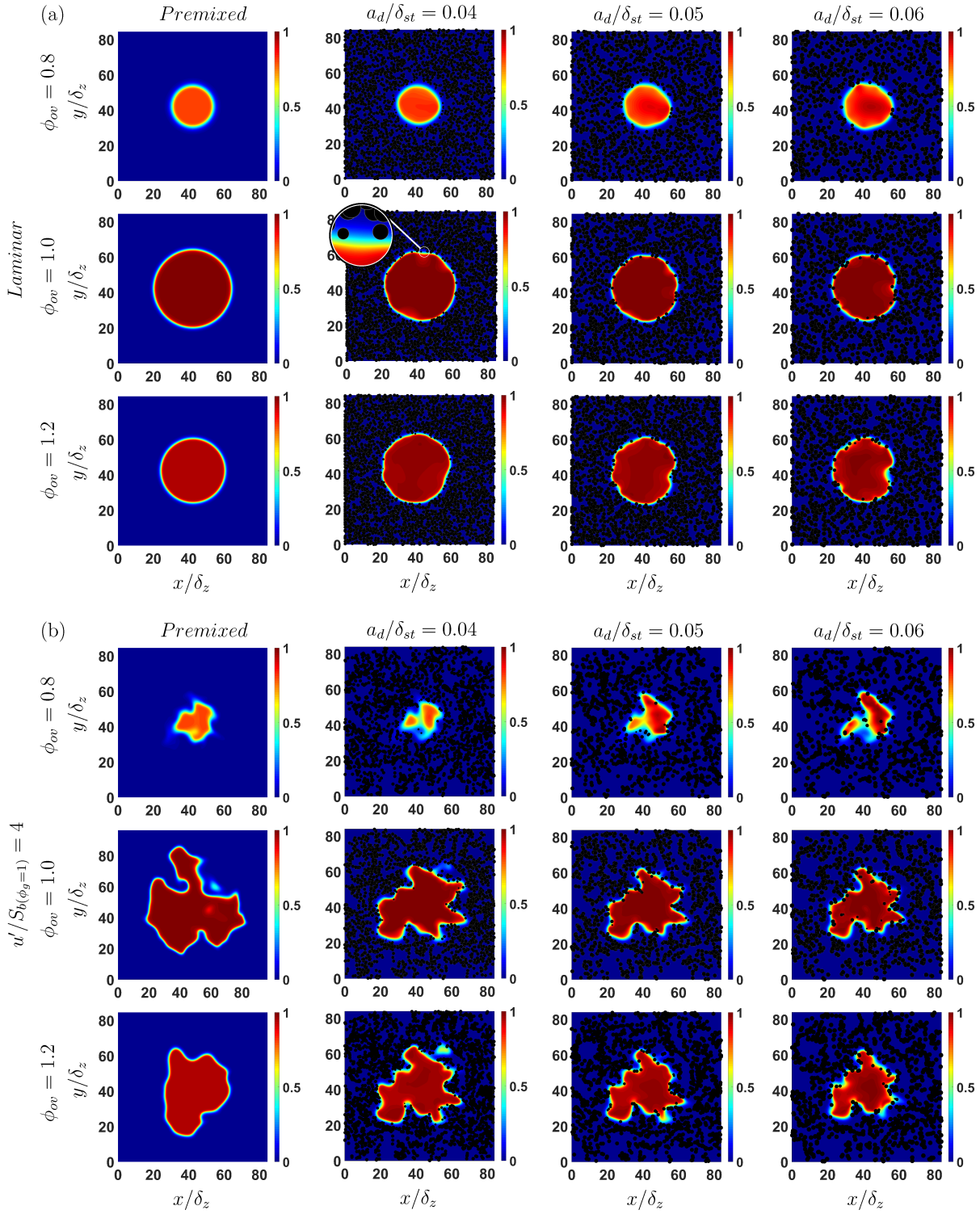

Figure 5.3: Distribution of T on the central $x-y$ mid-plane for laminar (a) and turbulent (b) flames with $\phi_{ov} = 0.8$, 1.0 and 1.2. Black dots show the droplets residing on the plane (not to scale). All figures correspond to $t = 2.52\alpha_{T_o}/S^2_{b(\phi_g=1)}$.

value of a_d/δ_{st} and accordingly the extent of droplet-induced deformation of laminar flame increases with an increase in ϕ_{ov}. This is reflected in the widening of the PDF of $\kappa_m \times \delta_{st}$ with increasing ϕ_{ov} for a given value of a_d/δ_{st} in the laminar droplet cases. The evaporation rate decreases with increasing a_d/δ_{st}, and thus the large droplets survive relatively longer within the flame. Therefore, the laminar flame front deformation is greater in extent for larger values of a_d/δ_{st} for a given value of ϕ_{ov}. This can be substantiated by the narrower PDFs of $\kappa_m \times \delta_{st}$ in droplet cases for smaller values of a_d/δ_{st} for a given value of ϕ_{ov}. The signature of droplet-induced flame wrinkling is less obvious from the curvature PDFs for turbulent flames although the turbulent droplet cases show wider curvature PDFs than in the corresponding turbulent premixed cases for $\phi_{ov} = 1.0$ and 1.2. The PDFs of $\kappa_m \times \delta_{st}$ for the droplet cases with $\phi_{ov} = 0.8$ are comparable to the curvature PDFs for the corresponding turbulent premixed flame case.

The PDFs of $|\overrightarrow{N} \cdot \overrightarrow{r}|$ are shown for $c = 0.1$,0.5 and 0.9 isosurfaces in Fig. 5.6. The PDFs of $|\overrightarrow{N} \cdot \overrightarrow{r}|$ are represented by delta functions at $|\overrightarrow{N} \cdot \overrightarrow{r}| = 1.0$ for laminar premixed flames irrespective of the equivalence ratio values. Although the PDFs of $|\overrightarrow{N} \cdot \overrightarrow{r}|$ for laminar droplet cases show peak values at 1.0, these cases show finite probability of finding $|\overrightarrow{N} \cdot \overrightarrow{r}| < 1.0$ which is an indication of an imperfect spherical shape. A further investigation for laminar spray flames shows that the extent of departure from the perfectly spherical shape increases with the increasing droplet size and also with increasing overall equivalence ratio. The extent of departure from a perfectly spherical shape in turbulent cases is greater than laminar flames for both premixed and droplet cases. The probability of finding a perfectly spherical flame surface (i.e. $|\overrightarrow{N} \cdot \overrightarrow{r}| = 1.0$) in turbulent droplet cases is smaller than the corresponding turbulent premixed flame case for $\phi_{ov} = 1.2$, whereas the probability of finding $|\overrightarrow{N} \cdot \overrightarrow{r}| = 1.0$ is comparable for turbulent premixed and droplet cases for $\phi_{ov} = 0.8$ and 1.0. It has been discussed in the context of Fig. 5.5 that the flame front deformation due to droplets is relatively stronger for $\phi_{ov} = 1.2$ than for $\phi_{ov} = 0.8$ and 1.0. As a result of this, the flow-induced flame deformation does not completely eclipse the droplet-induced wrinkling effects in $\phi_{ov} = 1.2$ droplet cases and some of the effects of flame wrinkling induced by droplets can be discerned for initial $u'/S_{b(\phi_g=1)} = 4.0$, but for this turbulence intensity droplet-induced wrinkling effects are masked by flame wrinkling due to turbulence for $\phi_{ov} = 0.8$ and 1.0. It has been found that the PDFs of $|\overrightarrow{N} \cdot \overrightarrow{r}|$ remain mostly insensitive to the value of a_d/δ_{st} for a given value of ϕ_{ov} in turbulent droplet cases considered here.

The extent of flame wrinkling plays a key role in determining the growth of flame surface area. Figure 5.7a shows the temporal evolutions of flame surface area normalised by its initial value for all cases with different overall equivalence ratios $\phi_{ov} = 0.8$,1.0 and 1.2. The value of A/A_0 decreases with increasing a_d/δ_{st} for the droplet cases with $\phi_{ov} = 1.0$ and 1.2 under both laminar and turbulent flow conditions, but the droplet cases with $\phi_{ov} = 0.8$ behave in

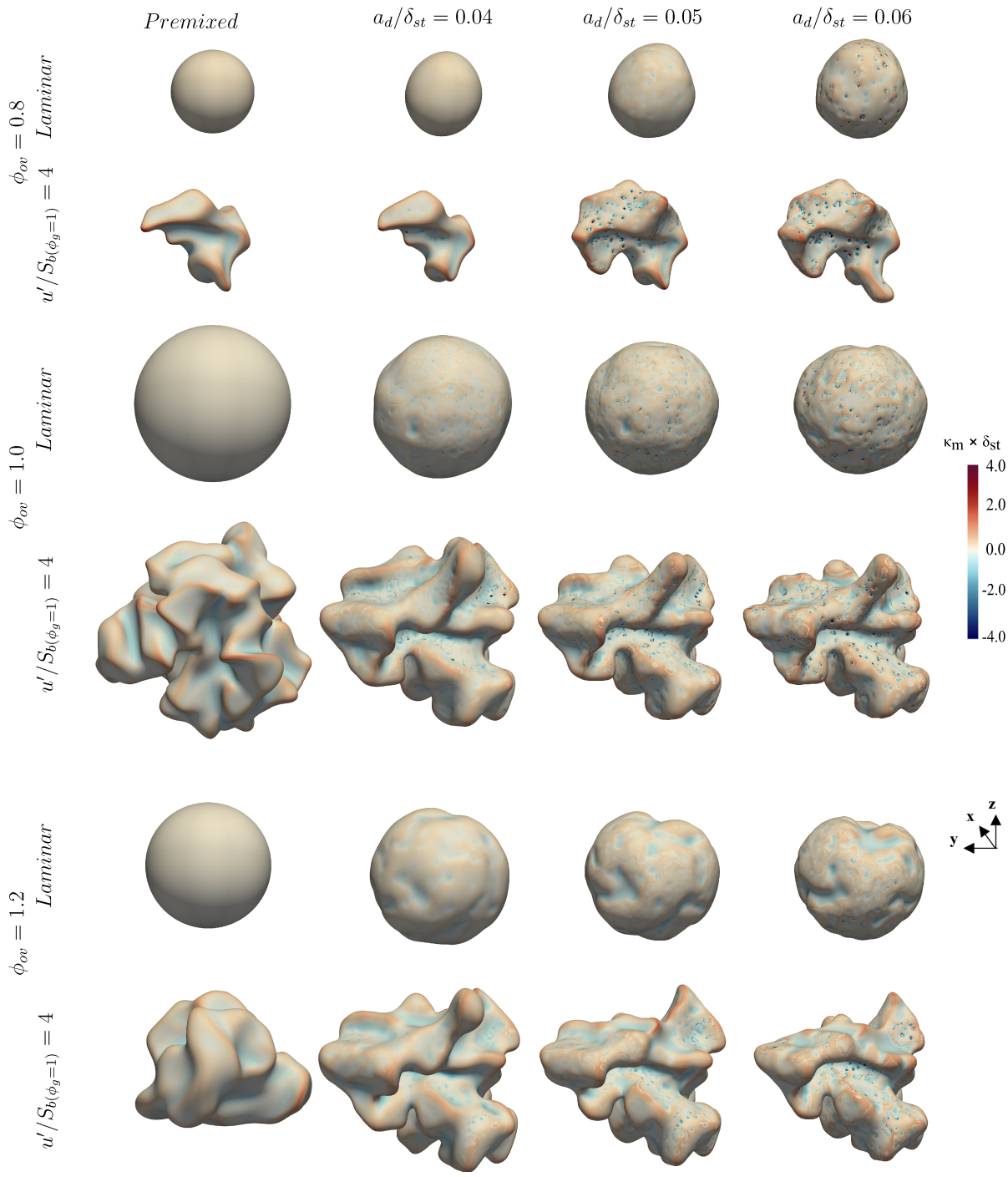

Figure 5.4: Instantaneous view of $c = 0.5$ isosurface coloured with local values of $\kappa_m \times \delta_{st}$ for the cases with $\phi_{ov} = 0.8$ (1^{st} and 2^{nd} rows), $\phi_{ov} = 1.0$ (3^{rd} and 4^{th} rows) and $\phi_{ov} = 1.2$ (5^{th} and 6^{th} rows) at $t = 2.52\alpha_{T_o}/S^2_{b(\phi_g=1)}$.

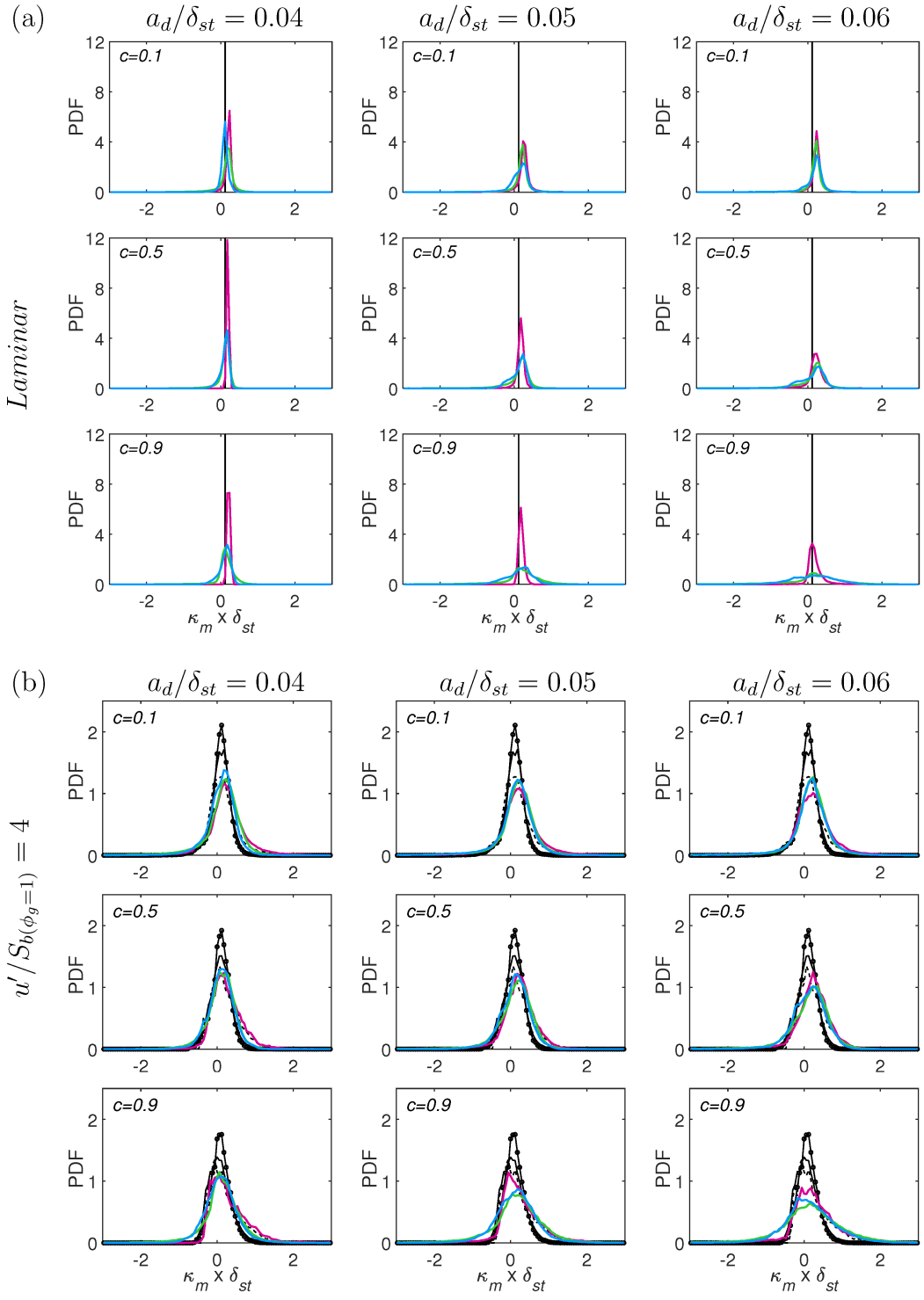

Figure 5.5: PDFs of $\kappa_m \times \delta_{st}$ for $c = 0.1, 0.5$ and 0.9 isosurfaces for the premixed flame with $\phi_{ov} = 0.8$ (- - - -), $\phi_{ov} = 1.0$ (——), $\phi_{ov} = 1.2$ (—o—) and for all droplet cases with initial $\phi_{ov} = 0.8$ (——), $\phi_{ov} = 1.0$ (——), $\phi_{ov} = 1.2$ (——) for laminar (a) and turbulent (b) conditions. Same colour keys are used in Figs. 5.6-5.8,5.10-5.12.

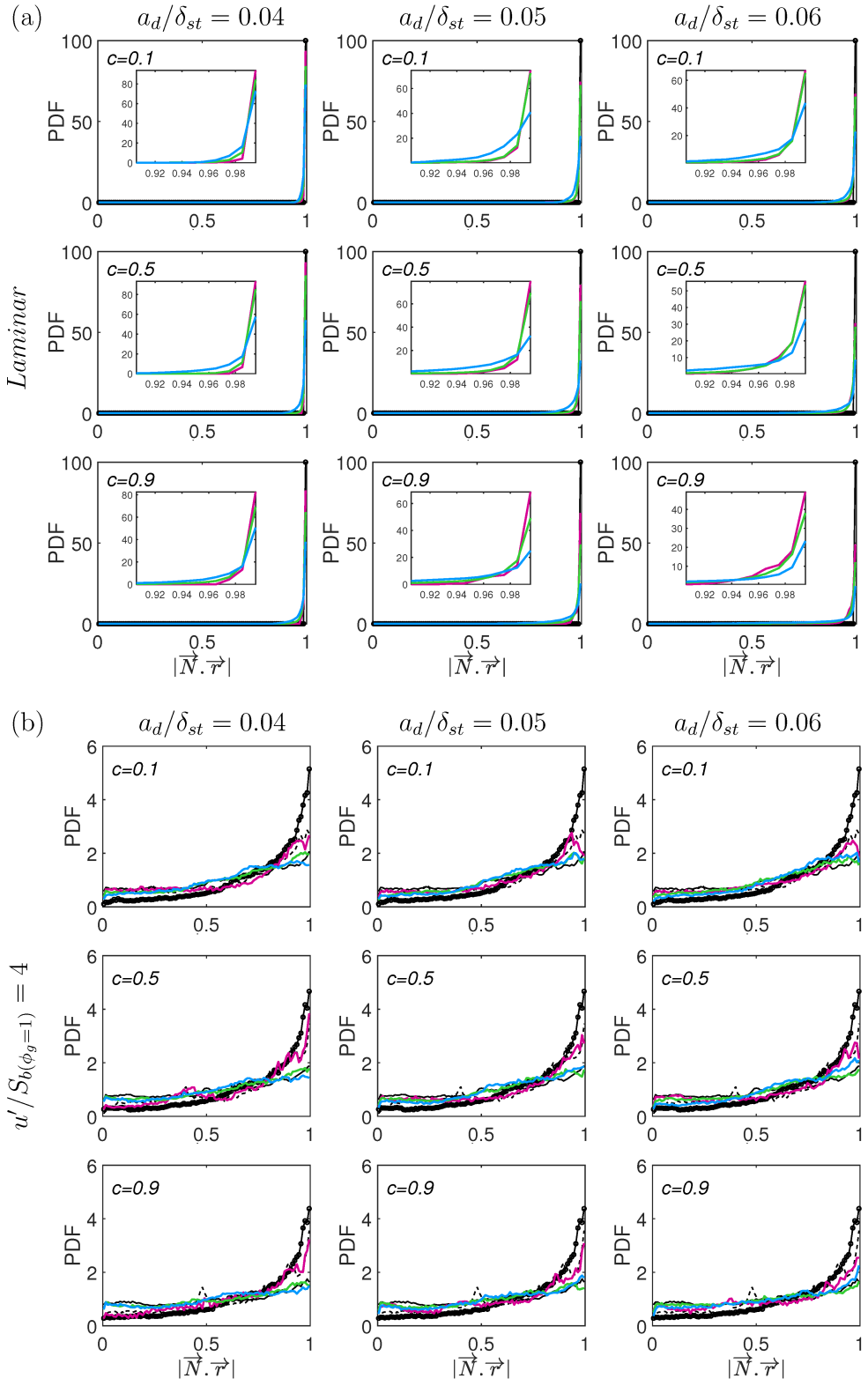

Figure 5.6: PDFs of $|\vec{N}.\vec{r}|$ for $c = 0.1$, 0.5 and 0.9 isosurfaces for laminar (a) and turbulent (b) conditions. See Fig. 5.5 caption for the colour keys.

the opposite manner. Under laminar conditions, A/A_0 in droplet cases increases faster than the corresponding gaseous premixed flame for $\phi_{ov} = 0.8$ and 1.0. By contrast, A/A_0 for the laminar droplet case with initial $a_d/\delta_{st} = 0.04$ remains comparable to that for the corresponding laminar premixed flame for $\phi_{ov} = 1.2$, whereas the growth rates of A/A_0 for the laminar droplet cases with initial $a_d/\delta_{st} = 0.05$ and 0.06 have been found to be smaller than that in the corresponding laminar premixed flame for $\phi_{ov} = 1.2$. Under turbulent condition, A/A_0 values for the droplet cases with initial $a_d/\delta_{st} = 0.05$ and 0.06 have been found to be smaller than the corresponding gaseous premixed flame for $\phi_{ov} = 1.0$ and 1.2, whereas A/A_0 in droplet cases assumes higher values than the corresponding turbulent premixed flame for initial $a_d/\delta_{st} = 0.04$ for $\phi_{ov} = 1.0$ and 1.2, and for all droplet diameters considered here for $\phi_{ov} = 0.8$. The difference in A/A_0 values between droplet and premixed gaseous flames decreases under turbulent conditions for a given set of values of ϕ_{ov} and a_d/δ_{st}. This is consistent with the observations from Figs. 5.5 and 5.6, which indicate that the effects of flame wrinkling due to droplets play a marginal role in determining the overall flame front corrugation and flame area generation under turbulent conditions.

It is important to understand that the initial value of flame surface area A_0 (i.e. $\int_V |\nabla c| dV$) for spherical flames with the burned gas radius $r_0 = 2\delta_{st}$ is not the same for all cases considered here. As the distribution of $|\nabla c|$ (i.e. the magnitude of $|\nabla c|$ and the volume over which $|\nabla c|$ assumes non-zero values) varies from one case to another, the values of A_0 for these cases have been found to be different in spite of having the same burned gas radius $r_0 = 2\delta_{st}$. In order to provide a comparison between the actual flame surface areas of different cases, the temporal evolutions of flame surface area A normalised by the initial value for the stoichiometric laminar premixed flame kernel $(A_{0,pre})_{st}$ (i.e. $A/(A_{0,pre})_{st}$) for all cases considered here are shown in Fig. 5.7b. It can be clearly seen from Fig. 5.7b that $A/(A_{0,pre})_{st}$ for the premixed stoichiometric flame assumes the highest value among the cases considered here under both laminar and turbulent conditions. Figure 5.7b shows that $A/(A_{0,pre})_{st}$ values for the droplet case with initial $a_d/\delta_{st} = 0.04$ are marginally smaller than that in the gaseous premixed flame for $\phi_{ov} = 0.8$ under both laminar and turbulent conditions. This is consistent with the earlier observations from Figs. 5.5 and 5.6, which demonstrated that the flame front distortion for the $\phi_{ov} = 0.8$ droplet case with initial $a_d/\delta_{st} = 0.04$ is comparable to the corresponding premixed flame. However, $A/(A_{0,pre})_{st}$ values for $\phi_{ov} = 0.8$ droplet cases with initial $a_d/\delta_{st} = 0.05$ and 0.06 have been found to be greater than the corresponding premixed flame cases under both laminar and turbulent conditions. The laminar and turbulent droplet cases with $\phi_{ov} = 1.0$ exhibit smaller values of $A/(A_{0,pre})_{st}$ than the corresponding premixed flame cases and the value of $A/(A_{0,pre})_{st}$ decreases with increasing droplet size. In the case of $\phi_{ov} = 1.2$, the laminar and turbulent droplet cases with initial $a_d/\delta_{st} = 0.04$ show greater

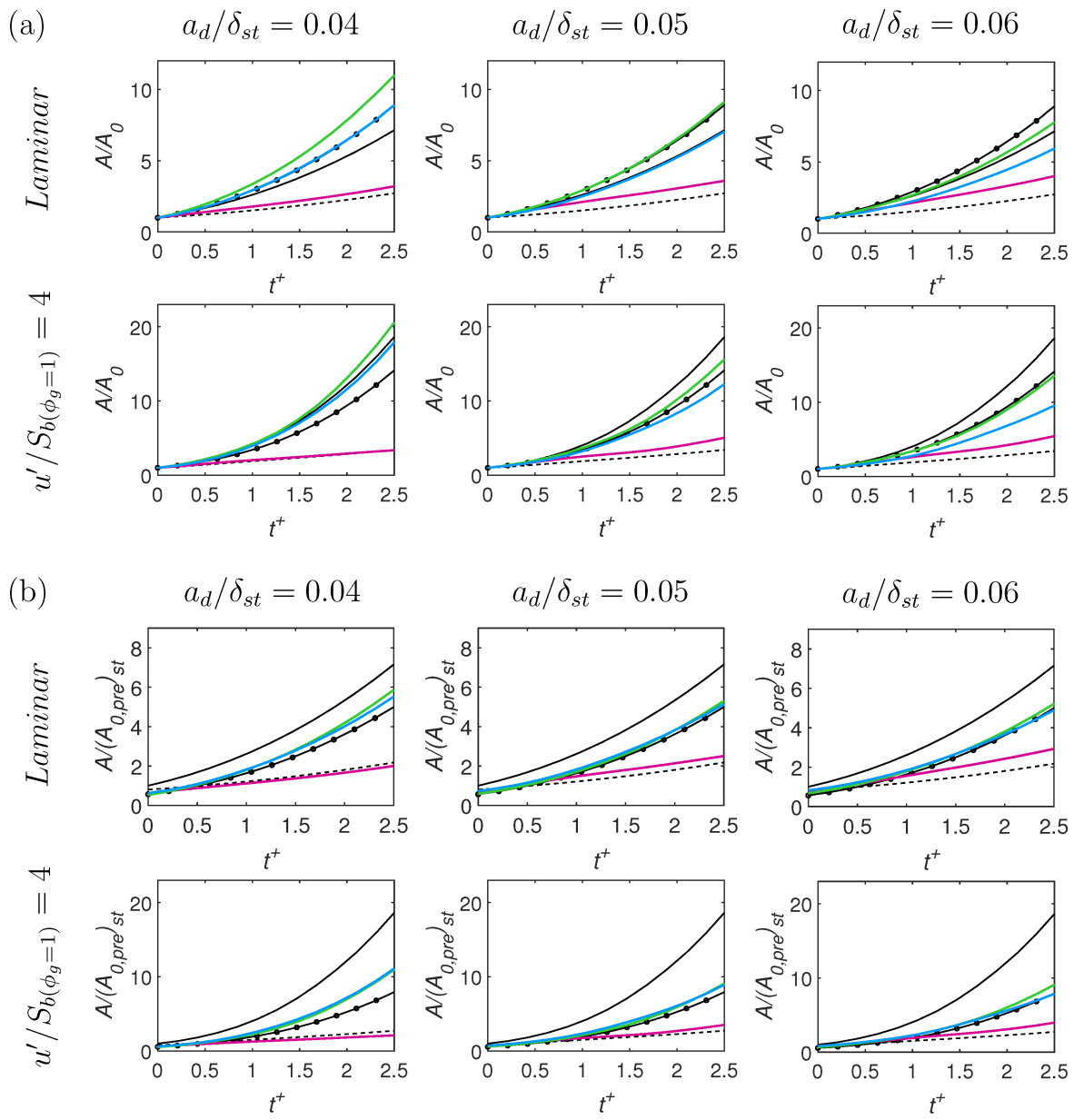

Figure 5.7: (a) Temporal evolution of normalised flame surface area A/A_0; (b) Temporal evolution of flame surface area normalised by initial value of stoichiometric premixed flame $A/(A_{0,pre})_{st}$. See Fig. 5.5 caption for the colour keys.

Table 5.2: Normalised flame speed $S_A/S_{b(\phi_{ov})}$, which quantifies the growth rate of flame surface area A.

	$\phi_{ov} = 0.8$		$\phi_{ov} = 1.0$		$\phi_{ov} = 1.2$	
a_d/δ_{st}	*Laminar*	$u'/S_{b(\phi_g=1)} = 4.0$	*Laminar*	$u'/S_{b(\phi_g=1)} = 4.0$	*Laminar*	$u'/S_{b(\phi_g=1)} = 4.0$
0.04	3.30	3.48	5.46	7.96	6.17	10.12
0.05	3.90	5.30	4.87	6.93	5.60	8.48
0.06	4.57	5.97	4.69	6.78	5.17	7.59
Premixed	3.18	4.10	5.42	10.44	5.83	8.15

value of $A/(A_{0,pre})_{st}$ than the corresponding premixed flames with an equivalence ratio of 1.2. The values of $A/(A_{0,pre})_{st}$ for the laminar and turbulent $\phi_{ov} = 1.2$ droplet cases with initial $a_d/\delta_{st} = 0.05$ and 0.06 have been found to be comparable to the values obtained for the corresponding premixed flames. The $A/(A_{0,pre})_{st}$ values for turbulent flames are greater than the values obtained in the corresponding laminar flames due to flame surface area generation under turbulence.

The variation of flame speed based on the flame surface area, S_A with droplet diameter and overall equivalence ratio is shown in Table 5.2, which indicates that the presence of droplets enhances the normalised flame speed $S_A/S_{b(\phi_{ov})}$ for $\phi_{ov} = 0.8$ except for the initial $a_d/\delta_{st} = 0.04$ case under turbulent conditions. However, for $\phi_{ov} = 1.0$, only the small droplets with initial $a_d/\delta_{st} = 0.04$ under laminar conditions demonstrate higher $S_A/S_{b(\phi_{ov})}$ than the corresponding laminar premixed flame and this tendency is evident for both laminar and turbulent conditions for $\phi_{ov} = 1.2$. Normalised flame speed $S_A/S_{b(\phi_{ov})}$ increases with increasing droplet diameter for $\phi_{ov} = 0.8$, whereas it shows just the opposite trend for $\phi_{ov} = 1.0$ and 1.2. These findings are consistent with the observations made from Fig. 5.7, but Table 5.2 provides quantitative measure of the effects of ϕ_{ov} and a_d on the flame surface area evolution in spherically expanding turbulent spray flames.

It is instructive to look into the statistical behaviours of the equivalence ratio in the gaseous phase ϕ_g and the magnitude of reaction progress variable gradient $|\nabla c|$ in order to explain the $A/(A_{0,pre})_{st}$ and $S_A/S_{b(\phi_{ov})}$ behaviours shown in Fig. 5.7 and Table 5.2, respectively.

5.3 Reaction Zone Structure

The PDFs of gaseous phase equivalence ratio ϕ_g within the region given by $0.01 \leq c \leq 0.99$ for all cases considered here are shown in Fig. 5.8. Although a peak of the ϕ_g-PDF can be discerned at $\phi_g \approx \phi_{ov}$ in Fig. 5.8, there is a significant probability of finding fuel-air mixtures with $\phi_g < \phi_{ov}$ and $\phi_g > \phi_{ov}$. However, the probability of finding $\phi_g < \phi_{ov}$ supersedes the

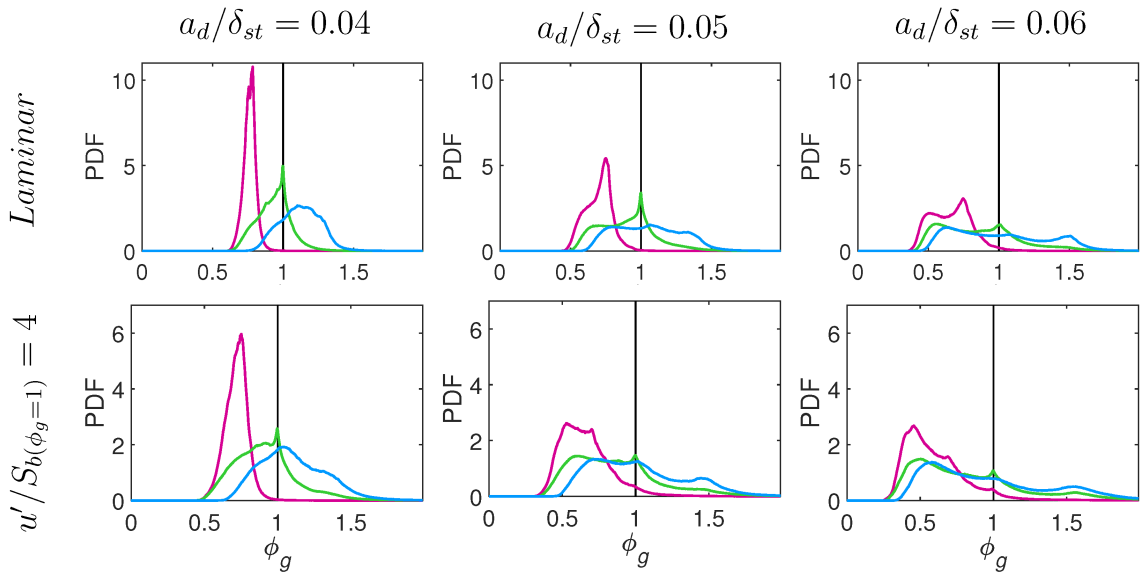

Figure 5.8: PDF of ϕ_g in the region corresponding to $0.01 \leq c \leq 0.99$. See Fig. 5.5 caption for the colour keys.

probability of obtaining $\phi_g > \phi_{ov}$ for all values of ϕ_{ov} and a_d/δ_{st}, which is consistent with the observations made from Fig. 5.2. The evaporation rate is slower for larger droplets, and thus the probability of finding $\phi_g < \phi_{ov}$ increases with increasing a_d/δ_{st}. Moreover, evaporation of droplets produce localised fuel-rich pockets, which are more frequent for larger droplets due to slower evaporation. Thus, the width of the PDF increases with increasing droplet diameter for both laminar and turbulent cases. In turbulent flows, the evaporated fuel is transported to the locations far from the evaporation sites by the dispersion process due to turbulent fluid motion, and this increases the probability of finding $\phi_g < \phi_{ov}$ in turbulent droplet cases. It can especially be seen from Fig. 5.8 that combustion takes place predominantly in fuel-lean mode for the turbulent cases for all values of ϕ_{ov} and a_d/δ_{st} considered here.

It can be seen from Fig. 5.8 that a mild peak of the ϕ_g-PDF is obtained at $\phi_g = 1.0$ for $\phi_{ov} = 1.0$ and 1.2 cases. This can be explained in terms of the mode of combustion, which can be characterised by the flame index FI [94].The percentages of heat release rate arising from the premixed and non-premixed modes of combustion are shown in Fig. 5.9 for laminar and turbulent droplet cases. For laminar $\phi_{ov} = 0.8$ droplet cases, the total heat release rate arises due to the premixed mode of combustion. For laminar $\phi_{ov} = 1.0$ and 1.2 droplet cases, heat release rate arises also predominantly due to the premixed mode of combustion but a non-negligible percentage of total heat release rate is obtained from the non-premixed mode of combustion. The contribution of the non-premixed mode of combustion to the overall heat release drops with increasing droplet diameter. Moreover, the contribution of the non-premixed

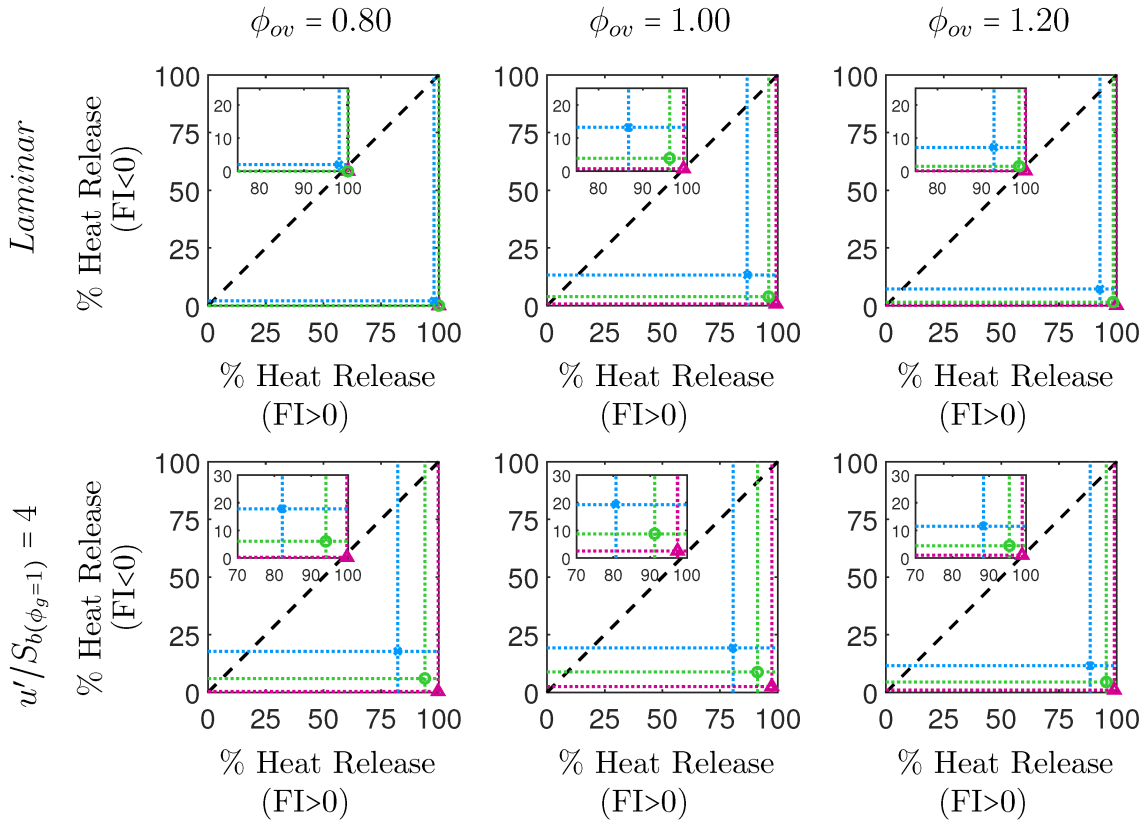

Figure 5.9: Percentage of heat release arising from premixed ($FI > 0$) and non-premixed ($FI < 0$) modes of combustion for all droplet cases with initial $a_d/\delta_{st} = 0.04$ (△), 0.05 (◯), 0.06 (×).

mode of combustion is relatively smaller in the laminar $\phi_{ov} = 1.2$ case than in the laminar $\phi_{ov} = 1.0$ case. The slower evaporation of droplets induces greater mixture inhomogeneity for cases with larger droplets, which eventually gives rise to a greater extent of non-premixed combustion contribution to the overall heat release. The non-premixed flame is formed at the stoichiometric mixture (i.e. $\phi_g = 1.0$) and the likelihood of obtaining $\phi_g = 1.0$ is greater in the laminar $\phi_{ov} = 1.0$ case than in the laminar $\phi_{ov} = 1.2$ case (see Fig. 5.8). Thus, the percentage contribution of non-premixed combustion to the total heat release rate is greater in the $\phi_{ov} = 1.0$ cases than in the $\phi_{ov} = 1.2$ cases.

The total heat release rate arises due to the premixed mode of combustion for the $\phi_{ov} = 0.8$ droplet case for small droplets with initial $a_d/\delta_{st} = 0.04$. However, a non-negligible contribution to the overall heat release rate in the $\phi_{ov} = 0.8$ droplet cases comes from the non-premixed mode of combustion for droplet diameters with initial $a_d/\delta_{st} = 0.05$ and 0.06. Droplets with $\phi_{ov} = 0.8$ mostly complete their evaporation on the unburned gas side (see Fig. 5.2) and create fuel-lean mixture ahead of the flame under laminar flow conditions. However, under turbulent

conditions, some droplets penetrate into the burned gas side without complete evaporation, where they evaporate relatively readily and create unburned fuel pockets. The evaporated fuel vapour diffuses back from the burned gas side and mixes with the excess unused air to form the pockets of stoichiometric mixture where non-premixed flame can be obtained. Turbulence promotes and increases the contribution of a non-premixed combustion for the droplet cases with $\phi_{ov} = 1.0$ and 1.2. The turbulent fluid motion disperses evaporated fuel from the droplet sites to the surrounding gaseous mixture, which increases the mixing rate between the evaporated fuel and the surrounding air and the probability to obtain locally stoichiometric mixture to support non-premixed combustion.

The distributions of ϕ_g and c determine the statistical behaviours of $|\nabla c|$ as the flame thickness $\delta_{(\phi_g)}$ scales as: $\delta_{(\phi_g)} \sim (1/(max|\nabla c|_L)) \sim \alpha_{T0}/S_{b(\phi_g)}$. While the laminar burning velocity $S_{b(\phi_g)}$ attains its maximum value (i.e. a value slightly greater than $S_{b(\phi_g=1)}$) for $\phi_g \approx 1.10$ for the present thermo-chemistry [75], it can be expected that the flame thickness is greater than the stoichiometric premixed flame for $\phi_g < 1$ and $\phi_g \gg 1.10$. Thus, $|\nabla c|$ distribution with c (e.g. the value of $max|\nabla c|_L$ and the value of c at which this maximum value is obtained) is expected to be different depending on ϕ_g. The PDFs of $|\nabla c| \times \delta_{st}$ for $c = 0.1$,0.5, and 0.9 isosurfaces for all laminar and turbulent cases are shown in Figs. 5.10a and 5.10b, respectively. It can be seen from Fig. 5.10a that the droplet cases with $\phi_{ov} = 0.8$ show greater values of $|\nabla c|$ than the corresponding premixed flame. The laminar $\phi_{ov} = 1.0$ and 1.2 droplet cases with initial $a_d/\delta_{st} = 0.04$ show higher probability of finding greater values of $|\nabla c|$ than that in the corresponding premixed cases. A similar qualitative trend has been observed for $c = 0.1$ and 0.9 in the laminar $\phi_{ov} = 1.0$ droplet case with initial $a_d/\delta_{st} = 0.05$. The likelihood of having both greater and smaller values of $|\nabla c|$ than that in the corresponding premixed case is almost the same at $c = 0.5$ in the $\phi_{ov} = 1.0$ and 1.2 laminar droplet cases with initial $a_d/\delta_{st} = 0.05$. By contrast, $|\nabla c|$ for the laminar $\phi_{ov} = 1.0$ and 1.2 droplet cases with initial $a_d/\delta_{st} = 0.06$ assumes smaller values than that in the corresponding premixed flame case for $c = 0.5$ and 0.9 but the converse is true for $c = 0.1$. It can be seen from Fig. 5.10b that the turbulent droplet cases with $\phi_{ov} = 1.0$ and 1.2 exhibit greater likelihood of smaller magnitudes of $|\nabla c|$ than the corresponding premixed turbulent flames and this tendency becomes more prevalent for larger droplet diameters due to the predominant availability of fuel-lean mixtures as a result of slower evaporation of droplets. However, the PDFs of $|\nabla c|$ for the turbulent $\phi_{ov} = 0.8$ droplet cases with initial $a_d/\delta_{st} = 0.04$ are comparable to the corresponding premixed flame, and this remains valid for $c = 0.1$ in the cases with initial $a_d/\delta_{st} = 0.05$ and 0.06. The $\phi_{ov} = 0.8$ droplet cases with initial $a_d/\delta_{st} = 0.05$ and 0.06 exhibit wider PDFs for $c = 0.5$ and 0.9 with greater likelihood of obtaining greater values of $|\nabla c|$ than the corresponding premixed flame cases.

The integral, which yields the flame surface area, A is influenced by the magnitude of

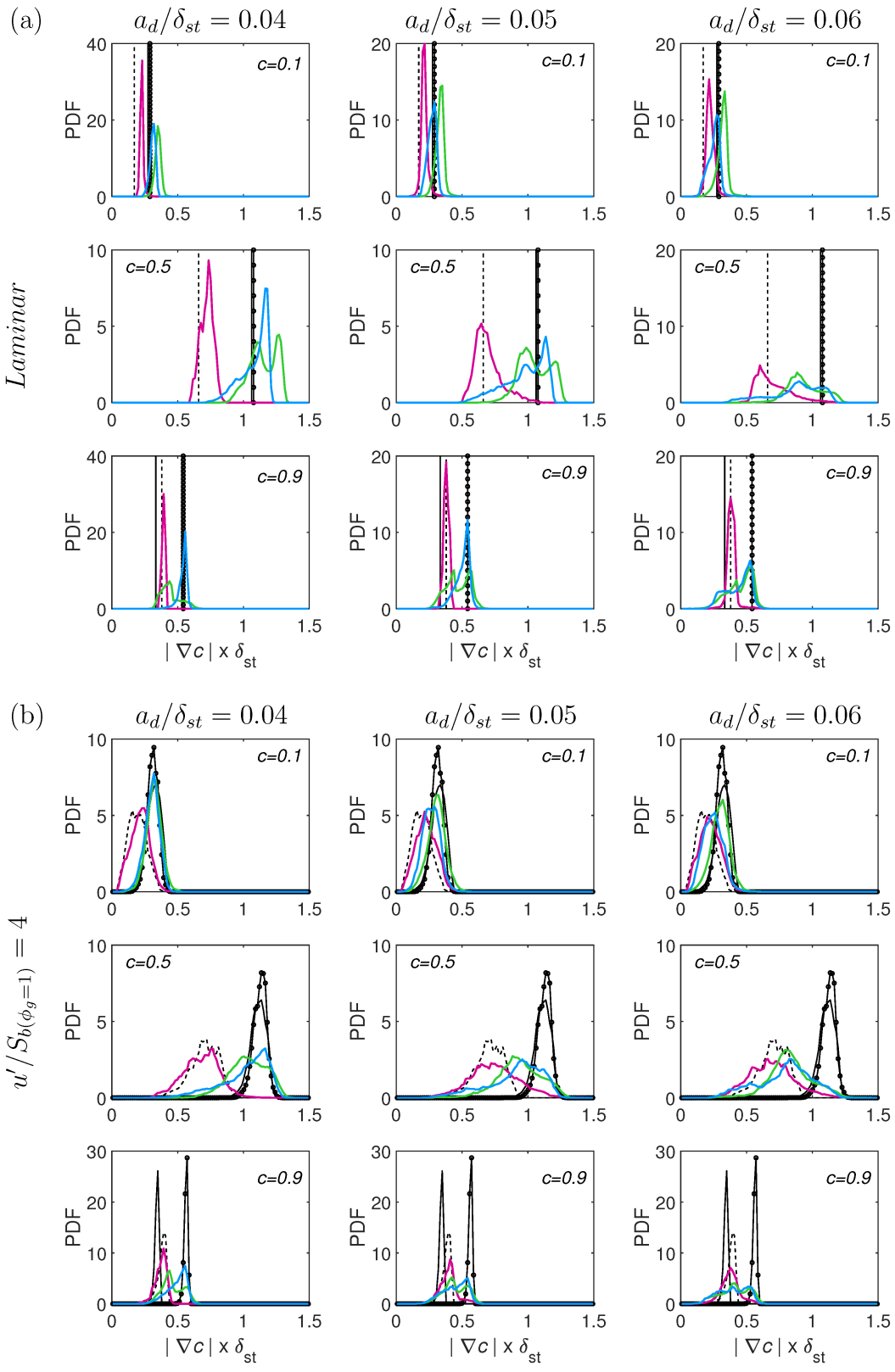

Figure 5.10: PDFs of $|\nabla c| \times \delta_{st}$ on $c = 0.1$, 0.5 and 0.9 isosurfaces under laminar (a) and turbulent (b) conditions. See Fig. 5.5 caption for the colour keys.

$|\nabla c|$ and the volume over which $|\nabla c|$ assumes non-zero values. For $\phi_{ov} = 0.8$, mostly higher magnitudes of $|\nabla c|$ of the droplet cases with initial $a_d/\delta_{st} = 0.05$ and 0.06 are responsible for yielding greater values of flame surface area A than in the corresponding premixed flames. However, the smaller volume of the region where large magnitudes of $|\nabla c|$ are obtained in the $\phi_{ov} = 0.8$ droplet case with initial $a_d/\delta_{st} = 0.04$ is responsible for yielding slightly smaller value of flame surface area A than that in the corresponding premixed flames.

The predominance of smaller magnitudes of $|\nabla c|$ in the laminar $\phi_{ov} = 1.0$ droplet cases with initial $a_d/\delta_{st} = 0.05$ and 0.06 in comparison to those of the corresponding premixed case are principally responsible for yielding smaller values of A_0 than $A_{0,pre}$ in spite of all cases having same initial burned gas radius (i.e. $r_0 = 2\delta_{st}$). Figures 5.10a and b show that the $\phi_{ov} = 1.0$ droplet cases exhibit greater probability of finding small values of $|\nabla c|$ than the corresponding premixed flame cases except for the laminar droplet flame case with $a_d/\delta_{st} = 0.04$, and the probability of finding smaller values of $|\nabla c|$ is greater for initial $a_d/\delta_{st} = 0.06$ droplet cases than in the cases with initial $a_d/\delta_{st} = 0.05$. This along with smaller volume over which $|\nabla c|$ assumes non-zero values (see Fig. 5.1 for the region with $0.01 \leq c \leq 0.99$) gives rise to smaller $A/(A_{0,pre})_{st}$ in the $\phi_{ov} = 1.0$ droplet cases with $a_d/\delta_{st} = 0.05$ and 0.06 in comparison to the corresponding premixed case. Thicker flame (i.e. larger flame volume) in the $\phi_{ov} = 1.0$ laminar droplet cases with initial $a_d/\delta_{st} = 0.05$ and 0.06 in comparison to the corresponding droplet case with initial $a_d/\delta_{st} = 0.04$ gives rise to greater values of A_0 for larger droplet diameters in spite of higher probability of obtaining smaller values of $|\nabla c|$ and identical values of r_0. In the $\phi_{ov} = 1.0$ laminar droplet cases with initial $a_d/\delta_{st} = 0.05$ and 0.06, the smaller magnitude of $|\nabla c|$ is principally responsible for yielding smaller value of A_0 than $(A_{0,pre})_{st}$ in spite of all cases having same initial burned gas radius $r_0 = 2\delta_{st}$. Although the probability of finding smaller values of $|\nabla c|$ in the $\phi_{ov} = 1.2$ droplet cases with initial $a_d/\delta_{st} = 0.05$ and 0.06 is greater than the corresponding premixed flame cases, the thicker droplet flames yield flame surface areas A, which are comparable to the values obtained for the $\phi_{ov} = 1.2$ premixed flame cases subjected to similar flow conditions. Higher probability of finding greater values of $|\nabla c|$ in the $\phi_{ov} = 1.2$ droplet cases with $a_d/\delta_{st} = 0.04$ than that in the corresponding premixed cases is principally responsible for giving rise to greater values of A than in the corresponding premixed flame cases.

The probability of finding local high values of $|\nabla c|$ is greater in turbulent cases than in the corresponding laminar case for both droplet and premixed flames, which is consistent with higher values of $A/(A_{0,pre})_{st}$ in turbulent flames. It can be seen from Fig. 5.10 that the probability of finding greater magnitude of $|\nabla c|$ increases with increasing a_d for droplet cases for $\phi_{ov} = 0.8$ because of the greater availability of more reactive mixture than $\phi_g \leq 0.8$ (see Fig. 5.8). This is principally responsible for an increase in flame surface area with increasing

droplet diameter for $\phi_{ov} = 0.8$. By contrast, slower evaporation of larger droplets for $\phi_g = 1.0$ and 1.2 gives rise to higher probability of fuel-lean mixtures and smaller magnitudes of $|\nabla c|$. This in turn is principally responsible for a decrease in flame surface area with increasing droplet diameter for $\phi_g = 1.0$ and 1.2.

5.4 Extent of Burning

The effects of ϕ_{ov} and a_d on evaporation characteristics affect not only the mixture composition in the gaseous phase and flame surface area but also influences the extent of burning. This can be substantiated from Fig. 5.11a where the temporal evolutions of the volume-integrated fuel reaction rate magnitude $\Omega_F = \int_V |\dot{w}_F| dV$ normalised by its initial value (i.e. $\Omega_F/\Omega_{F0} = \int_V |\dot{w}_F| dV / \left[\int_V |\dot{w}_F| dV\right]_{t=0}$) are shown for all cases considered here. It can be seen from Fig. 5.11a that Ω_F/Ω_{F0} increases rapidly with time for all cases considered here. The $\phi_{ov} = 0.8$ droplet cases exhibit smaller values of Ω_F/Ω_{F0} than in the corresponding fuel-lean premixed flames for both laminar and turbulent conditions. The value of Ω_F/Ω_{F0} decreases with increasing droplet diameter under both laminar and turbulent conditions for $\phi_{ov} = 1.0$. However, Ω_F/Ω_{F0} in the laminar $\phi_{ov} = 1.0$ droplet cases has been found to be greater than in the corresponding premixed flame, whereas Ω_F/Ω_{F0} values for turbulent droplet cases have been found to be smaller than the corresponding premixed flames. The values of Ω_F/Ω_{F0} increase with decreasing droplet size for $\phi_{ov} = 1.2$ and Ω_F/Ω_{F0} values for droplet cases remain smaller than the corresponding premixed flames under both laminar and turbulent conditions except for the cases with initial $a_d/\delta_{st} = 0.04$. Since initial values of volume integrated fuel reaction rate Ω_{F0} are different for all cases, the temporal evolutions of $\Omega_F/\left(\Omega_{F0,pre}\right)_{st}$ are presented in Fig. 5.11b to gain a better understanding of the relative magnitudes of Ω_F. It can be seen from Fig. 5.11b that $\Omega_F/\left(\Omega_{F0,pre}\right)_{st}$ for all the $\phi_{ov} = 1.0$ droplet cases is smaller than the corresponding stoichiometric premixed flames. The presence of droplets enhances the value of $\Omega_F/\left(\Omega_{F0,pre}\right)_{st}$ in comparison to premixed flame for $\phi_{ov} = 0.8$ in the droplet cases with initial $a_d/\delta_{st} = 0.05$ and 0.06 for both laminar and turbulent conditions, but the values of $\Omega_F/\left(\Omega_{F0,pre}\right)_{st}$ for the droplet case with initial $a_d/\delta_{st} = 0.04$ have been found to be comparable to the values obtained for the corresponding premixed flames. The enhancement of $\Omega_F/\left(\Omega_{F0,pre}\right)_{st}$ due to droplets for $\phi_{ov} = 1.2$ has been found for both laminar and turbulent cases with $a_d/\delta_{st} = 0.04$, but just the opposite trend is observed for the droplet cases with initial $a_d/\delta_{st} = 0.05$ and 0.06.

The dependences of $\Omega_F/\left(\Omega_{F0,pre}\right)_{st}$ on ϕ_{ov} and a_d are determined by their influences on flame surface area and the volume-integrated reaction rate of progress variable to the flame surface area. The influences of ϕ_{ov} and a_d on flame surface area A have already been shown

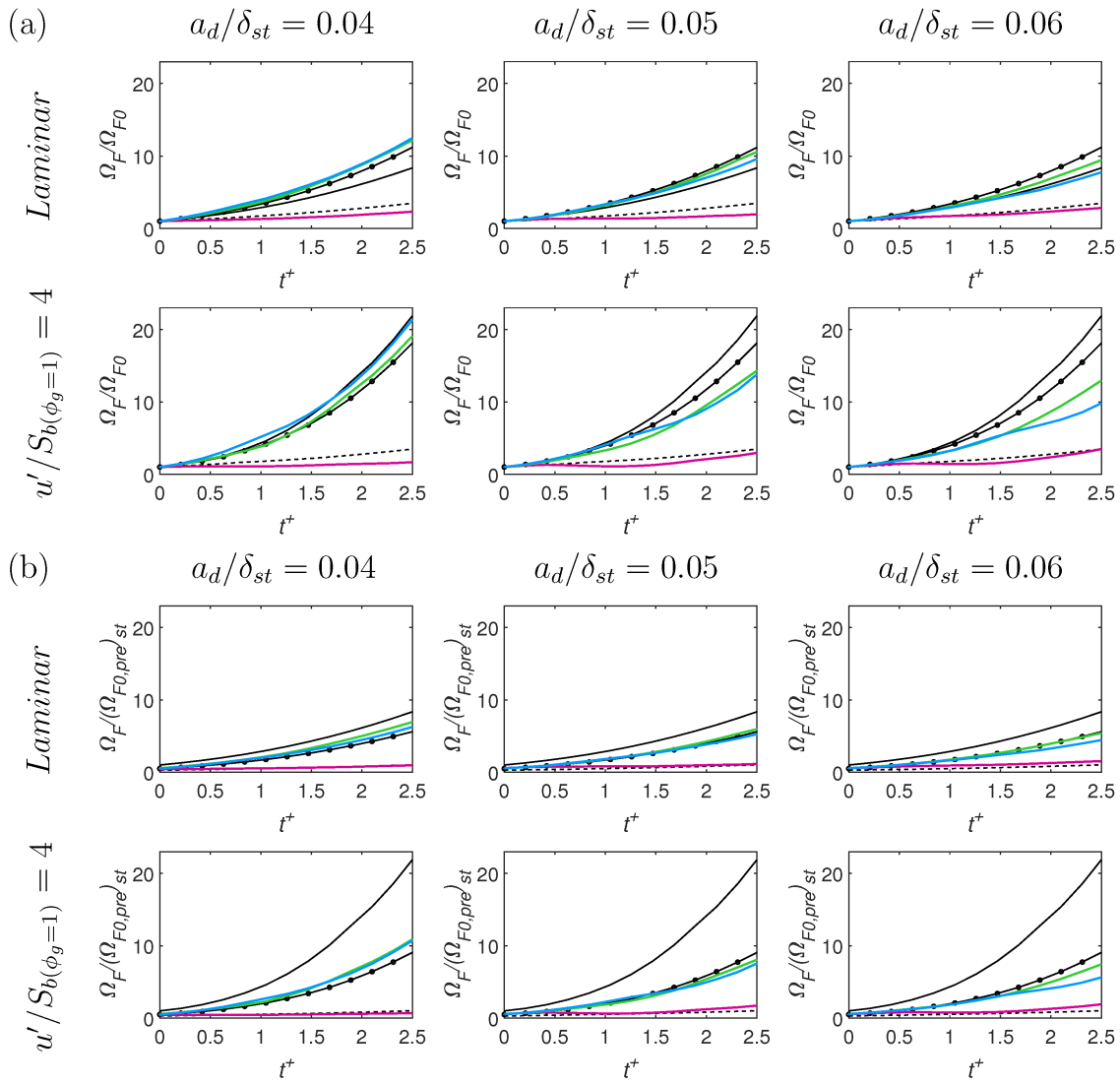

Figure 5.11: Temporal evolutions of (a) volume integrated fuel reaction rate magnitude normalised by its initial value Ω_F/Ω_{F0}; (b) volume integrated fuel reaction rate magnitude normalised by Ω_{F0} value (i.e. $\Omega_F/\left(\Omega_{F0,pre}\right)_{st}$) for the stoichiometric laminar premixed flame. See Fig. 5.5 caption for the colour keys.

in Fig. 5.7b and thus the temporal evolutions of the volume-integrated reaction rate of progress variable to the flame surface area $S = \left[\rho_0 S_{b(\phi_g)}\right]^{-1} \int_V \dot{w}_c dV / \int_V |\nabla c| dV$ for all cases considered here are shown in Fig. 5.12a. In all cases S deviates from unity due to the stretch rate induced by mean positive curvature of statistically spherical flames, which has been discussed elsewhere [57, 60] and will not be elaborated here. Figure 5.12a shows that S for the droplet cases assumes greater values than the corresponding premixed flames for $\phi_{ov} = 0.8$ and the values of S for droplet cases with initial $a_d/\delta_{st} = 0.05$ and 0.06 are found to be greater than the cases with initial $a_d/\delta_{st} = 0.04$. The possibility of obtaining more reactive (i.e. $\phi_g > \phi_{ov} = 0.8$) fuel-air mixtures is relatively greater for the cases with initial $a_d/\delta_{st} = 0.05$ and 0.06 than in the cases with initial $a_d/\delta_{st} = 0.04$ (see Fig. 5.8) and this contributes to the higher values of the volume-integrated reaction rate of progress variable per unit flame surface area for the cases with initial $a_d/\delta_{st} = 0.05$ and 0.06. For $\phi_{ov} = 1.0$ and 1.2, the values of S for the initial $a_d/\delta_{st} = 0.04$ cases remain comparable to that in the corresponding premixed flames but S decreases with increasing initial droplet size. The probability of finding less reactive fuel-lean mixture for $\phi_{ov} = 1.0$ and 1.2 droplet cases increases with increasing a_d/δ_{st} due to slower evaporation of larger droplets. This contributes to the smaller values of S in the $\phi_{ov} = 1.0$ and 1.2 droplet cases and also decreasing trend of S with increasing a_d/δ_{st}.

The combined influences of ϕ_{ov} and a_d/δ_{st} on A and S ultimately determine the extent of burning which can be quantified in terms of the volume of the burned gas with $c \geq 0.99$ (i.e. V_b). The temporal evolution of the normalised burned gas volume $V_b/(4\pi r_0^3/3)$ for all cases considered here is shown in Fig. 5.12b. The combination of the larger values of A and S than the premixed flame for $\phi_{ov} = 0.8$ gives rise to an increase in the burned gas volume in comparison to the corresponding premixed flame for the droplet cases with initial $a_d/\delta_{st} = 0.05$ and 0.06. The burned gas volume for the $\phi_{ov} = 0.8$ droplet cases with initial $a_d/\delta_{st} = 0.04$ remains comparable to the corresponding premixed flame cases. The smaller values of S and A yield smaller burned gas volume in the $\phi_{ov} = 1.0$ and 1.2 droplet cases with initial $a_d/\delta_{st} = 0.05$ and 0.06 in comparison to that in the corresponding premixed flames. The smaller value of S in the $\phi_{ov} = 1.0$ droplet cases with initial $a_d/\delta_{st} = 0.04$ than in the corresponding premixed flames dominates over greater flame surface area for the droplet cases to yield a smaller burned gas volume in comparison to that in the premixed flame cases. The combination of the larger values of A and S in the laminar $\phi_{ov} = 1.2$ droplet case with initial $a_d/\delta_{st} = 0.04$ than the corresponding laminar premixed flame gives rise to an increase in burned gas volume in comparison to the corresponding premixed flame for the droplet cases. Thus, the burned gas volume drops with increasing a_d/δ_{st} for $\phi_{ov} = 1.0$ and 1.2. It can be seen from Fig. 5.12b that the largest burned gas volume is obtained for the stoichiometric premixed flame case for both laminar and turbulent conditions analysed in this section. Moreover, it can be seen from Fig.

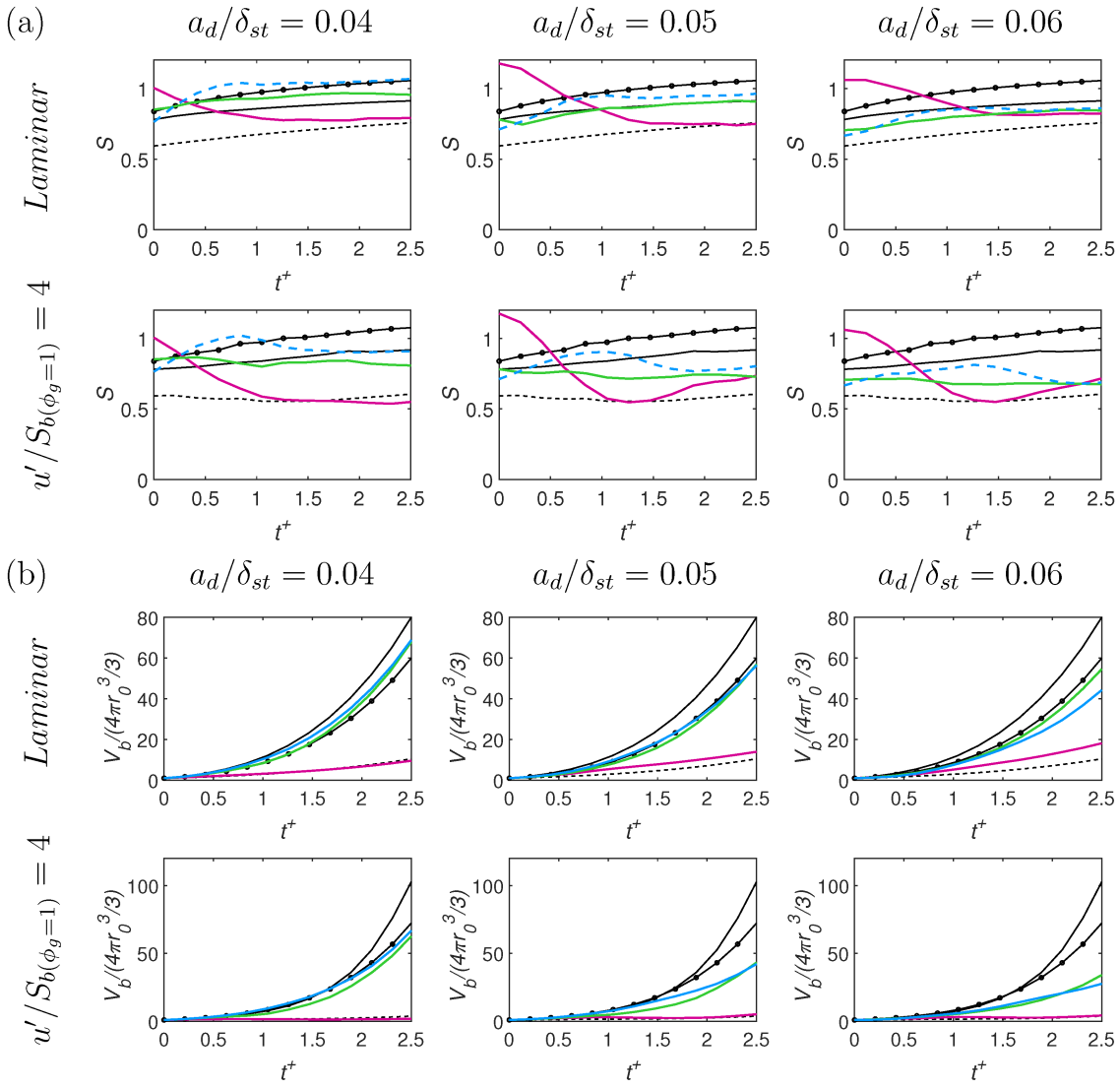

Figure 5.12: Temporal evolutions of (a) the ratio of volume-integrated product formation rate to the flame surface area S and (b) normalised volume $V_b/(4\pi r_0^3/3)$ of the region with $c \leq 0.99$. See Fig. 5.5 caption for the colour keys.

Table 5.3: Normalized flame speed $S_V/S_{b(\phi_{ov})}$, which quantifies the growth rate of the burned gas volume V_b.

	$\phi_{ov} = 0.8$		$\phi_{ov} = 1.0$		$\phi_{ov} = 1.2$	
a_d/δ_{st}	*Laminar*	$u'/S_{b(\phi_g=1)} = 4.0$	*Laminar*	$u'/S_{b(\phi_g=1)} = 4.0$	*Laminar*	$u'/S_{b(\phi_g=1)} = 4.0$
0.04	3.03	1.03	5.34	5.70	6.43	6.63
0.05	2.97	3.45	4.90	4.34	5.81	5.00
0.06	4.07	2.10	4.91	3.73	5.21	4.14
Premixed	3.55	2.32	5.50	6.63	6.25	7.28

5.12b that the burned gas volume increases under turbulent conditions for $\phi_{ov} = 1.0$ and 1.2 irrespective of a_d/δ_{st} values principally due to greater amount of flame area generation under turbulence than in laminar conditions. The value of S under turbulent condition decreases in comparison to the laminar flame value for $\phi_{ov} = 0.8$ because the stretch rate effects due to curvature are expected to be stronger in these cases due to high Karlovitz number values [93]. The small values of S dominate over increased A under turbulent conditions to give rise to a reduction in the burned gas mass under turbulent conditions for $\phi_{ov} = 0.8$ cases except for the droplet case with initial $a_d/\delta_{st} = 0.06$ where the enhancement of flame surface area dominates over reduced S to yield an enhanced burned gas volume under the turbulent condition analysed here.

The evaluated values of normalised flame speed $S_V/S_{b(\phi_g)}$ are summarised in Table 5.3. It can be seen from Table 5.3 that the growth of burned gas volume for the droplet cases remains mostly smaller than the corresponding premixed flames. However, for $\phi_{ov} = 0.8$, large droplets with initial $a_d/\delta_{st} = 0.05$ and 0.06 show greater $S_V/S_{b(\phi_g)}$ values compared with the corresponding premixed flames with the same ϕ_{ov} under laminar and turbulent conditions and for $\phi_{ov} = 1.2$, burned gas volume can grow faster for small droplets with initial $a_d/\delta_{st} = 0.04$ than the corresponding premixed flame under laminar conditions. Furthermore, turbulence significantly affects the normalised flame speed $S_V/S_{b(\phi_g)}$ and increases the growth rate of burned gas volume for large droplets with $\phi_{ov} = 0.8$ and for small droplets with $\phi_{ov} = 1.0$ and 1.2. The enhancement of the extent of burning with increasing droplet size for overall fuel-lean mixtures is consistent with previous experimental findings by Hayashi et al. [118] and Lawes and Saat [119]. Furthermore, the enhanced extent of burning for overall fuel-rich mixtures for small droplets is also qualitatively consistent with experimental observations by Hayashi et al. [118] and Lawes and Saat [119].

5.5 Flame Speed Characteristics of Spherically Expanding Turbulent Spray Flames

The local flame propagation can be characterised with the help of different flame speeds, which focus on different aspects of the underlying combustion physics. The displacement speed S_d and consumption speed S_c are two widely used flame speeds, which are often used to identify the flame propagation characteristics [57–59, 80, 113, 210–213]. The displacement speed S_d indicates the speed with which the flame surface moves normal to itself with respect to an initially coincident material surface and is dependent on both chemical reaction rate and molecular diffusion rate within the flame [57–59, 80, 210]. By contrast, the consumption speed S_c is related to the integrated reaction rate in the flame normal direction [113, 210–213]. However, experimental evaluation of local displacement and consumption speeds (i.e. S_d and S_c) is a challenging task for three-dimensional flame surfaces under turbulent conditions. The challenges associated with the precise evaluation of flame speed were discussed by Abdel-Gayed et al. [166] for statistically spherical turbulent premixed flames. Nwagwe et al. [214] analysed the growth of the burned gas kernel by considering a mean radius of the flame for the purpose of an effective comparison between numerical and experimental data. Considerable uncertainty still exists about the experimental evaluations of flame speeds for spherically expanding turbulent flames. Therefore, a number of different experimental approaches [212, 213, 215] have been suggested for the flame speed evaluations, which need further validation.

The advances in high performance computing have enabled DNS of turbulent reacting flows, which offer three-dimensional spatially and temporally resolved information for reliable evaluations of S_d and S_c. Poinsot et al. [210] used two-dimensional laminar simulations of Bunsen burner premixed flames to compare the statistics of S_d and S_c, and revealed that flame curvature significantly influences the statistics of displacement speed in turbulent premixed flames [57–59, 73, 80, 81, 83–88], whereas the consumption speed remains unaffected by flame curvature for unity Lewis number flames. These findings have subsequently been verified for turbulent statistically planar premixed flames [113, 211]. The strain rate and curvature dependences of displacement speed for statistically planar premixed turbulent flames have been investigated in detail based on both detailed chemistry DNS [84–89] and simple chemistry DNS [57–59, 73, 80–83] data and it has been found that local displacement speed shows negative correlation with curvature in the absence of significant differential diffusion of heat and mass. The combined reaction and normal diffusion components of displacement speed S_d have been found to be negatively correlated with tangential strain rate a_T, whereas the tangential diffusion component of S_d correlates positively with a_T [57, 59, 73, 80–82]. These two correlations ultimately determine the tangential strain rate dependence of displacement speed

in statistically planar premixed turbulent flames [57, 59, 73, 80–82]. The statistics of displacement speed and scalar gradient in statistically spherical turbulent premixed flames can be considerably different from the corresponding statistically planar premixed flames [58, 60, 80]. These differences originate because of the strain rate and curvature dependences of reactive scalar gradient in the presence of mean positive curvature in spherically expanding flames. The differences in flame speeds and their curvature and stretch rate dependences between the statistically planar and spherical flames also depend on the mean flame radius [59, 60, 80]. Similarly, it has also been reported by Mizutani and Nishimoto [62] that propagation of statistically spherical flames expanding in droplet-laden mixtures can be considerably different from statistically planar spray flames.

In addition to chemical reaction rate and molecular diffusion rate, turbulent flame propagation in droplet-laden mixtures is affected by the additional physical mechanisms arising from evaporation and partial mixing of evaporated fuel with the surrounding air. Flame structure and flame propagation characteristics have been analytically [155–157], experimentally [149, 151, 153], and numerically [47, 48, 51–56, 68] investigated for statistically planar and jet spray flames. Moreover, the ignition performance of droplet-laden mixtures has been reported for a range of overall equivalence ratios and droplet diameters using the carrier phase DNS [42–46, 135]. Wacks et al. [47] and Wacks and Chakraborty [48] carried out three-dimensional DNS with a modified single step Arrhenius chemical mechanism to analyse the influences of droplet diameter and overall equivalence ratio on the flame speed statistics for statistically planar flames propagating in droplet-laden mixtures. It has been demonstrated by Wacks et al. [47] and Wacks and Chakraborty [48] that the magnitudes of the components of density-weighted displacement speed due to mixture inhomogeneity and droplet evaporation are small compared to the reaction and normal diffusion components. However, the analyses of Wacks et al. [47] and Wacks and Chakraborty [48] were conducted for statistically planar flames, and thus it needs to be assessed if the previously drawn conclusions for statistically planar flames are also valid for spherically expanding flames.

The DNS of spherically expanding flames propagating into turbulent mono-sized droplet-laden mixtures have been utilised in this section to analyse the statistical behaviours of displacement speed S_d and consumption speed S_c for different initial droplet diameters and overall equivalence ratios (i.e. $\phi_{ov} = 0.8, 1.0$ and 1.2). In this respect, the main objectives of the current analysis are: (a) to demonstrate and explain the effects of initial droplet diameter and the overall equivalence ratio on displacement speed and consumption speed statistics in spherically expanding turbulent flames propagating into initially mono-sized droplet-laden mixtures, (b) to relate displacement and consumption speeds with the rates of flame area generation and the burned gas volume in spherically expanding turbulent spray flames.

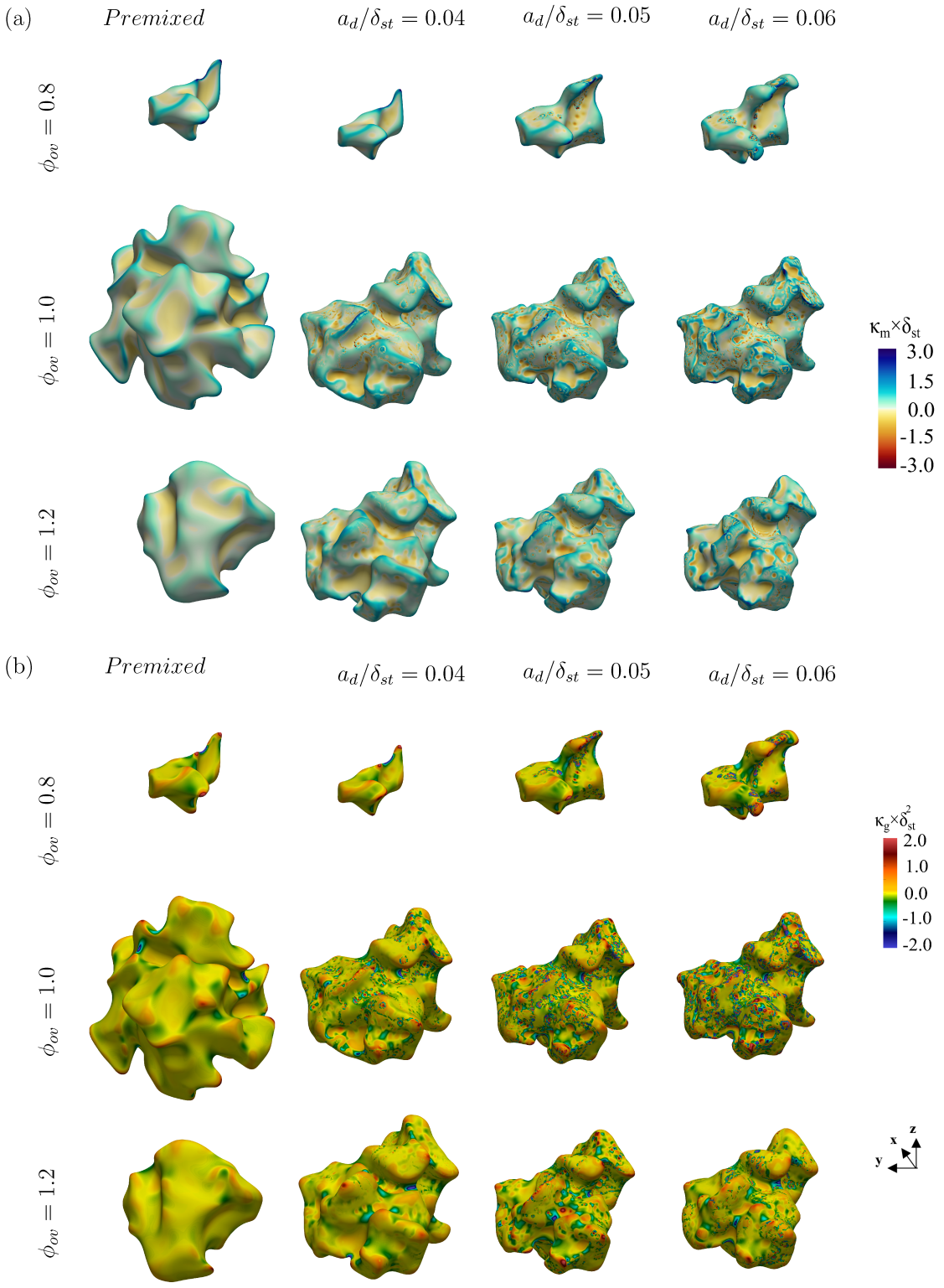

Figure 5.13: Instantaneous view of $c = 0.8$ isosurface coloured with normalised (a) mean curvature $\kappa_m \times \delta_{st}$ and (b) Gauss curvature $\kappa_g \times \delta_{st}^2$ for premixed gaseous (1^{st} column) and droplet (2^{nd}-4^{th} columns) cases with initial $\phi_{ov} = 0.8$ (1^{st} and 4^{th} rows), $\phi_{ov} = 1.0$ (2^{nd} and 5^{th} rows) and $\phi_{ov} = 1.2$ ($3^{rd}$and 6^{th} rows) at $t = 2.52\alpha_{T0}/S^2_{b(\phi_g=1)}$.

In order to illustrate the effects of flame-droplet interaction, the instantaneous views of the $c = 0.8$ isosurface (where the maximum value of the reaction rate of reaction progress variable $\dot{w}_c$ is obtained and thus is considered to be the flame surface for the rest of this section) are shown in Fig. 5.13 where the isosurfaces are coloured by the local normalised values of mean curvature $\kappa_m \times \delta_{st}$ and Gauss curvature $\kappa_g \times \delta_{st}^2$ [199]. The quantities κ_g and κ_m can be used to identify flame surface topologies. For example, negative (positive) values of κ_m with positive values of κ_g represent cup concave (convex) topologies and negative κ_g values indicate hyperbolic saddle geometries. A zero value of κ_g implies either tile convex (for $\kappa_m > 0$) or tile concave (for $\kappa_m < 0$) or flat surface (for $\kappa_m = 0$) topologies.

It can be seen from Fig. 5.13a that the premixed gaseous cases exhibit a smooth flame surface structure with moderate positive and negative values of $\kappa_m \times \delta_{st}$ for all values of equivalence ratio. Spray flames show a qualitatively similar behaviour as that of the premixed gaseous flames for $\phi_{ov} = 0.8$, but dimples can be seen on the flame surface for the spray cases with $\phi_{ov} = 1.0$ and 1.2. These dimples originate due to flame-droplet interaction and similar droplet induced flame wrinkling was reported in experiments by Hayashi et al. [118], Lawes and Saat [119] and Thimothée et al. [216]. Flame morphology in laminar spherically expanding spray flames was compared with laminar gaseous premixed flames by Thimothée et al. [216]. It was observed by Thimothée et al. [216] that gaseous premixed flames exhibit a smooth flame surface, whereas the presence of droplets induces deformation of spray flame surfaces. They also demonstrated that the droplet-induced flame wrinkling strengthens with increasing overall equivalence ratios and droplet diameter, which is qualitatively consistent with the present numerical findings. The spray flames for $\phi_{ov} = 1.0$ exhibit dimples with small radii of curvature, which is reflected in their large negative mean curvature values. The dimples on the flame surface of spray flames with $\phi_{ov} = 1.2$ are shallower than the corresponding $\phi_{ov} = 1.0$ cases because of the greater likelihood of more droplets interacting with the flame surface due to larger number density in the $\phi_{ov} = 1.2$ cases.

The most probable value of normalised Gauss curvature $\kappa_g \times \delta_{st}^2$ remains mostly close to zero in the gaseous premixed cases, which indicates the dominance of tile type flame topologies. This is found to be consistent with previous findings by Jenkins and Cant [170]. Moreover, the flame surface in the spray cases shows considerable probability of finding negative $\kappa_g \times \delta_{st}^2$ values, which implies saddle convex or concave topologies depending on the sign of $\kappa_m \times \delta_{st}$.

The effects of flame-droplet interaction on flame wrinkling and flame topologies can be quantified with the help of the joint PDFs between $\kappa_g \times \delta_{st}^2$ and $\kappa_m \times \delta_{st}$, which are presented in Fig. 5.14. The boundary of $\kappa_g = \kappa_m^2$ is shown by the parabola in black in Fig. 5.14. The spread of the $\kappa_g \times \delta_{st}^2$ and $\kappa_m \times \delta_{st}$ values in the joint PDFs for the droplet cases is greater

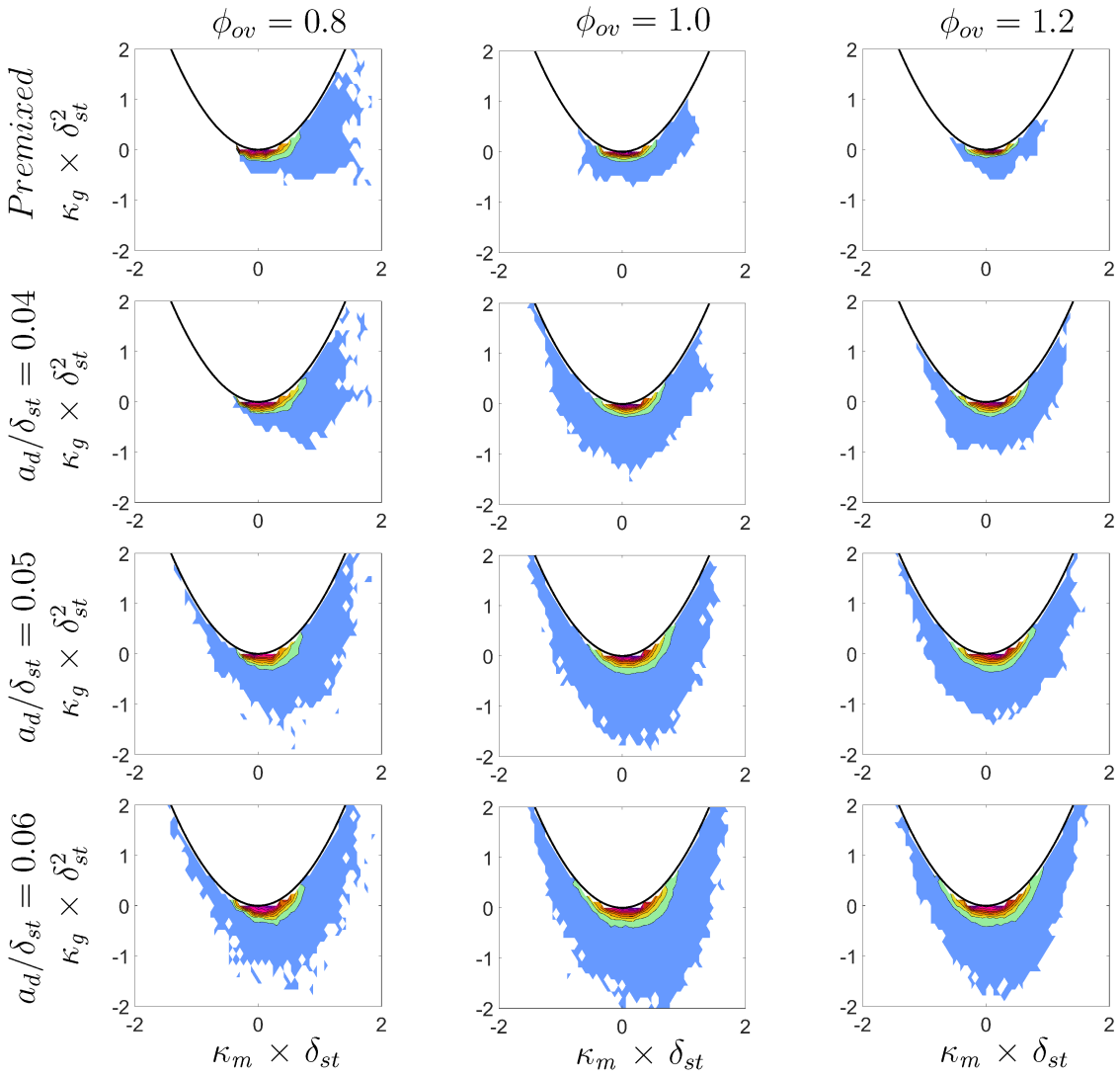

Figure 5.14: Joint PDFs of normalised mean curvature $\kappa_m \times \delta_{st}$ and normalised Gauss curvature $\kappa_g \times \delta_{st}^2$ on $c = 0.8$ isosurface for premixed and spray flames with different overall equivalence ratios (1^{st}-3^{rd} columns).

Table 5.4: Normalised burning rate $\Omega^{\dagger}$ and normalised flame surface area $A^{\dagger}$ values for the cases considered in this chapter. *GP* in the table header refers to the gaseous premixed flame case.

	$\phi_{ov}=0.8$				$\phi_{ov}=1.0$				$\phi_{ov}=1.2$			
a_d/δ_{st}	0.04	0.05	0.06	*GP*	0.04	0.05	0.06	*GP*	0.04	0.05	0.06	*GP*
$\Omega^{\dagger}$	2.66	5.97	6.58	3.80	34.15	25.45	23.59	66.02	32.70	23.28	17.47	27.66
$A^{\dagger}$	8.03	13.48	15.25	10.45	42.29	35.01	34.97	71.81	42.89	34.42	30.22	30.59

than the corresponding premixed flame cases. This is indicative of the droplet-induced flame wrinkling in the droplet cases, which is consistent with the observations made from Fig. 5.13. Figure 5.14 shows that the likelihood of obtaining $\kappa_m > 0$ is greater than that of $\kappa_m < 0$ for all cases considered here because these spherically expanding cases are expected to exhibit flame surface elements, which are predominantly convex to the unburned mixture. The cases with $\phi_{ov} = 0.8$ show a higher probability of finding cup convex topologies than the corresponding $\phi_{ov} = 1.0$ and 1.2 cases because of the smaller mean flame radius and burned gas volume due to mostly fuel-lean combustion for $\phi_{ov} = 0.8$ (see Fig. 5.2). Moreover, the probability of finding saddle topologies increases with increasing droplet size for all values of overall equivalence ratio due to the increased extent of droplet-induced flame wrinkling. However, the flame surface in large droplet cases (i.e. initial $a_d/\delta_{st} = 0.05$ and 0.06) for $\phi_{ov} = 0.8$ exhibits predominantly convex saddle topologies, whereas the flame surfaces in $\phi_{ov} = 1.0$ and 1.2 cases exhibit considerable probability of finding negative saddle topologies due to the significant extent of wrinkling arising from the interaction with the high number density of droplets.

The droplet-induced flame wrinkling acts to increase flame surface area in spherically expanding flames propagating into droplet mists. The variations of normalised burning rate $\Omega^{\dagger}$ and flame surface area $A^{\dagger}$ for different initial droplet diameters and overall equivalence ratios are listed in Table 5.4. The normalised burning rate $\Omega^{\dagger}$ and flame surface area $A^{\dagger}$ are evaluated as $\Omega^{\dagger} = (1/(\rho_0 S_{b(\phi_g=1)} 4\pi r_0^2)) \int_V \dot{w}_c dV$ and $A^{\dagger} = (1/4\pi r_0^2) \int_v |\nabla c| dV$, respectively. It can be seen from Table 5.4 that flame surface area and volume integrated burning rate for the spray flame cases with large droplets (i.e. initial $a_d/\delta_{st} = 0.05$ and 0.06) are found to be greater than the corresponding gaseous premixed flame case for $\phi_{ov} = 0.8$ and this tendency strengthens with increasing a_d/δ_{st}. However, both $\Omega^{\dagger}$ and $A^{\dagger}$ values for the initial $a_d/\delta_{st} = 0.04$ case for $\phi_{ov} = 0.8$ are smaller than the corresponding gaseous premixed flame case. By contrast, both $\Omega^{\dagger}$ and $A^{\dagger}$ increase with decreasing a_d/δ_{st} for $\phi_{ov} = 1.0$ and 1.2 and these values for the spray flame cases with $\phi_{ov} = 1.0$ are found to be smaller than the corresponding gaseous premixed flame cases.

The evaporation rates are high for small droplets, and thus the evaporated gaseous fuel gets more time to mix with the surrounding air before combustion than in the case of larger droplets. Moreover, the extent of droplet-induced flame wrinkling and flame area generation increases with increasing droplet size. For $\phi_{ov} = 0.8$ cases with initial $a_d/\delta_{st} = 0.04$, the droplet-induced flame wrinkling remains weak (see Figs. 5.13 and 5.14) and combustion takes place in a gaseous mixture with overwhelming probability of finding $\phi_g < 0.8$ in spite of rapid evaporation of small droplets (see Fig. 5.14). This gives rise to both smaller burned gas volume and accordingly smaller flame surface area in the case with initial $a_d/\delta_{st} = 0.04$ and the corresponding gaseous premixed flame case for $\phi_{ov} = 0.8$. However, relatively slower evaporation rate in the $\phi_{ov} = 0.8$ cases with initial $a_d/\delta_{st} = 0.05$ and 0.06 in comparison to the initial $a_d/\delta_{st} = 0.04$ case, gives rise to the higher probability of finding more reactive fuel-air mixture than $\phi_g > 0.8$ within the flame (see Fig. 5.8) and this tendency strengthens with increasing droplet diameter. This along with the increasing extent of droplet-induced flame wrinkling with increasing a_d/δ_{st} gives rise to the increasing trends of $\Omega^{\dagger}$ and $A^{\dagger}$ with increasing droplet size for $\phi_{ov} = 0.8$. It can be seen from Fig. 5.8 that gaseous phase combustion takes place predominantly under fuel-lean mode in the $\phi_{ov} = 1.0$ and 1.2 cases (see Fig. 5.8) and this tendency strengthens with increasing droplet size because of the slow evaporation rate of large droplets. This gives rise to overwhelming probability of combustion of less reactive gaseous fuel-air mixture in the droplet cases in comparison to the corresponding gaseous premixed flame cases for $\phi_{ov} = 1.0$ and 1.2, and this tendency strengthens further with increasing droplet size. This, in turn, gives rise to smaller value of the burned gas volume for droplet cases than the corresponding premixed flame cases, and thus $\Omega^{\dagger}$ shows a decreasing trend with increasing a_d/δ_{st} for $\phi_{ov} = 1.0$ and 1.2 cases. This decrease in burned gas volume with increasing a_d/δ_{st} overcomes the effects of increased droplet-induced flame surface wrinkling for larger droplets and gives rise to a decreasing trend of $A^{\dagger}$ with increasing a_d/δ_{st} for $\phi_{ov} = 1.0$ and 1.2 cases.

The effects of a_d/δ_{st} and ϕ_{ov} on $\Omega^{\dagger}$ and $A^{\dagger}$ are the outcomes of the variations of flame propagation characteristics in response to the changes in droplet diameter and overall equivalence ratio, which will be discussed next in this section.

The statistical behaviour of S_d^* is governed by $\dot{w}_c$, $\dot{S}_{liq,c}$, $\dot{A}_c$ and $\nabla\cdot(\rho D\nabla c)$ which appear on the right side of the transport equation of the reaction progress variable, c (see Eq. 2.52). The mean values of the terms $\dot{w}_c$, $\dot{S}_{liq,c}$, $\dot{A}_c$ and $\nabla\cdot(\rho D\nabla c)$ conditional on c are shown in Fig. 5.15. The molecular diffusion term $\nabla\cdot(\rho D\nabla c)$ is the only term whose mean value plays a significant role in the preheat zone (i.e. $c < 0.5$) and the mean value of $\nabla\cdot(\rho D\nabla c)$ remains positive in the preheat zone (i.e. $c < 0.5$) for both gaseous premixed and droplet cases. However, in both gaseous premixed and droplet cases the mean value of $\nabla\cdot(\rho D\nabla c)$ assumes negative values in the reaction zone (i.e. $0.9 \leq c \leq 0.5$) and also towards the burned gas side of the flame. The

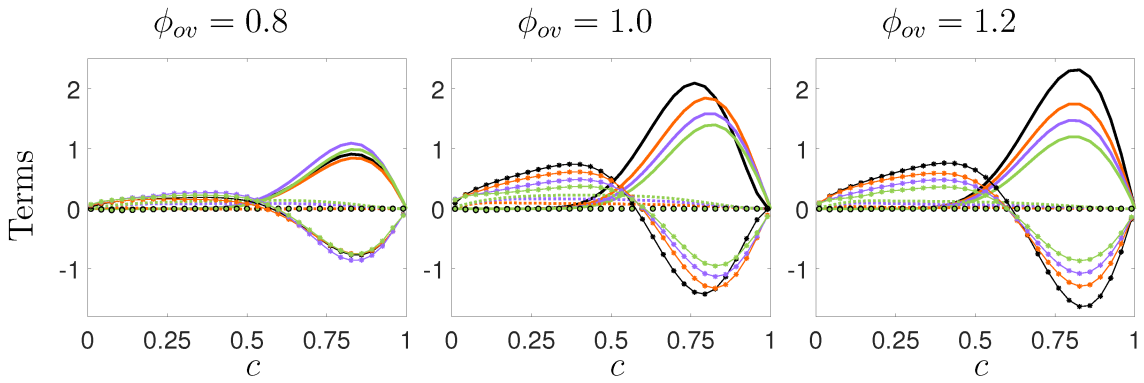

Figure 5.15: Variations of mean values of $\dot{w}_c$ (continuous line), $\nabla\cdot(\rho D\nabla c)$ (continuous line with star marker), $\dot{A}_c$ (dotted line) and $\dot{S}_{liq,c}$ (circle marker with black edges) conditional on c for droplet cases with initial $a_d/\delta_{st} = 0.04$ (orange colour), 0.05 (purple colour) and 0.06 (green colour) and also for the gaseous premixed case (black colour). All terms are normalised by $\delta_{st}/\rho_0 S_{b(\phi_g=1)}$.

mean reaction rate $\dot{w}_c$ assumes deterministically positive values, and its peak value is obtained at around $c = 0.8$ for both gaseous premixed and droplet cases. This justifies the choice of the $c = 0.8$ isosurface as the flame surface in this analysis. The positive mean value of $\dot{w}_c$ and negative mean value of $\nabla\cdot(\rho D\nabla c)$ remain in approximate equilibrium in the reaction zone. The mean values of the terms associated with droplet evaporation $\dot{S}_{liq,c}$ and mixture inhomogeneity $\dot{A}_c$ remain much smaller in magnitude in comparison to the magnitudes of the mean values of $\dot{w}_c$ and $\nabla\cdot(\rho D\nabla c)$ throughout the flame irrespective of the values of a_d/δ_{st} and ϕ_{ov}. The same behaviour in terms of relative magnitudes is obtained when the mean values of $\dot{w}_c$, $\dot{S}_{liq,c}$, $\dot{A}_c$ and $\nabla\cdot(\rho D\nabla c)$ conditional on ξ are considered, which are not presented here for the sake of brevity. The highest magnitude of the mean values of $\dot{w}_c$ and $\nabla\cdot(\rho D\nabla c)$ are obtained for $\xi \approx \xi_{st}$ when their mean values are evaluated conditional on ξ. The mean values of $\dot{w}_c$ conditional on ξ for $\phi_{ov} = 1.0$ are presented in Fig. 4.13 and thus are not presented here and qualitatively similar behaviour has been observed for $\phi_{ov} = 0.8$ and 1.2.

It can be seen from Fig. 5.15 that the mean value of $\dot{w}_c$ decreases with increasing a_d for $\phi_{ov} = 1.0$ and 1.2 cases and in these droplet cases the mean value of $\dot{w}_c$ remains smaller than the corresponding gaseous premixed flame case. By contrast, the cases with large droplets (i.e. initial $a_d/\delta_{st} = 0.05$ and 0.06) exhibit higher peak mean values of $\dot{w}_c$ than the corresponding premixed flame case for $\phi_{ov} = 0.8$ and the peak mean value of $\dot{w}_c$ increases with increasing a_d/δ_{st}. However, the peak mean value of $\dot{w}_c$ remains smaller than the corresponding premixed flame case for initial $a_d/\delta_{st} = 0.04$ for $\phi_{ov} = 0.8$. The mean behaviour of $\dot{w}_c$ is qualitatively consistent with the behaviour of $\Omega^{\dagger}$reported in Table 5.4. As the peak (negative) magnitude of the molecular diffusion rate $\nabla\cdot(\rho D\nabla c)$ is obtained in the reaction zone where it remains in

approximate equilibrium with the mean reaction rate $\dot{w}_c$, the variations of the peak magnitudes of $\nabla \cdot (\rho D \nabla c)$ in response to the changes of a_d/δ_{st} and ϕ_{ov} are qualitatively similar to those obtained for the mean values of $\dot{w}_c$.

The PDFs of displacement speed $S_d^*/S_{b(\phi_g=1)}$ and its components $S_i^*/S_{b(\phi_g=1)}$ where ($i = r,n,t,z+s$) on $c = 0.8$ isosurface are shown in Fig. 5.16. A comparison of the PDFs $S_d^*/S_{b(\phi_g=1)}$ between premixed gaseous and droplet cases reveals that premixed gaseous flames with $\phi_{ov} = 1.0$ and 1.2 exhibit higher probability of obtaining positive $S_d^*/S_{b(\phi_g=1)}$ than in droplet cases. In all cases a finite probability of finding negative $S_d^*/S_{b(\phi_g=1)}$ is observed, which suggests that locally the flame moves opposite to the flame normal direction instead of propagating into unburned gases. The negative values of $S_d^*/S_{b(\phi_g=1)}$ are expected in these flames according to the scaling analysis by Peters [93] because all these cases represent $Ka > 1$ combustion. As the Karlovitz number values are expected to be higher in the droplet cases than the corresponding gaseous premixed flame because of predominantly fuel-lean combustion, the probability of finding negative $S_d^*/S_{b(\phi_g=1)}$ has been found to be higher in these droplet cases. Moreover, the mean values of $S_d^*/S_{b(\phi_g=1)}$ of the premixed gaseous flames with $\phi_{ov} = 1.0$ and 1.2 remain greater than the droplet cases. Furthermore, the probability of finding positive values of $S_d^*/S_{b(\phi_g=1)}$ decreases with increasing a_d/δ_{st}. In the case of $\phi_{ov} = 0.8$, the PDFs of $S_d^*/S_{b(\phi_g=1)}$ for the gaseous premixed flame and the initial $a_d/\delta_{st} = 0.04$ case remain comparable but the PDFs of $S_d^*/S_{b(\phi_g=1)}$ for the initial $a_d/\delta_{st} = 0.05$ and 0.06 cases show higher probability of finding positive $S_d^*/S_{b(\phi_g=1)}$ than the corresponding premixed flame case. This suggests that the flame kernel propagates faster for increasing droplet diameter for $\phi_{ov} = 0.8$ and can exhibit faster propagation rate than the corresponding premixed flame. By contrast, the propagation rate of the droplet cases remain smaller than the corresponding premixed flames for $\phi_{ov} = 1.0$ and 1.2, and the propagation rate decreases with increasing diameter. These findings are consistent with the trends of $\Omega^\dagger$ and $A^\dagger$ reported in Table 5.4.

It is necessary to analyse the statistical behaviours of the different components of displacement speed (see Eq. 2.60) in order to explain the origin of its negative value, and to isolate different physical mechanisms, which lead to the differences in flame propagation between gaseous premixed and droplet flame cases. The PDFs of $S_r^*/S_{b(\phi_g=1)}$ and $S_n^*/S_{b(\phi_g=1)}$ exhibit positive and negative values, respectively in the reaction zone, and they exhibit wider distributions for droplet cases than the corresponding premixed flame cases. The variations of equivalence ratio give rise to a large spread of values of $\dot{w}_c$ and $|\nabla c|$ on a given c isosurface, which contribute to the larger spreads of the values of $S_r^*/S_{b(\phi_g=1)}$ and $S_n^*/S_{b(\phi_g=1)}$ in the droplet cases than in the corresponding premixed cases. The PDFs of normalised tangential diffusion component of displacement speed $S_t^*/S_{b(\phi_g=1)} = -2\rho D\kappa_m/\rho_0 S_{b(\phi_g=1)}$ exhibit predominantly negative values for all cases due to the predominance of positive κ_m (i.e. convex

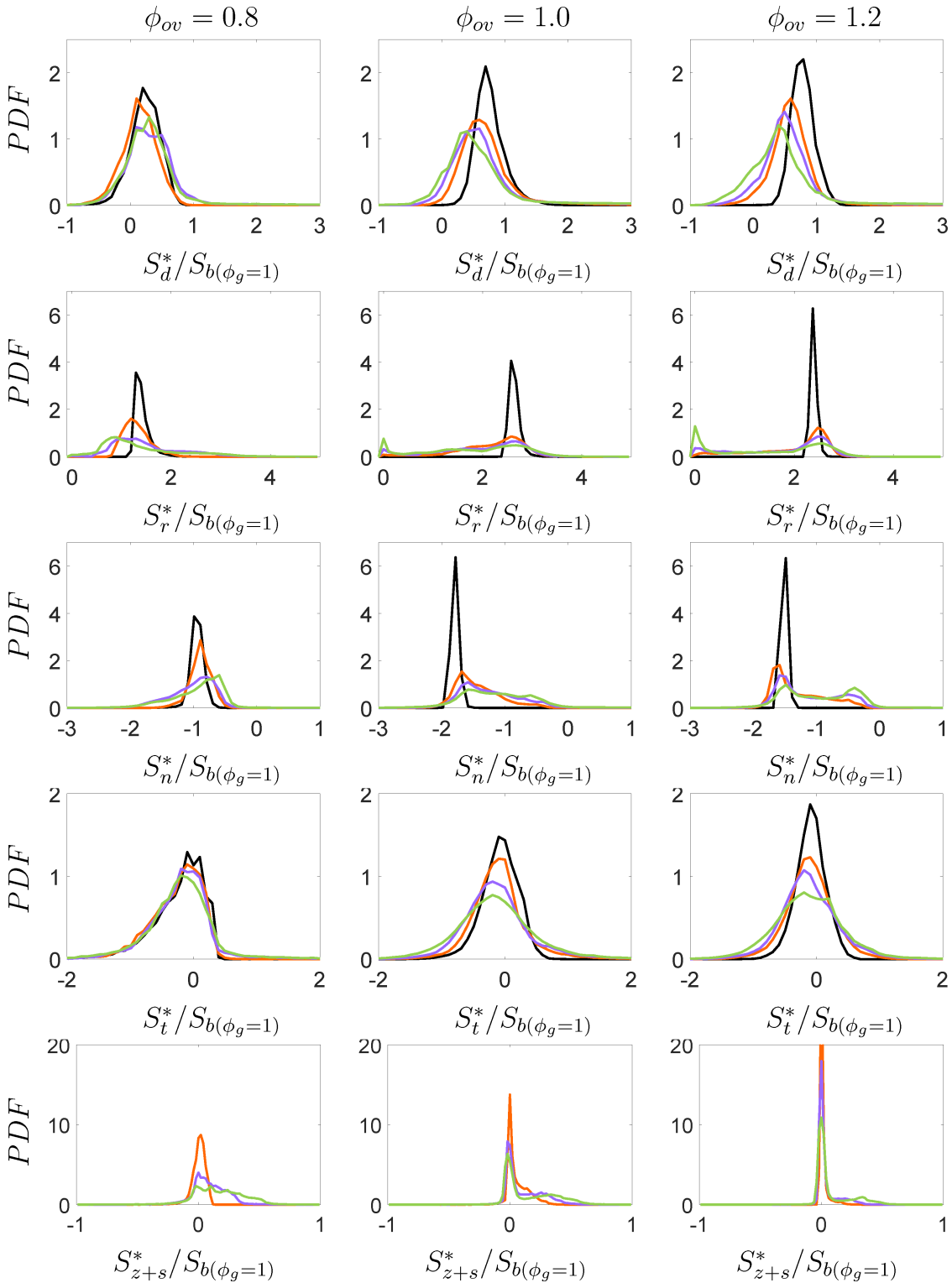

Figure 5.16: PDFs of $S_i^*/S_{b(\phi_g=1)}$ (1^{st}-5^{th} rows) where $(i = d, r, n, t, z+s)$ on $c = 0.8$ for droplet cases with initial $a_d/\delta_{st} = 0.04$ (——), 0.05 (——) and 0.06 (——) and for premixed gaseous case (——).

flame topologies), as shown in Fig. 5.14. The PDFs of $S_t^*/S_{b(\phi_g=1)}$ for the droplet cases are wider than the corresponding premixed flames because of wider curvature distributions (see Fig. 5.14) arising from droplet-induced flame wrinkling. The positive $S_r^*/S_{b(\phi_g=1)}$, and negative $S_n^*/S_{b(\phi_g=1)}$ and $S_t^*/S_{b(\phi_g=1)}$ values at $c=0.8$ are consistent with the mean variations of $\dot{w}_c$ and $\nabla\cdot(\rho D\nabla c)$ shown in Fig. 5.15.

It can be seen from Fig. 5.16 that the probability of finding high positive (negative) values of $S_r^*/S_{b(\phi_g=1)}$ ($S_n^*/S_{b(\phi_g=1)}$) decreases with increasing a_d for $\phi_{ov}=1.0$ and 1.2 cases and in these droplet cases the mean and most probable values of $S_r^*/S_{b(\phi_g=1)}$ and the magnitude of the mean and the most probable $S_n^*/S_{b(\phi_g=1)}$ remain smaller than the corresponding gaseous premixed flame case. By contrast, the cases with large droplets (e.g. initial $a_d/\delta_{st}=0.05$ and 0.06 cases) exhibit higher probability of finding positive (negative) values of $S_r^*/S_{b(\phi_g=1)}$ ($S_n^*/S_{b(\phi_g=1)}$) than the corresponding premixed flame case for $\phi_{ov}=0.8$ and the most probable value of $S_r^*/S_{b(\phi_g=1)}$ and the magnitude of the most probable negative value of $S_n^*/S_{b(\phi_g=1)}$ increases with increasing a_d/δ_{st}.

The PDFs of the normalised values of the components associated with droplet evaporation and mixture inhomogeneity $S_{(z+s)}^*/S_{b(\phi_g=1)}$ are presented together in Fig. 5.16. The PDFs of $S_{(z+s)}^*/S_{b(\phi_g=1)}$ peak around zero (i.e. the most probable value remains close to zero) for all droplet cases but a long tail is observed for positive values for large droplets (i.e. initial $a_d/\delta_{st}=0.05$ and 0.06 cases). This is also consistent with the observations made from Fig. 5.15, which revealed that the magnitudes of the mean values of the terms associated with droplet evaporation $\dot{S}_{liq,c}$ and mixture inhomogeneity $\dot{A}_c$ remain much smaller than the magnitudes of the mean values of $\dot{w}_c$ and $\nabla\cdot(\rho D\nabla c)$ for all values of a_d/δ_{st} and ϕ_{ov}. This is also found to be consistent with the previous findings by Wacks et al. [47] in the case of statistically planar flames propagating into droplet-laden mixtures.

It can be inferred from Fig. 5.16 that locally negative values of $S_d^*/S_{b(\phi_g=1)}$ are obtained when the negative values of $S_{(n+t)}^*/S_{b(\phi_g=1)}$ overcome the positive contribution of $S_r^*/S_{b(\phi_g=1)}$. However, in all cases the probability of finding positive values of $S_d^*/S_{b(\phi_g=1)}$ supersedes that of finding negative values, which suggests that the flame kernels grow in size with time for all cases considered here in spite of local instances where the flame retreats into the burned gas instead of propagating into the unburned gas.

The PDFs of normalised consumption and displacement speeds (i.e. $S_c/S_{b(\phi_g=1)}$ and $S_d^*/S_{b(\phi_g=1)}$) are compared in Fig. 5.17 for all cases considered here. It can be seen from Fig. 5.17 that the consumption speed remains deterministically positive, whereas the PDF of $S_d^*/S_{b(\phi_g=1)}$ exhibits finite probability of finding negative values although the mean value remains positive for all cases (see Fig. 5.16). As the consumption speed S_c is principally determined by $\dot{w}_c$ (see Eq. 2.61), the variations of $S_c/S_{b(\phi_g=1)}$ in response to the changes of a_d/δ_{st}

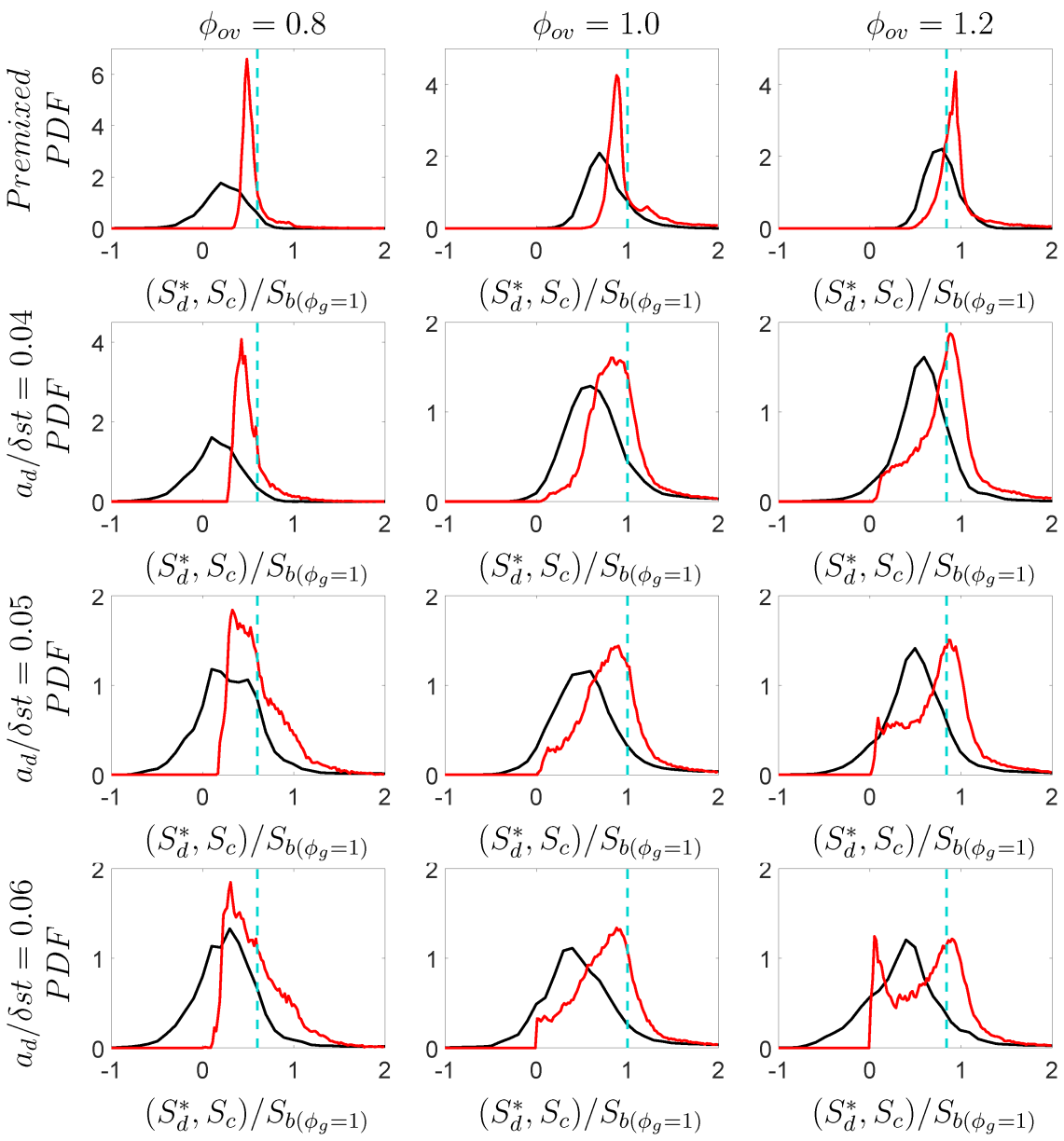

Figure 5.17: PDFs of $S_d^*/S_{b(\phi_g=1)}$ (——) and $S_c/S_{b(\phi_g=1)}$ (——) on $c = 0.8$ for premixed gaseous case (1^{st} row) and for droplet cases with initial $a_d/\delta_{st} = 0.04$ (2^{nd} row), 0.05(3^{rd} row) and 0.06 (4^{th} row). The value of $S_{b(\phi_g=\phi_ov)}/S_{b(\phi_g=1)}$ is shown by the vertical cyan line.

Table 5.5: Correlation coefficients for $S_d^* - S_c$, $S_c - \kappa_m$, $S_c - a_T$, $S_d^* - \kappa_m$ and $S_d^* - a_T$ on the $c = 0.8$ isosurface for all cases considered here. *GP* in the table header refers to the gaseous premixed flame case.

		$S_d^* - S_c$	$S_c - \kappa_m$	$S_c - a_T$	$S_d^* - \kappa_m$	$S_d^* - a_T$
$\phi_g = 0.8$	*GP*	-0.23	0.258	-0.14	-0.87	0.508
	$a_d/\delta_{st} = 0.04$	0.109	0.116	0.020	-0.83	0.508
	$a_d/\delta_{st} = 0.05$	0.382	0.091	0.162	-0.597	0.378
	$a_d/\delta_{st} = 0.06$	0.330	0.132	0.090	-0.457	0.304
$\phi_g = 1.0$	*GP*	0.070	0.004	-0.053	-0.849	0.614
	$a_d/\delta_{st} = 0.04$	0.209	0.254	-0.015	-0.592	0.321
	$a_d/\delta_{st} = 0.05$	0.258	0.285	0.118	-0.473	0.302
	$a_d/\delta_{st} = 0.06$	0.281	0.298	0.129	-0.342	0.263
$\phi_g = 1.2$	*GP*	-0.0687	0.0983	-0.077	-0.912	0.650
	$a_d/\delta_{st} = 0.04$	0.302	0.438	-0.036	-0."4	0.448
	$a_d/\delta_{st} = 0.05$	0.337	0.413	0.118	-0.319	0.389
	$a_d/\delta_{st} = 0.06$	0.362	0.412	0.215	-0.255	0.357

and ϕ_{ov} are qualitatively similar to those obtained for $S_r^*/S_{b(\phi_g=1)}$ (see Fig. 5.16). However, it can be seen from Fig. 5.17 that the probability of finding positive values of $S_c/S_{b(\phi_g=1)}$ is greater than that in the case of $S_d^*/S_{b(\phi_g=1)}$ for all cases considered here. Furthermore, the most probable value of $S_c/S_{b(\phi_g=1)}$ remains greater than $S_d^*/S_{b(\phi_g=1)}$ for all cases. Moreover, the most probable values of $S_d^*/S_{b(\phi_g=1)}$ remain smaller than $S_{b(\phi_g=\phi_{ov})}/S_{b(\phi_g=1)}$, whereas the most probable values of $S_c/S_{b(\phi_g=1)}$ are found to be comparable to $S_{b(\phi_g=\phi_{ov})}/S_{b(\phi_g=1)}$ for all cases considered here. In the case of unity Lewis number spherically expanding premixed flames, the net positive stretch rate acts to decrease $S_d^*/S_{b(\phi_g=1)}$ in comparison to $S_{b(\phi_g=\phi_{ov})}/S_{b(\phi_g=1)}$ but $S_c/S_{b(\phi_g=1)}$ remains unaffected [24]. The stretch rate effects on $S_d^*/S_{b(\phi_g=1)}$ are further augmented by the higher value of Ka due to the presence of predominantly fuel-lean mixtures in the reaction zone for the droplet cases considered here. Figure 5.17 further reveals that there is considerable difference between the statistical behaviours and magnitudes of S_c and S_d^*, which is consistent with previous findings [210, 211] in the case of statistically planar premixed turbulent flames. This can be substantiated from the contours of joint PDFs of $S_c/S_{b(\phi_g=1)}$ with $S_d^*/S_{b(\phi_g=1)}$ on $c = 0.8$ shown in Fig. 5.18. It can be seen from Fig. 5.18 that $S_c/S_{b(\phi_g=1)}$ and $S_d^*/S_{b(\phi_g=1)}$ are weakly negatively correlated for the $\phi_g = 0.8$ gaseous premixed case, whereas this correlation remains weak with no clear trend for the premixed cases with $\phi_g = 1.0$ and 1.2. The correlation between $S_c/S_{b(\phi_g=1)}$ and $S_d^*/S_{b(\phi_g=1)}$ remains weakly positive for all droplet cases.

It is worthwhile to note that the consumption speed has been found to be weakly correlated with curvature κ_m and tangential strain rate $a_T = (\delta_{ij} - N_i N_j)\partial u_i/\partial x_j$ for all premixed flame

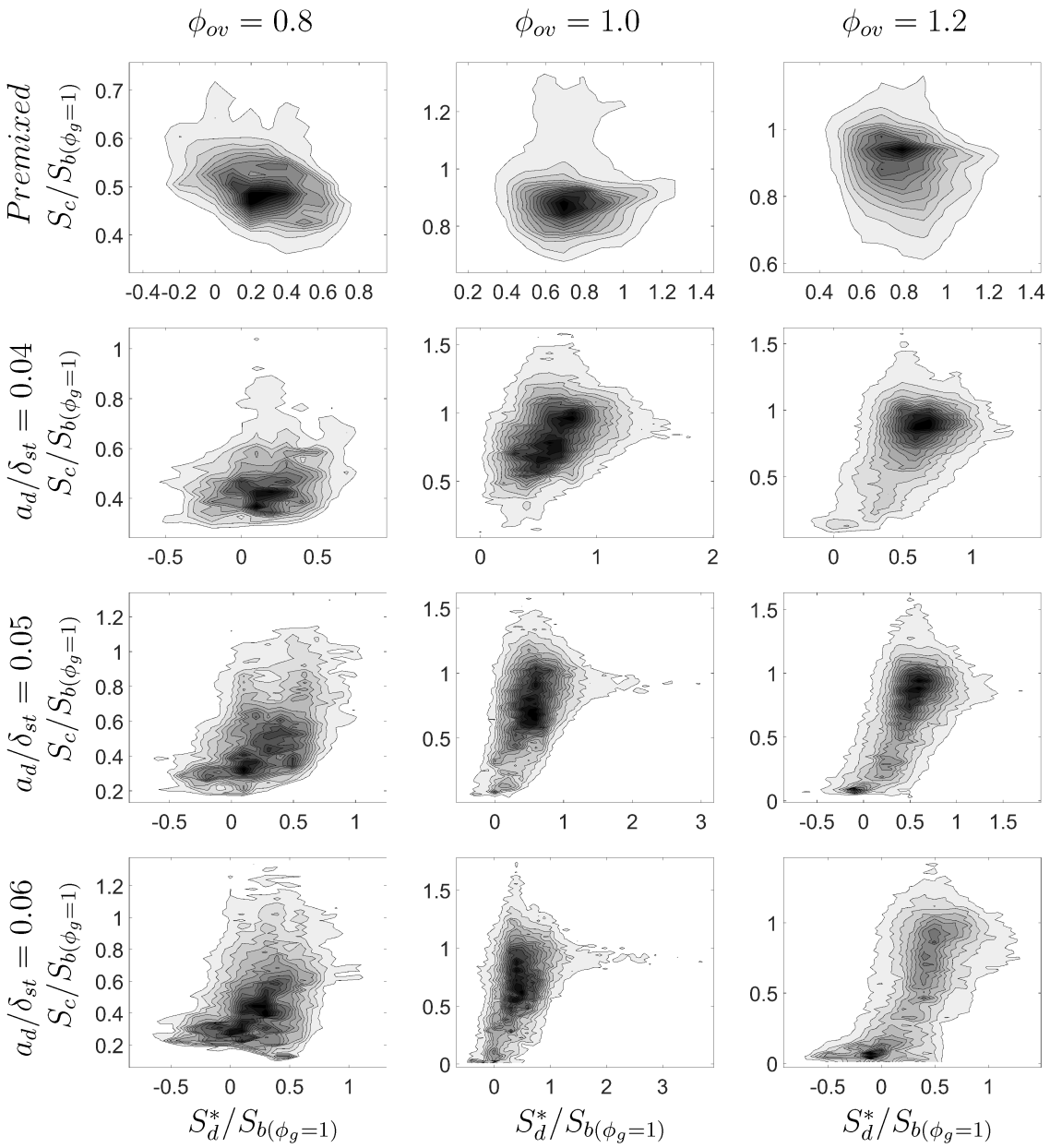

Figure 5.18: Contours of joint PDF of $S_c/S_{b(\phi_g=1)}$ and $S_d^*/S_{b(\phi_g=1)}$ on $c = 0.8$ isosurface for premixed gaseous cases (1^{st} row) and droplet cases with initial droplet diameters $a_d/\delta_{st} = 0.04$ (2^{nd} row), 0.05 (3^{rd} row) and 0.06 (4^{th} row).

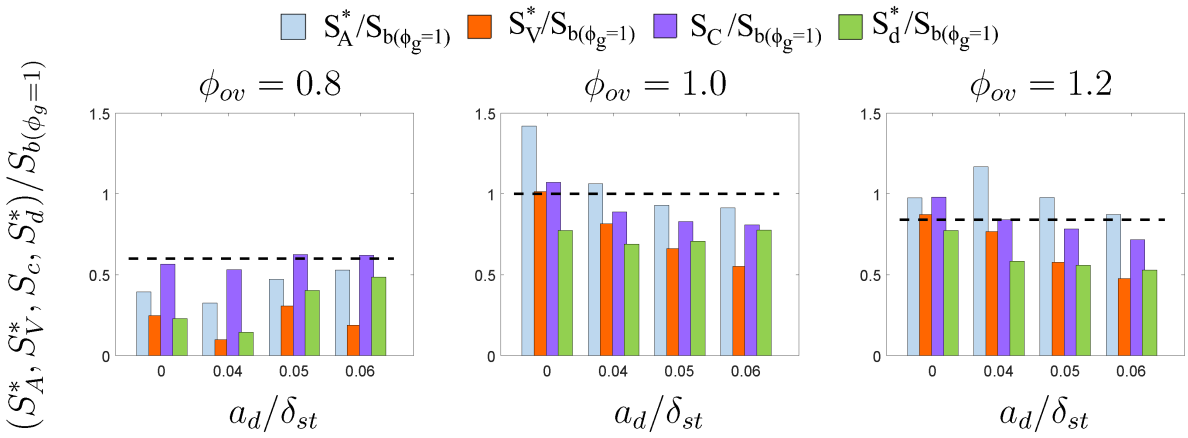

Figure 5.19: Mean values of $S_c/S_{b(\phi_g=1)}$ and $S_d^*/S_{b(\phi_g=1)}$ on $c = 0.8$ isosurface along with alternative flame speeds $S_A^*/S_{b(\phi_g=1)}$ and $S_V^*/S_{b(\phi_g=1)}$ for the cases with $\phi_{ov} = 0.8$, 1.0 and 1.2. The value of $S_{b(\phi_g=\phi_{ov})}/S_{b(\phi_g=1)}$ is shown by the horizontal black dashed line.

cases considered here and this can be substantiated from the correlation coefficients listed in Table 5.5. By contrast, S_d^* is negatively correlated with κ_m, whereas a positive correlation is obtained between S_d^* and a_T for the premixed flame cases, as demonstrated by the correlation coefficients listed in Table 5.5. The physical explanations behind these correlations have been provided elsewhere [58, 59, 80] and thus are not repeated here. Moreover, it has been demonstrated in Refs. [58, 59] that the strength of the displacement speed correlations with tangential strain rate and curvature depends on the mean flame radius. Furthermore, the effects of heat release and turbulence evolution within the flame are different for different equivalence ratios, which along with the difference in mean flame radius give rise to differences in correlation strengths of S_d^* with κ_m and a_T between $\phi_g = 0.8$, 1.0 and 1.2 premixed turbulent cases. For the droplet cases, a_T and κ_m dependences of S_d^* remain qualitatively similar to the corresponding premixed flames. However, in the droplet cases, the variation of ϕ_g on a given c isosurface gives rise to several qualitatively similar correlation branches with differing strengths. As a result, the net correlations of S_d^* with κ_m and a_T in droplet cases are weaker than the corresponding premixed flame cases, and these correlations weaken with increasing droplet diameter as this increases the extent of ϕ_g variations on a given c isosurface (shown in Fig. 5.8). The combination of weak κ_m and a_T dependences of S_c and relatively stronger curvature and strain rate correlations with S_d^* gives rise to weak interrelation between S_c and S_d^* for all cases. These correlations should not be associated with any physical mechanism because of the small magnitudes of the correlation coefficients irrespective of their signs.

The flame speeds S_A and S_V provide a measure of growth rate of flame surface area and burned gas volume. Figure 5.19 shows the variations of $S_A^*/S_{b(\phi_g=1)} = \rho_b S_A/(\rho_0 S_{b(\phi_g=1)})$ and

$S_V^*/S_{b(\phi_g=1)} = \rho_b S_V/(\rho_0 S_{b(\phi_g=1)})$ along with the mean values of normalised consumption speed $S_c/S_{b(\phi_g=1)}$ and density-weighted displacement speed $S_d^*/S_{b(\phi_g=1)}$ on the $c = 0.8$ isosurface for different values of normalised initial droplet diameter a_d/δ_{st} and the overall equivalence ratio ϕ_{ov}, where $\rho_b = m_b/V_b$ is the burned gas density with m_b being the burned gas mass with $c \geq 0.99$. It is evident from Fig. 5.19 that the mean value of $S_c/S_{b(\phi_g=1)}$ remains greater than $S_d^*/S_{b(\phi_g=1)}$ for all values of ϕ_{ov} and a_d/δ_{st}, which is consistent with the findings from Fig. 5.18.

The presence of droplets enhances the normalised flame speed $S_A^*/S_{b(\phi_g=1)}$ for $\phi_{ov} = 0.8$ except for the initial $a_d/\delta_{st} = 0.04$ case under turbulent conditions. Normalised flame speed $S_A^*/S_{b(\phi_g=1)}$ increases with increasing droplet diameter for $\phi_{ov} = 0.8$, whereas it shows just the opposite behaviour for $\phi_{ov} = 1.0$ and 1.2. For $\phi_{ov} = 0.8$, large droplets with initial $a_d/\delta_{st} = 0.05$ and 0.06 show greater $S_V^*/S_{b(\phi_g=1)}$ values than that in the case with initial $a_d/\delta_{st} = 0.04$. Moreover, $S_V^*/S_{b(\phi_g=1)}$ in the case of initial $a_d/\delta_{st} = 0.05$ for $\phi_{ov} = 0.8$ has been found to be greater than that in the corresponding premixed flame case. Furthermore, turbulence significantly affects the normalised flame speed $S_V^*/S_{b(\phi_g=1)}$ and augments the growth rate of burned gas volume for large droplets with $\phi_{ov} = 0.8$ and for small droplets with $\phi_{ov} = 1.0$ and 1.2. The enhancement of the extent of burning with increasing (decreasing) droplet size for overall fuel-lean (fuel-rich) mixtures is qualitatively consistent with previous experimental findings [119]. The physical explanations for the aforementioned variations of $S_A^*/S_{b(\phi_g=1)}$ and $S_V^*/S_{b(\phi_g=1)}$ with a_d/δ_{st} and ϕ_{ov} have been provided in Sections 5.2 and 5.4 and thus are not repeated here.

The horizontal dashed black line in Fig. 5.19 provides the value of $S_{b(\phi_g=\phi_{ov})}/S_{b(\phi_g=1)}$, which reveals that S_A^* and S_V^* remain smaller than $S_{b(\phi_g=0.8)}$ in all cases with $\phi_{ov} = 0.8$, whereas in the $\phi_{ov} = 1.2$ cases S_A^* assumes greater values than $S_{b(\phi_g=1.2)}$ but S_V^* remains smaller than $S_{b(\phi_g=1.2)}$. However, premixed gaseous case and small droplets with $\phi_{ov} = 1.0$ exhibit higher S_A^* values than $S_{b(\phi_g=1)}$. In premixed gaseous cases with $\phi_{ov} = 1.0$ and 1.2, S_V^* remains comparable with $S_{b(\phi_g=\phi_{ov})}$. The mean values of S_d^* and S_c tend to be smaller than $S_{b(\phi_{ov}=\phi_g)}$ for all droplet cases irrespective of the values of ϕ_{ov} and a_d, which is consistent with the observations made from Fig. 5.17. However, the extent of deviation of S_d^* from $S_{b(\phi_{ov}=\phi_g)}$ is greater than the difference between $S_{b(\phi_{ov}=\phi_g)}$ and S_c, which is also consistent with theoretical expectations for positively stretched flames [24].

It can be seen from Fig. 5.19 that the magnitudes of $S_A^*/S_{b(\phi_g=1)}$ and the mean value of $S_c/S_{b(\phi_g=1)}$ remain comparable for all cases considered here irrespective of the values of a_d/δ_{st} and ϕ_{ov}. Moreover, the magnitudes of $S_V^*/S_{b(\phi_g=1)}$ and the mean value of $S_d^*/S_{b(\phi_g=1)}$ assume comparable values for all cases considered here except for the large droplets (e.g. initial $a_d/\delta_{st} = 0.06$) for $\phi_{ov} = 0.8$, and the agreement between the mean values of $S_d^*/S_{b(\phi_g=1)}$ and

$S_V^*/S_{b(\phi_g=1)}$ improves with increasing droplet size for $\phi_{ov} = 1.0$ and 1.2. Thus, the findings of Fig. 5.19 suggest that the evaluation of S_A^* may provide an approximate quantitative estimation of the mean value of S_c, but approximating the mean density-weighted displacement speed is a more challenging task. However, the mean density-weighted displacement speed can be approximately estimated by S_V^* for large droplets in the case of overall stoichiometric and fuel-rich mixtures.

5.6 Summary of Key Findings

Three dimensional DNS of spherically expanding flames propagating into n-heptane droplet-laden mixtures have been carried out to analyse the influences of overall equivalence ratio on flame-droplet-turbulence interactions. The main findings are listed below:

- The burned gas temperature for laminar and turbulent globally fuel-lean droplet cases with initial $a_d/\delta_{st} = 0.04$ is found to be comparable with the the corresponding fuel-lean premixed cases while local temperature drop exists for laminar and turbulent globally stoichiometric and fuel-rich droplet cases with initial $a_d/\delta_{st} = 0.04$.

- As a result of smaller number density of droplets, the appearance of dimpled flame surface fades in globally fuel-lean droplet cases in comparison to globally stoichiometric droplet cases. However, droplet induced flame deformation evolves from small densely packed dimples in the globally stoichiometric droplet cases into large distributed dimples in the globally fuel-rich droplet cases due to the evaporation of clustered droplets. For a given droplet diameter, the cases with initial $\phi_{ov} = 1.0$ exhibit the highest flame area generation ratio while the cases with initial $\phi_{ov} = 0.8$ remain the lowest in the cases considered in this study.

- Evaporated liquid droplets generate overwhelmingly lean mixture in the flame compared to the corresponding premixed gaseous case (i.e. $\phi_g < \phi_{ov}$). The greatest probability of obtaining the stoichiometric mixture composition is observed in the laminar and turbulent globally stoichiometric droplet cases for all droplet diameters. Thus, the proportion of heat release arising from non-premixed mode of combustion is higher in globally stoichiometric droplet cases than in the globally fuel-lean and -rich droplet cases.

- The extent of burning is examined in terms of the temporal evolutions of the volume-integrated fuel reaction rate magnitude normalised by its initial value Ω_F/Ω_{F0}. The values of Ω_F/Ω_{F0} for the droplet cases with initial $\phi_{ov} = 0.8$ are found to be significantly smaller than those with initial $\phi_{ov} = 1.0$ and 1.2. The discrepancy between globally

fuel-lean and stoichiometric droplet cases diminishes with increasing droplet diameter for both under laminar and turbulent flow conditions.

- The temporal behaviour of the burned gas volume shows an important dependence on the overall equivalence ratio. Under both laminar and turbulent conditions, large droplets with initial $\phi_{ov} = 0.8$ have greater burned gas volume than small droplets while an opposite trend is observed for large droplets with initial $\phi_{ov} = 1.0$ and 1.2.

- Flame-droplet interactions considerably affect the distribution of the flame topologies in spray flames. Tilelike local geometries associated with small values of Gauss curvature are found as prevalent feature in premixed gaseous flames. However, droplet cases show a high availability of saddle topologies which occur at negative values of Gauss curvature.

- Under globally fuel-lean conditions, the peak mean value of reaction rate for large droplets with initial $a_d/\delta_{st} = 0.05$ and 0.06 becomes greater than the corresponding premixed flame cases and it declines with decreasing droplet diameter. Contrary to this, the droplet cases with initial $\phi_{ov} = 1.0$ and 1.2 exhibit lower peak mean values than the corresponding premixed flame cases.

- The higher probability of finding positive values of density-weighted displacement speed indicates greater propagation rate for large droplet cases with initial $\phi_{ov} = 0.8$ in comparison to the corresponding premixed flame. For the cases with initial $\phi_{ov} = 1.0$ and 1.2, spray flames propagates slower than the corresponding premixed flames as a result of the greater availability of negative values of of density-weighted displacement speed. Furthermore, the most probable values of density-weighted displacement speed are found smaller than the laminar burning velocity while the most probable values of consumption speed assume comparable values with the laminar burning velocity for all cases.

Chapter 6

Effects of Inertia and Two-Phase Coupling

This chapter discusses the possible impacts of droplet inertia on the evolution of reacting mixture composition, flame surface area and burned gas volume by comparing inertial and hypothetical inertialess droplet cases. In addition to this, the interaction between liquid and gaseous phases is examined based on the source terms due to two-phase coupling arising from droplet evaporation in different governing equations for the gaseous carrier phase.

6.1 Effects of Inertia

The properties of liquid fuel droplets in the presence of a combustible gaseous medium play pivotal roles in the combustion processes in droplet-laden mixtures because the size and number density of the droplets may significantly affect the burning characteristics [43, 47, 118, 119, 149, 151, 155, 159, 217–219]. The dynamic motion of liquid droplets in the carrier gaseous phase determines the mixture composition and flame-droplet interactions, which play key roles in the combustion processes in droplet-laden mixtures. Jog et al. [217] demonstrated the impacts of droplet motion on the flame structure and its modelling for n-heptane droplets. Atzler et al. [218, 219] experimentally investigated the effects of droplet inertia in globally stoichiometric laminar spherically expanding spray flames. It has been proposed that a lag between the droplet and gaseous phase velocities may lead to the local enrichment of fuel vapour in the reaction zone, which can give rise to flame oscillation under some conditions [218, 219]. A similar trend was reported by Lawes and Saat [119] for spherically expanding spray flames indicating that droplet inertia yields a larger equivalence ratio locally for overall fuel-lean mixtures.

Table 6.1: Simulation parameters considered in Section 6.1.

Parameter	Value
a_d/δ_{st}	$0.04, 0.05$ and 0.06
ϕ_{ov}	1.0
$u'/S_{b(\phi_g=1)}$	$0.0, 4.0$ and 8.0
L_{11}/δ_{st}	2.5
Pr	0.7
Le	1.0
$\gamma = C_p^G/C_v^G$	1.4

Flame propagation statistics of spherically expanding turbulent spray flames have been discussed in several experimental [118, 119] and numerical [43–46, 164] studies. However, a systematic understanding of the effects of droplet inertia on the combustion characteristics is still lacking. The purpose of this section is to analyse the influences of droplet inertia on turbulent flame propagation for spherically expanding flames propagating into mono-sized droplet mists with an overall equivalence ratio of unity. The main objective of the current analysis is to compare the reaction zone structure and the evolution of flame surface area and burned gas volume between the actual droplet movement and hypothetical inertialess droplet motion (where the droplets are assumed to have mass but they follow the fluid velocity and thus does not have any acceleration because the relative velocity between particles and the carrier gaseous phase vanishes) under the same flow conditions so that the effects of droplet inertia on flame structure and burning rate under laminar and turbulent conditions can be understood in isolation. For these hypothetical inertialess droplet simulations, $d\overrightarrow{x}_d/dt = \overrightarrow{u}$ and $d\overrightarrow{u}_d/dt = 0$ are considered for numerical experiments and the rest of the expressions for the liquid transport equations (see Eqs. 2.8c and 2.8d) remain unchanged. Parameters used for the simulations in this section are given in Table 5.1

The instantaneous fields of c on the central $x-y$ mid-plane for laminar and turbulent flames with initial $a_d/\delta_{st} = 0.06$ are exemplarily shown in Fig. 6.1 for both inertialess and inertial droplets. Figure 6.1 shows that the droplets decrease in size due to evaporation as they approach the flame for both cases. It can be discerned from Fig. 6.1 that the spatial distributions of droplets are significantly different between inertial and inertialess cases. Moreover, the burned gas region in the inertialess case has been found to be smaller than that obtained for inertial droplets. It is possible to have a smaller burned gas region on a given two-dimensional central mid-plane due to out of plane flame movement but it will be shown later that the burned gas volumes in the inertialess droplet cases have indeed been found to be smaller than in the corresponding inertial droplet cases. Furthermore, inertial droplet cases exhibit larger number density of droplets within the flame than in the cases with inertialess droplets (e.g.

number density of droplets in the region given by $0.01 \leq c \leq 0.99$ in the inertialess droplet cases shown in Fig. 6.1 is 0.86, 0.89 and 0.98 times of the corresponding values for the inertial droplet cases under laminar and turbulent conditions with initial $u'/S_{b(\phi_g=1)} = 4.0$ and 8.0, respectively and the same qualitative behaviour is observed for other values of a_d/δ_{st}). This behaviour is consistent with the experimental observations [119, 218, 219], which suggest that droplets do not couple with gas velocity due to their inertia and therefore can be entrained in the reaction zone. Figure 6.1 reveals that more droplets escape through the flame into the burned gas region due to fluid motion in the inertial droplet cases compared to the corresponding inertialess droplet cases.

As more droplets enter into the flame for inertial droplets, they evaporate due to high temperature and supply fuel vapour in the gaseous phase, which yields a higher value of gaseous equivalence ratio ϕ_g within the flame. This can be substantiated from Fig. 6.2 where the PDFs of ϕ_g in the region corresponding to $0.01 \leq c \leq 0.99$ for inertialess (dashed lines) and inertial (solid lines) droplet cases with initial $a_d/\delta_{st} = 0.04, 0.05$ and 0.06 are shown. The PDFs of ϕ_g in the cases with inertial droplets exhibit a peak at $\phi_g = 1.0$ due to the diffusion mode of burning in spite of overwhelming probability of finding fuel-lean gaseous mixture (i.e. $\phi_g < 1.0$) because the evaporation of droplets is not sufficient to produce $\phi_g = 1.0$ mixture even though ϕ_{ov} remains unity. The probability of finding $\phi_g < 1.0$ mixture within the flame increases with increasing $u'/S_{b(\phi_g=1)}$ because the evaporated fuel is more readily dispersed from the evaporation sites and mixes with surrounding air for large values of $u'/S_{b(\phi_g=1)}$ and this trend is observed for both inertial and inertialess droplets. Figure 6.2 reveals that the probability of finding $\phi_g < 1.0$ is greater for the inertialess droplet cases than in the inertial droplet cases and the peak of the PDF at $\phi_g = 1.0$ is absent for the inertialess cases with initial $u'/S_{b(\phi_g=1)} = 8.0$. Moreover, local pockets of $\phi_g > 1.0$ are obtained all the inertial droplet cases, which arise due to evaporation of fuel vapour from a cloud of droplets in the regions of low mixing rate within the flame but the low number of density of inertialess droplets within the flame eliminates the probability of finding $\phi_g > 1.0$ within the flame. This behaviour is qualitatively similar to the previous experimental findings [119, 218, 219] where a lag between the droplet and gaseous phase velocities was conjectured to responsible for richer mixtures than expected in the reaction zone. It becomes prohibitively expensive to match the exact experimental conditions in DNS, but it has been demonstrated in previous section (see Fig. 4.7) that the variations in flame surface area and burned gas volume during early stages of flame kernel development in response to the droplet diameter for the inertial droplet cases considered here are in qualitative agreement with experimental results [119].

The initial values of Damköhler and Karlovitz numbers for a stoichiometric premixed flame with initial $u'/S_{b(\phi_g=1)} = 4.0\,(8.0)$ are 1.31 and 3.49 (0.65 and 9.88), respectively.

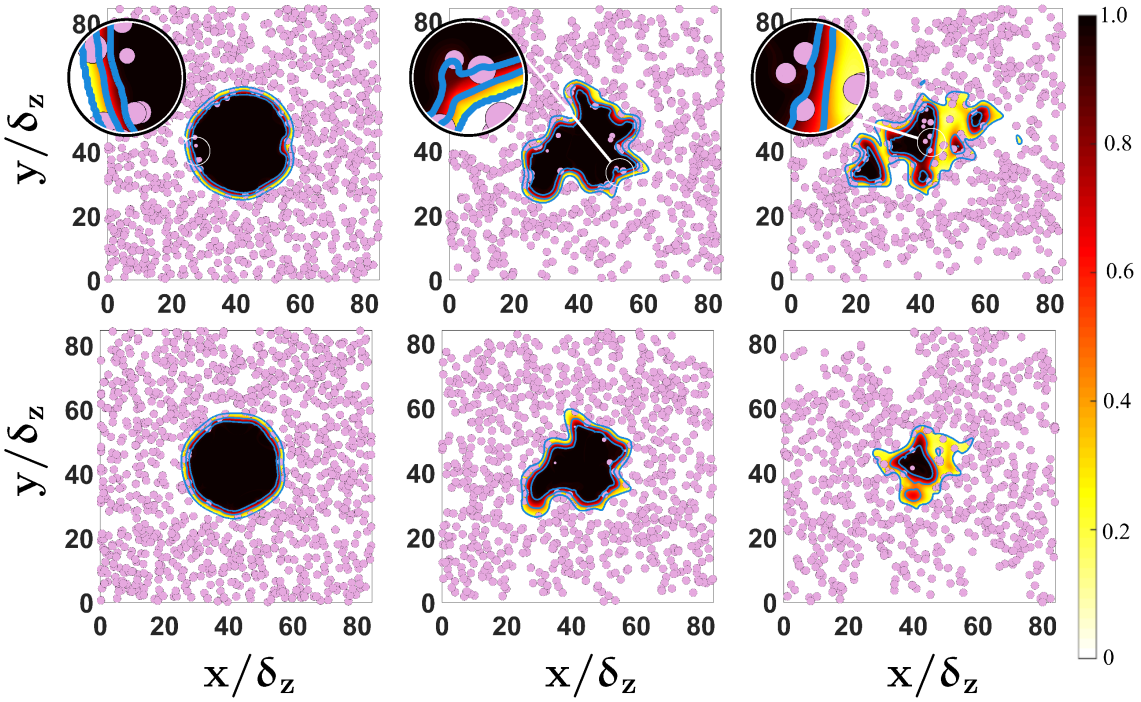

Figure 6.1: Distribution of c (blue lines show $c = 0.1, 0.5$ and 0.9 contours from outer to inner periphery) on the central $x-y$ mid-plane for laminar (1^{st} column) and turbulent flames with initial $u'/S_{b(\phi_g=1)} = 4.0$, 8.0 ($2^{nd} - 3^{rd}$ columns) for inertial (1^{st} row) and inertialess (2^{nd} row) droplet cases with initial $a_d/\delta_{st} = 0.06$. Pink dots show the droplets residing on the plane (not to the scale). Figures 6.1-6.5 correspond to $t = 2.1\alpha_{T0}/S^2_{b(\phi_g=1)}$.

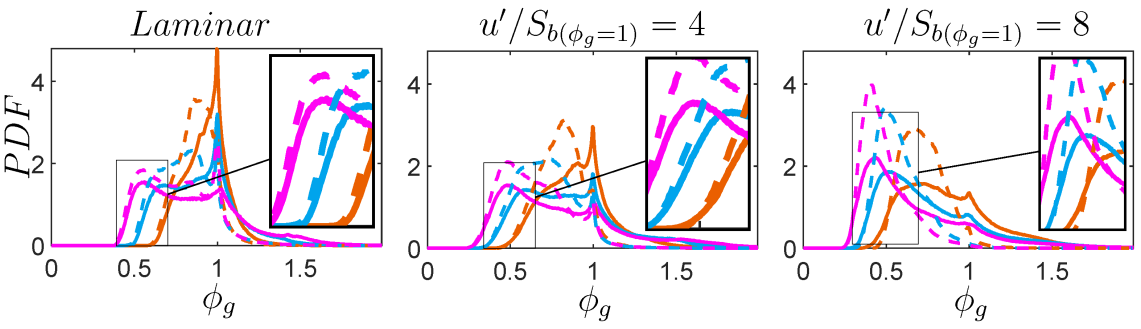

Figure 6.2: PDFs of gaseous equivalence ratio, ϕ_g in the region corresponding to $0.01 \leq c \leq 0.99$ for laminar and turbulent inertial (solid line) and inertialess (dashed line) droplet cases with initial $a_d/\delta_{st} = 0.04$ (——), 0.05 (——) and 0.06 (——).

The predominance of fuel-lean combustion in all the droplet cases implies that the characteristic values of Damköhler number $Da_{(\phi_g)}$ (Karlovitz number $Ka_{(\phi_g)}$) are likely to smaller (greater) than the values obtained for a gaseous stoichiometric premixed flame and this tendency strengthens further with increasing $u'/S_{b(\phi_g=1)}$ due to greater likelihood of obtaining $\phi_g < 1$ within the flame. This further indicates that combustion predominantly takes place in the thickened flame regime with $Da_{(\phi_g)} < 1$ and $Ka_{(\phi_g)} > 1$ for all cases but this tendency is more prevalent in the case of inertialess droplets because of the greater availability of $\phi_g < 1$ mixtures. In the thickened flame regime, turbulent eddies are likely to cause disturbance to the flame structure leading to local flame thickening, which can be discerned from Fig. 6.1. The combination of the predominant fuel-lean combustion (because the flame thickness scales as $\delta \sim \alpha_{T0}/S_{b(\phi_g)}$) and burning in the thickened flame regime leads to a thicker flame in the case of inertialess droplets than in the case of inertial droplets. This can be substantiated from Fig. 6.3 where the mean values of $|\nabla c| \times \delta_{st}$ conditional upon c are presented for different a_d/δ_{st} for both laminar and turbulent flow conditions. The peak mean value of $|\nabla c|$ provides a measure of the inverse of the flame thickness (i.e. $|\nabla c|_{max} \sim 1/\delta$) [193] and Fig. 6.3 shows that the peak mean values of $|\nabla c| \times \delta_{st}$ for the inertialess droplet cases remain smaller than the corresponding inertial droplet cases. The peak mean value of $|\nabla c| \times \delta_{st}$ also decreases with increasing a_d/δ_{st} due to the greater likelihood of fuel-lean combustion for larger droplets. The effects of $u'/S_{b(\phi_g=1)}$ on the behaviours of $|\nabla c| \times \delta_{st}$ for the inertial droplet cases considered here have been discussed in the previous section (see Section 4.1) and thus will not be repeated here. Figure 6.3 shows that the influences of $u'/S_{b(\phi_g=1)}$ on the mean behaviour of $|\nabla c| \times \delta_{st}$ for the inertialess droplets remain qualitatively similar to those for inertial droplets.

The combination of smaller number density of droplets and predominant fuel-lean combustion in the inertialess droplet cases has implications on the droplet-induced flame wrinkling. The droplet-induced flame wrinkling can be illustrated by the PDFs of $\kappa_m \times \delta_{st}$ which are exemplarily shown for $c = 0.8$ isosurface in Fig. 6.4 for the laminar, initial $u'/S_{b(\phi_g=1)} = 4.0$ and 8.0 cases for droplets with initial $a_d/\delta_{st} = 0.04, 0.05$ and 0.06. For a perfectly spherical flame, the PDF of $\kappa_m \times \delta_{st}$ is expected to be a delta function, but the droplet-induced flame wrinkling leads to a range of curvature values in the droplet cases even under laminar conditions. Figure 6.4 shows that the width of the curvature PDFs increases with increasing a_d/δ_{st} for the laminar case as the large droplets take more time to evaporate and thus survive longer within the flame to induce flame wrinkling. The widening of $\kappa_m \times \delta_{st}$ PDFs with increasing a_d/δ_{st} becomes less apparent in turbulent cases because the flame wrinkling induced by fluid motion increasingly eclipses the flame deformation induced by droplets with increasing $u'/S_{b(\phi_g=1)}$, which is consistent with previous experimental findings [118, 119]. However, $\kappa_m \times \delta_{st}$ PDFs for the inertialess droplet cases show higher peaks (or smaller widths) than that

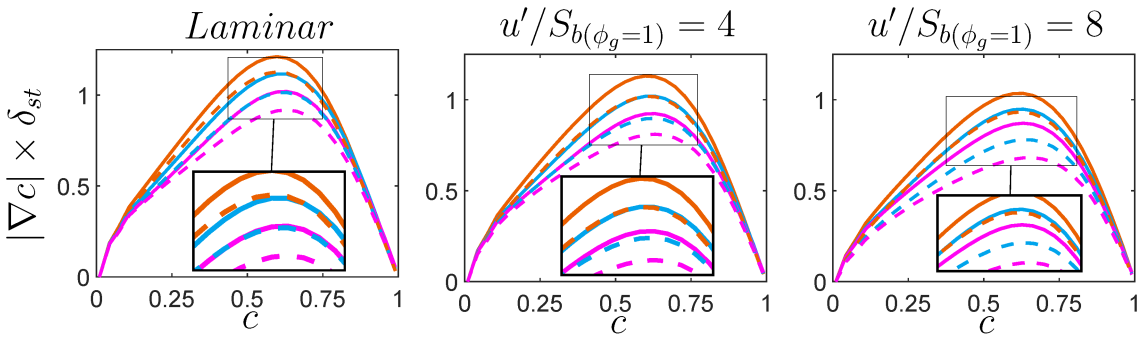

Figure 6.3: Variation of the mean values of $|\nabla c| \times \delta_{st}$ conditional on c for all cases. See Fig. 6.2 caption for the colour keys.

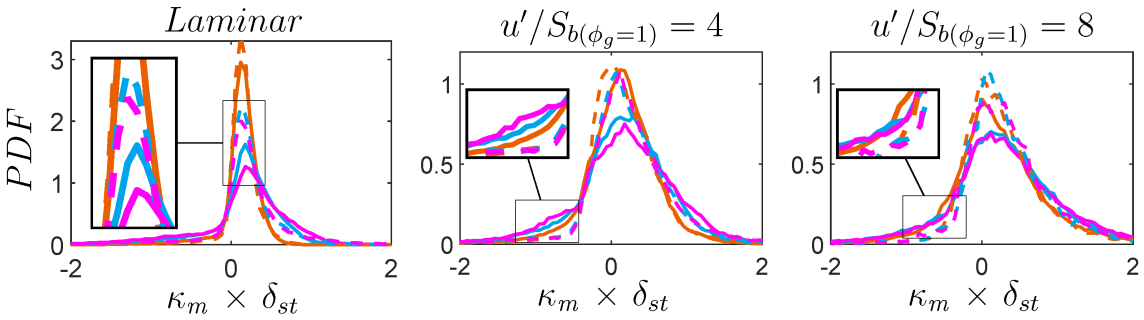

Figure 6.4: PDFs of $\kappa_m \times \delta_{st}$ for $c = 0.8$ isosurface for all cases. See Fig. 6.2 caption for the colour keys.

in the corresponding inertial droplet cases. Figure 6.4 shows that all cases exhibit the overwhelming probability of finding $\kappa_m > 0$, which is expected for spherically expanding flames. However, the probability of finding $\kappa_m < 0$ increases with increasing $u'/S_{b(\phi_g=1)}$.

The greater likelihood of $\phi_g < 1$ in the inertialess droplet cases also has implications on the flame structure. Figure 6.5 demonstrates the contributions of premixed and non-premixed mode of combustion to the total heat release rate. Laminar cases exhibit a higher contribution of premixed mode to the total heat release rate than those in turbulent flow conditions because of the weaker mixing rate under laminar conditions (see Fig. 6.2). The percentage of overall heat release rate arising from the non-premixed mode of combustion strengthens with increasing a_d for both inertial and inertialess droplets due to the slow evaporation of large droplets. The diffusion flame stabilises at the stoichiometric mixture, and thus the reduced availability of $\phi_g = 1.0$ mixture within the flame for inertialess droplets (see Fig. 6.2) leads to the smaller extent of heat release due to the non-premixed mode of combustion in comparison to the iner-

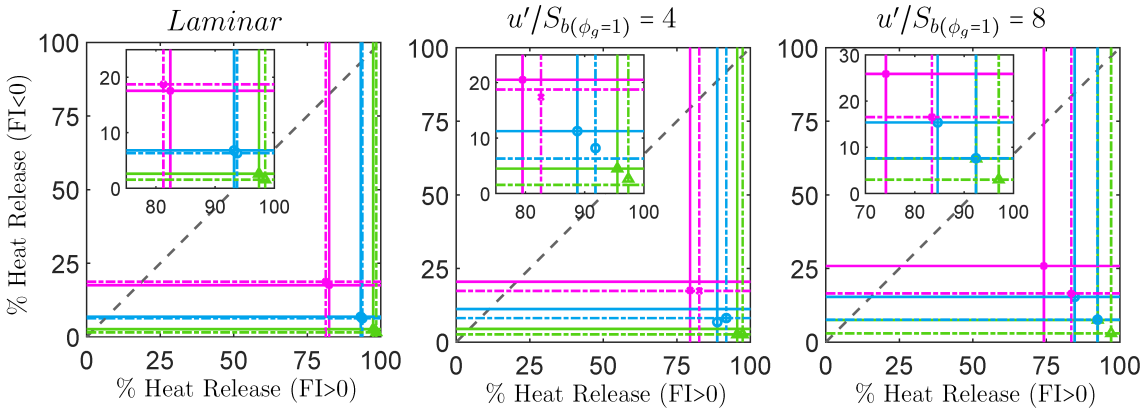

Figure 6.5: Percentage of heat release arising from premixed ($FI > 0$) and non-premixed ($FI < 0$) modes of combustion for inertial (solid line) and inertialess (dashed line) droplet cases with initial $a_d/\delta_{st} = 0.04$ (△), 0.05 (◯), 0.06 (×).

tial droplets. Although there can be local occurrences of edge flame propagation, heat release in these cases takes place predominantly under premixed mode, and therefore such cases were referred to as premixed sprays in previous studies [150, 156].

As the rate of heat release is the highest for the stoichiometric mixtures, the reduced extent of heat release rate due to non-premixed combustion in the case of inertialess droplets gives rise to smaller extent of burning in comparison to the inertial droplet cases. This can be substantiated from Figs. 6.6 and 6.7 where the temporal evolutions of flame surface area $A = \int_V |\nabla c| dV$ (normalised by $4\pi r_0^2$) and volume of the gas with $c \geq 0.99$ normalised by $4\pi r_0^3/3$ (i.e. $V_b/[(4\pi r_0^3)/3]$) are shown, respectively. Figures 6.6 and 6.7 reveal that $A/4\pi r_0^2$ and $V_b/[(4\pi r_0^3)/3]$ for inertialess droplets assume smaller values than those obtained for inertial droplets. It can further be seen from Figs. 6.6 and 6.7 that both A and V_b decrease with increasing a_d in spite of higher percentage of heat release due to non-premixed combustion for larger droplet diameters (see Fig. 6.5). This behaviour arises due to the reduced burning rate as a result of high probability of finding fuel-lean mixtures within the flame due to slow evaporation rate for large droplets (see Fig. 6.4). Figure 6.6 reveals that the temporal evolution of $A/4\pi r_0^2$ for the cases with inertialess droplets follows a similar behaviour at early stages of kernel development but the trend changes considerably at later times. The temporal evolution of $A/4\pi r_0^2$ for the initial $u'/S_{b(\phi_g=1)} = 8.0$ case especially shows a decreasing trend for large inertialess droplets (e.g. initial $a_d/\delta_{st} = 0.05$ and 0.06) at $t > 1.20\alpha_{T0}/S^2_{b(\phi_g=1)}$ and this decreasing trend is observed also for $V_b/[(4\pi r_0^3)/3]$ for the inertialess droplets with initial $a_d/\delta_{st} = 0.06$ for the initial $u'/S_{b(\phi_g=1)} = 8.0$ case.

The inertialess droplets track the fluid velocity, which is directed from the centre of the kernel towards the unburned gas. This leads to depletion of droplets from the flame with time

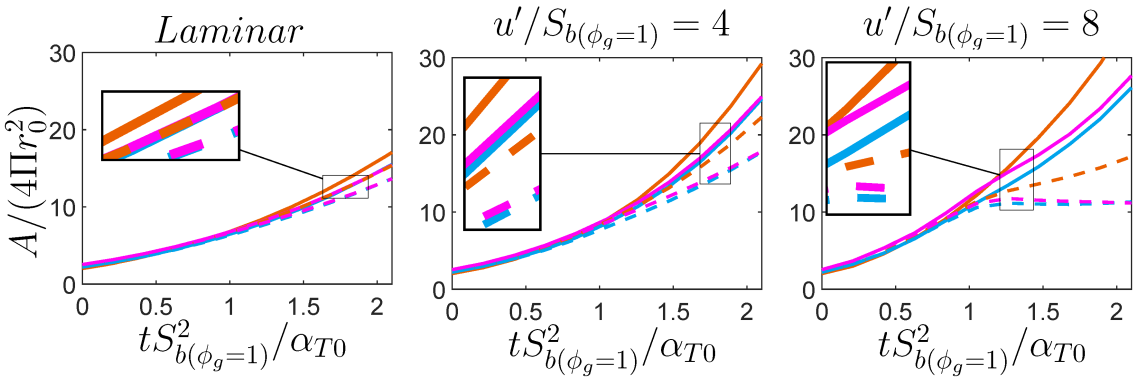

Figure 6.6: Temporal evolution of normalised flame surface area $A/4\pi r_0^2$. See Fig. 6.2 caption for the colour keys.

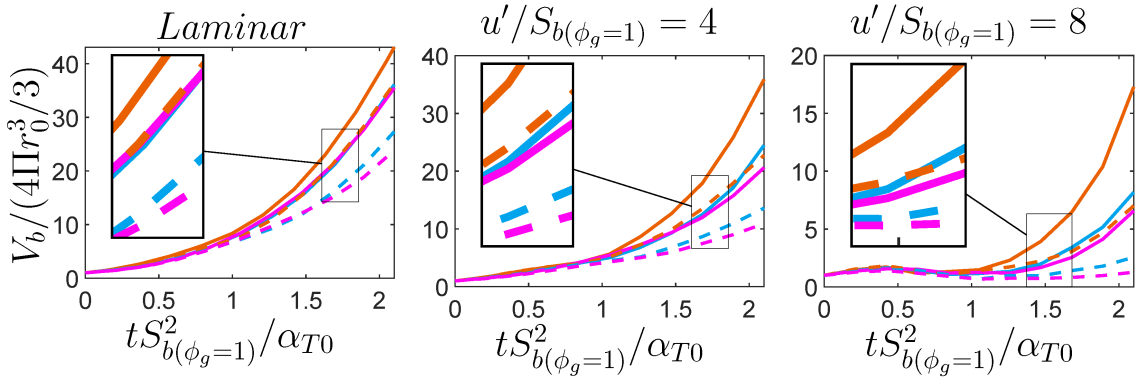

Figure 6.7: Temporal evolution of burned gas volume $V_b/(4\pi r_0^3/3)$ of the region with $c \geq 0.99$. See Fig. 6.2 caption for the colour keys.

and thus reduces the availability of evaporated fuel within the burned gas, which is further aided by faster dispersion of evaporated fuel vapour from sparsely distributed evaporation sites due to higher rate of mixing for larger values of $u'/S_{b(\phi_g=1)}$. Thus, the reduced number density of the droplets within the flame for slowly evaporating large inertialess droplets (e.g. initial $a_d/\delta_{st} = 0.05$ and 0.06 cases) under strong diffusion of fuel vapour from the evaporation sites for large values of $u'/S_{b(\phi_g=1)}$ gives rise to a reduction in the mean value of ϕ_g within the flame as time progresses and eventually the mixture within the flame becomes so fuel-lean that the heat release rate is superseded by the heat transfer from the flame kernel. Under these conditions, the flame kernels for large inertialess droplets (e.g. initial $a_d/\delta_{st} = 0.05$ and 0.06 cases) under high turbulence intensity (e.g. initial $u'/S_{b(\phi_g=1)} = 8.0$ case) shrink instead of growing with time. This is responsible for decreasing trends of $A/4\pi r_0^2$ and $V_b/[(4\pi r_0^3)/3]$ for large turbulence intensity at late times (i.e. $t > 1.20\alpha_{T0}/S_{b(\phi_g=1)}^2$), which may lead to eventual flame extinction.

6.2 Statistics of Two-Phase Coupling in Turbulent Spherically Expanding Flames in Fuel-Droplet Mists

Turbulent combustion of droplet-laden mixtures involves complex interactions between combustion, heat transfer, droplet evaporation and fluid turbulence. A thorough knowledge of the interaction between liquid droplets and carrier gaseous phase is necessary for the purpose of the fundamental understanding and modelling of turbulent spray flames. The experimental observations for spherically expanding spray flames revealed that the interactions between flame, turbulence and droplets are strongly affected by droplet diameter and overall equivalence ratio [119]. The coupling between dispersed and carrier phases plays a fundamental role in predicting the transport of mass, momentum and energy in the carrier gaseous phase for reacting [50] and non-reacting [220] turbulent multi-phase flows. DNS provide an important opportunity to analyse the statistical behaviours of the contributions in the carrier phase due to its coupling with the dispersed phase in droplet-laden mixtures thanks to recent advancements in high-performance computing [41, 44, 45, 47, 50, 105, 220]. Baba and Kurose [70] used a DNS database as a reference to validate a modified flamelet/progress variable approach for gaseous and spray flames. Gaseous phase total enthalpy was found to be affected significantly by the heat and mass transfer from the dispersed liquid phase. It was suggested that new combustion models are needed for more accurate prediction of gaseous temperature in case of spray combustion. Sreedhara and Huh [54] proposed a simple linear model for the conditional evaporation rate and compared the model with DNS data for n-heptane spray

Table 6.2: Simulation parameters considered in Section 6.2.

Parameter	Value
a_d/δ_{st}	0.04, 0.05 and 0.06
ϕ_{ov}	0.8, 1.0 and 1.2
$u'/S_{b(\phi_g=1)}$	4.0
L_{11}/δ_{st}	2.5
Pr	0.7
Le	1.0
$\gamma = C_p^G/C_v^G$	1.4

flames. They found that droplet size and velocity play a vital role on the flame characteristics. Wang and Rutland [67] reported that the overall equivalence ratio plays a key role in the spray flame behaviour and in the modelling of evaporation, reaction and scalar dissipation rates. Previous DNS analyses ([99, 100]) indicated that the gaseous phase combustion takes place predominantly in fuel-lean mode even for the overall fuel-rich fuel-air mixtures because of the differences in time-scales for evaporation and chemical reactions, which, in turn, influence the resulting combustion and mixing processes. A thorough understanding of the aforementioned behaviour and its influence on the subsequent combustion processes necessitate a detailed analysis of the interaction between liquid and gaseous phases, which serves as the motivation for the current analysis. To meet this objective, the statistics of liquid and gaseous phase interactions in turbulent combustion of droplet-laden mixtures is considered in the current analysis. In this respect, the main objectives are (a) to reveal the influences of overall equivalence ratio and droplet diameter on the terms arising from coupling between the Eulerian (i.e. gaseous carrier phase) and Lagrangian (i.e. droplets) phases in the conservation equations of mass, momentum, energy, reaction progress variable, and mixture fraction in the gaseous phase for spherically expanding flames propagating into droplet-laden mixtures, (b) to explain the observed behaviours of the aforementioned influences based on physical principles and indicate their modelling implications. Table 6.2 summarises the parameters used for the present simulations.

The statistically spherical flames in mono-sized droplet-mists are exemplarily visualized in Fig. 6.8 by reaction progress variable isosurface $c = 0.5$ for $\phi_{ov} = 0.8, 1.0$ and 1.2 in the case of the largest droplet diameter (i.e. $a_d/\delta_{st} = 0.06$). It can be seen from Fig. 6.8 that the flames surrounded by liquid n-heptane droplets (shown by green spheres) are wrinkled principally due to turbulent fluid motion. A lean overall equivalence ratio (i.e. $\phi_{ov} = 0.8$) yields a smaller droplet number density in comparison to stoichiometric overall equivalence ratio (i.e. $\phi_{ov} = 1.0$) and this implies relative smaller availability of evaporated fuel in the gaseous carrier phase than in the case of $\phi_{ov} = 1.0$. Hence, the case with $\phi_{ov} = 0.8$ has a

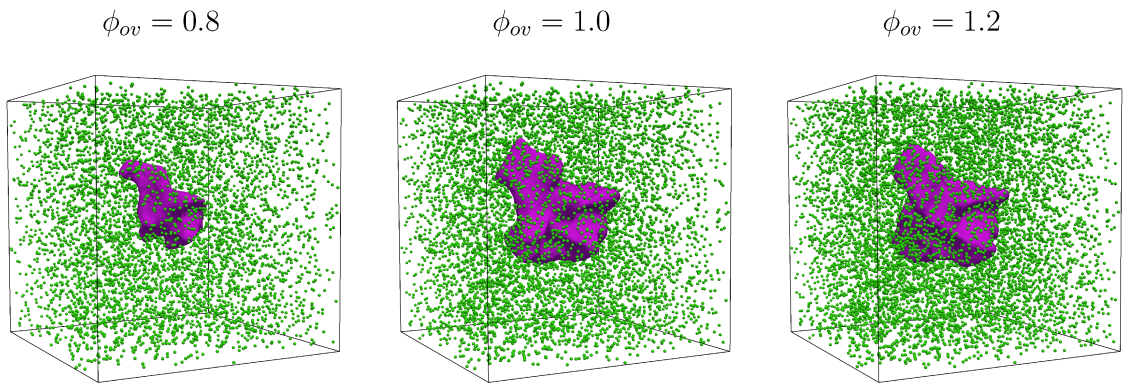

Figure 6.8: Instantaneous isosurfaces of reaction progress variable $c = 0.5$ for $\phi_{ov} = 0.8, 1.0$ and 1.2 cases with initial $a_d/\delta_{st} = 0.06$ at simulation time of $2.1t_{chem}$. Green spheres represent liquid droplets (not to the scale).

smaller volume of $c \geq 0.5$ than the corresponding $\phi_{ov} = 1.0$ and 1.2 cases.

As droplets interact with the spherically expanding flame, they get heated and create gaseous fuel in their surroundings as a result of evaporation. This process leads to an inhomogeneous combustible gaseous fuel-air mixture in the domain. Liquid droplets shrink in size as they move through the flame and some droplets escape through the flame due to turbulent fluid motion and finally evaporate in the fully burned gas region. The gaseous phase equivalence ratio ϕ_g in the unburned gas remains smaller than the overall equivalence ratio ϕ_{ov} for all droplet diameters but this trend is more prominent for larger droplets (see Fig. 5.2). Occurrences of locally fuel-rich/lean regions within the flame are strongly dependent on droplet size and number density of droplets and this behaviour of evaporating droplets can be substantiated from the PDFs of normalised gaseous equivalence ratio ϕ_g/ϕ_{ov}, which are shown in Fig. 6.9 for different c ranges. It can be seen from Fig. 6.9 that the gaseous phase equivalence ratio ϕ_g remains smaller than the overall equivalence ratio ϕ_{ov} throughout the flame but this tendency is particularly prevalent towards the unburned gas side of the flame (i.e. small values of c). Furthermore, Fig. 6.9 shows that the probability of finding $\phi_g < \phi_{ov}$ increases with increasing droplet diameter due to slow evaporation of large droplets. This is reflected in the decreasing trend of the mean value of ϕ_g/ϕ_{ov} with increasing a_d. The most probable value of the gaseous equivalence ratio ϕ_g remains close to the overall equivalence ratio ϕ_{ov} for small droplets with initial $a_d/\delta_{st} = 0.04$ due to the high evaporation rate of small droplets. It can be discerned from Fig. 6.9 that both the most probable and mean values of ϕ_g/ϕ_{ov} also mildly increase with increasing values of c due to complete evaporation of some of the droplets which enter into the flame structure. However, Fig. 6.9 shows that there is also a finite probability of finding $\phi_g/\phi_{ov} > 1.0$ for all cases but this tendency strengthens for large droplets towards

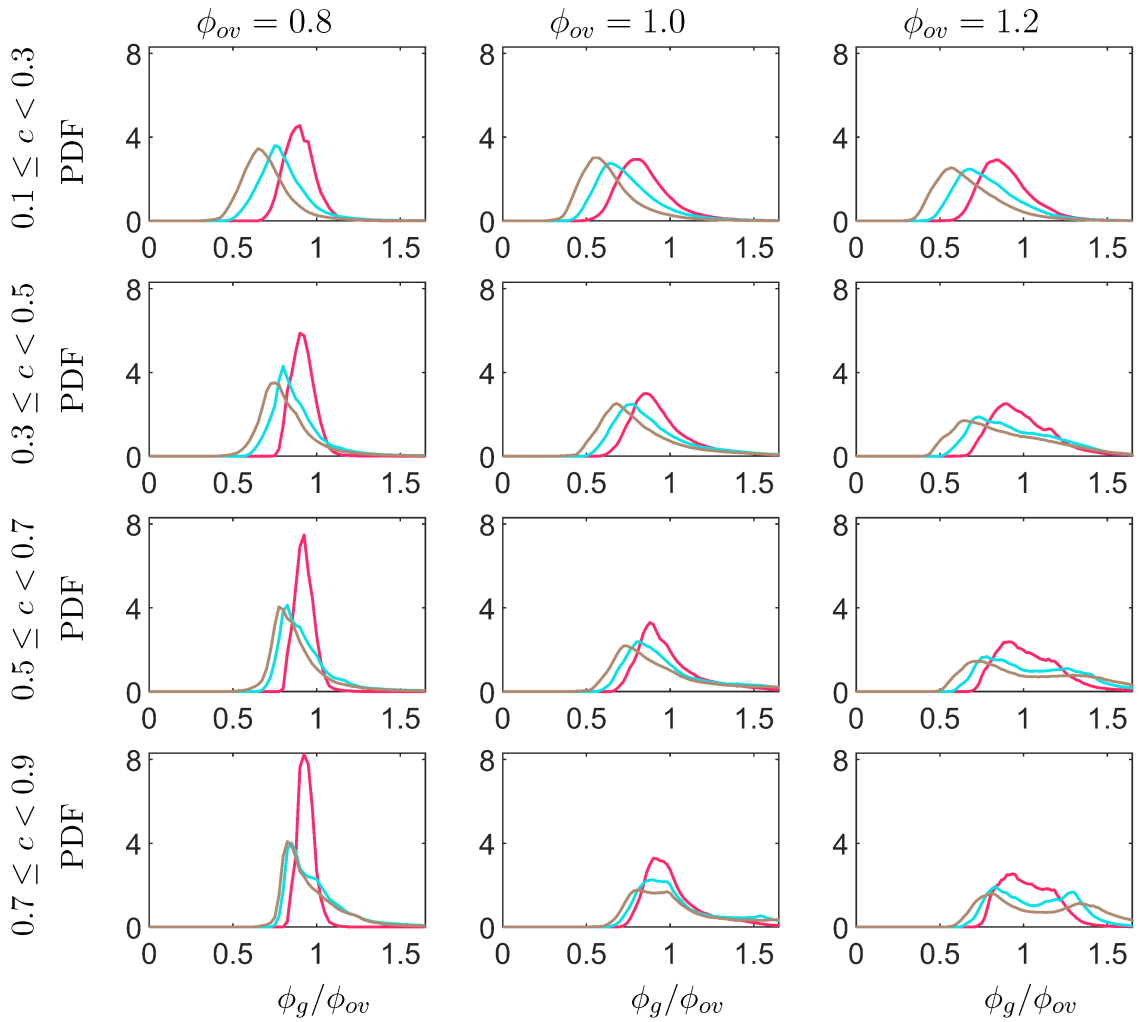

Figure 6.9: PDFs of ϕ_g/ϕ_{ov} on different c ranges for different initial droplet radii $a_d/\delta_{st} = 0.04$ (——), 0.05 (——) and 0.06 (——) cases and for different overall equivalent ratios $\phi_{ov} = 0.8$ (1^{st} column), 1.0 (2^{nd} column) and 1.2 (3^{rd} column).

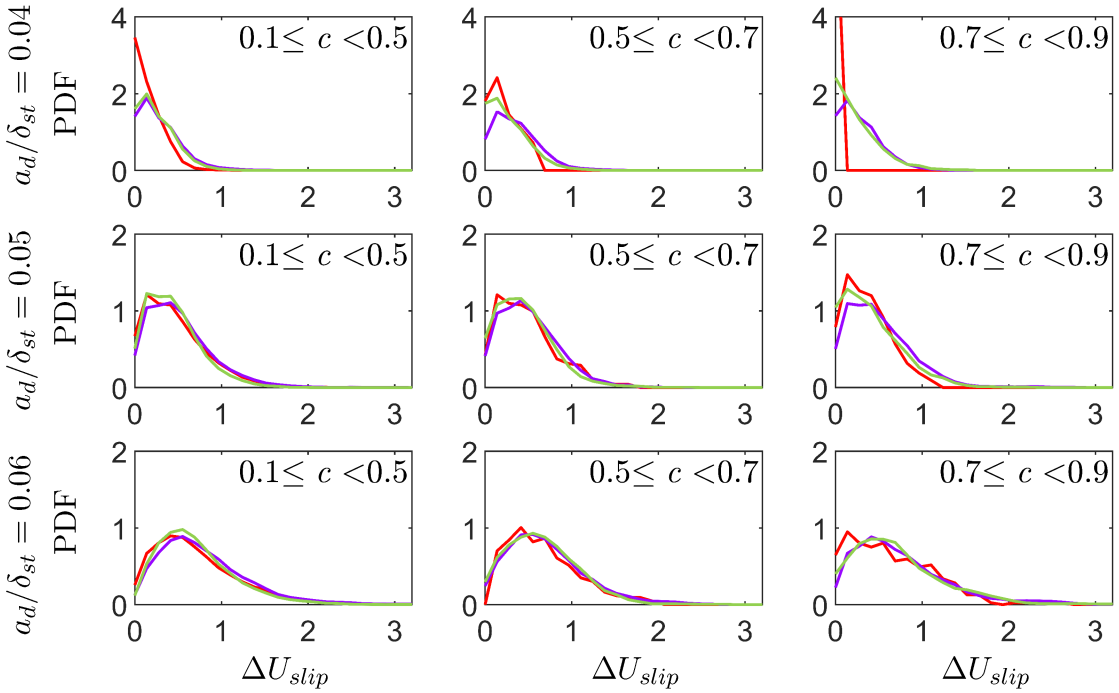

Figure 6.10: PDFs of ΔU_{slip} on different c ranges for different $\phi_{ov} = 0.8$ (——), 1.0 (——) and 1.2 (——) cases and for different initial droplet radii $a_d/\delta_{st} = 0.04$, 0.05 and 0.06 with initial turbulence intensity $u'/S_{b(\phi_g=1)} = 4.0$.

the burned gas side of the flame, which can also be seen in the ϕ_g distributions shown in Fig. 5.2. For example, slow evaporation of large droplets with initial $a_d/\delta_{st} = 0.06$ can generate locally fuel-rich pockets in the reaction zone when the evaporated fuel vapour from isolated evaporation sites does not mix sufficiently with the surrounding air. However, this trend is less prominent in the cases with initial $a_d/\delta_{st} = 0.04$ due to faster evaporation of droplets and larger number density of evaporation sites than in the initial $a_d/\delta_{st} = 0.06$ case for a given value of ϕ_{ov}. This tendency progressively weakens with increasing ϕ_{ov} and can be seen most prominently for $\phi_{ov} = 0.8$ because of small number density of droplets. The above discussion suggests that the evaporation characteristics of droplets play a key role in the mixture distribution and subsequent combustion in the gaseous phase. Thus, it is worthwhile to consider the effects of droplets on the evolutions of key quantities in the gaseous carrier phase.

It can be appreciated from Eqs. 2.7a-2.11 that the velocity difference between the droplets and the surrounding carrier gas (known as slip velocity) is likely to affect the momentum transport of the gaseous carrier phase and also the droplet movement. Therefore, it is worthwhile to examine the statistical properties of the normalised magnitude of the slip velocity, $\Delta U_{slip} = |\overrightarrow{u}(\overrightarrow{x}_d,t) - \overrightarrow{u}_d|/S_{b(\phi_g=1)}$. The PDFs of the normalised slip velocity $\triangle U_{slip} = |\overrightarrow{u}(\overrightarrow{x}_d,t) - \overrightarrow{u}_d|/S_{b(\phi_g=1)}$, are presented in Fig. 6.10 for different regions within the flame.

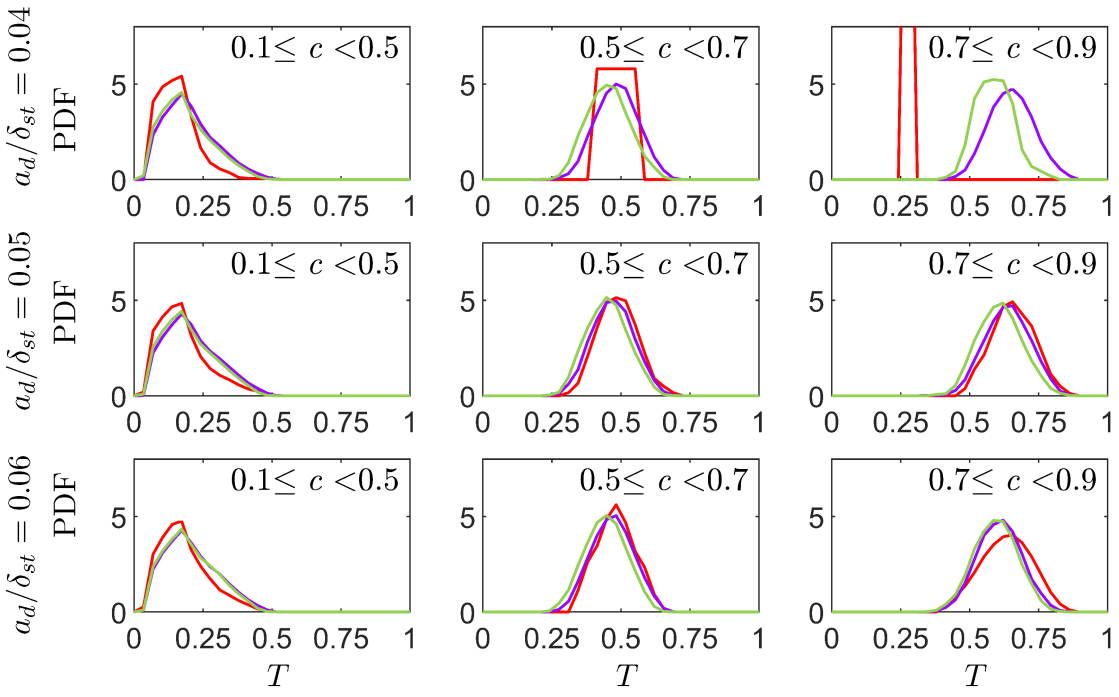

Figure 6.11: PDFs of non-dimensional temperature difference between droplets and surrounding gaseous phase T on different c ranges for different $\phi_{ov} = 0.8$, 1.0 and 1.2 cases and for different initial droplet radii $a_d/\delta_{st} = 0.04$, 0.05 and 0.06 with initial turbulence intensity $u'/S_{b(\phi_g=1)} = 4.0$. See Fig. 6.10 caption for the colour keys.

These PDFs are computed using samples from the droplet positions for different ranges of reaction progress variable, c across the flame. It can be seen from Fig. 6.10 that the probability of obtaining higher magnitude of ΔU_{slip} increases with increasing droplet diameter because larger droplets are subjected to stronger inertial effects which yield a deviation of droplet velocity from gaseous phase velocity. This behaviour also influences the distribution of the gaseous equivalence ratio. The maximum value of ΔU_{slip} remains close to unity for all values of ϕ_{ov} in the cases with the initial droplet diameter $a_d/\delta_{st} = 0.04$ except for the rear end of the reaction zone (i.e. $0.7 \leq c < 0.9$) in the $\phi_{ov} = 0.8$ case due to the combination of a small droplet number density and relatively rapid evaporation of small droplets. Furthermore, the PDFs of ΔU_{slip} peak at zero value for the initial droplet diameter $a_d/\delta_{st} = 0.04$, whereas the peak PDF values are obtained at non-zero values of ΔU_{slip} for droplets with initial diameters of $a_d/\delta_{st} = 0.05$ and 0.06. For larger droplets (i.e. initial $a_d/\delta_{st} = 0.06$ cases) the PDFs of ΔU_{slip} show a wider distribution in the flame but the distributions of ΔU_{slip} remain mostly insensitive to the variations of ϕ_{ov}.

It is possible for some droplets to penetrate into the flame structure and even escape into the burned gas. This implies that there is a temperature difference between the gaseous phase

and droplets. The statistical behaviour of the droplet temperature in turn affects the source term arising from two-phase coupling in the energy conservation equation (see Eq. 2.7b). Figure 6.11 shows the PDFs of non-dimensional temperature difference between the droplets and surrounding gaseous phase, $T = (\hat{T} - T_d)/(T_{ad(\phi_g=1)} - T_0)$ for different ranges of c. In the preheat zone (i.e. $0.1 \leq c < 0.5$), T remains smaller than 0.5 for all cases considered in this section. As droplets move further towards the reaction zone, the most probable values of T increase for the initial $a_d/\delta_{st} = 0.05$ and 0.06 cases for all values of ϕ_{ov} and also for the initial $a_d/\delta_{st} = 0.04$ case for $\phi_{ov} = 1.0$ and 1.2, which suggests that the droplets in these cases may not fully evaporate even when the reaction zone is approached and this eventually gives rise to predominantly fuel-lean mixture within the flame. In the initial $a_d/\delta_{st} = 0.04$ case for $\phi_{ov} = 0.8$, the PDF of T at the rear end of reaction zone is found to be narrower and the most probable value of θ has been found to be smaller than those in the corresponding $\phi_{ov} = 1.0$ and 1.2 cases. Due to smaller number density, the number of droplets which survive in the reaction zone, and the gaseous phase equivalence ratio ϕ_g remain small in the $\phi_{ov} = 0.8$ case with initial $a_d/\delta_{st} = 0.04$ in comparison to those in the corresponding $\phi_{ov} = 1.0$ and 1.2 cases. This leads to smaller burned gas temperature (see Fig 5.3) and consequently smaller most probable value and narrower PDF of T in the $\phi_{ov} = 0.8$ case with initial $a_d/\delta_{st} = 0.04$ than in the corresponding $\phi_{ov} = 1.0$ and 1.2 cases.

The slip velocity and temperature difference between droplets and the gaseous carrier phase, in turn, affect the evaporation rate through the temperature dependence of the Spalding number B_d, which plays a key role in the evolution of droplet diameter. The source terms associated with two-phase coupling arising from droplet evaporation in the gaseous phase conservation equations provide physical insights into the flame-droplet interactions, which is important for the purpose of understanding the contributions of droplets to the Eulerian phase transport equations of mass, momentum, energy and scalars such as mixture fraction and reaction progress variable.

Scatter plots of the normalised source term in the mass conservation equation $\Gamma_m \times \delta_{st}/\rho_0 S_{b(\phi_g=1)}$ with reaction progress variable c coloured by normalised source terms in momentum transport equations $\{\dot{S}_{u_1}, \dot{S}_{u_2}, \dot{S}_{u_3}\} \times \delta_{st}/\rho_0 S^2_{b(\phi_g=1)}$ (see Eq. 2.7a) are shown in Fig. 6.12. The mean values of $\Gamma_m \times \delta_{st}/\rho_0 S_{b(\phi_g=1)}$ conditional on c are shown by the black lines. The $\phi_{ov} = 0.8$ cases exhibit negligible droplet contributions on the burned gas side due to small number density. It can be seen from Fig. 6.12 that the scatter increases with increasing ϕ_{ov} due to the increases in the number of evaporation sites. The small droplets evaporate rapidly, and thus the droplets with initial $a_d/\delta_{st} = 0.04$ mostly evaporate towards the unburned gas side of the flame front. Although the evaporation rate increases with decreasing diameter for individual droplets, the large droplets survive longer within the flame due to their larger size

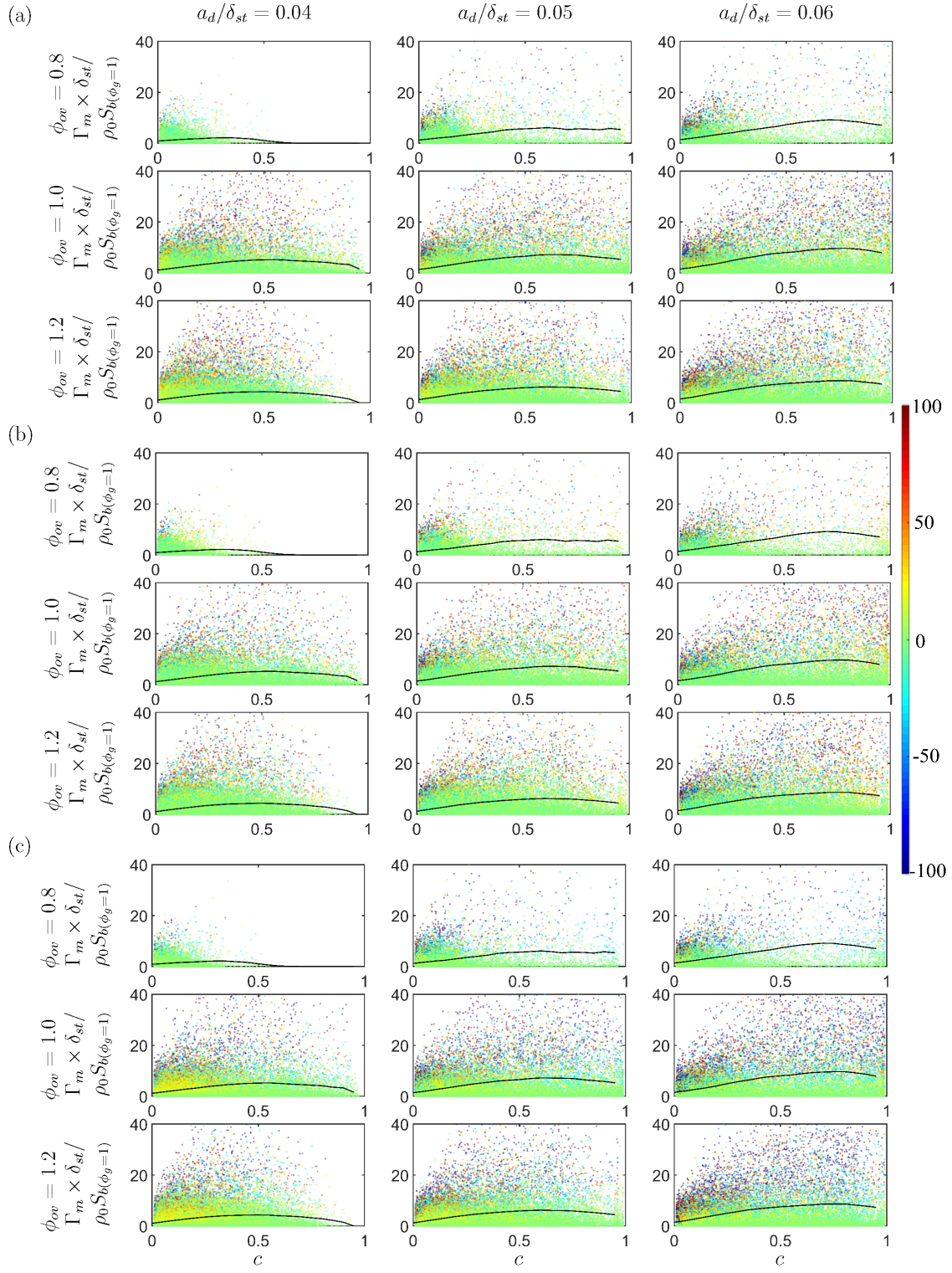

Figure 6.12: Scatter of $\Gamma_m \times \delta_{st}/\rho_0 S_{b(\phi_g=1)}$ as a function of c coloured with (a) $\dot{S}_{u_1} \times \delta_{st}/\rho_0 S^2_{b(\phi_g=1)}$, (b) $\dot{S}_{u_2} \times \delta_{st}/\rho_0 S^2_{b(\phi_g=1)}$ and (c) $\dot{S}_{u_3} \times \delta_{st}/\rho_0 S^2_{b(\phi_g=1)}$ for different values of ϕ_{ov}. Black line shows the variation of the mean values of $\Gamma_m \times \delta_{st}/\rho_0 S_{b(\phi_g=1)}$ conditional on c in Figs.6.12-6.16.

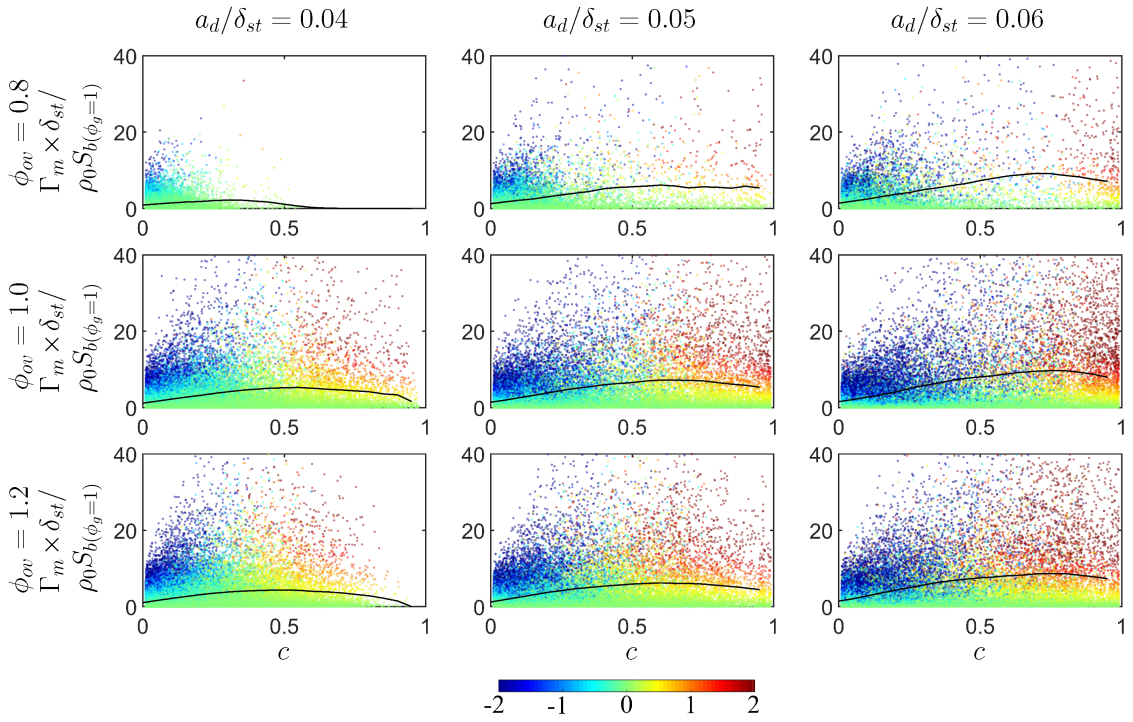

Figure 6.13: Scatter of $\Gamma_m \times \delta_{st}/\rho_0 S_{b(\phi_g=1)}$ as a function of c coloured with $\dot{S}_e \times \delta_{st}/\rho_0 C_p T_0 S_{b(\phi_g=1)}$ for different values of ϕ_{ov}.

and slow evaporation rate. Thus, the mean values of $\Gamma_m \times \delta_{st}/\rho_0 S_{b(\phi_g=1)}$ conditional on c within the flame for initial $a_d/\delta_{st} = 0.05$ and 0.06 cases remain greater than that in the initial $a_d/\delta_{st} = 0.04$ case. This trend is particularly prominent for large values of c due to high values of temperature associated with these samples.

Figures 6.12a-c demonstrate that strong negative and positive contributions of $\{\dot{S}_{u_1}, \dot{S}_{u_2}, \dot{S}_{u_3}\} \times \delta_{st}/\rho_0 S^2_{b(\phi_g=1)}$ are found predominantly in the unburned gas region where high values of $\Gamma_m \times \delta_{st}/\rho_0 S_{b(\phi_g=1)}$ exist for the initial $a_d/\delta_{st} = 0.04$ cases for $\phi_{ov} = 0.8$. However, local occurrences of large positive and negative values of $\{\dot{S}_{u_1}, \dot{S}_{u_2}, \dot{S}_{u_3}\} \times \delta_{st}/\rho_0 S^2_{b(\phi_g=1)}$ are obtained throughout the flame front for $\phi_{ov} = 1.0$ and 1.2 cases but this tendency, especially towards the burned gas side, strengthens for larger droplet cases (i.e. initial $a_d/\delta_{st} = 0.05$ and 0.06 cases). In spite of local occurrences of high positive and negative values of $\{\dot{S}_{u_1}, \dot{S}_{u_2}, \dot{S}_{u_3}\} \times \delta_{st}/\rho_0 S^2_{b(\phi_g=1)}$, the most probable value of these terms $\{\dot{S}_{u_1}, \dot{S}_{u_2}, \dot{S}_{u_3}\} \times \delta_{st}/\rho_0 S^2_{b(\phi_g=1)}$ remains generally positive.

Scatter plots of $\Gamma_m \times \delta_{st}/\rho_0 S_{b(\phi_g=1)}$ with c coloured by the normalised source term associated with two-phase coupling in the energy conservation equation (i.e. $\dot{S}_e \times \delta_{st}/\rho_0 C_p T_0 S_{b(\phi_g=1)}$, (see Eq. 2.7b)) are shown in Fig. 6.13 as a function of reaction progress variable c. Figure 6.13 shows that $\dot{S}_e \times \delta_{st}/\rho_0 C_p T_0 S_{b(\phi_g=1)}$ assumes predominantly negative values in the unburned

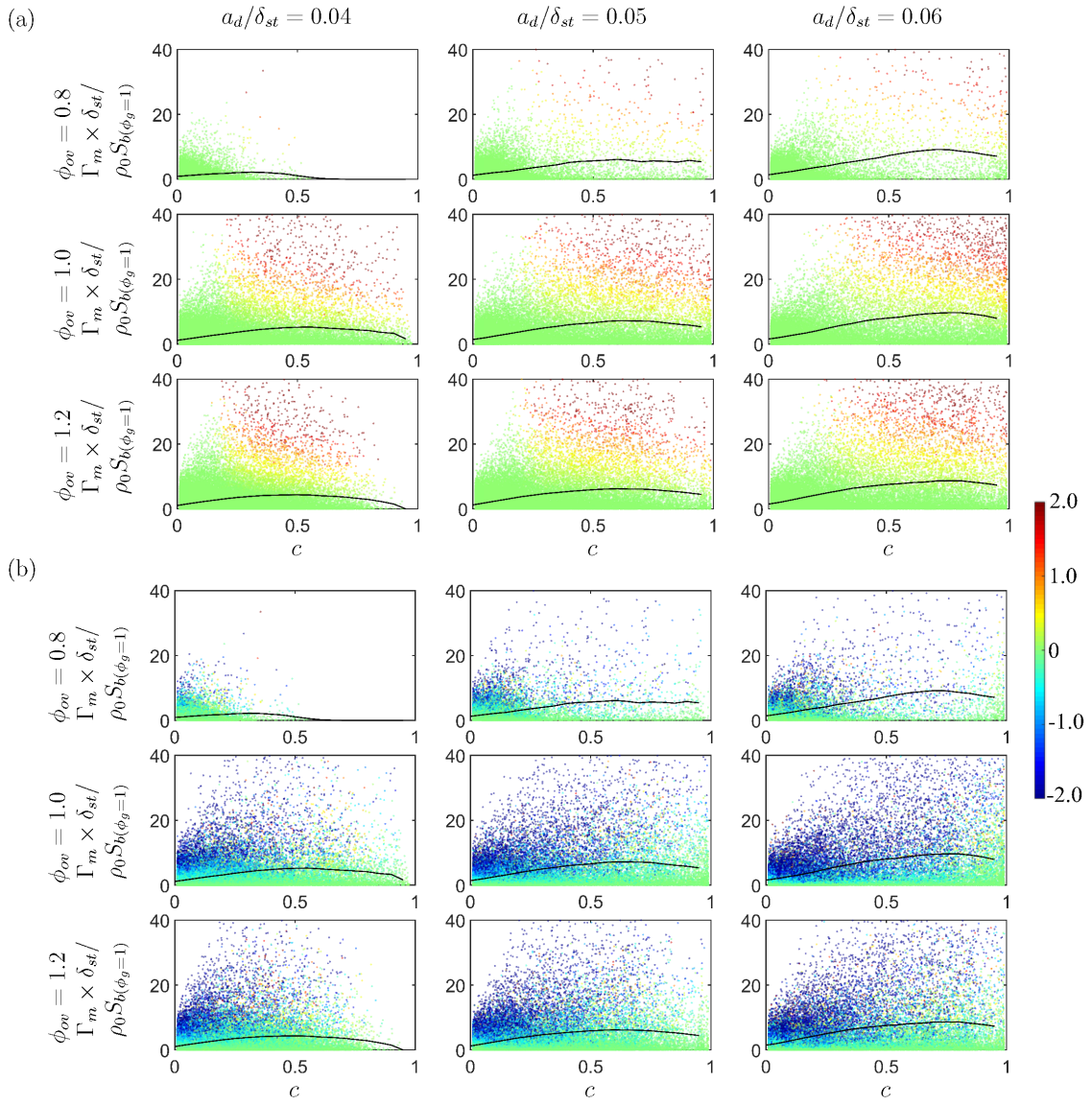

Figure 6.14: Scatter of $\Gamma_m \times \delta_{st}/\rho_0 S_{b(\phi_g=1)}$ as a function of c coloured with the terms (a) $\dot{S}_{e,1} \times \delta_{st}/\rho_0 C_p T_0 S_{b(\phi_g=1)}$ and (b) $\dot{S}_{e,2} \times \delta_{st}/\rho_0 C_p T_0 S_{b(\phi_g=1)}$ which constitute the total normalised source term associated with droplet evaporation in the energy transport equation $\dot{S}_e \times \delta_{st}/\rho_0 C_p T_0 S_{b(\phi_g=1)} = (\dot{S}_{e,1} + \dot{S}_{e,2}) \times \delta_{st}/\rho_0 C_p T_0 S_{b(\phi_g=1)}$.

gas side whereas the trend changes in burned gas to positive values. This behaviour can be explained in the following manner. The source term associated with droplet evaporation in the energy transport equation can be rearranged as:

$$\dot{S}_e = -(1/V)\left[\sum_d C_p^L T_d (dm_d/dt) + \sum_d C_p^L m_d (dT_d/dt)\right] \tag{6.1}$$

Here, droplet diameter and temperature are two important parameters which have influences on the sign of contribution. The evaporation of droplets leads to $(dm_d/dt) < 0$, which acts to give rise to a positive value of $\dot{S}_e$. Therefore, a negative value of $\dot{S}_e$ is obtained when (dT_d/dt) is positive (i.e. $dT_d/dt > 0$) and positive $\sum_d C_p^L m_d (dT_d/dt)$ dominates over negative $\sum_d C_p^L T_d (dm_d/dt)$. In order to understand behaviour of $\dot{S}_e$ across the flame, it is useful to consider the contributions of its two components $\dot{S}_{e,1} = -(1/V)\sum_d C_p^l T_d (dm_d/dt)$ and $\dot{S}_{e,2} = -(1/V)\sum_d C_p^L m_d (dT_d/dt)$. Accordingly, the scatter of $\Gamma_m \times \delta_{st}/\rho_0 S_{b(\phi_g=1)}$ as a function of c are coloured by the terms $\dot{S}_{e,1} \times \delta_{st}/\rho_0 C_p T_0 S_{b(\phi_g=1)}$ and $\dot{S}_{e,2} \times \delta_{st}/\rho_0 C_p T_0 S_{b(\phi_g=1)}$ in Figs. 6.14a and 6.14b, respectively. Towards the unburned gas side negative $\dot{S}_{e,2}$ overwhelms positive $\dot{S}_{e,1}$ (see Fig. 6.14) to yield predominantly negative values of $\dot{S}_e$. It can be seen from Figs. 6.12 and 6.13 that $\Gamma_m = -(1/V)\sum_d (dm_d/dt)$ remains positive and its magnitude increases from the unburned to burned gas side for $\phi_{ov} = 1.0$ and 1.2 cases and it is not clearly evident for $\phi_{ov} = 0.8$ because droplets are not present towards the burned gas side due to small number density. The large positive values of $\Gamma_m = -(1/V)\sum_d (dm_d/dt)$ and relatively large values of T_d towards the burned gas side lead to predominantly positive values of $\dot{S}_{e,1}$ (see Fig. 6.14a), which eventually leads to positive values of $\dot{S}_e$ towards the burned gas side. However, on the unburned gas side, the magnitudes of $\Gamma_m = -(1/V)\sum_d (dm_d/dt)$ (and therefore $\dot{S}_{e,1}$) remain small in magnitude (see Fig. 6.14a), and thus the positive value of dT_d/dt is responsible for negative values of $\dot{S}_{e,2}$ and $\dot{S}_e$ (see Fig. 6.14b). However, it is possible to have locally negative values of dT_d/dt on both unburned and burned gas side of the flame. It has already been discussed and can also be seen from Fig. 5.3 that some of droplets escape through the flame and reach the burned gas side due to turbulent fluid motion and get heated up. Some of these droplets are brought back into the relatively cold gases from the burned gas by turbulent vortical motion, and heat transfer can locally take place from these hot droplets to the locally cooler carrier gaseous phase (in other words $dT_d/dt < 0$ and locally positive values of $\dot{S}_{e,2}$ in Fig. 6.14b), and this tendency strengthens with increasing ϕ_{ov} as the possibility of droplets reaching the high temperature zone, escaping through the flame and eventually coming back to low temperature gas, increases with increasing number density. This locally negative (positive) value of $dT_d/dt(\dot{S}_{e,2})$ also acts to promote positive values of $\dot{S}_e$ towards the burned gas side of the flame.

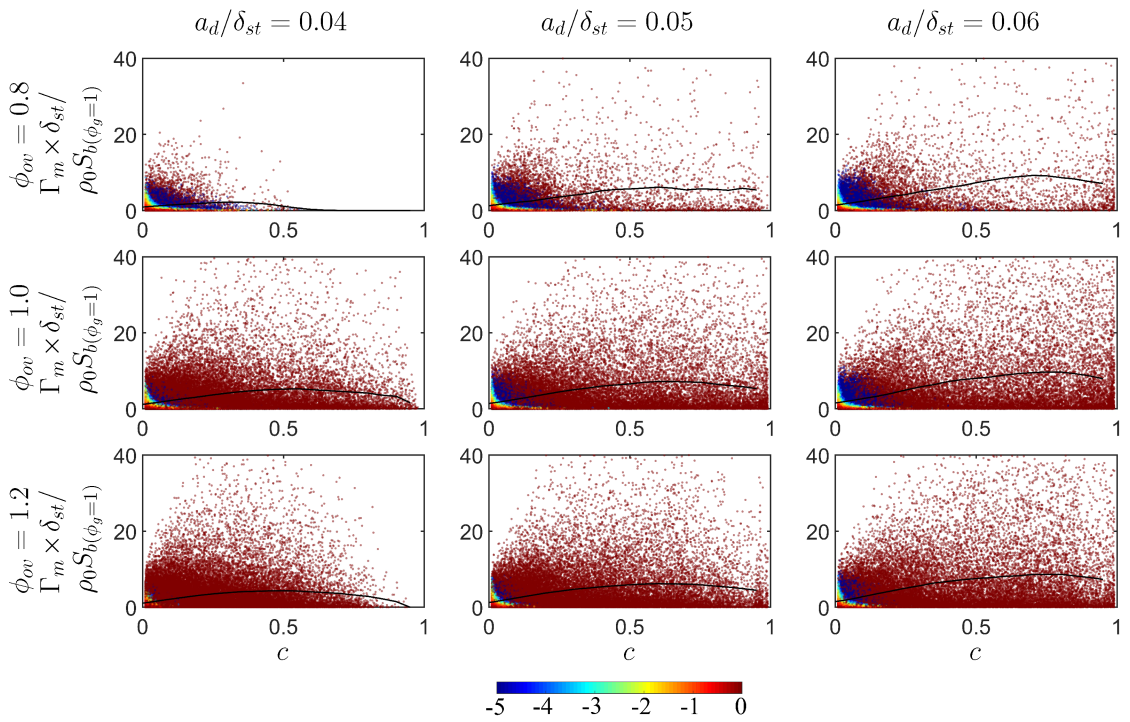

Figure 6.15: Scatter of $\Gamma_m \times \delta_{st}/\rho_0 S_{b(\phi_g=1)}$ as a function of c coloured with $\dot{S}_c^* \times \delta_{st}/\rho_0 S_{b(\phi_g=1)}$ for different values of ϕ_{ov}.

It has been demonstrated in Eqs. 2.52 and 2.56 that the evaporation rate (in the other words the source term in the mass conservation equation in the gaseous phase) affects the evolution of reaction progress variable and mixture fraction and therefore it is worthwhile to examine the effects of two-phase coupling on reaction progress variable and mixture fraction transport equations. The scatter plots of $\Gamma_m \times \delta_{st}/\rho_0 S_{b(\phi_g=1)}$ with c coloured by the normalised source terms due to droplet evaporation in reaction progress variable (see Eq. 2.52) and mixture fraction transport equations (see Eq. 2.56) are shown in Figs. 6.15 and 6.16, respectively. Figure 6.15 reveals that droplet evaporation has limited influence on the transport equation of c and relatively high magnitudes of negative $\dot{S}_c^*$ are obtained only at the leading edge of the flame front. It has been demonstrated earlier that the magnitude of the mean value of $\dot{S}_{liq,c}$ remains small in comparison to those of $\nabla \cdot (\rho D \nabla c)$ throughout the flame (and also $\dot{w}_c$ in the reaction zone) (see Fig. 5.15) and combustion in these cases takes place predominantly in premixed mode. The high probabilities of small values of $\Gamma_m \times \delta_{st}/\rho_0 S_{b(\phi_g=1)}$ within the flame, which is further damped on multiplication with c and the small magnitudes of $\dot{S}_{liq,c}$ [47] lead to small magnitudes of $\dot{S}_c^*$ irrespective of ϕ_{ov} and a_d. This suggests that the reaction progress variable evolution in the carrier gaseous phase in these flames resembles to the progress variable evolution in stratified mixtures and the evaporation affects the reaction progress variable transport

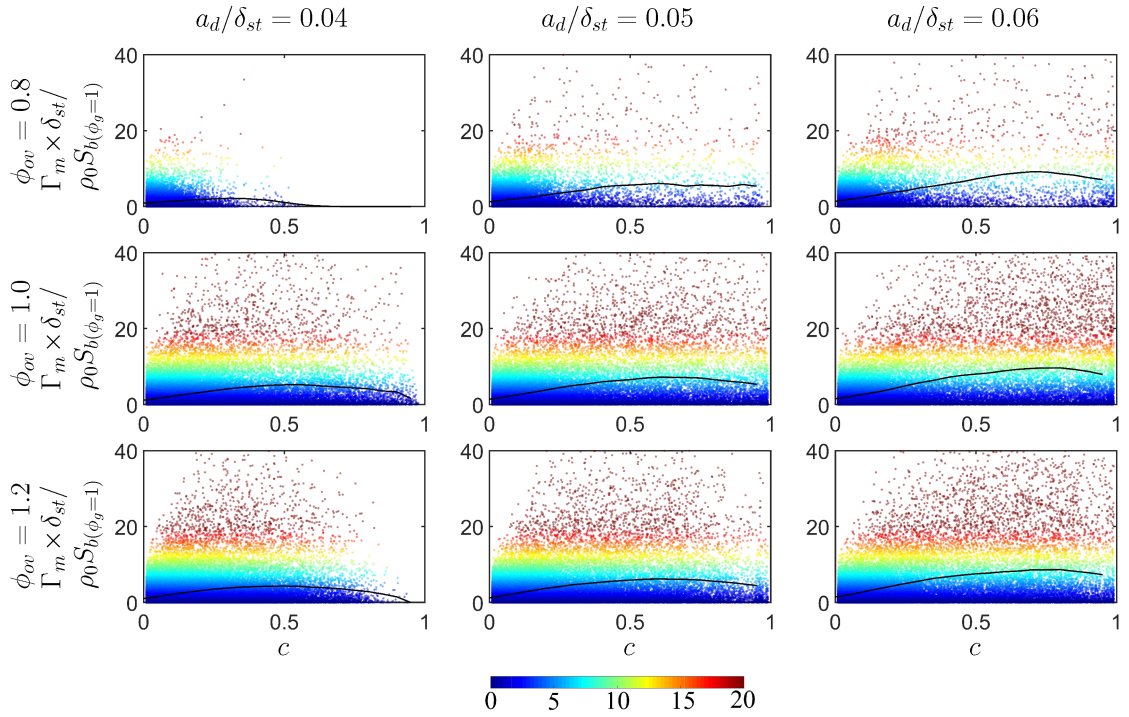

Figure 6.16: Scatter of $\Gamma_m \times \delta_{st}/\rho_0 S_{b(\phi_g=1)}$ as a function of c coloured with $\dot{S}^*_\xi \times \delta_{st}/\rho_0 S_{b(\phi_g=1)}$ for different values of ϕ_{ov}.

principally through the reaction rate of the resulting inhomogeneous mixture but not through $\dot{S}^*_c$. Therefore, the modelling of reaction progress variable evolution employed for turbulent stratified flames can be utilised for the kind of droplet-laden flames considered here and $\dot{S}^*_c$ can be ignored from the reaction progress variable evolution without incurring significant errors.

Figure 6.16 shows that $\dot{S}^*_\xi$ remains small for most of the samples within the flame front but large magnitudes of $\dot{S}^*_\xi$ are associated with large values of Γ_m and this trend strengthens with increasing droplet diameter for a given overall equivalence ratio. It is worthwhile to note that the variation of mixture fraction ξ provides a measure of mixture inhomogeneity. The extent of mixture inhomogeneity increases as a result of evaporation, which is reflected in the increasing trend of $\dot{S}^*_\xi$ with increasing Γ_m. This is consistent with previously mentioned locally fuel-rich pockets in the reaction zone for large droplets (e.g. initial $a_d/\delta_{st} = 0.06$ cases) with overall lean equivalence ratio $\phi_{ov} = 0.8$, whereas this behaviour is not observed for small droplets with initial $a_d/\delta_{st} = 0.04$ due to faster evaporation of droplets. The simultaneous occurrence of large magnitudes of $\dot{S}^*_\xi$ and Γ_m suggests that the possible model expressions for these quantities cannot be independent of each other.

6.3 Summary of Key Findings

The dynamic motion of liquid droplets in terms of droplet inertia and the implications of the two-phase coupling have been analysed for turbulent spherically expanding flames propagating into droplet-laden mixtures using three dimensional DNS. The main findings can be summarised as follows:

- Evaporation of inertial droplets leads a reacting mixture which has a greater likelihood of obtaining stoichiometric composition in the flame compared to that of inertialess droplets. Locally fuel-rich pockets are barely formed within the flame for the cases with inertialess droplets due to the presence of smaller number of droplets within the flame.

- As the number density of droplets within the flame is greater for inertial droplet cases than the corresponding inertialess droplet cases, the degree of droplet-induced flame wrinkling enhances in inertial droplet cases and this is quantified with the broader PDFs of flame curvature for inertial droplet cases.

- The flame front becomes thicker in the inertialess droplet cases in comparison to the corresponding inertial droplet cases. The reduced availability of stoichiometric mixture in inertialess droplet cases induces the decline of the percentage of heat release rate associated with non-premixed combustion. Furthermore, flame surface area and burned gas volume for the inertialess droplet cases are found to be smaller than the corresponding cases with inertial droplets.

- The effect of overall equivalence ratio on the slip velocity is found to be insignificant for the cases considered in this thesis. However, the broader spread of slip velocity in the cases with large droplets indicates the importance of droplet diameter on the behaviour of slip velocity.

- The evaporation rate is expressed based on the source term in the mass conservation equation in the gaseous phase and the mean evaporation rate of large droplets remains greater than that of small droplets in the region close to the burned gas side.

- The rapid evaporation of droplets in the reaction zone leads high values of dm_d/dt in magnitude which yields positive contribution of the source term associated with two-phase coupling to the energy conservation equation along with the relatively large values of droplet temperature.

- The source terms arising due to droplet evaporation considerably contribute to the mass, momentum, energy and mixture fraction conservation equations in the gaseous phase,

but the contribution of droplet evaporation is found to be relatively modest for the reaction progress variable transport equation.

Chapter 7

Effects of Configuration: V-Shaped Spray Flames

This chapter investigates the gaseous phase combustion behaviour in a V-shaped flame configuration where fuel is supplied in the form of liquid droplets such that an overall equivalence ratio of unity is maintained in the unburned gas. The gaseous premixed V-shaped flames with the same flow conditions are utilised to compare the flame propagation in V-shaped spray flames with that in the corresponding gaseous premixed flame cases. Furthermore, the behaviours of some important features of spray combustion including flame wrinkling, the composition of reacting mixture and flame propagation in V-shaped spray flames are compared to those in spherically expanding spray flames.

7.1 Flame-Droplet-Turbulence Interaction

The V-shaped flame is one of the most commonly used laboratory-scale configurations, which has been extensively investigated in previous experimental [116, 117, 221–228] and numerical [63, 64, 229–232] studies. Smith and Gouldin [221] proposed an experimental methodology to measure turbulent flame speed in V-shaped turbulent methane-air flames with different equivalence ratios and turbulence intensities. Veynante et al. [222, 223] used experimental data of turbulent premixed propane-air V-flames to analyse the flame surface density transport statistics. Gouldin [224] and Shepherd [225] investigated the burning and flame propagation rates by measuring the flame surface area in turbulent premixed V-shaped flames. Shepherd [225] compared a stagnation point flame with a V-shaped flame and identified important differences in flame structure and burning rate between the two flames. A similar conclusion was drawn by Dunstan et al. [63] based on DNS. Sattler et al. [226] observed a linear increase

in the mean flamelet area with downstream distance by taking measurements at several axial distances from the stabilizing rod for turbulent premixed methane/air V-flames. The flame topology and flame brush thickness for turbulent V-flames at different turbulence intensities have been experimentally investigated by Kheirkhah and Gulder [233]. Vena et al. [116, 117] experimentally analysed flame topology and heat release rate statistics for turbulent V-flames for stratified iso-octane/air mixtures. It was shown by Vena et al. [116] that equivalence ratio gradients have significant effects on flame wrinkling in comparison to the corresponding fully premixed reference flame. Sponfeldner et al. [227] concentrated on the statistical behaviours of principal strain-rates and the local flamelet normal vector in their experimental analysis of turbulent premixed V-flames.

Detailed and parametric analyses of V-shaped flames based on DNS emerged with the advancements of high-performance computers. Alshaalan and Rutland [229] performed a three-dimensional DNS analysis with a single-step chemical mechanism to analyse the adiabatic and non-adiabatic flame-wall interactions in a V-flame configuration. Domingo et al. [230] utilised two-dimensional DNS and LES of turbulent premixed V-flames for the development and validation of FSD-PDF closures in the context of LES. Bell et al. [231] carried out three-dimensional DNS for a laboratory-scale turbulent premixed V-shaped flame and reported a good agreement in the mean flame structure and the mean axial and transverse velocities between the DNS results and experimental data. Wu et al. [232] investigated the ignition and propagation of a V-shaped premixed ethylene-air turbulent flame using LES and an increase in flame angle is observed relative to the laminar cases. Dunston et al. [63, 64] performed an extensive three-dimensional DNS analysis with single-step chemistry for premixed V-flames under different turbulence intensities. The expression derived for the turbulent displacement speed showed a similar trend with the turbulent consumption speed in the downstream of the flame. However, qualitative differences between the turbulent displacement and consumption speeds originate due to turbulent and molecular diffusion [63].

Despite significant practical relevance of turbulent combustion of droplet-laden mixtures, the V-flame configuration has rarely been used [228] for the analysis of spray combustion. Letty et al. [228] carried out experiments to understand the combustion behaviour of V-shaped flames in heptane droplet-laden mixtures. They compared temperature distributions between droplets and gaseous phase mixture and indicated that the presence of droplets significantly alters the temperature of the gaseous mixture. However, the flame propagation statistics for droplet-laden mixtures in a V-shaped flame configuration are still incompletely understood due to the complex interaction between droplets, flame and the background fluid flow. To address this gap in the existing literature, three-dimensional carrier phase DNS simulations with modified single-step chemistry have been performed in this section for three different

Table 7.1: Simulation parameters considered in Chapter 7.

Parameter	Value
Initial droplet diameter, a_d/δ_{st}	$0.04, 0.05$ and 0.06
Overall Equivalence ratio, ϕ_{ov}	1.0
Heat release parameter, $\tau = (T_{ad(\phi_g=1)} - T_0)/T_0$	6.54
Unburned gas temperature at the inlet, T_0	300 K
Mean velocity at the inlet, $u_{mean}/S_{b(\phi_g=1)}$	5.0 and 10.0
Inlet turbulence, $u'/S_{b(\phi_g=1)}$	2.0
Integral length scale, L_{11}/δ_{st}	2.5
Prandtl number, Pr	0.7
Lewis number, Le	1.0
Ratio of specific heats, $\gamma = C_p^G/C_v^G$	1.4
Stokes number, St	0.13

droplet diameters for an overall equivalence ratio of unity in the unburned droplet-laden mixture. The important simulation parameters used in this chapter are summarised in Table 7.1. In this respect, the main objectives of this analysis are: (i) to demonstrate the evolution of the gaseous reacting mixture composition within the flame at different axial locations from the flame holder for V-shaped flames propagating in droplet-laden mixtures, (ii) to explain the influences of droplet diameter and mean inflow velocity on the reaction zone structure and flame propagation characteristics at different axial locations from the flame holder and to explain the differences in flame structure arising from supplying the fuel in liquid form by comparing to a turbulent gaseous stoichiometric premixed V-shaped flame, (iii) to indicate implications of the above findings in the context of modelling of turbulent combustion of droplet-laden mixtures.

The contours of reaction progress variable c, gaseous equivalence ratio ϕ_g and fuel reaction rate magnitude $|\dot{w}_F| \times \delta_{st}/\rho_0 S_{b(\phi_g=1)}$ on the central $x-y$ mid-plane at $t = 2.0t_{flow}$ are shown in Fig. 7.1 for initial droplet diameters $a_d/\delta_{st} = 0.04, 0.05, 0.06$ with a mean inlet velocity of $u_{mean}/S_{b(\phi_g=1)} = 5.0$. The droplets residing on the plane are illustrated by grey dots. It can be seen from the reaction progress variable distributions shown in Fig. 7.1 that the background fluid turbulence creates wrinkling on the flame surface. It is worth noting that fuel is supplied in the form of liquid droplets at the inlet which is placed on the left-hand side of the domain. Liquid fuel droplets, distributed randomly but statistically uniform in space at the inlet plane, are introduced with a temperature of $T_0 = 300K$. The mass flux of liquid fuel at the inlet plane is estimated based on the values of u_{mean} and ϕ_{ov}. These droplets shrink in size due to evaporation as they approach the flame (see insets in Fig. 7.1) and the combustion of the evaporated gaseous fuel sustains the V-shaped flame. It can be seen from Fig. 7.1 that small droplets with initial $a_d/\delta_{st} = 0.04$ mostly complete their evaporation by halfway in the streamwise direction

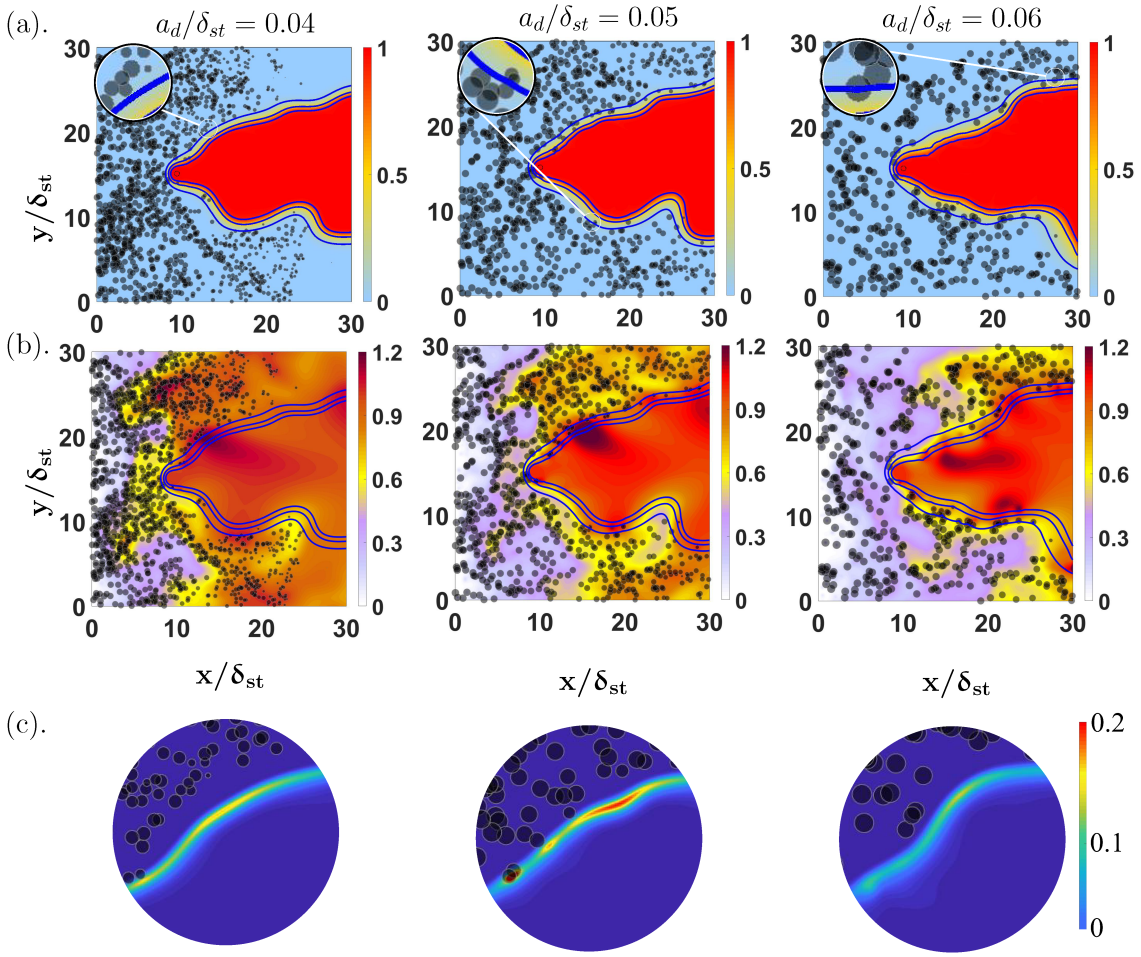

Figure 7.1: Instantaneous distributions of (a) reaction progress variable c (b) gaseous equivalence ratio ϕ_g and (c) fuel reaction rate magnitude $|\dot{w}_F| \times \delta_{st}/\rho_0 S_{b(\phi_g=1)}$ on the central $x-y$ midplane for initial $a_d/\delta_{st} = 0.04, 0.05, 0.06$ at $t = 2.0t_{flow}$. Blue lines show $c = 0.1, 0.5$ and 0.9 contours from outer to inner periphery and grey dots show the droplets residing on the plane (not to scale).

due to their high evaporation rate, whereas large droplets with initial $a_d/\delta_{st} = 0.05$ and 0.06 survive longer due to their lower evaporation rate and interact more with the flame than smaller droplets. Although an overall stoichiometric fuel-air mixture is provided in the unburned gas (note that fuel in the gaseous phase is absent at the inlet), the evaporation ahead of the flame is not sufficient to produce a gaseous stoichiometric mixture (i.e. $\phi_g = 1.0$) and this tendency is particularly prevalent for the case with initial $a_d/\delta_{st} = 0.06$. Although the gaseous phase combustion in V-flames takes place under $\phi_g < 1.0$ for all droplet cases, the likelihood of finding fuel-air mixture corresponding to $\phi_g \approx 1.0$ is comparatively higher for the initial $a_d/\delta_{st} = 0.04$ case. This behaviour arises due to the faster evaporation of smaller droplets. Some of the droplets penetrate the flame structure in the $a_d/\delta_{st} = 0.06$ case and they eventually evaporate in the reaction zone and in the burned gas to produce local islands of fuel-rich (i.e. $\phi_g > 1.0$) mixtures. It is worth noting that the evaporation of droplets leads to higher availability of fuel vapour, which in turn gives rise to local islands of high reaction rate magnitude $|\dot{w}_F| \times \delta_{st}/\rho_0 S_{b(\phi_g=1)}$ as can be seen from Fig. 7.1c where the magnified views of the regions with $\phi_g \approx 1.0$ are shown. The latent heat of evaporation L_v affects the temporal evolution of droplet temperature dT_d/dt through the Spalding number B_d. Most droplets complete their evaporation process in the reaction zone, and thus the latent heat of evaporation acts to reduce the temperature and reaction rate magnitude, but the availability of the fuel vapour due to evaporation tends to increase reaction rate magnitude. The relative strengths of these two competing effects determine the net effect of the latent heat on the reaction zone. However, the extraction of the latent heat reduces the temperature of the gas within the preheat zone which acts to reduce the most probable burned gas temperature in comparison to the adiabatic flame temperature of the stoichiometric mixture. This was discussed earlier by Nakamura et al. [52] and Wacks et al. [47] and the qualitatively similar behaviour has been observed in the flames considered here and thus are not explicitly shown here.

In order to illustrate the composition of the gaseous phase mixture within the flame, the PDFs of the gaseous phase equivalence ratio ϕ_g within the region given by $0.01 \leq c \leq 0.09$ at three different axial locations (i.e. at distances $x/\delta_{st} = 9, 13$ and 17 from the flame holder, which are indicated as locations A, B and C, respectively) are presented in Fig. 7.2. It is evident from Fig. 7.2 that combustion predominantly takes place under fuel-lean mode for all locations and droplet diameters. However, the cases with small droplets (i.e. initial $a_d/\delta_{st} = 0.04$ and 0.05 cases) show a considerable likelihood of finding $\phi_g \approx 1.0$, especially at locations B and C. Furthermore, the PDF of ϕ_g for large droplets with initial $a_d/\delta_{st} = 0.06$ shows a mild peak at $\phi_g = 1.0$ at all locations but the probability of obtaining $\phi_g < 1.0$ remains greater than that of finding $\phi_g \geq 1.0$ in all cases. The probability of having a fuel-lean mode of combustion decreases in the downstream direction due to the increased availability of fuel vapour as a

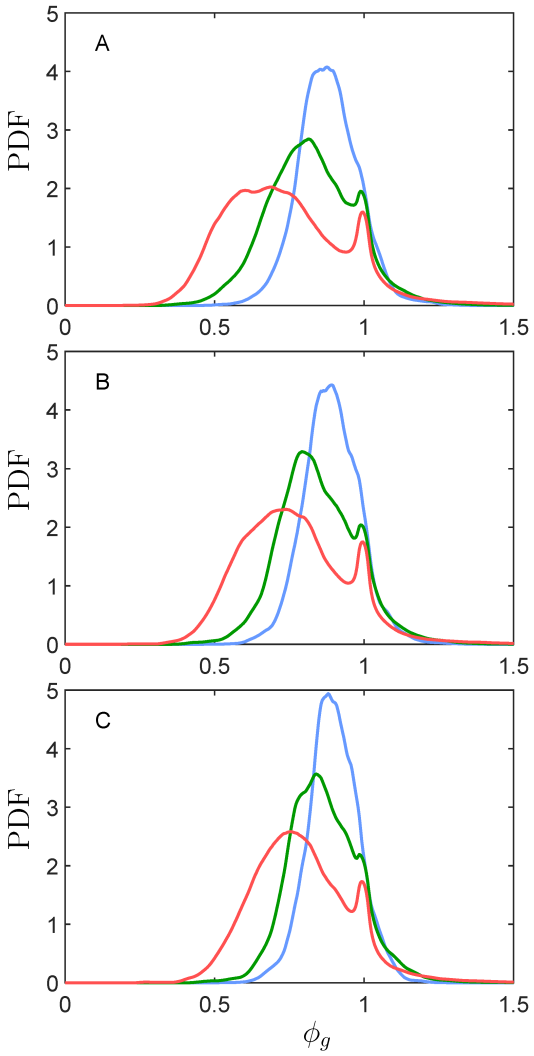

Figure 7.2: PDFs of ϕ_g in the region corresponding to $0.01 \leq c \leq 0.99$ at different locations A, B and C (top to bottom) for initial $a_d/\delta_{st} = 0.04$ (——), 0.05 (——) and 0.06 (——).

result of evaporation of droplets. For example, the droplet number density $\rho_N^{1/3}\delta_{th}$ in the region corresponding to $0.01 \leq c \leq 0.99$ drops by 30%, 4% and 1.14% at location C in comparison to location A for the cases with initial $a_d/\delta_{st} = 0.04, 0.05$ and 0.06, respectively. Therefore, the flame at plane A is leaner than in plane C, which can be substantiated from the fact that the time-averaged values of ϕ_g for $a_d/\delta_{st} = 0.04$ are $0.88, 0.89$ and 0.90, for $a_d/\delta_{st} = 0.05$ are $0.83, 0.85$ and 0.87, for $a_d/\delta_{st} = 0.06$ are $0.74, 0.77$ and 0.79, at locations A, B and C, respectively. It is worth noting that the PDFs of ϕ_g in Fig. 7.2 are shown only for $0.01 \leq c \leq 0.99$. Furthermore, a comparison between Figs. 7.1a and 7.1b reveals that it is possible that there are local islands of highly fuel-rich mixtures in the fully burned regions. This highly fuel-rich mixture composition is formed because of the mixing of evaporated vapour from the neighbourhood of a droplet and also due to small number of droplets which escape through the flame due to turbulent motion and complete the evaporation in the high temperature zone in the region with $c = 1.0$. Some of these unburned fuel-pockets eventually diffuse into the flame and mix with the air diffusing from the unburned gas side to give rise to local diffusion mode of burning, which will be discussed later in this chapter. Moreover, a close inspection of Fig. 7.2 reveals that the peak value of the PDF of ϕ_g at location C is found close to $\phi_g = 1.0$ (i.e. most probable value of ϕ_g is going to be close to 1.0). This clearly indicates that the PDF of ϕ_g within the flame is likely to see a peak at $\phi_g = 1.0$ and a mean value of ϕ_g close to unity in the case of $a_d/\delta_{st} = 0.04$ at a location which is further away from the flame holder than the location C. This behaviour can also be discerned from the distributions of ϕ_g in Fig. 7.1b. It is worth noting that the fuel-lean nature of the gaseous reacting mixture is qualitatively consistent with the previous findings for laminar flame calculations [115], statistically planar turbulent spray flames [48] and spherically expanding turbulent spray flames (see Section 4.2). Thus, this fuel-lean nature of the gaseous phase combustion for globally stoichiometric (i.e. $\phi_{ov} = 1.0$) spray flames has been found to be mostly independent of the flame configuration but is influenced by the liquid droplet size, turbulence intensity and number density of liquid droplets [1, 48]. However, droplets interact with both statistically planar and spherically expanding flames at all stages of their propagation into the unburned gas but in turbulent V-spray flames, droplets travel in the mean flow direction during the evaporation process. As a result, the frequency of flame-droplet interaction decreases and the mean value of ϕ_g increases in the downstream direction.

It is worth noting that droplets do not evaporate instantly and the evaporated fuel vapour does not immediately homogeneously mix to produce a mixture with $\phi_g = 1.0$ even when the overall equivalence ratio ϕ_{ov} takes a value of 1.0. Thus the limiting case for small diameter is a gaseous stratified mixture flame but not a premixed flame, but this stratification cannot be a priori characterised. It has been shown in previous analyses on stratified combustion [77, 234]

Table 7.2: Variation of the mean droplet diameter normalised by its initial value $a_{d,m}/a_d$ in the unburned gas region at locations A, B and C.

	a_d/δ_{st}	0.04	0.05	0.06
A	$0 \leq c < 0.1$	0.36	0.60	0.74
	$0.1 \leq c < 0.3$	0.25	0.45	0.64
	$0.3 \leq c < 0.5$	Absent	0.33	0.54
B	$0 \leq c < 0.1$	0.29	0.54	0.70
	$0.1 \leq c < 0.3$	0.20	0.39	0.59
	$0.3 \leq c < 0.5$	Absent	0.29	0.49
C	$0 \leq c < 0.1$	0.23	0.49	0.67
	$0.1 \leq c < 0.3$	0.15	0.32	0.54
	$0.3 \leq c < 0.5$	Absent	0.27	0.43

that the burning rate and flame front thickness for stratified mixture with a mean equivalence ratio of $\phi_g = 1.0$ can be smaller than in the stoichiometric premixed flames due to smaller burning rates of $\phi_g < 1.0$ and $\phi_g > 1.0$ mixtures.

The mean droplet diameters for $0 \leq c < 0.1$, $0.1 \leq c < 0.3$ and $0.3 \leq c < 0.5$ at locations A, B and C are shown in Table 7.2. It is worth noting that only few droplets survive for $c > 0.5$ so the statistical average based on limited samples are not meaningful. It can be seen from Table 7.2 that the mean droplet size decreases due to evaporation as c increases but the differences in the mean droplet diameter increase within the flame because smaller droplets evaporate faster. It can also be seen from Table 7.2 that the mean droplet size in the region corresponding to $0 \leq c < 0.1$ remains comparable to the initial values of a_d/δ_{st} for large droplets, whereas smaller droplets are mostly evaporated when they reach location A as shown in Fig. 7.1. The evaporation process before reaching the location A leads to significant diameter differences between the cases with different droplet diameters in the V-flame configuration. Therefore, the mean droplet sizes in the zones corresponding to $0 \leq c < 0.1$, $0.1 \leq c < 0.3$ and $0.3 \leq c < 0.5$ consist of a wide spread of droplet diameter at location A due to high (low) evaporation rate of small (large) droplets.

The Damköhler and Karlovitz numbers for the stoichiometric gaseous mixture based on the inlet values of $u'/S_{b(\phi_g=1)}$ and L_{1V}/δ_{st} are 1.25 and 1.79, respectively. The predominant likelihood of fuel-lean combustion in these droplet V-flame cases is expected to increase the Karlovitz number and decrease the Damköhler number of the underlying combustion process in comparison to $Da_{(\phi_g=1)}$ and $Ka_{(\phi_g=1)}$, respectively. The local Damköhler number can alternatively be estimated by $Da_L = L_{turb}S_{b,\xi}^2/u_{rms}\alpha_{T0}$ with $L_{turb} = \tilde{k}^{1.5}/\tilde{\varepsilon}$ and $u_{rms} = \sqrt{2\tilde{k}/3}$ being local turbulent length scale and root-mean-square velocity with $\tilde{k}$ and $\tilde{\varepsilon}$ being the Favre-averaged turbulent kinetic energy and its dissipation rate, respectively. Here $S_{b,\xi}$ is the lam-

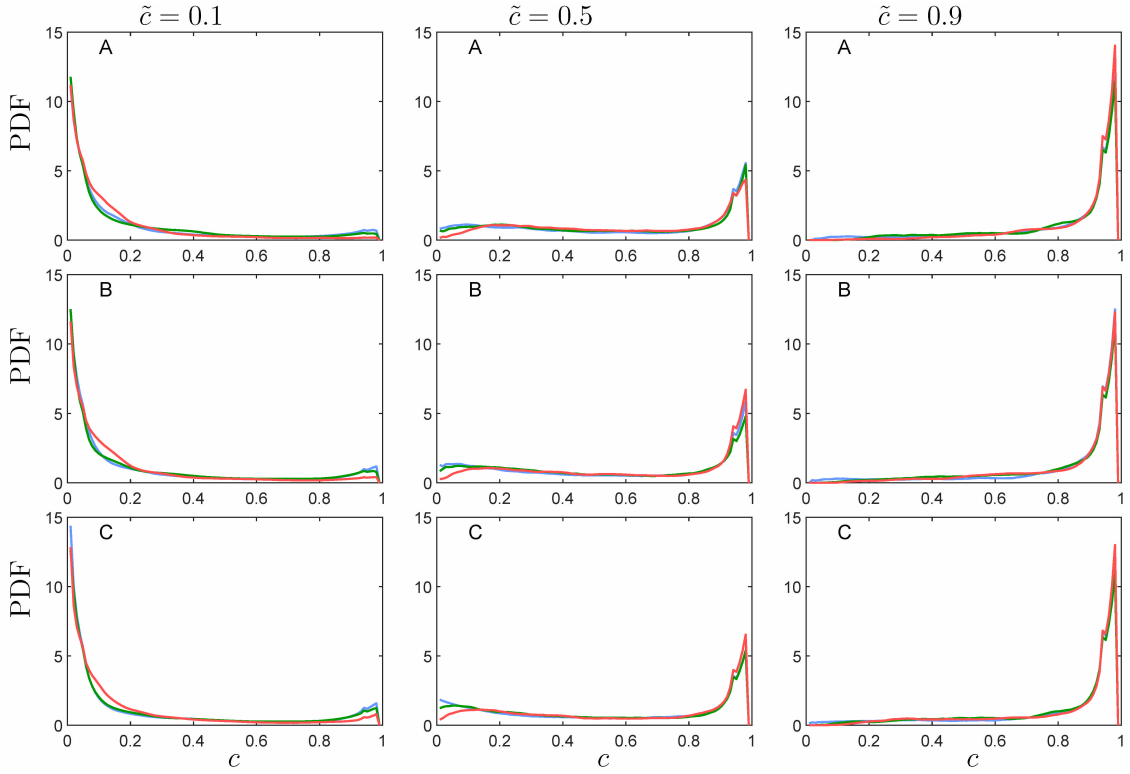

Figure 7.3: PDFs of c conditional on $\tilde{c} = 0.1, 0.5$ and 0.9 at different locations A, B and C (top to bottom) for initial $a_d/\delta_{st} = 0.04$, 0.05 and 0.06 with a mean inlet velocity of $u_{mean}/S_{b(\phi_g=1)} = 5.0$. See Fig. 7.2 caption for the colour keys.

inar burning velocity corresponding to $\phi_R = \tilde{\xi}(1-\xi_{st})/[\xi_{st}(1-\tilde{\xi})]$. The local values of the Damköhler number are exemplarily provided at the location corresponding to $\tilde{c} = 0.5$, which for $a_d/\delta_{st} = 0.04$ are 0.79, 0.92 and 1.09, for $a_d/\delta_{st} = 0.05$ are $0.49, 0.71$ and 1.00, for $a_d/\delta_{st} = 0.06$ are $0.27, 0.40$ and 0.62, for the premixed case are $3.66, 3.93$ and 3.99 at locations A, B and C, respectively. Similarly, the corresponding values of the local Karlovitz number ($Ka_L = (u_{rms}/S_{b,\xi})^{1.5}(L_{turb}S_{b,\xi}/\alpha_{T0})^{-0.5}$) based on $\tilde{k}$, $\tilde{\varepsilon}$ and $S_{b,\xi}$ values at the location corresponding to $\tilde{c} = 0.5$ for $a_d/\delta_{st} = 0.04$ are $1.79, 1.74$ and 1.79, for $a_d/\delta_{st} = 0.05$ are $2.60, 2.18$ and 1.87, for $a_d/\delta_{st} = 0.06$ are $4.12, 3.33$ and 2.75, for the premixed case are $3.77, 3.39$ and 2.91 at locations A, B and C, respectively. According to these estimated values of Da_L and Ka_L, combustion takes places in the thin reaction zones regime [93]. The expression "thin reaction zones regime" refers to a condition where the reaction zone thickness remains smaller than the Kolmogorov length scale, and thus the reaction processes remain quasi-laminar. In this sense, the reaction occurs in a thin region in comparison to the dissipative length scale of turbulence. The differences in Da_L and Ka_L values between gaseous premixed and droplet flames arise due to the differences in respective $S_{b,\xi}$, $\tilde{k}$ and $\tilde{\varepsilon}$ values originating from mix-

ture composition and also due to the difference in turbulence evolution within the flame front. This behaviour can be further illustrated by the PDFs of reaction progress variable c on the isosurfaces of the Favre-averaged reaction progress variable $\tilde{c} = 0.1, 0.5$ and 0.9 at locations A, B and C, which are shown in Fig. 7.3, whereas the contours of $\tilde{c} = 0.1, 0.5$ and 0.9 for the cases considered here are shown in Fig. 7.4a. In this thesis, the Favre averaging is carried out by averaging in time (i.e. over flow through time t_{flow}) and space (i.e. spanwise z-direction). For high values of Damköhler number (i.e. $Da_{(\phi_g)} \gg 1$), the PDFs of c are expected to be bimodal with impulses at $c = 0.0$ and $c = 1.0$ [235], but Fig. 7.3 shows that the PDFs of c do not remain bimodal (in fact the PDFs are nearly monomodal in some instances for the cases considered here) and the probability of finding reacting mixture (i.e. $0.0 < c < 1.0$) remains significant for all locations irrespective of the value of $\tilde{c}$. The departure of the PDFs of c from the bimodal distribution with impulses at $c = 0.0$ and $c = 1.0$ provides the signature of low Damköhler number combustion (i.e. $Da_{(\phi_g)} < 1$) for the cases considered in this section. This suggests that combustion in these V-shaped flames takes place in the thickened flame regime and this behaviour is prominent for the case with initial $a_d/\delta_{st} = 0.06$, where local occurrences of flame thickening can be discerned from Fig. 7.1. Moreover, the appearance of the morphology of these V-flame surfaces has been found to be qualitatively similar to the experimental visualisations of premixed V-flames in the thickened flame regime [233]. The turbulent Reynolds number remains moderate for all cases considered in this section. Turbulence decays within the flame and kinematic viscosity increases with increasing c as a result of temperature rise. This clearly suggests that the flame is weakly turbulent, and the effects of intermittency are expected to be prevalent in these flames. As a consequence, the internal flame structure remains quasi-laminar in nature but the combination of $Da < 1$ and weak turbulence suggests that the local occurrences of flame-front thickening take place due to penetration of occasional turbulent eddies within the preheat zone and thus the preheat zone is perturbed, but the reaction zone remains quasi-laminar. This is consistent with the aforementioned Karlovitz number values suggesting the thin reaction zones regime combustion [93] in the cases considered in this section.

7.2 Flame Brush Thickness and Flame Angle

It can be seen from Fig. 7.4 that the distance between $\tilde{c} = 0.1$ and 0.9 isosurfaces (i.e. $\delta_{T(0.1-0.9)}$) at a given x-location increases in the downstream direction from the flame holder, which is consistent with turbulent diffusion theory [21, 93, 236, 237]. This behaviour is qualitatively similar to turbulent premixed V-flame simulations [63, 64, 233]. The flame brush

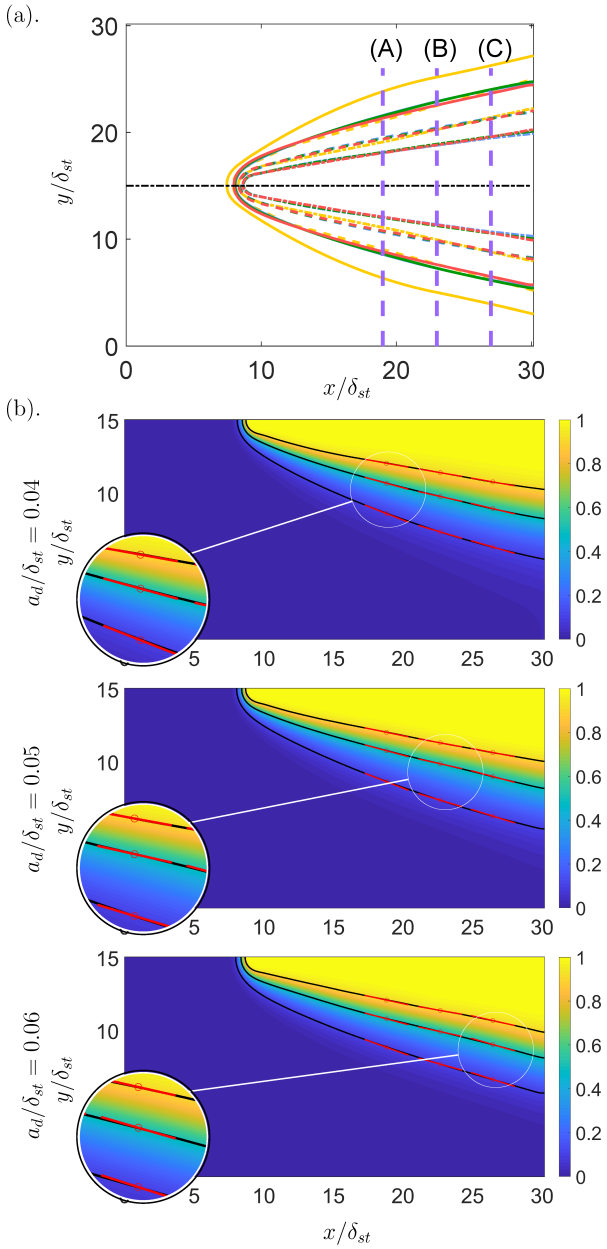

Figure 7.4: (a) Contours of $\tilde{c} = 0.1$ (solid line), 0.5 (dashed line) and 0.9 (dotted line) contours for gaseous premixed (——) case and droplet cases with initial droplet diameter $a_d/\delta_{st} = 0.04$ (——), 0.05 (——) and 0.06 (——). The dashed purple lines show the sampling locations (A, B, C from left to right), and the dotted black line shows the flame centre, (b) Distributions of $\tilde{c}$ at the bottom half of the domain for initial $a_d/\delta_{st} = 0.04$ (1^{st} row), 0.05 (2^{nd} row) and 0.06 (3^{rd} row) with a mean inlet velocity of $u_{mean}/S_{b(\phi_g=1)} = 5.0$. Black lines show the contour lines of $\tilde{c} = 0.1, 0.5$ and 0.9 from outer to the inner periphery and red lines are tangents to contour lines at locations A, B and C (left to right).

Table 7.3: Flame brush thickness at locations A, B and C for the gaseous premixed flame case (GP) and spray flames with different droplet diameters for a mean inlet velocity of $u_{mean}/S_{b(\phi_g=1)} = 5.0$.

a_d/δ_{st}	GP	0.04	0.05	0.06
$\delta_{T(0.1-0.9)}/\delta_{st}$ at A	3.14	3.45	3.38	3.23
$\delta_{T(0.1-0.9)}/\delta_{st}$ at B	3.34	4.13	4.00	3.75
$\delta_{T(0.1-0.9)}/\delta_{st}$ at C	3.70	4.50	4.40	4.06
$\delta_{T,\bar{c}}/\delta_{st}$ at A	3.04	3.50	3.33	3.18
$\delta_{T,\bar{c}}/\delta_{st}$ at B	3.12	4.27	4.12	3.83
$\delta_{T,\bar{c}}/\delta_{st}$ at C	3.35	4.79	4.97	4.35
$\delta_{T,\tilde{c}}/\delta_{st}$ at A	2.47	2.82	2.69	2.72
$\delta_{T,\tilde{c}}/\delta_{st}$ at B	2.34	3.28	3.12	3.09
$\delta_{T,\tilde{c}}/\delta_{st}$ at C	2.37	3.84	3.62	3.45

thickness $\delta_{T,\tilde{c}}$ at a given location can be quantified as:

$$\delta_{T,\tilde{c}} = 1/max|\nabla\tilde{c}| \tag{7.1}$$

Alternatively, a flame brush thickness $\delta_{T,\bar{c}}$ can be defined as:

$$\delta_{T,\bar{c}} = 1/max|\nabla\bar{c}| \tag{7.2}$$

The values of $\delta_{T(0.1-0.9)}/\delta_{st}$, $\delta_{T,\tilde{c}}/\delta_{st}$ and $\delta_{T,\bar{c}}/\delta_{st}$ are reported in Table 7.3 for locations A, B and C. It can be seen from Table 7.3 that the values of $\delta_{T,\bar{c}}/\delta_{st}$ and $\delta_{T(0.1-0.9)}/\delta_{st}$ for the droplet cases remain close to each other, but the value of $\delta_{T,\tilde{c}}/\delta_{st}$ remains smaller than $\delta_{T,\bar{c}}/\delta_{st}$ and $\delta_{T(0.1-0.9)}/\delta_{st}$. A comparison with the corresponding gaseous premixed flame indicates that the flame brush is thicker in droplet cases than in the premixed gaseous case. It has been shown in Fig. 7.2 that spray flames experience considerable amount of fuel-lean (i.e. $\phi_g < 1.0$) mixture, and the flamelet thickness ($\sim \alpha_{T0}/S_{b(\phi_g)}$) is expected to be greater, whereas laminar burning velocity $S_{b(\phi_g)}$ is smaller than the corresponding values for the stoichiometric premixed flame. Thus, the spray flames experience higher values of turbulence intensity $u'/S_{b(\phi_g)}$ and are expected to show greater values of flamelet thickness and a combination of these gives rise to greater values of flame brush thickness in the spray flames than in the stoichiometric premixed flames, which can be substantiated from Table 7.3. It is worth noting that the evolution of turbulence (i.e. rms turbulent velocity and length scale) within the spray flames for different droplet sizes are likely to be different, which plays a role in determining the flame brush thickness [238]. For example, the decay of turbulence across the flame is likely to be less rapid for large droplets in comparison to small droplets because the effects of heat release

Table 7.4: Flame angle θ for $\tilde{c}$ isosurfaces at locations A, B and C for the gaseous premixed flame case (*GP*) and spray flames with different droplet diameters for a mean inlet velocity of $u_{mean}/S_{b(\phi_g=1)} = 5.0$.

a_d/δ_{st}	GP	0.04	0.05	0.06
Flame angle $\theta_{\tilde{c}=0.1}$ for $\tilde{c}=0.1$ at A	16.06°	20.47°	20.42°	18.88°
Flame angle $\theta_{\tilde{c}=0.1}$ for $\tilde{c}=0.1$ at B	13.56°	15.76°	16.12°	14.80°
Flame angle $\theta_{\tilde{c}=0.1}$ for $\tilde{c}=0.1$ at C	17.12°	15.46°	16.58°	17.00°
Flame angle $\theta_{\tilde{c}=0.5}$ for $\tilde{c}=0.5$ at A	14.66°	14.66°	14.49°	11.72°
Flame angle $\theta_{\tilde{c}=0.5}$ for $\tilde{c}=0.5$ at B	7.21°	12.07°	12.06°	15.44°
Flame angle $\theta_{\tilde{c}=0.5}$ for $\tilde{c}=0.5$ at C	10.95°	13.04°	14.37°	14.99°
Flame angle $\theta_{\tilde{c}=0.9}$ for $\tilde{c}=0.9$ at A	13.46°	9.82°	11.20°	11.62°
Flame angle $\theta_{\tilde{c}=0.9}$ for $\tilde{c}=0.9$ at B	10.57°	9.31°	9.96°	9.49°
Flame angle $\theta_{\tilde{c}=0.9}$ for $\tilde{c}=0.9$ at C	10.54°	9.62°	10.22°	12.18°

are likely to be weaker due to burning of leaner mixtures. Therefore, the flame brush thickness for spray flames is not dictated only by the droplet diameter but also by the length scale and turbulence intensity within the flame brush, which is beyond the scope of this analysis. It is also worth noting that a premixed flame is not the limiting case of the small droplet diameter so it should not be expected that the premixed flame is going to follow the trend shown by the spray flames.

The change in the flame brush thickness in the flow direction indicates that the angles made by the tangent on the $\tilde{c} = 0.1, 0.5$ and 0.9 contours with the mean flow direction (i.e. x-direction) are expected to be different, which can also be verified from Table 7.4 where the angles $\theta_{\tilde{c}=0.1}$, $\theta_{\tilde{c}=0.5}$ and $\theta_{\tilde{c}=0.9}$ for $\tilde{c} = 0.1, 0.5$ and 0.9 isosurfaces are also listed for locations A, B and C. The angles $\theta_{\tilde{c}=0.1}$, $\theta_{\tilde{c}=0.5}$ and $\theta_{\tilde{c}=0.9}$ are evaluated by using the slope of the tangents at locations A, B and C on the contour lines of $\tilde{c} = 0.1, 0.5$ and 0.9, as shown in Fig. 7.4b.

It can be seen from Fig. 7.4 that the contours of $\tilde{c}$ are mildly curved for the cases considered in this section. However, this trend weakens with increasing $\tilde{c}$ value, which can be substantiated from $\theta_{\tilde{c}=0.1}$, $\theta_{\tilde{c}=0.5}$, $\theta_{\tilde{c}=0.9}$ values listed in Table 7.4. The flame angle $\theta_{\tilde{c}=0.9}$ for droplet cases is found to be smaller than that for the gaseous premixed case, whereas the flame angle $\theta_{\tilde{c}=0.1}$ for droplet cases remains larger than that for the gaseous premixed case at most locations. These differences originate as a result of the differences in flame brush thicknesses reported in Table 7.3, which in turn originate due to the differences between the composition of the gaseous mixture within the flame and the evolution characteristics of turbulence within the flame brush. It can be seen from Table 7.4 that $\theta_{\tilde{c}=0.1}$ changes appreciably with the axial distance and a similar qualitative trend is observed for $\theta_{\tilde{c}=0.5}$ but the variation of $\theta_{\tilde{c}=0.5}$ in the axial distance is much weaker than that of $\theta_{\tilde{c}=0.1}$. Moreover, $\theta_{\tilde{c}=0.9}$ does not change much in

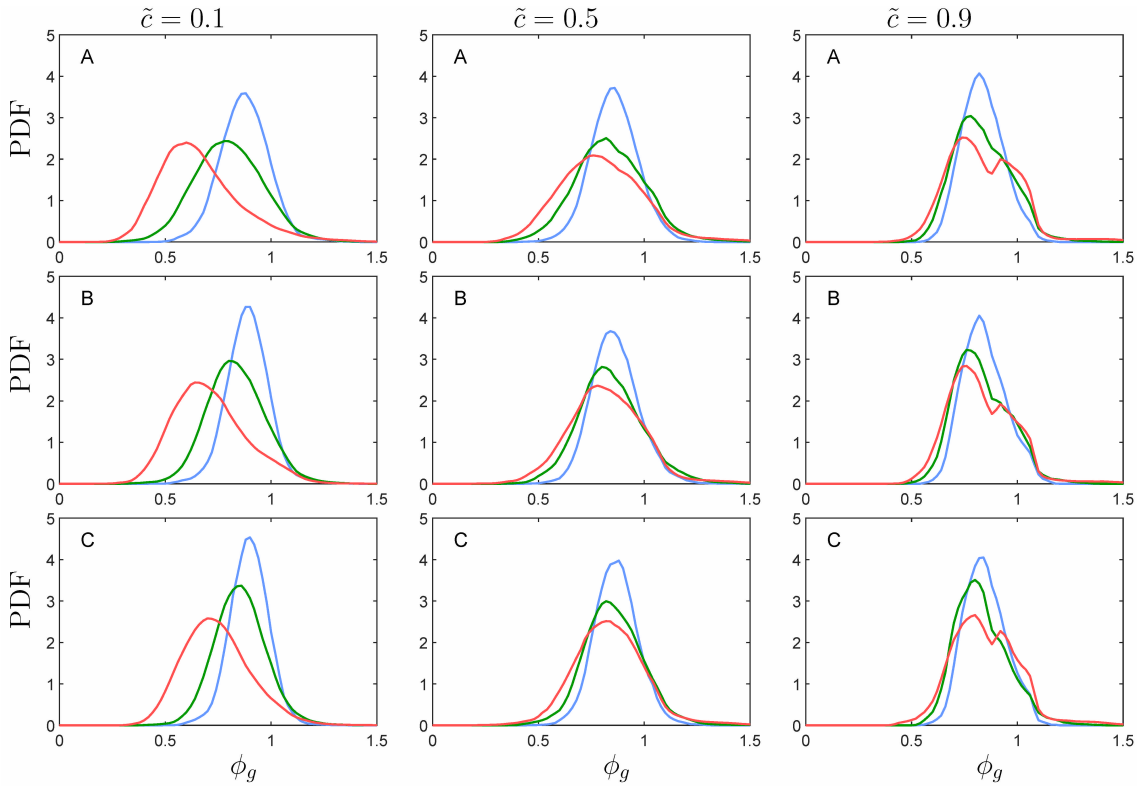

Figure 7.5: PDFs of ϕ_g conditional on $\tilde{c} = 0.1, 0.5$ and 0.9 isosurfaces at different locations A, B and C (top to bottom) for initial $a_d/\delta_{st} = 0.04$, 0.05 and 0.06 with a mean inlet velocity of $u_{mean}/S_{b(\phi_g=1)} = 5.0$. See Fig. 7.2 caption for the colour keys.

the axial direction for the cases considered in this section. In order to explain this behaviour, the PDFs of ϕ_g on $\tilde{c} = 0.1, 0.5$ and 0.9 isosurfaces at different axial locations are shown in Fig. 7.5. It is evident from Fig. 7.5 that the PDFs of ϕ_g are considerably different for different droplet diameters with higher probabilities of finding fuel-lean mixture for bigger droplet diameters. However, Fig. 7.5 shows that the mean value of ϕ_g increases in the downstream direction but the difference in the PDFs of ϕ_g decreases with increasing $\tilde{c}$, and with the axial distance because of the increased extents of droplet evaporation. Thus, the increase in the mean value of ϕ_g in the downstream direction is most prominent for $\tilde{c} = 0.1$, which gives rise to its curved contours and relatively significant variations of $\theta_{\tilde{c}=0.1}$ in the axial direction. Figure 7.5 reveals that the mean ϕ_g values for $\tilde{c} = 0.9$ contours do not change appreciably in the downstream direction, and therefore, the contours of $\tilde{c} = 0.9$ remain straight for the cases considered here. Moreover, the gaseous equivalence ratio ϕ_g values remain comparable for $\tilde{c} = 0.5$ and 0.9 for different droplet diameters, and therefore, these contours almost coincide with each other for different values of a_d/δ_{st}. It is worth noting that the variation of the PDFs shown in Fig. 7.5 in the flow direction remains weaker than that in Fig. 7.2. In Fig. 7.5, the

PDFs of ϕ_g are shown for a given $\tilde{c} = \bar{\rho}^{-1} \int_0^{1.0} \rho c P(c) dc$ isosurface where $P(c)$ is the PDF of c and $\bar{\rho}$ is the mean density. Thus ϕ_g from different c values contribute to this and the gaseous phase equivalence ratio ϕ_g values for small values of c are expected to be small. Consequently, the PDFs of ϕ_g from locations A to C in Fig. 7.5 do not change as much as the PDFs in Fig. 7.2 change from the location A to location C.

7.3 Reaction Zone Structure

The flame angles and flame brush thicknesses are dependent on the reacting mixture composition in the gaseous phase, flame wrinkling and flame propagation rates. Thus, it is worthwhile to examine the statistical behaviours of gaseous equivalence ratio ϕ_g, flame curvature κ_m, mode of combustion and local consumption and density-weighted displacement speeds (i.e. S_c and S_d^*).

The presence of droplets significantly affects the flame morphology and induces flame wrinkling due to flame-droplet interaction [119]. In order to understand the flame-droplet interaction, the instantaneous views of $c = 0.5$ isosurfaces, coloured by local values of flame curvature $\kappa_m \times \delta_{st}$ for all cases considered in this section are shown in Fig. 7.6. It can be seen from Fig. 7.6 that the flame surface remains smooth for the gaseous premixed flame case, and also for the droplet case with small droplets, which evaporate rapidly ahead of the flame and do not significantly interact with the flame surface. By contrast, the flame surfaces are significantly affected by large droplets and exhibit dimples in addition to the flame wrinkles induced by the turbulent flow field. The occurrences of flame-droplet interaction events increase in the downstream direction for larger droplets because they can survive longer in the domain due to their lower evaporation rate and bigger size.

The PDFs of local normalised flame curvature $\kappa_m \times \delta_{st}$ of the $c = 0.8$ isosurface at different planes (i.e. A, B and C) for all droplet cases and the gaseous premixed flame case considered in this section are shown in Fig. 7.7. The PDFs of $\kappa_m \times \delta_{st}$ peak at around zero value and show similar widths for all droplet cases at locations A, B and C. However, the width on the PDF of $\kappa_m \times \delta_{st}$ marginally increases with increasing a_d/δ_{st}, which bears the signature of droplet-induced flame wrinkling for larger droplets. This behaviour is consistent with previous computational findings for spherically expanding spray flames (see Section 4.2) for weak turbulence intensities. Furthermore, a comparison between gaseous premixed and droplet cases reveals that PDFs of $\kappa_m \times \delta_{st}$ for spray flames have a wider distribution at planes A and B where droplet-flame interactions mainly occur. However, the difference in the distributions of $\kappa_m \times \delta_{st}$ between spray and gaseous premixed flame cases decreases in the flow direction because droplets increasingly evaporate in the axial direction and flame-droplet interaction

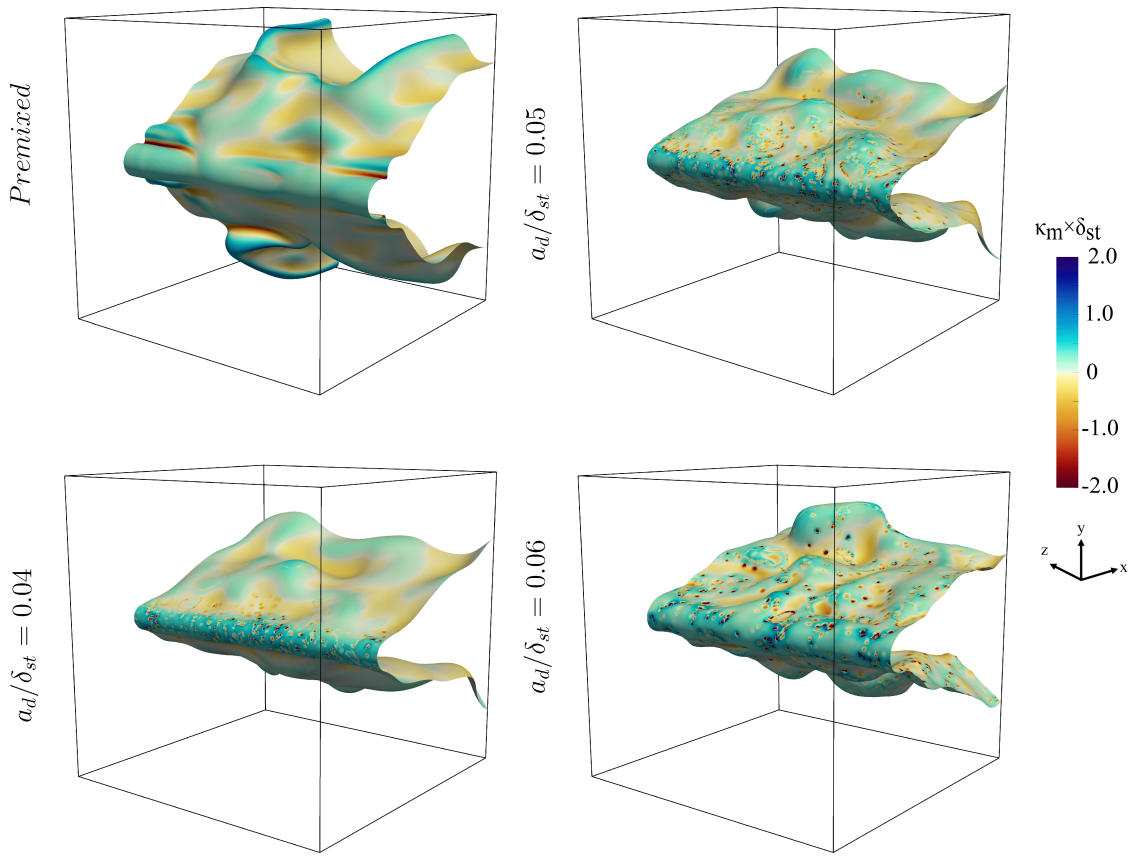

Figure 7.6: Instantaneous views of $c = 0.5$ isosurface coloured with $\kappa_m \times \delta_{st}$ values for gaseous premixed and spray flames with initial $a_d/\delta_{st} = 0.04, 0.05, 0.06$ at $t = 2.0t_{flow}$.

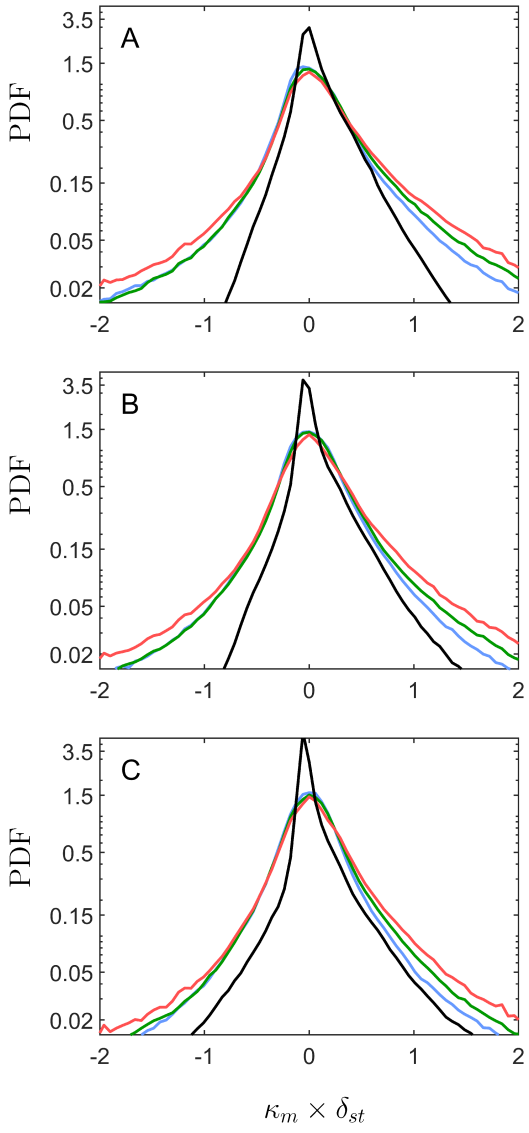

Figure 7.7: PDFs of $\kappa_m \times \delta_{st}$ of the $c = 0.8$ isosurface at locations A, B, and C (top to bottom) for gaseous premixed (——) and V-shaped spray flames with initial $a_d/\delta_{st} = 0.04$, 0.05 and 0.06. See Fig. 7.2 caption for the colour keys.

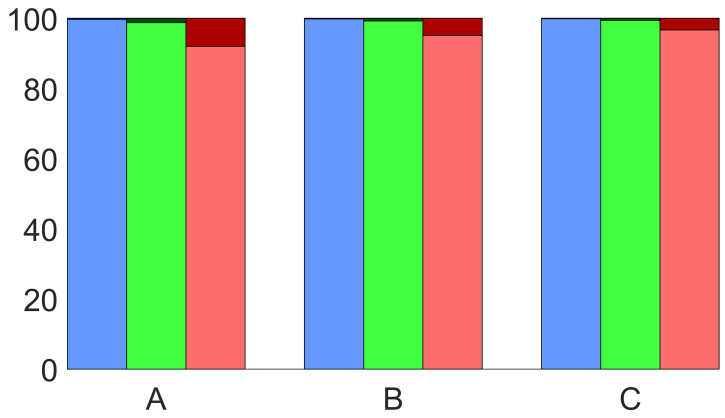

Figure 7.8: Percentage of heat release arising from premixed (for initial $a_d/\delta_{st} = 0.04$ (■), 0.05(■), 0.06 (■)) and non-premixed (for initial $a_d/\delta_{st} = 0.04$ (■), 0.05 (■), 0.06 (■)) modes of combustion at locations A, B and C (left to right).

becomes less frequent. The differences in the widths of $\kappa_m \times \delta_{st}$ PDFs are consistent with the differences in flame brush thicknesses for different droplets.

The percentages of heat release rate arising from the premixed and non-premixed modes of combustion are demonstrated in Fig. 7.8 for all droplet cases considered in this section at locations A, B and C. Figure 7.8 indicates that for all cases heat release mostly takes place under premixed mode at all locations. Thus, the gaseous phase combustion in these cases takes place mostly in stratified mixtures. However, it can be discerned from Fig. 7.8 that the percentage of overall heat release due to non-premixed combustion is greater in extent in the case with initial $a_d/\delta_{st} = 0.06$ than the corresponding cases with initial $a_d/\delta_{st} = 0.04$ and 0.05. A careful examination of Fig. 7.2 reveals that there is a small peak at $\phi_g = 1.0$ in the PDFs of ϕ_g for the initial $a_d/\delta_{st} = 0.06$ case, which originates due to the non-premixed mode of combustion. Due to slow evaporation rate of large droplets with the initial $a_d/\delta_{st} = 0.06$ case gives rise to higher likelihood of obtaining local islands of high and low fuel concentration than the other corresponding cases with smaller droplets, and this gives rise to the strengthening of the non-premixed mode of combustion in the case of large droplets (e.g. cases with initial $a_d/\delta_{st} = 0.06$). A small number of droplets in the case of large droplet diameter (e.g. cases with initial $a_d/\delta_{st} = 0.06$) escape through the flame due to turbulent motion and complete the evaporation in the high temperature zone in the region with $c = 1.0$. Some of these unburned fuel-pockets eventually diffuse into the flame and mix with the air diffusing from the unburned gas side to give rise to local diffusion mode of burning.

7.4 Statistical Analysis of Flame Speeds

As the heat release takes place predominantly under premixed mode, it is necessary to analyse the flame propagation statistics for the flames considered in this section. For this reason, it is worthwhile to analyse the terms on the right-hand side of the transport equation of reaction progress variable c (see Eq. 2.52), as they govern the statistical behaviours of density-weighted displacement speed S_d^*. The mean values of the terms $\dot{w}_c$, $\dot{S}_{liq,c}$, $\dot{A}_c$ and $\nabla\cdot(\rho D\nabla c)$ conditional on c for locations A, B and C are shown in Fig. 7.9. The terms contributing to the flame displacement speed S_d are ensemble averaged for a given value of c for 30 equally spaced bins of c between 0.01 and 0.99, and these values are subsequently time-averaged before presenting in Fig. 7.9. The same approach was adopted in several previous analyses [45, 46, 73, 81, 82, 191].

Figure 7.9 suggests that the mean molecular diffusion term $\nabla\cdot(\rho D\nabla c)$ takes positive values in the preheat zone (i.e. $c<0.5$), whereas it assumes negative values and remains in approximate balance with the positive mean value of $\dot{w}_c$ in the reaction zone (i.e. $0.5\leq c\leq 0.9$) for both gaseous premixed and spray V-shaped flames. It is evident from Fig. 7.9 that the mean values of $\dot{w}_c$ for droplet cases are smaller than the gaseous premixed case. This trend originates due to slower burning of stratified mixtures with $\phi_g<1.0$ and $\phi_g>1.0$ in the droplet cases than in the stoichiometric (i.e. $\phi_g=1.0$) premixed flame. The mean values of $\dot{w}_c$ decreases with increasing droplet diameter due to the increased propensity of fuel-lean burning in the gaseous phase. Furthermore, the mean values for all terms show similar trends at locations A, B, C for all droplet diameters. The mean values of the terms arising due to droplet evaporation $\dot{S}_{liq,c}$ and mixture inhomogeneity $\dot{A}_c$ remain much smaller in magnitude in comparison to the magnitudes of the mean values of $\dot{w}_c$ and $\nabla\cdot(\rho D\nabla c)$ throughout the flame, which is consistent with previous findings for statistically planar [47] and spherically expanding (see Section 5.5) flames. It can further be seen from Fig. 7.9 that the mean value of $\rho S_d|\nabla c|=[\nabla\cdot(\rho D\nabla c)+\dot{w}_c+\dot{S}_{liq,c}+\dot{A}_c]$ remains smaller than the mean value of $\rho_0 S_{b(\phi_g=1)}|\nabla c|$ for all cases considered here in spite of having an overall equivalence ratio of unity (i.e. $\phi_{ov}=1.0$) in the unburned gas. This suggests that the surface-weighted value of density-weighted displacement speed (i.e. ratio of averaged/filtered values of $S_d^*|\nabla c|$ and $|\nabla c|$) [191, 239] in all cases remains smaller than $S_{b(\phi_g=1)}$ due to the predominance of the fuel-lean mixture within the flame in spite of having $\phi_{ov}=1.0$ in the unburned gas. Figure 7.9 also reveals that the mean value of $\rho_0 S_{b(\phi_g=1)}|\nabla c|$ decreases with increasing droplet diameter. The inverse of the maximum mean value of $|\nabla c|$ provides a measure of the flamelet thickness (i.e. $\delta\sim 1/max|\nabla c|$) at a given location. The smaller peak mean value of $\rho_0 S_{b(\phi_g=1)}|\nabla c|$ for larger droplets indicates a thicker flame because $\rho_0 S_{b(\phi_g=1)}$ remains the same for all cases. As the probability of finding fuel-lean mixture increases for larger droplets, the small values of

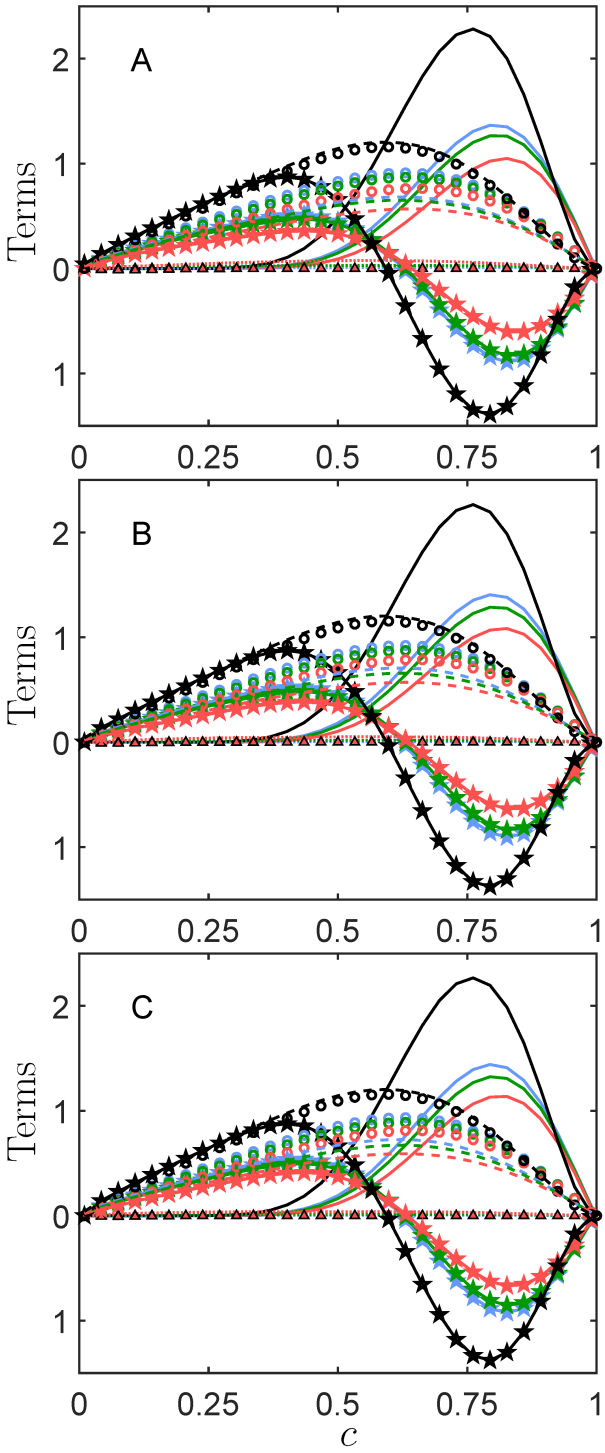

Figure 7.9: Variations of mean values of $\dot{w}_c$ (solid line), $\nabla\cdot(\rho D\nabla c)$ (line with star marker), $\dot{A}_c$ (dotted line), $\dot{S}_{liq,c}$ (triangle marker), $\rho S_d|\nabla c|$ (dashed line) and $\rho_0 S_{b(\phi_g=1)}|\nabla c|$ (circle) conditional on c for premixed gaseous (——) and droplet cases with initial $a_d/\delta_{st}=0.04$ (——), 0.05 (——) and 0.06 (——) at locations A,B,C (top to bottom). All terms are normalised by $\delta_{st}/\rho_0 S_{b(\phi_g=1)}$.

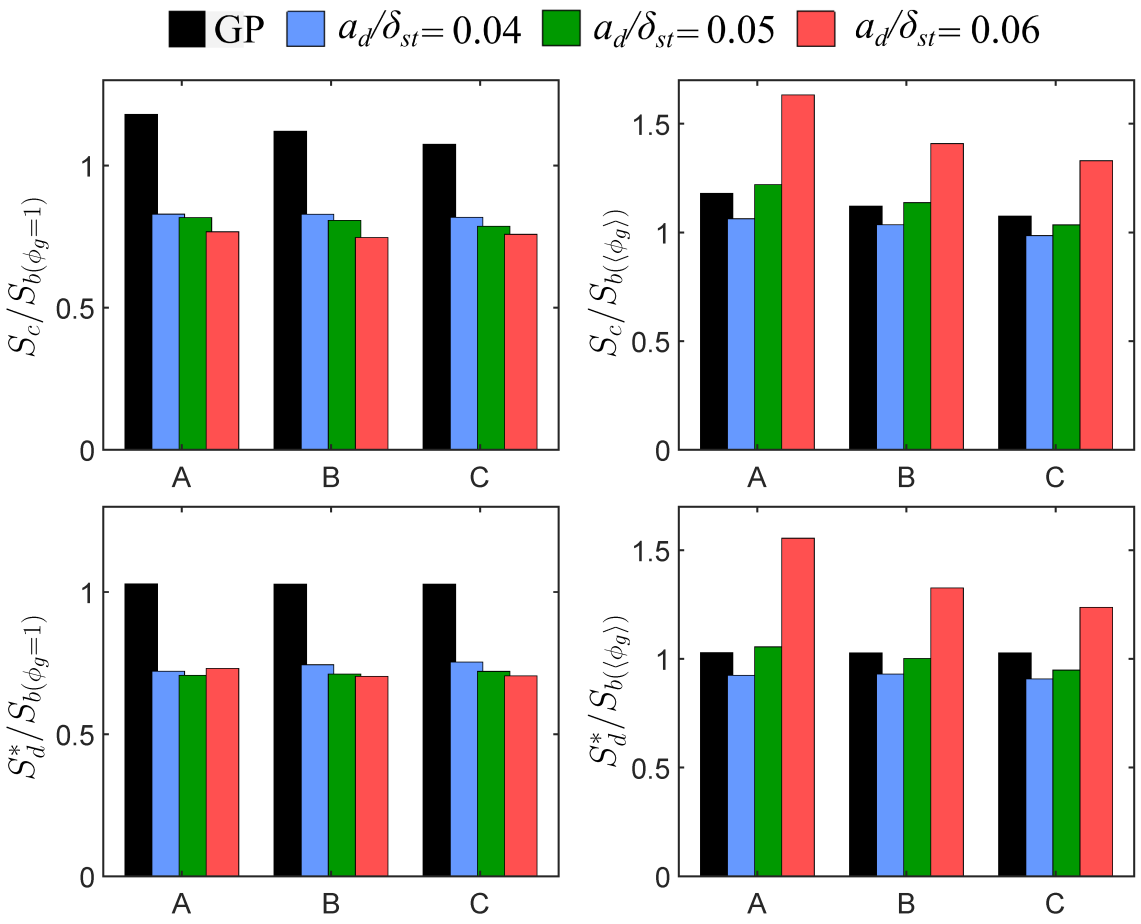

Figure 7.10: The mean values of $S_c/S_{b(\phi_g=1)}$, $S_d^*/S_{b(\phi_g=1)}$, $S_c/S_{b(\langle\phi_g\rangle)}$ and $S_d^*/S_{b(\langle\phi_g\rangle)}$ on the $c = 0.8$ isosurface at locations $A-C$.

$S_{b(\phi_g)}$ are more likely for larger droplets and accordingly flamelet thickness (which scales as $\delta \sim \alpha_{T0}/S_{b(\phi_g)}$) increases with increasing droplet diameter. Thus, the occurrences of local flame thickening for large values of a_d/δ_{st} showed in Fig. 7.1 is consistent with the observations regarding local flame thickening for large droplets.

The aforementioned behaviours of $\nabla\cdot(\rho D\nabla c)$, $\dot{w}_c$, $\dot{S}_{liq,c}$ and $\dot{A}_c$ affect the statistical behaviours of S_d^*, whereas $\dot{w}_c$ and the flame thickness determine the behaviour of consumption speed S_c. The normalised mean values of consumption speed $S_c/S_{b(\phi_g=1)}$ and $S_c/S_{b(\langle\phi_g\rangle)}$ and density-weighted displacement speed $S_d^*/S_{b(\phi_g=1)}$ and $S_d^*/S_{b(\langle\phi_g\rangle)}$ evaluated on the $c = 0.8$ isosurface at locations A, B and C are shown in Fig. 7.10 where $\langle\phi_g\rangle$ is the averaged equivalence ratio on the $c = 0.8$ isosurface at this location and $S_{b(\langle\phi_g\rangle)}$ is the laminar burning velocity corresponding to $\langle\phi_g\rangle$. As the consumption speed S_c is directly dependent on $\dot{w}_c$, the mean values of $S_c/S_{b(\phi_g=1)}$ show a qualitatively similar trend as the mean values of $\dot{w}_c$. Therefore, the mean values of consumption speed for the gaseous premixed V-shaped flame

Table 7.5: Time averaged normalised values of $A_s = \int_V |\nabla c| dV$, $A_{p,\tilde{c}}$, $\Omega_F = \int_V |\dot{w}_F| dV / \rho_0 \delta_{st}^2 S_{b(\phi_g=1)}$, $S = \int_V \dot{w}_c dV / \left[\rho_0 S_{b(\phi_g=1)} \int_V |\nabla c| dV\right]$, $S' = \int_V \dot{w}_c dV / \left[\rho_0 S_{b(\phi_f)} \int_V |\nabla c| dV\right]$ for the gaseous premixed flame case (GP) and spray flames with different droplet diameters.

a_d/δ_{st}	GP	0.04	0.05	0.06
A_s/δ_{st}^2	1797	1722	1684	1708
$A_{p,\tilde{c}=0.1}/\delta_{st}^2$	1600	1494	1499	1498
$A_{p,\tilde{c}=0.5}/\delta_{st}^2$	1495	1404	1408	1413
$A_{p,\tilde{c}=0.9}/\delta_{st}^2$	1432	1350	1354	1358
Ω_F	118	75	68	58
S	1.06	0.77	0.71	0.60
S'	1.00	1.00	1.11	1.41

case assume considerably greater values than those for droplet cases. However, the mean values of $S_d^*/S_{b(\phi_g=1)}$ remain different from the mean values of $S_c/S_{b(\phi_g=1)}$ due to the combined influences of $\dot{S}_{liq,c}$, $\dot{A}_c$, $\nabla\cdot(\rho D\nabla c)$ and $\dot{w}_c$ (but predominantly due to $\nabla\cdot(\rho D\nabla c)$ and $\dot{w}_c$). The mean values of $S_d^*/S_{b(\phi_g=1)}$ for a given value of a_d/δ_{st} remain comparable at locations A, B and C but slight variations can be discerned between the mean values corresponding to these locations. The mean values of $S_d^*/S_{b(\phi_g=1)}$ remain close to unity for the gaseous premixed case. Moreover, the mean values of $S_c/S_{b(\phi_g=1)}$ show decreasing trends with increasing a_d/δ_{st} because of the greater likelihood of obtaining fuel-lean mixtures for larger droplets (see Figs. 7.2 and 7.5).

Another alternative way to present the mean values of consumption and density-weighted displacement speeds is to normalise them with respect to the laminar burning velocity $S_{b(\langle\phi_g\rangle)}$ for the mean equivalence ratio $\langle\phi_g\rangle$ within the flame. However, the value of $S_{b(\langle\phi_g\rangle)}$ changes from one location to another, and therefore, the relative magnitudes of S_c and S_d^* cannot be assessed from the values of $S_c/S_{b(\langle\phi_g\rangle)}$ and $S_d^*/S_{b(\langle\phi_g\rangle)}$. The values of $S_{b(\langle\phi_g\rangle)}$ remain smaller than $S_{b(\phi_g=1)}$ for all the droplet cases considered here and this tendency is most prominent for large droplet diameters (e.g. initial droplet size of $a_d/\delta_{st} = 0.06$). This can be seen from the wider PDFs of ϕ_g with increasing a_d/δ_{st} in Figs. 7.2 and 7.5, and therefore, the probability of obtaining burning more reactive $\phi_g(\approx 1.0) > \langle\phi_g\rangle$ mixture increases with increasing droplet size in the droplet cases. This leads to increasing trends of $S_c/S_{b(\langle\phi_g\rangle)}$ and $S_d^*/S_{b(\langle\phi_g\rangle)}$ with increasing a_d/δ_{st} in contrast to the variations of $S_c/S_{b(\phi_g=1)}$ and $S_d^*/S_{b(\phi_g=1)}$, and this behaviour is more prominent at location A than in locations B and C since the leaner combustion yields small laminar burning velocities at location A.

The time-averaged values of flame surface area A_s, the normalised volume integrated fuel

reaction rate magnitude Ω_F (the volume integrated reaction progress variable reaction rate $\Omega_c = \int_V \dot{w}_c dV / \rho_0 \delta_{st}^2 S_{b(\phi_g=1)}$ shows the same qualitative trend and thus is not shown here) and the normalised ratio of volume-integrated product formation rate to the flame surface area $S = \int_V \dot{w}_c dV / \left[\rho_0 S_{b,st} \int_V |\nabla c| dV\right]$ are listed in Table 7.5, which shows that A_s remains comparable for all cases with different initial droplet diameter. The probability of finding smaller values of $|\nabla c|$ is greater in the case with initial $a_d/\delta_{st} = 0.05$ than in the case with initial $a_d/\delta_{st} = 0.04$, which contributes to the smaller flame surface area A_s for the initial $a_d/\delta_{st} = 0.05$ case than that in the $a_d/\delta_{st} = 0.04$ case. Although the probability of finding smaller values of $|\nabla c|$ is greater in the case with initial $a_d/\delta_{st} = 0.06$ than in the case with initial $a_d/\delta_{st} = 0.05$, but the larger droplets in the initial $a_d/\delta_{st} = 0.06$ case lead to more flame-wrinkling and increase the total flame volume to yield a flame area which is greater than that in the initial $a_d/\delta_{st} = 0.05$ case but still smaller than in the initial $a_d/\delta_{st} = 0.04$ case considered in this section. Furthermore, the time-averaged flame surface area of gaseous premixed V-shaped flame remains slightly larger than those for droplet cases.

The time-averaged value of Ω_F decreases with increasing a_d/δ_{st} as the probability of fuel-lean combustion increases with increasing droplet size, which is consistent with the decreasing trend of the mean values of $\dot{w}_c$ with increasing a_d (see Fig. 7.9). The integral $\int_V \dot{w}_c dV$ can be expressed as: $\int_V \dot{w}_c dV \approx \rho_0 S_c A_s$ and therefore $S_c < S_{b(\phi_g=1)}$ from Fig. 7.10 implies that $S = \int_V \dot{w}_c dV / \left[\rho_0 S_{b(\phi_g=1)} \int_V |\nabla c| dV\right]$ is expected to be smaller than unity for the cases considered in this section. The reduction of $\int_V \dot{w}_c dV$ dominates over the increase in flame surface area A_s for large droplets and ultimately gives rise to a decreasing trend of S with increasing a_d, which is also consistent with the decreasing trends of $S_c/S_{b(\phi_g=1)}$ with increasing a_d/δ_{st}. It can be seen from Table 7.5 that the ratio S stays close to unity for the gaseous premixed V-shaped flame, since the mean values of $\dot{w}_c + \nabla \cdot (\rho D \nabla c)$ and $\rho_0 S_{b(\phi_g=1)} |\nabla c|$ remain close to each other (see Fig. 7.9).

It has been demonstrated in Fig. 7.8 that most of the heat release in these flames takes place due to the premixed mode of combustion. It has been demonstrated in several previous analyses that the equality between the enhancements of burning rate and flame surface area in turbulent premixed flames with respect to their laminar counterparts (which is commonly referred to as Damköhler's first hypothesis) remains valid for statistically planar turbulent premixed flames even for the thickened flame regimes (i.e. for small (large) values of Damköhler (Karlovitz) number) [240–242] even though Damköhler's first hypothesis[243] was originally proposed for large values of Damköhler number (i.e. $Da \gg 1$). As the combustion in these spray flames takes place in the thickened flame regime, it is worthwhile to assess if Damköhler's first hypothesis remains valid for these flames.

Figure 7.9 implies that the mean value of $\left[\dot{S}_{liq,c} + \dot{A}_c\right]$ remains much smaller than the mean

value of $\rho_0 S_d^* |\nabla c|$. As $\int_V \nabla \cdot (\rho D \nabla c) dV = 0$, the integral $\int_V \dot{w}_c dV$ can be approximated as:

$$\int_V \dot{w}_c dV \approx \sum \langle \rho S_d |\nabla c| | c = c^* \rangle V_{c=c^*} \tag{7.3}$$

where $\langle Q | c = c^* \rangle$ is the mean value of a general quantity Q conditional upon $c = c^*$ and $V_{c=c^*}$ is the volume of the samples corresponding to $c = c^*$. It can be seen from Fig. 7.9 that the mean value of $\rho S_d |\nabla c|$ remains smaller than $\rho_0 S_{b(\phi_g=1)} |\nabla c|$ which leads to $S < 1.0$ for all cases. According to Damköhler's first hypothesis [243], the enhancements of burning rate and flame surface under turbulence are proportional to each other, which implies a unity value of S (i.e. $S = 1.0$) [244]. Thus, the non-unity values of S indicate a departure from Damköhler's first hypothesis and suggest that Damköhler's first hypothesis in its original form is not valid for turbulent spray flames. It can further be seen from Table 7.5 that S remains smaller than unity for all the droplet cases but $S' = \int_V \dot{w}_c dV / \left[\rho_0 S_{b(\phi_f)} \int_V |\nabla c| dV \right]$ (where ϕ_f is the volume-averaged gaseous phase equivalence ratio in the region corresponding to $0.01 \leq c \leq 0.99$) values are closer to unity and greater than the value of $S = \int_V \dot{w}_c dV / \left[\rho_0 S_{b(\phi_g=1)} \int_V |\nabla c| dV \right]$ because $S_{b(\phi_f)} / S_{b(\phi_g=1)}$ remains smaller than unity. However, Table 7.5 suggests that the departure of S' from 1.0 can also be significant for the large droplets (e.g. initial droplet size of $a_d / \delta_{st} = 0.06$), and thus the conclusions regarding Damköhler's first hypothesis in its original form do not change if S' is used.

It is possible to define a turbulent burning velocity S_T as: $S_T = \int_V \dot{w}_c dV / (\rho_0 A_{p,\tilde{c}}) = S(A_s / A_{p,\tilde{c}}) S_{b(\phi_g=1)}$ where $A_{p,\tilde{c}}$ is the flame area of the $\tilde{c}$ isosurface with respect to which S_T is evaluated. The values of $A_{p,\tilde{c}=0.1}$, $A_{p,\tilde{c}=0.5}$ and $A_{p,\tilde{c}=0.9}$ for the cases considered in this section are listed in Table 7.5. It is evident from Table 7.5 that A_s and $A_{p,\tilde{c}}$ assume comparable values for different values of a_d, and thus a decreasing trend of S with increasing droplet diameter gives rise to a reduction in turbulent burning velocity S_T with an increase in droplet diameter. This can be substantiated from Table 7.6 where $S_T / S_{b(\phi_g=1)}$ for the $\tilde{c} = 0.1$ and 0.5 isosurfaces are presented. It is also worth noting that $S_T / S_{b(\phi_g=1)}$ remains smaller than unity (i.e. $S_T / S_{b(\phi_g=1)} < 1.0$) for the droplet cases considered here but it should be considered that the normalised laminar burning velocity $S_{b(\langle \phi_g \rangle)} / S_{b(\phi_g=1)}$ for the mean gaseous phase equivalence ratio ranges between $0.78 - 0.83$, $0.67 - 0.76$, $0.47 - 0.57$ between locations A to C (with higher value at location C) for initial values of $a_d / \delta_{st} = 0.04$, 0.05 and 0.06, respectively. This suggests that $S_T / S_{b(\langle \phi_g \rangle)}$ remains greater than unity for all cases as given in Table 7.6, and thus the overall burning rate gets enhanced under turbulence and this augmentation is the most prominent for the case with the largest droplets as this case experiences the largest value of $S_T / S_{b(\langle \phi_g \rangle)}$ among the flames considered here. It can be seen from Table 7.6 that turbulent burning velocity S_T for the gaseous stoichiometric turbulent premixed flame assumes values greater than the corresponding laminar burning velocity (i.e. $S_T / S_{b(\phi_g=1)} > 1.0$). This further

Table 7.6: Turbulent burning velocity S_T based on the surface area for $\tilde{c} = 0.1$ and 0.5 isosurfaces for the gaseous premixed flame case (*GP*) and spray flames with different droplet diameters for a mean inlet velocity of $u_{mean}/S_{b(\phi_g=1)} = 5.0$.

a_d/δ_{st}	GP	0.04	0.05	0.06
$S_{T,\tilde{c}=0.1}/S_{b(\phi_g=1)}$	1.19	0.88	0.80	0.69
$S_{T,\tilde{c}=0.1}/S_{b,(\langle\phi_g\rangle,A)}$	-	1.13	1.19	1.47
$S_{T,\tilde{c}=0.1}/S_{b,(\langle\phi_g\rangle,B)}$	-	1.10	1.13	1.30
$S_{T,\tilde{c}=0.1}/S_{b,(\langle\phi_g\rangle,C)}$	-	1.06	1.05	1.21
$S_{T,\tilde{c}=0.5}/S_{b(\phi_g=1)}$	1.27	0.94	0.85	0.73
$S_{T,\tilde{c}=0.5}/S_{b,(\langle\phi_g\rangle,A)}$	-	1.21	1.27	1.55
$S_{T,\tilde{c}=0.5}/S_{b,(\langle\phi_g\rangle,B)}$	-	1.18	1.20	1.38
$S_{T,\tilde{c}=0.5}/S_{b,(\langle\phi_g\rangle,C)}$	-	1.13	1.12	1.28

suggests that the values of $S_T/S_{b(\phi_g=1)}$ for spray V-flames are smaller than the corresponding turbulent premixed gaseous flame and $S_T/S_{b(\phi_g=1)}$ decreases with increasing droplet diameter.

7.5 Effects of Mean Inflow Velocity

A comparison of gaseous mixture composition for the droplet cases with $u_{mean}/S_{b(\phi_g=1)} = 5.0$ and 10 can be made for different initial droplet diameters (i.e. $a_d/\delta_{st} = 0.04, 0.05, 0.06$) from the distributions of gaseous phase equivalence ratio in the mid-plane presented in Fig. 7.11. Gaseous equivalence ratio in the unburned gas region can reach at stoichiometric value (i.e. $\phi_g = 1.0$) for small droplet cases with initial $a_d/\delta_{st} = 0.04$ due to their high evaporation rates, however, ϕ_g mostly remains smaller than unity (i.e. $\phi_g < 1.0$) for large droplet cases with initial $a_d/\delta_{st} = 0.05$ and 0.06 as a result of their slow evaporation rates. Furthermore, in case of $u_{mean}/S_{b(\phi_g=1)} = 5.0$, small droplets mostly complete their evaporation by halfway in the streamwise direction, but the residence time of small droplets is not sufficient for a completed evaporation for the case of $u_{mean}/S_{b(\phi_g=1)} = 10.0$. As residence time of droplets is inversely linked with the mean flow velocity, mixture composition for all droplet sizes tends to be leaner for a higher $u_{mean}/S_{b(\phi_g=1)}$ due to shorter mean advection time in comparison to the evaporation timescale.

The effects of mean flow velocity on the composition of the gaseous phase mixture within the flame can be illustrated by the PDFs of the gaseous phase equivalence ratio ϕ_g within the flame characterised by $0.01 \leq c \leq 0.99$. It can be seen from Fig. 7.12 that combustion predominantly occurs under fuel-lean mode at all locations for both mean inflow velocities.

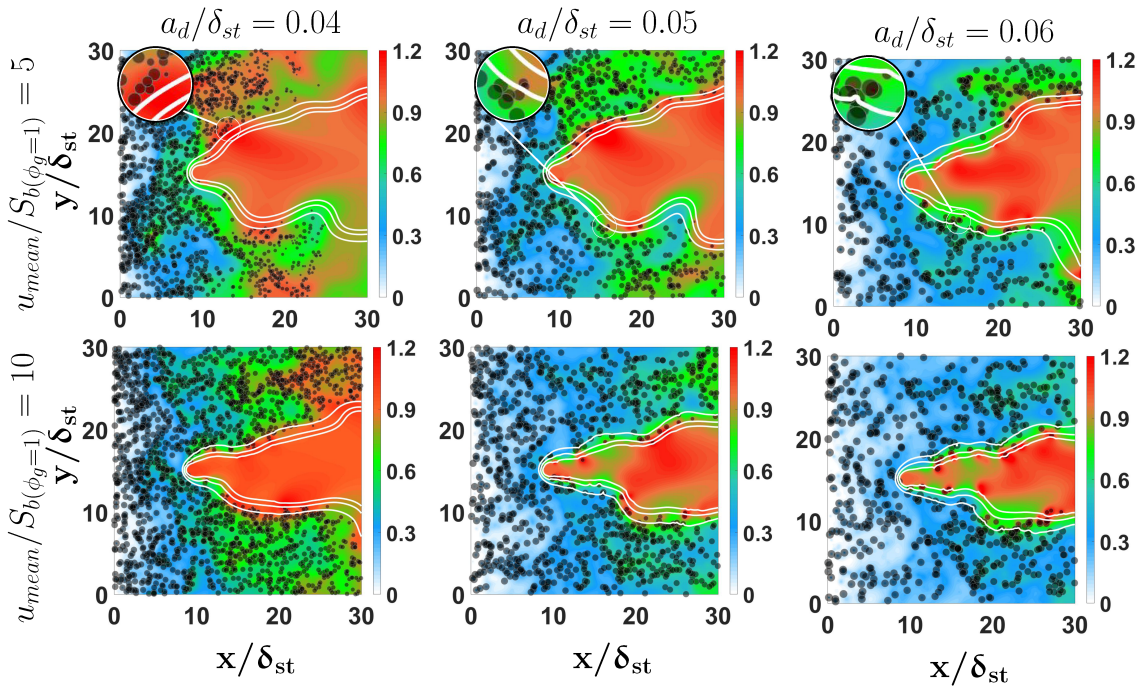

Figure 7.11: Instantaneous fields of gaseous equivalence ratio, ϕ_g on the central x-y midplane for initial $a_d/\delta_{st} = 0.04, 0.05, 0.06$ with $u_{mean}/S_{b(\phi_g=1)} = 5.0$ (1^{st} row) and 10 (2^{nd} row) at $t = 2.0t_{flow}$. White lines illustrate $c = 0.1, 0.5$ and 0.9 contours from outer to inner periphery and the droplets residing on the plane are indicated by grey dots (not to scale).

Although, evaporation of small droplets (i.e. initial $a_d/\delta_{st} = 0.04$ case) yields comparable ϕ_g distributions at locations B and C for both mean flow velocities, the PDF of ϕ_g at location A shows a higher probability of obtaining $\phi_g < 1.0$ for the case with $u_{mean}/S_{b(\phi_g=1)} = 10.0$ than in the case of $u_{mean}/S_{b(\phi_g=1)} = 5.0$. The differences in distributions of ϕ_g between the cases with $u_{mean}/S_{b(\phi_g=1)} = 5.0$ and 10.0 become prominent for large droplet cases with initial $a_d/\delta_{st} = 0.05$ and 0.06. The probability of finding gaseous mixtures with $\phi_g < 1.0$ has been found to be greater for the $u_{mean}/S_{b(\phi_g=1)} = 10.0$ cases than in the $u_{mean}/S_{b(\phi_g=1)} = 5.0$ cases, whereas the probability of finding $\phi_g \geq 1.0$ remain comparable for both mean inflow velocity conditions. This behaviour is a result of combined effect of shorter residence time of droplets for large mean velocities and the evaporation characteristics of droplets within the flame. It can be seen from Fig. 7.11 that droplets can be found in the unburned gas throughout the simulation domain for the initial $a_d/\delta_{st} = 0.04$ case for $u_{mean}/S_{b(\phi_g=1)} = 10.0$, whereas the droplets with the same initial diameter almost complete their evaporation process by the middle of the simulation domain for $u_{mean}/S_{b(\phi_g=1)} = 5.0$. This tendency is less prominent in the large droplet cases (e.g. initial $a_d/\delta_{st} = 0.05$ and 0.06 cases) due to their slow evaporation rates. An increase in the mean inflow velocity reduces the residence time of the droplets in

comparison to their evaporation time, and therefore, the droplets can traverse farther in the axial direction without completing their evaporation process for large values of $u_{mean}/S_{b(\phi_g=1)}$, and consequently in these cases less fuel vapour becomes available in the gaseous phase than in the cases with smaller mean flow velocity. Furthermore, large droplets, which reach at the flame and escape through the flame without complete evaporation, eventually evaporate completely in the high temperature zone in the burned gas (i.e. $c \approx 1.0$). The resulting evaporated fuel vapour diffuses from the high temperature burned gas region into the flame and mixes with the excess air diffusing from the unburned gas side to give rise to local pockets of stoichiometric mixture (i.e. $\phi_g = 1.0$) where diffusion mode of combustion is obtained. The predominance of fuel-lean combustion in the gaseous phase for higher mean inflow velocity cases can be verified by comparing the time-averaged values of ϕ_g given for $a_d/\delta_{st} = 0.04$ with $u_{mean}/S_{b(\phi_g=1)} = 5\,(10)$ are $0.88\,(0.84)$, $0.89\,(0.87)$ and $0.90\,(0.88)$, for $a_d/\delta_{st} = 0.05$ with $u_{mean}/S_{b(\phi_g=1)} = 5\,(10)$ are $0.83\,(0.75)$, $0.85\,(0.77)$ and $0.87\,(0.79)$, for $a_d/\delta_{st} = 0.06$ with $u_{mean}/S_{b(\phi_g=1)} = 5\,(10)$ are $0.74\,(0.66)$, $0.77\,(0.69)$ and $0.79(0.70)$, at locations A, B and C, respectively. These values further indicate that tendency of fuel-lean nature of combustion decreases in the downstream direction due to increased availability of fuel vapour as a result of evaporation of droplets, which is consistent with the observations of previous section (see Section 7.1).

The local Damköhler number values based on $S_{b,\tilde{\xi}}$ at the location corresponding to $\tilde{c} = 0.5$, which for $a_d/\delta_{st} = 0.04$ with $u_{mean}/S_{b(\phi_g=1)} = 5\,(10)$ are $0.79\,(0.75)$, $0.92\,(0.94)$ and $1.09\,(1.27)$, for $a_d/\delta_{st} = 0.05$ with $u_{mean}/S_{b(\phi_g=1)} = 5\,(10)$ are $0.49\,(0.26)$, $0.71\,(0.57)$ and $1.00\,(0.73)$, for $a_d/\delta_{st} = 0.06$ with $u_{mean}/S_{b(\phi_g=1)} = 5\,(10)$ are $0.27\,(0.07)$, $0.40\,(0.14)$ and $0.62\,(0.26)$ at locations A, B and C, respectively. The local Damköhler number Da_L for the premixed case with $u_{mean}/S_{b(\phi_g=1)} = 5\,(10)$ are $3.66(0.73), 3.93(0.93)$, and $3.99(1.14)$ at locations A, B and C, respectively. Similarly, the corresponding values of the local Karlovitz number values based on $S_{b,\tilde{\xi}}$ at the location corresponding to $\tilde{c} = 0.5$ for $a_d/\delta_{st} = 0.04$ with $u_{mean}/S_{b(\phi_g=1)} = 5\,(10)$ are $1.79\,(1.16)$, $1.74\,(1.09)$ and $1.79\,(1.06)$, for $a_d/\delta_{st} = 0.05$ with $u_{mean}/S_{b(\phi_g=1)} = 5\,(10)$ are $2.60\,(3.05)$, $2.18\,(2.08)$ and $1.87\,(1.96)$, for $a_d/\delta_{st} = 0.06$ with $u_{mean}/S_{b(\phi_g=1)} = 5\,(10)$ are $4.12\,(7.98)$, $3.33\,(5.37)$ and $2.75\,(3.96)$ at locations A, B and C, respectively. The corresponding values for the premixed case with $u_{mean}/S_{b(\phi_g=1)} = 5\,(10)$ are $3.77\,(1.82), 3.39\,(1.82)$, and $2.91\,(1.82)$ at locations A, B and C, respectively. According to these estimated values of Da_L and Ka_L, the gaseous phase combustion nominally takes places in the thin reaction zones regime [93]. The predominance of low Damköhler number combustion can be substantiated from the PDFs of reaction progress variable c for different values of Favre average values of reaction progress variable $\tilde{c}$. Figure 7.13 shows the PDFs of reaction progress variable c for the Favre-averaged reaction progress variable values $\tilde{c} = 0.1$,

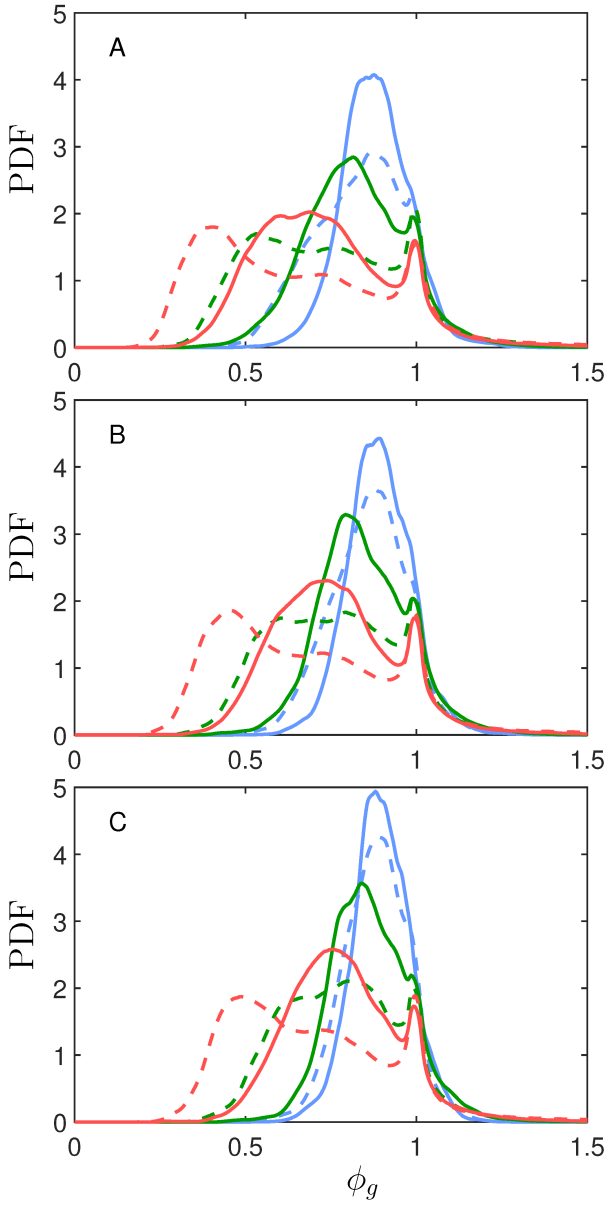

Figure 7.12: PDFs of ϕ_g in the region corresponding to $0.01 \leq c \leq 0.99$ at different locations A, B and C (top to bottom) for initial $a_d/\delta_{st} = 0.04$, 0.05 and 0.06 with $u_{mean}/S_{b(\phi_g=1)} = 5.0$ (continuous line) and 10.0 (dashed line). See Fig. 7.2 caption for the colour keys.

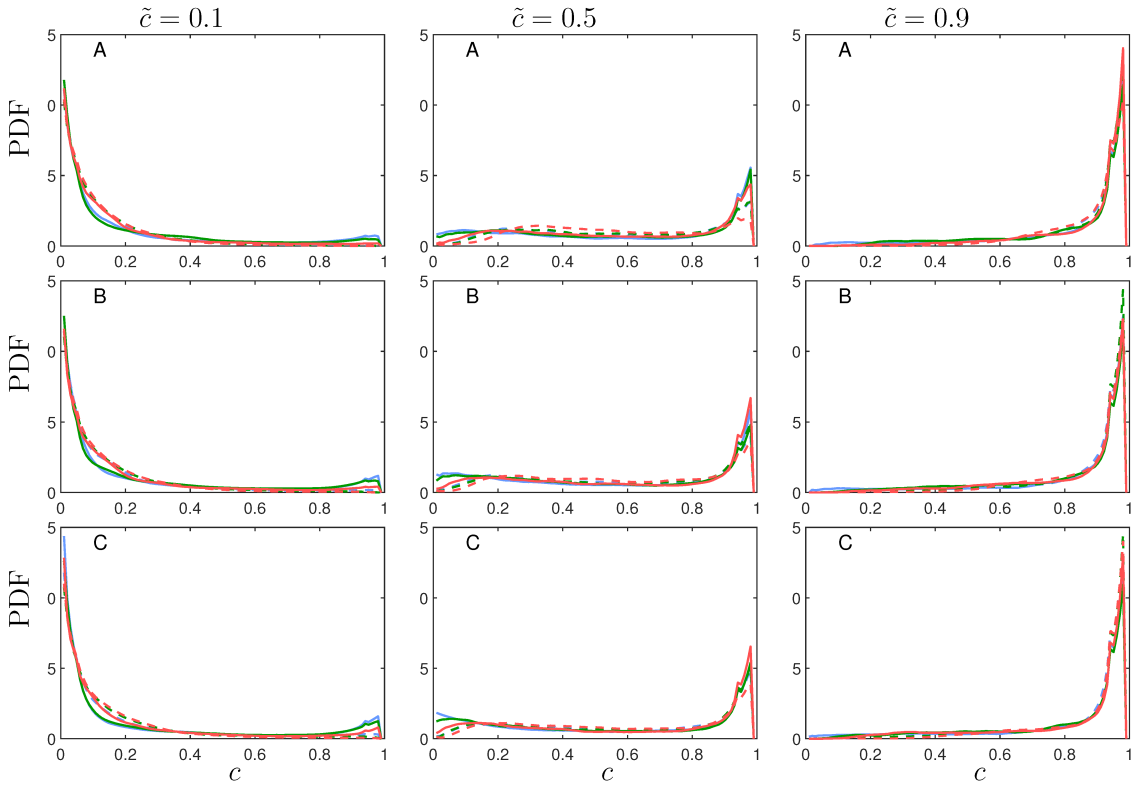

Figure 7.13: PDFs of c conditional on $\tilde{c} = 0.1$, 0.5, 0.9 at different locations A, B and C (top to bottom) for initial $a_d/\delta_{st} = 0.04$, 0.05 and 0.06 with $u_{mean}/S_{b(\phi_g=1)} = 5.0$ (solid line) and 10.0 (dashed line). See Fig. 7.2 caption for the colour keys.

0.5 and 0.9 at locations A, B and C, whereas the contours of $\tilde{c} = 0.1$, 0.5 and 0.9 for the cases considered here are shown in Fig. 7.14. The PDFs of c are supposed to show a bimodal distribution with peaks at $c = 0.0$ and $c = 1.0$ for high values of Damköhler number [235]. However, Fig 7.13 reveals that the PDFs of c do not exhibit bimodal distribution for the most cases considered in this study. The departure of PDF of c from bimodal distribution with impulses at $c = 0.0$ and $c = 1.0$ shows the tendency of low Damköhler number combustion for the cases considered in this section. Figure 7.13 further demonstrates that the PDFs of c for the cases considered here show mostly mono-modal distributions and this tendency strengthens with increasing mean inflow velocity.

The small values of Damköhler number and high values of Karlovitz number are indicative of the thickened flame regime of combustion [93] and local occurrences of flame thickening can be discerned from the contours of c in Fig. 7.11. This along with the flame wrinkling determines the flame brush thickness in the V-flame cases considered in this analysis. The flame brush thickness $\delta_{T(0.1-0.9)}$ can be defined as the distance between $\tilde{c} = 0.1$ and 0.9 isosurfaces for a given location, as shown in Fig. 7.14. The values of flame brush thickness, $\delta_{T(0.1-0.9)}/\delta_{st}$

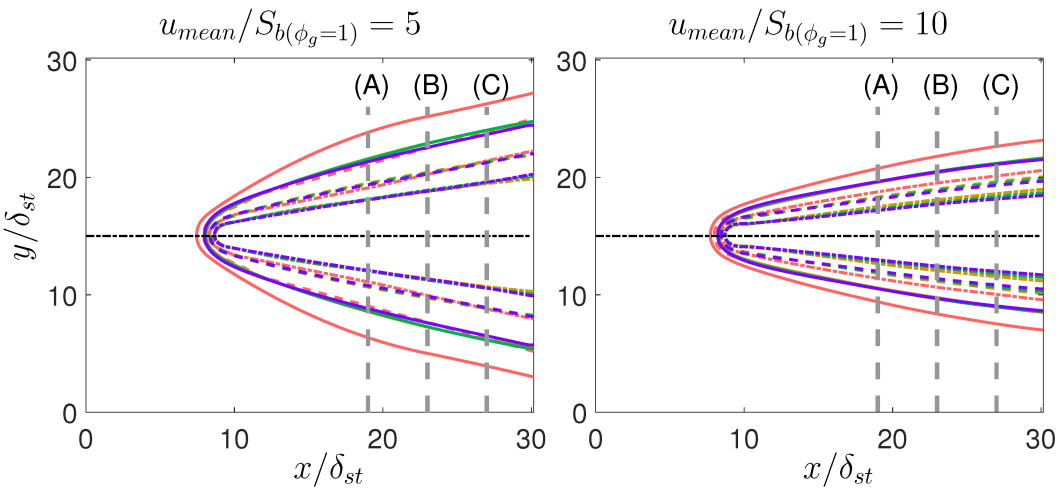

Figure 7.14: Contours of $\tilde{c} = 0.1$ (solid line), 0.5 (dashed line) and 0.9 (dotted line) contours for gaseous premixed (——) case and droplet cases with initial droplet diameter $a_d/\delta_{st} = 0.04$ (——), 0.05 (——) and 0.06 (——) with $u_{mean}/S_{b(\phi_g=1)} = 5.0$ (left) and 10.0 (right). The dashed grey lines show the sampling locations (A, B, C from left to right), and the dotted black line shows the flame centre.

for V-flame cases under droplet-laden mixtures are presented and compared to the corresponding stoichiometric turbulent premixed gaseous flame cases in Table 7.7. It can be seen from Table 7.7 that the flame brush thickness $\delta_{T(0.1-0.9)}/\delta_{st}$ increases in the downstream and decreases with increasing droplet diameter for the cases with low mean flow velocity. On the contrary, flame brush becomes wider for large droplet cases with $u_{mean}/S_{b(\phi_g=1)} = 10.0$. According to turbulent diffusion velocity, flame brush thickness for a V-shaped flame is correlated with the distance from flame holder and flow parameters (i.e. bulk mean velocity u_{mean}, root-mean-square u' and integral length scale l_t) [233, 237, 245]. Kheirkhah and Gulder [233] demonstrated the effects of equivalence ratio on flame brush thickness under different flow conditions (i.e. u'/u_{mean}) for V-shaped premixed flames. The flame brush thickness can alternatively be estimated using the expressions: $\delta_{T,\tilde{c}} = 1/max|\nabla\tilde{c}|$ and $\delta_{T,\bar{c}} = 1/max|\nabla\bar{c}|$. Reported values of $\delta_{T,\tilde{c}}$ and $\delta_{T,\bar{c}}$ in Table 7.7 exhibit qualitatively similar trends as that of $\delta_{T(0.1-0.9)}$ in response to the changes in flow conditions and droplet diameter. The values of flame brush thickness of gaseous premixed V-shaped flames with $u_{mean}/S_{b(\phi_g=1)} = 10.0$ remain comparable to those of small droplet case while the gaseous premixed flame has a thinner flame brush than in the droplet cases for $u_{mean}/S_{b(\phi_g=1)} = 5.0$.

The flame brush thickness depends both on the Zel'dovich thickness $\delta_{(\phi)} \sim \alpha_{T0}/S_{b(\phi)}$, and also on the flame wrinkling which is dependent on $L_{11}/\delta_{(\phi)}$ [238]. This suggests that $\delta_{(\phi)}$ (resp. $L_{11}/\delta_{(\phi)}$) is expected to increase (resp. decrease) with increasing droplet diameter due to greater likelihood of fuel-lean combustion (where $\phi_g < 1.0$ and $S_{b(\phi)} < S_{b(\phi_g=1)}$) for

Table 7.7: Flame brush thickness at locations A, B and C for the gaseous premixed flame case (*GP*) and spray flames with different droplet diameters.

	a_d/δ_{st}	GP	0.04	0.05	0.06
$u_{mean}/S_{b(\phi_g=1)} = 5.0$	$\delta_{T(0.1-0.9)}/\delta_{st}$ at A	3.14	3.45	3.38	3.23
	$\delta_{T(0.1-0.9)}/\delta_{st}$ at B	3.34	4.13	4.00	3.75
	$\delta_{T(0.1-0.9)}/\delta_{st}$ at C	3.70	4.50	4.40	4.06
	$\delta_{T,\tilde{c}}/\delta_{st}$ at A	3.04	3.50	3.33	3.18
	$\delta_{T,\tilde{c}}/\delta_{st}$ at B	3.12	4.27	4.12	3.83
	$\delta_{T,\tilde{c}}/\delta_{st}$ at C	3.35	4.79	4.97	4.35
	$\delta_{T,\tilde{c}}/\delta_{st}$ at A	2.47	2.82	2.69	2.72
	$\delta_{T,\tilde{c}}/\delta_{st}$ at B	2.34	3.28	3.12	3.09
	$\delta_{T,\tilde{c}}/\delta_{st}$ at C	2.37	3.84	3.62	3.45
$u_{mean}/S_{b(\phi_g=1)} = 10.0$	$\delta_{T(0.1-0.9)}/\delta_{st}$ at A	2.01	2.08	2.35	2.45
	$\delta_{T(0.1-0.9)}/\delta_{st}$ at B	2.27	2.31	2.66	2.77
	$\delta_{T(0.1-0.9)}/\delta_{st}$ at C	2.51	2.56	2.84	2.93
	$\delta_{T,\tilde{c}}/\delta_{st}$ at A	1.90	1.96	2.19	2.29
	$\delta_{T,\tilde{c}}/\delta_{st}$ at B	2.28	2.21	2.62	2.63
	$\delta_{T,\tilde{c}}/\delta_{st}$ at C	2.63	2.46	2.85	2.84
	$\delta_{T,\tilde{c}}/\delta_{st}$ at A	1.62	1.72	1.96	2.09
	$\delta_{T,\tilde{c}}/\delta_{st}$ at B	1.87	1.90	2.23	2.29
	$\delta_{T,\tilde{c}}/\delta_{st}$ at C	2.13	2.09	2.44	2.46

larger droplets. The smaller extent of flame wrinkling due to smaller values of $L_{11}/\delta_{(\phi)}$ as a result of higher likelihood of fuel-lean combustion for larger droplets overcomes the effects of the thickening of the flame front for small values of $u_{mean}/S_{b(\phi_g=1)}$. This gives rise to a decrease in flame brush thickness with increasing a_d/δ_{st} for $u_{mean}/S_{b(\phi_g=1)} = 5.0$. However, the greater likelihood of the thickening of flame front due to the predominance of fuel-lean combustion in the case of large diameters overcomes the effects of weakened flame wrinkling for small values of $L_{11}/\delta_{(\phi)}$ for $u_{mean}/S_{b(\phi_g=1)} = 10.0$ cases, which is reflected in the increasing trend of flame brush thickness with increasing droplet diameter. The changes in flame brush thickness in the mean flow direction lead to the variation of flame angle for V-shaped flames. Furthermore, slightly curved nature of $\tilde{c}$ isosurfaces yields to significant differences in flame angle in the mean flow direction from location A to C. The contours of Favre averaged reaction progress variable presented in Fig. 7.14 also demonstrate that the variations of mean inflow velocity and droplet diameter give rise to significant differences in the angles made by the tangent on the $\tilde{c} = 0.1$, 0.5 and 0.9 contours with the mean flow direction (i.e. x-direction). The angles $\theta_{\tilde{c}=0.1}$, $\theta_{\tilde{c}=0.5}$ and $\theta_{\tilde{c}=0.9}$ for $\tilde{c} = 0.1$, 0.5 and 0.9 isosurfaces are provided in Table 7.8 for locations A, B and C where these angles are calculated using the slopes of the tangent on the respective $\tilde{c}$ isosurfaces at a given axial location. It can be seen from Fig.7.14 that

Table 7.8: Flame angle θ (i.e. the angle the tangent on the $\tilde{c}$ isosurface at a given location makes with the midline) for $\tilde{c}$ isosurfaces for the gaseous premixed flame case (*GP*) and spray flames with different droplet diameters.

	a_d/δ_{st}	GP	0.04	0.05	0.06
$u_{mean}/S_{b(\phi_g=1)} = 5.0$	Flame angle $\theta_{\tilde{c}=0.1}$ for $\tilde{c} = 0.1$ at *A*	16.06°	20.47°	20.42°	18.88°
	Flame angle $\theta_{\tilde{c}=0.1}$ for $\tilde{c} = 0.1$ at *B*	13.56°	15.76°	16.12°	14.80°
	Flame angle $\theta_{\tilde{c}=0.1}$ for $\tilde{c} = 0.1$ at *C*	17.12°	15.46°	16.58°	17.00°
	Flame angle $\theta_{\tilde{c}=0.5}$ for $\tilde{c} = 0.5$ at *A*	14.66°	14.66°	14.49°	11.72°
	Flame angle $\theta_{\tilde{c}=0.5}$ for $\tilde{c} = 0.5$ at *B*	7.21°	12.07°	12.06°	15.44°
	Flame angle $\theta_{\tilde{c}=0.5}$ for $\tilde{c} = 0.5$ at *C*	10.95°	13.04°	14.37°	14.99°
	Flame angle $\theta_{\tilde{c}=0.9}$ for $\tilde{c} = 0.9$ at *A*	13.46°	9.82°	11.20°	11.62°
	Flame angle $\theta_{\tilde{c}=0.9}$ for $\tilde{c} = 0.9$ at *B*	10.57°	9.31°	9.96°	9.49°
	Flame angle $\theta_{\tilde{c}=0.9}$ for $\tilde{c} = 0.9$ at *C*	10.54°	9.62°	10.22°	12.18°
$u_{mean}/S_{b(\phi_g=1)} = 10.0$	Flame angle $\theta_{\tilde{c}=0.1}$ for $\tilde{c} = 0.1$ at *A*	16.7°	13.8°	14.1°	13.4°
	Flame angle $\theta_{\tilde{c}=0.1}$ for $\tilde{c} = 0.1$ at *B*	12.0°	9.9°	10.1°	9.5°
	Flame angle $\theta_{\tilde{c}=0.1}$ for $\tilde{c} = 0.1$ at *C*	12.7°	11.9°	10.1°	9.7°
	Flame angle $\theta_{\tilde{c}=0.5}$ for $\tilde{c} = 0.5$ at *A*	14.0°	11.5°	11.0°	10.7°
	Flame angle $\theta_{\tilde{c}=0.5}$ for $\tilde{c} = 0.5$ at *B*	9.7°	8.2°	8.1°	7.3°
	Flame angle $\theta_{\tilde{c}=0.5}$ for $\tilde{c} = 0.5$ at *C*	11.0°	9.7°	9.4°	8.6°
	Flame angle $\theta_{\tilde{c}=0.9}$ for $\tilde{c} = 0.9$ at *A*	12.4°	9.8°	8.8°	8.8°
	Flame angle $\theta_{\tilde{c}=0.9}$ for $\tilde{c} = 0.9$ at *B*	8.7°	7.2°	6.8°	6.3°
	Flame angle $\theta_{\tilde{c}=0.9}$ for $\tilde{c} = 0.9$ at *C*	9.4°	7.7°	7.9°	6.8°

flame angles decrease with increasing mean inflow velocity, as expected, and the flame angles $\theta_{\tilde{c}=0.1}$, $\theta_{\tilde{c}=0.5}$ and $\theta_{\tilde{c}=0.9}$ for gaseous premixed flame are greater than those for droplet cases for $u_{mean}/S_{b(\phi_g=1)} = 10.0$ but the opposite trend is mostly observed for $u_{mean}/S_{b(\phi_g=1)} = 5.0$ except for the flame angle $\theta_{\tilde{c}=0.9}$ in the case of small droplet diameters. This behaviour originates due to differences in the evolution of the flame brush thickness in the mean flow direction (see Table 7.7). The flame angles at a given plane remain comparable for different droplet diameters for both mean inflow velocities considered in this section.

The variation of flame angle in the mean flow direction for different droplet sizes is consistent with the evolution of the distribution of reacting mixture composition at various $\tilde{c}$ isosurfaces. Figure 7.15 shows the PDFs of gaseous equivalence ratio on $\tilde{c} = 0.1$, 0.5 and 0.9 isosurfaces at different axial locations for both mean inflow velocities. Figure 7.15 indicates that the variation of the mean inflow velocity causes significant differences in the PDFs of ϕ_g at $\tilde{c} = 0.1$. Evaporated fuel in droplet cases with higher mean flow velocity burns leaner mixture at $\tilde{c} = 0.1$ than that with lower mean inflow velocity and the differences between the PDF profiles for different mean velocities decrease in the mean flow direction from *A* to *C* for $\tilde{c} = 0.1$. Additionally, ϕ_g distribution for $\tilde{c} = 0.5$ becomes comparable for a given

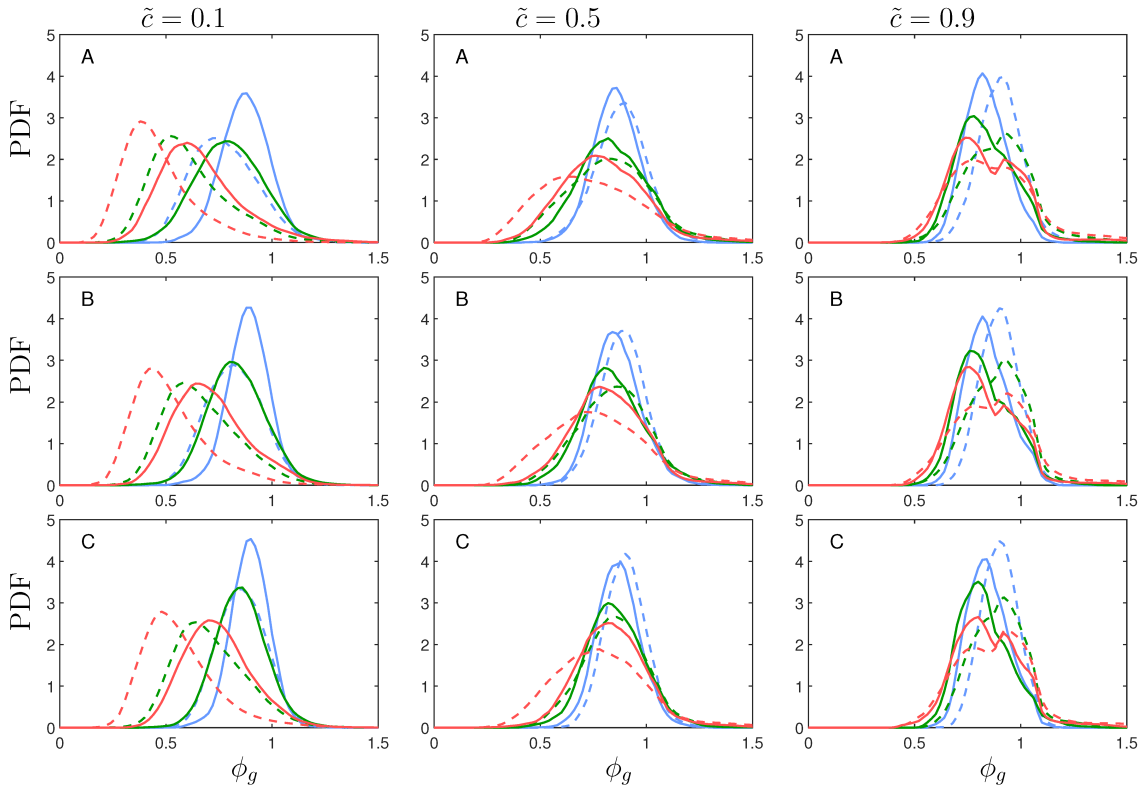

Figure 7.15: PDFs of ϕ_g conditional on $\tilde{c} = 0.1$, 0.5 and 0.9 isosurfaces at different locations A, B and C (top to bottom) for initial $a_d/\delta_{st} = 0.04$, 0.05 and 0.06 with $u_{mean}/S_{b(\phi_g=1)} = 5.0$ (continuous line) and 10.0 (dashed line). See Fig. 7.2 caption for the colour keys.

droplet diameter with different mean inflow velocities at all locations considered in this section. On the contrary, PDFs of ϕ_g for higher mean inflow velocity cases attain a peak value at $\phi_g \approx 1.0$ towards the burned gas side of the flame brush (e.g. $\tilde{c} = 0.9$) which implies that spray flames with $u_{mean}/S_{b(\phi_g=1)} = 10.0$ show greater probabilities of having stoichiometric mixture towards the burned gas side of the flame brush than in $u_{mean}/S_{b(\phi_g=1)} = 5.0$ cases. Droplets with a mean flow velocity $u_{mean}/S_{b(\phi_g=1)} = 10.0$ travel greater distances within the flame brush before completing their evaporation than in the case of $u_{mean}/S_{b(\phi_g=1)} = 5.0$. As a result, the droplets for $u_{mean}/S_{b(\phi_g=1)} = 10.0$ cases on average are bigger in size towards the unburned gas side of the flame brush than in the cases with $u_{mean}/S_{b(\phi_g=1)} = 5.0$ Therefore, droplets can penetrate further into flame brush before complete their evaporation in the high temperature region for $u_{mean}/S_{b(\phi_g=1)} = 10.0$ cases than in the corresponding $u_{mean}/S_{b(\phi_g=1)} = 5.0$ cases. Consequently, $u_{mean}/S_{b(\phi_g=1)} = 10.0$ cases exhibit higher probability of $\phi_g \approx 1.0$ towards the burned gas than in the corresponding $u_{mean}/S_{b(\phi_g=1)} = 5.0$ cases.

The droplets, which penetrate the flame, give rise to droplet-induced wrinkling on the flame surface. In order to demonstrate this, $c = 0.5$ isosurfaces coloured by local values of

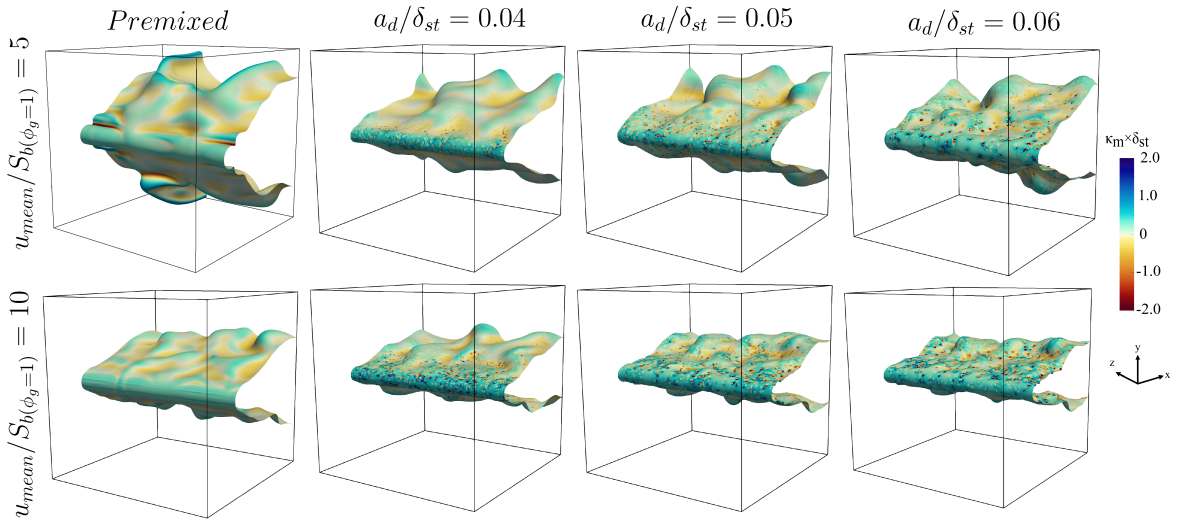

Figure 7.16: Instantaneous views of $c = 0.5$ isosurface coloured with $\kappa_m \times \delta_{st}$ values for gaseous premixed and spray flames with initial $a_d/\delta_{st} = 0.04, 0.05, 0.06$ for $u_{mean}/S_{b(\phi_g=1)} = 5.0$ (1^{st} row) and 10.0 (2^{nd} row) at $t = 2.0t_{flow}$.

flame curvature $\kappa_m \times \delta_{st}$ are exemplarily shown in Fig. 7.16. It is evident from Fig. 7.16 that flame surfaces for the gaseous premixed flames remain smooth irrespective of the mean inflow velocity and exhibit wrinkles induced by the turbulent fluid motion. Furthermore, small droplets with $u_{mean}/S_{b(\phi_g=1)} = 5.0$ rarely interact with the flame because they mostly evaporate before reaching the flame surface. However, a decrease in advection time in comparison to the evaporation timescale with increasing $u_{mean}/S_{b(\phi_g=1)}$ enhances the number of droplets interacting with the flame farther in the mean flow direction. This leads to greater propensity to obtain dimples on the flame surface for cases with higher mean inflow velocity. Moreover, flame wrinkling as a result of the dimples arising from flame-droplet interaction increases with increasing droplet diameter due to the slow evaporation rate of large droplets for a given mean inflow velocity. The larger droplets survive longer in the mean flow direction because of their slower evaporation rate, and thus the dimples become denser for larger droplet diameters and higher mean inflow velocities. This behaviour is consistent with previous experimental [119] and numerical (see Section 4.1) findings for spherically expanding flames propagating into droplet-laden mixtures.

The aforementioned droplet-induced flame surface deformation can be quantified with the help of the PDFs of flame surface curvature κ_m. Figure 7.17 shows the PDFs of local normalised flame curvature $\kappa_m \times \delta_{st}$ on the $c = 0.8$ isosurface at different planes (i.e. A, B and C) for all droplet cases and the corresponding gaseous premixed flame cases considered in this section. Although the PDFs of local normalised flame curvature $\kappa_m \times \delta_{st}$ are shown only for

$c = 0.8$ isosurface in Fig. 7.17, they show qualitatively similar behaviour for other values of c and thus are not presented for the sake of brevity. Figure 7.17 reveals that the PDFs of κ_m assume peak value at zero curvature at all locations for both gaseous premixed and droplet-laden flames. For droplet cases, the PDF profiles of $\kappa_m \times \delta_{st}$ broaden both for negative and positive values in comparison to the corresponding gaseous premixed flames due to flame-droplet interactions. The PDFs of $\kappa_m \times \delta_{st}$ for droplet cases widen with increasing mean inflow velocity, whereas an opposite trend is observed for gaseous premixed flames because the flame becomes increasingly narrow for increasing mean inflow velocity. It can be seen from Figs. 7.11 and 7.14, and Table 7.8 that the flame angle shrinks with increasing $u_{mean}/S_{b(\phi_g=1)}$, and thus the gaseous premixed flames shows greater range of both positive and negative curvature values in the case of smaller mean inflow velocity because of greater likelihood of the flame interaction with a range of different turbulent flow conditions. It has already been explained earlier that the greater availability of droplet within the flame brush increases the possibility of flame-droplet interaction for higher mean inlet velocities and this yields wider distributions of $\kappa_m \times \delta_{st}$ for all the droplet cases at all locations (i.e. A, B and C) with a higher possibility of finding negative and positive tails. Differences in PDF of κ_m between two mean inflow velocities for a given droplet diameter increase in the streamwise direction from A to C, since some of the droplets complete their evaporation before reaching the flame, especially farther in the streamwise direction for lower mean inflow velocity cases. Moreover, the widening of $\kappa_m \times \delta_{st}$ of droplet flame cases in comparison to the corresponding gaseous premixed flames increases with increasing droplet diameter because these droplets survive longer within the flame due to their slower evaporation rates and thus induce greater extents of flame-droplet interaction.

The wrinkling of c-isosurfaces in these flames, in turn, have implications on the burning rate statistics in premixed flames. Figure 7.18 shows the percentages of heat release rate arising from the premixed and non-premixed modes of combustion for all droplet cases considered in this section. It is evident from Fig. 7.18 that the premixed mode of combustion is the dominant contributor to the total heat release for all droplet cases at all locations considered in this section. However, the percentage of heat release associated with non-premixed combustion reaches non-negligible levels for large droplet cases particularly at higher mean inflow velocity. The slow evaporation of large droplets gives rise to the extent of mixture inhomogeneity in the gaseous phase and this increases the likelihood of non-premixed combustion for larger droplet cases. In the case of higher mean flow velocity, larger number of droplets pass through the flame and eventually evaporate in the burned gas region (i.e. $c \approx 1.0$) generating locally fuel-rich regions. Unburned fuel vapour from these fuel-rich pockets in the burned gas region eventually diffuses into the flame and mixes with the air diffusing from the predomin-

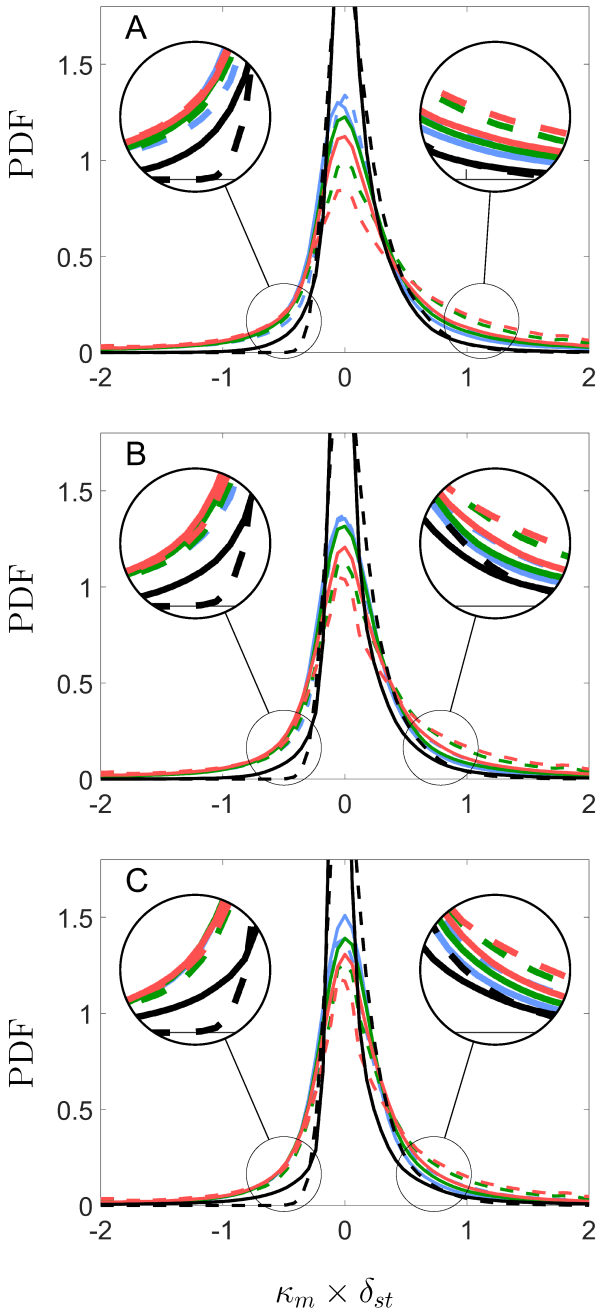

Figure 7.17: PDFs of $\kappa_m \times \delta_{st}$ of the $c = 0.8$ isosurface at locations A, B and C (top to bottom) for gaseous premixed (——) and V-shaped spray flames with initial $a_d/\delta_{st} = 0.04$, 0.05 and 0.06 for $u_{mean}/S_{b(\phi_g=1)} = 5.0$ (continuous line) and10.0 (dashed line). See Fig. 7.2 caption for the colour keys.

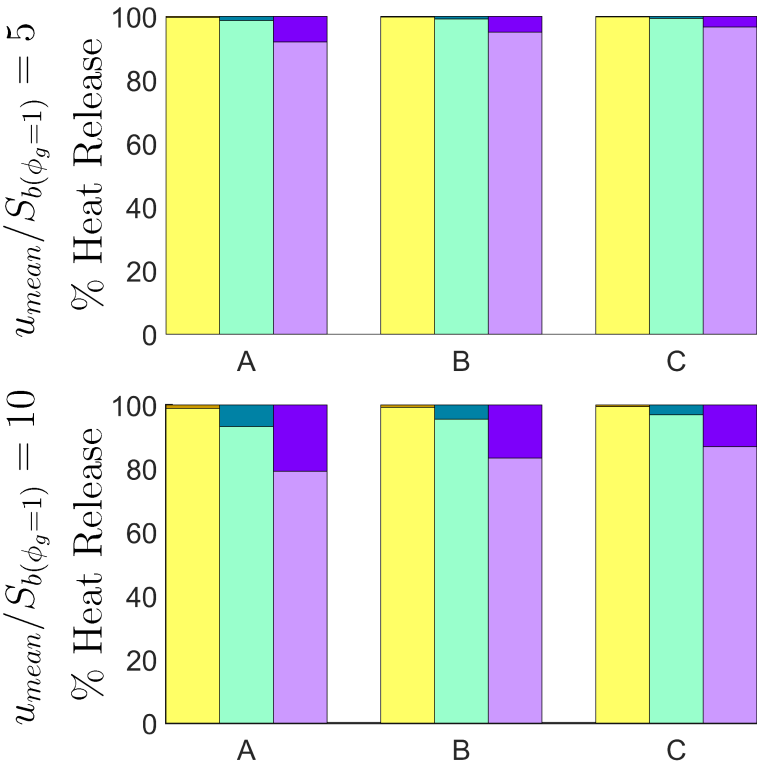

Figure 7.18: Percentage of heat release arising from premixed (for initial $a_d/\delta_{st} = 0.04$ (■), 0.05 (■), 0.06 (■)) and non-premixed (for initial $a_d/\delta_{st} = 0.04$ (■), 0.05 (■), 0.06 (■)) modes of combustion for $u_{mean}/S_{b(\phi_g=1)} = 5.0$ (1^{st} row) and 10.0 (2^{nd} row) at locations A, B and C (left to right).

antly fuel-lean unburned gas side to give rise to local diffusion mode of burning. Therefore, the extent of heat release due to the non-premixed mode of combustion increases with increasing $u_{mean}/S_{b(\phi_g=1)}$. As non-premixed combustion occurs where stoichiometric mixture is obtained, the mild peaks at $\phi_g \approx 1.0$ in the PDFs of ϕ_g in Fig. 7.12 are predominantly associated with the non-premixed mode of combustion in these droplet cases.

With the information that heat release predominantly takes place in premixed mode, it is worthwhile to analyse the flame propagation statistics in terms of density-weighted displacement speed S_d^* and consumption speed S_c. Therefore, it is instructive to analyse the mean behaviour of the terms, which drive the statistical behaviour of density-weighted displacement speed S_d^*. Figure 7.19 shows the mean values of the terms $\dot{w}_c$, $\dot{S}_{liq,c}$, $\dot{A}_c$ and $\nabla \cdot (\rho D \nabla c)$ conditional on c for locations A, B and C for the cases with different mean inflow velocities. Figure 7.19 indicates that the mean molecular diffusion term $\nabla \cdot (\rho D \nabla c)$ assumes positive values towards the preheat zone (i.e. $c < 0.5$) but becomes negative in the reaction zone (i.e. $0.5 \leq c \leq 0.9$) in contrast with the positive mean values of $\dot{w}_c$ for all cases considered in this section. Furthermore, since stratified mixtures with $\phi_g < 1.0$ and $\phi_g > 1.0$ burn slower in

the droplet cases than in the stoichiometric (i.e. $\phi_g = 1.0$) premixed flame, the mean values of $\dot{w}_c$ for droplets cases is expected to be smaller than the gaseous premixed case. Overwhelmingly leaner combustion trend in the case of larger droplets reduces to the mean values of $\dot{w}_c$ with increasing a_d and the differences in the mean values of $\dot{w}_c$ between the gaseous premixed and droplet cases are greater for $u_{mean}/S_{b(\phi_g=1)} = 10.0$ than those of the cases with $u_{mean}/S_{b(\phi_g=1)} = 5.0$ due to the predominance of fuel-lean combustion for higher inflow velocities (see Figs. 7.12 and 7.15). Although, the mean values of terms associated with droplet evaporation $\dot{S}_{liq,c}$ and mixture inhomogeneity $\dot{A}_c$ are negligible compared with the magnitudes of the mean values of $\dot{w}_c$ and $\nabla \cdot (\rho D \nabla c)$ throughout the flame in the cases with lower mean flow velocity, these mean values (i.e. $\dot{S}_{liq,c}$ and $\dot{A}_c$) slightly increase for higher mean inflow velocity cases. Figure 7.19 further shows that the mean value of $\rho S_d |\nabla c|$ remains comparable with the mean value of $\rho_0 S_{b(\phi_g=1)} |\nabla c|$ for the gaseous premixed V-flames with different mean flow velocities. However, the mean values of $\rho S_d |\nabla c| = [\nabla \cdot (\rho D \nabla c) + \dot{w}_c + \dot{S}_{liq,c} + \dot{A}_c]$ have been found to be smaller than those of $\rho_0 S_{b(\phi_g=1)} |\nabla c|$ for all droplet cases considered in this section. It can also be observed from Fig. 7.19 that the statistical behaviours of $\rho S_d |\nabla c|$ and $\rho_0 S_{b(\phi_g=1)} |\nabla c|$ are not significantly influenced by the variation of the mean inflow velocity for V-shaped flames. A decreasing trend of $\rho_0 S_{b(\phi_g=1)} |\nabla c|$ with increasing droplet diameter and mean inflow velocity for droplet cases suggests that the flame thickens with increasing droplet diameter and mean inflow velocity due to increased propensity for fuel-lean combustion. As the premixed combustion takes place in the flamelet regime, the background turbulent motion does not affect the flame structure and as a result the mean values of $\dot{w}_c$, $\nabla \cdot (\rho D \nabla c)$ and $\rho_0 S_{b(\phi_g=1)} |\nabla c|$ are not affected by the mean inflow velocity.

Although the statistical behaviour of density-weighted displacement speed S_d^* is strongly linked with the evolution of the aforementioned terms (i.e. $\nabla \cdot (\rho D \nabla c)$, $\dot{w}_c$, $\dot{S}_{liq,c}$, $\dot{A}_c$), consumption speed S_c is dependent only on $\dot{w}_c$ and the flame thickness. Figure 7.20 shows the normalised mean consumption speed $S_c/S_{b(\phi_g=1)}$ and density-weighted displacement speed, $S_d^*/S_{b(\phi_g=1)}$ calculated on $c = 0.8$ isosurface at locations A, B and C for both mean inflow velocities. A decreasing trend in $S_c/S_{b(\phi_g=1)}$ is observed for increasing droplet diameter for both inflow velocities. In addition, $S_c/S_{b(\phi_g=1)}$ for the premixed gaseous flame cases is found to be greater than droplet cases for both mean inflow velocities, which is consistent with the behaviour of the mean $\dot{w}_c$ presented in Fig.7.19. However, the mean value of $S_c/S_{b(\phi_g=1)}$ for droplet cases increases with increasing mean inflow velocity. It is important to note from Fig. 7.19 that the mean values of $\dot{w}_c$ and $|\nabla c|$ conditional upon c do not change with increasing $u_{mean}/S_{b(\phi_g=1)}$ irrespective of the location for premixed flames, and therefore, $S_c/S_{b(\phi_g=1)}$ remains mostly unaffected by the location and mean inflow velocity for gaseous premixed flame cases. It has already been demonstrated in the context of the discussion of Fig. 7.19 that the

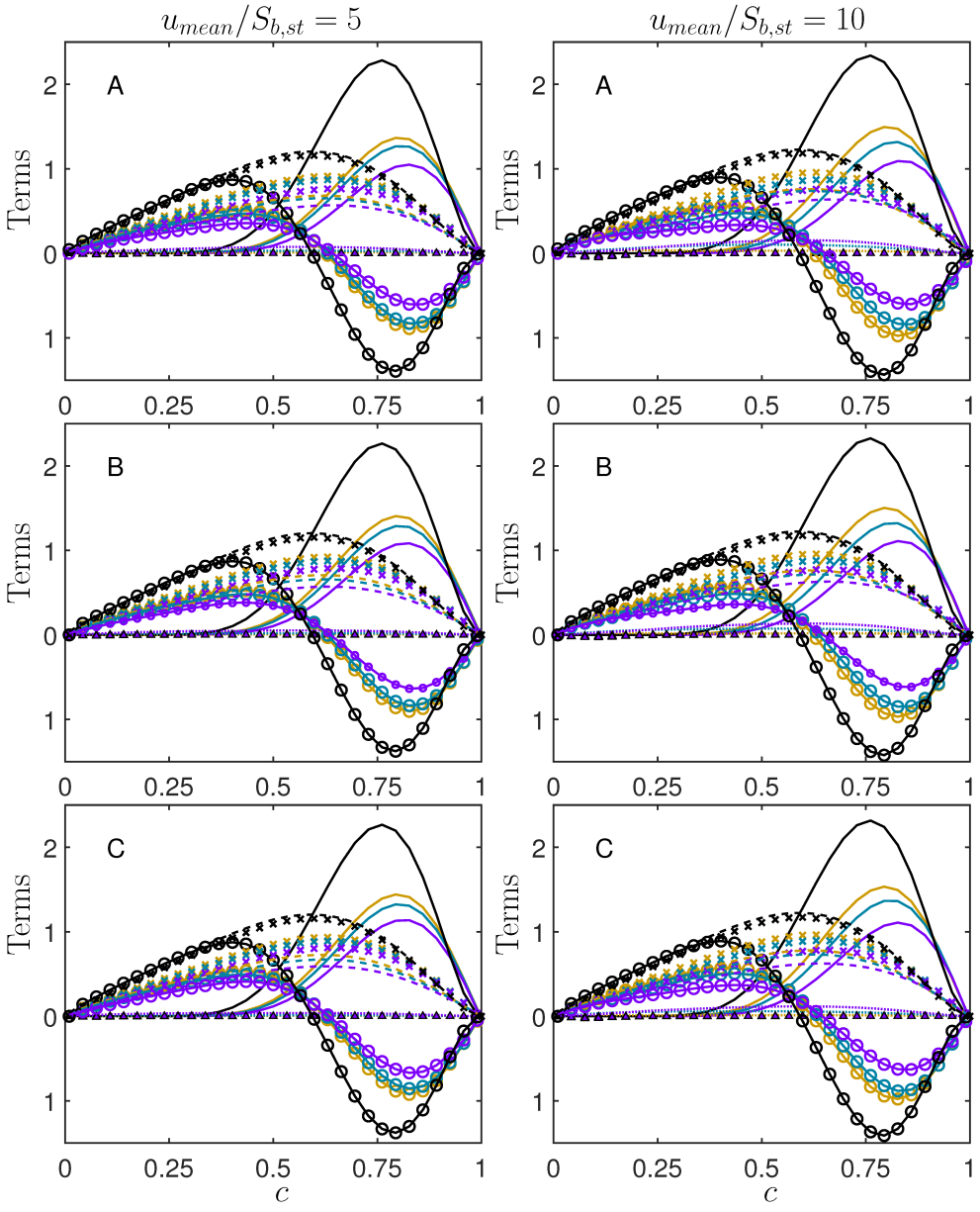

Figure 7.19: Variations of mean values of $\dot{w}_c$ (solid line), $\nabla\cdot(\rho D\nabla c)$ (line with circle marker), $\dot{A}_c$ (dotted line), $\dot{S}_{liq,c}$ (triangle marker), $\rho S_d|\nabla c|$ (dashed line) and $\rho_0 S_{b(\phi_g=1)}|\nabla c|$ (cross) conditional on c for premixed gaseous (——) and droplet cases with initial $a_d/\delta_{st} = 0.04$ (——), 0.05 (——) and 0.06 (——) for $u_{mean}/S_{b(\phi_g=1)} = 5.0$ (1^{st} column) and 10.0 (2^{nd} column) at locations A, B, C (top to bottom). All terms are normalised by $\delta_{st}/\rho_0 S_{b(\phi_g=1)}$.

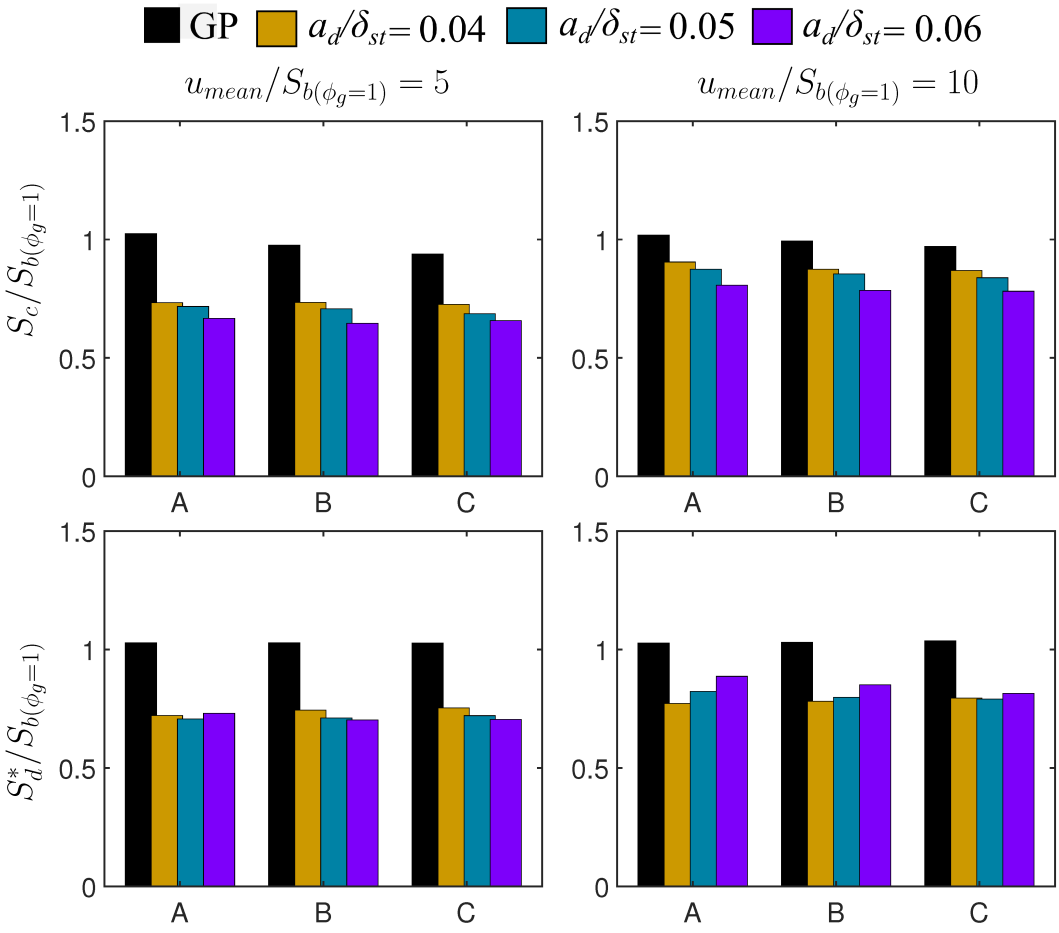

Figure 7.20: The mean values of $S_c/S_{b(\phi_g=1)}$ and $S_d^*/S_{b(\phi_g=1)}$ on the $c = 0.8$ isosurface at locations $A-C$ for the cases with $u_{mean}/S_{b(\phi_g=1)} = 5.0$ (1^{st} column) and 10.0 (2^{nd} column).

flame thickens and the mean value of $\dot{w}_c$ decreases with increasing $u_{mean}/S_{b(\phi_g=1)}$ and droplet diameter, and this reduction in mean reaction rate magnitude with increasing droplet diameter is responsible for the decreasing trend of $S_c/S_{b(\phi_g=1)}$ with increasing a_d. Although the mean value of $\dot{w}_c$ conditional upon c for droplet cases decreases with increasing $u_{mean}/S_{b(\phi_g=1)}$ as a result of greater likelihood of obtaining fuel-lean mixture in the gaseous phase (see Figs. 7.12 and 7.15), the increase in flamelet thickness for fuel-lean combustion contributes to the increase in the value of the integral $\int \dot{w}_c dn$, which is reflected in the increase in $S_c/S_{b(\phi_g=1)}$ with increasing the mean inflow velocity. The mean values of $S_c/S_{b(\phi_g=1)}$and $S_d^*/S_{b(\phi_g=1)}$ for the gaseous premixed flames remain identical at close to unity for different mean flow velocities. Moreover, the mean values of $S_d^*/S_{b(\phi_g=1)}$ for the droplet cases with $u_{mean}/S_{b(\phi_g=1)} = 5.0$ remain comparable. By contrast, the mean values of $S_d^*/S_{b(\phi_g=1)}$ for the droplet cases with $u_{mean}/S_{b(\phi_g=1)} = 10.0$ slightly increase with increasing droplet diameter at locations A and B.

Table 7.9: Time averaged normalised values of $A_s = \int_V |\nabla c| dV$, $A_{p,\tilde{c}}$, $\Omega_F = \int_V |\dot{w}_F| dV / \rho_0 \delta_{st}^2 S_{b(\phi_g=1)}$, $S = \int_V \dot{w}_c dV / \left[\rho_0 S_{b(\phi_g=1)} \int_V |\nabla c| dV\right]$ and turbulent burning velocity S_T based on the surface area for $\tilde{c} = 0.1$ and 0.5 isosurfaces for the gaseous premixed flame case (*GP*) and spray flames with different droplet diameters..

	a_d/δ_{st}	GP	0.04	0.05	0.06
$u_{mean}/S_{b(\phi_g=1)} = 5.0$	A_s/δ_{st}^2	1797	1722	1684	1708
	$A_{p,\tilde{c}=0.1}/\delta_{st}^2$	1600	1494	1499	1498
	$A_{p,\tilde{c}=0.5}/\delta_{st}^2$	1495	1404	1408	1413
	$A_{p,\tilde{c}=0.9}/\delta_{st}^2$	1432	1350	1354	1358
	Ω_F	118	75	68	58
	S	1.06	0.77	0.71	0.60
	$S_{T,\tilde{c}=0.1}/S_{b(\phi_g=1)}$	1.19	0.88	0.80	0.69
	$S_{T,\tilde{c}=0.5}/S_{b(\phi_g=1)}$	1.27	0.94	0.85	0.73
$u_{mean}/S_{b(\phi_g=1)} = 10.0$	A_s/δ_{st}^2	1554	1490	1526	1665
	$A_{p,\tilde{c}=0.1}/\delta_{st}^2$	1487	1419	1422	1425
	$A_{p,\tilde{c}=0.5}/\delta_{st}^2$	1436	1370	1372	1374
	$A_{p,\tilde{c}=0.9}/\delta_{st}^2$	1385	1336	1336	1337
	Ω_F	102	64	59	53
	S	1.05	0.74	0.68	0.56
	$S_{T,\tilde{c}=0.1}/S_{b(\phi_g=1)}$	1.10	0.78	0.73	0.65
	$S_{T,\tilde{c}=0.5}/S_{b(\phi_g=1)}$	1.14	0.80	0.76	0.68

The time-averaged values of flame surface area $A_s = \int_V |\nabla c| dV$, the normalised volume-integrated fuel reaction rate magnitude $\Omega_F = \int_V |\dot{w}_F| dV / \rho_0 \delta_{st}^2 S_{b(\phi_g=1)}$ and the normalised ratio of volume-integrated product formation rate to the flame surface area $S = \int_V \dot{w}_c dV / \left[\rho_0 S_{b(\phi_g=1)} \int_V |\nabla c| dV\right]$ are reported in Table 7.9 for V-shaped flames with $u_{mean}/S_{b(\phi_g=1)} = 5.0$ and 10.0. Table 7.9 reveals that A_s increases with increasing droplet diameter for the cases with higher mean inflow velocity while A_s values remain comparable for droplet cases with lower mean inflow velocity. It can further be observed that for lower mean inflow velocity case, A_s of the gaseous premixed case is larger than those of the droplet cases with initial $a_d/\delta_{st} = 0.04$ and 0.05, however, this value remains smaller than that for the case with initial $a_d/\delta_{st} = 0.06$ in the case of $u_{mean}/S_{b(\phi_g=1)} = 10.0$. This behaviour originates due to greater extent of droplet-induced flame wrinkling for large droplet cases. The relative magnitudes of flame area of a given $\tilde{c}$ isosurfaces for droplet and gaseous premixed flame cases follow the same qualitative trend as that of A_s irrespective of the mean inflow velocity. The increase in the mean flow velocity yields smaller values of Ω_F for all droplet cases due to higher probability of finding $\phi_g < 1$ in the reacting mixture composition in these cases. Furthermore, $\int_V \dot{w}_c dV$ changes in proportion to that of flame surface area A_s for the gaseous premixed flames

according to Damköhler's first hypothesis [243], and therefore, S remains close to unity in these cases. A marginal change is observed in $S = \int_V \dot{w}_c dV / \left[\rho_0 S_{b(\phi_g=1)} \int_V |\nabla c| dV\right]$ values when the mean flow velocity increases. However, $S < 1$ in the droplet cases is indicative of fuel-lean combustion because a laminar stoichiometric premixed flame is expected to have $S = 1$. The increased propensity of fuel-lean combustion leads to a slight decrease in S with increasing $u_{mean}/S_{b(\phi_g=1)}$.

Table 7.9 presents the normalised values of S_T and A_p for the $\tilde{c} = 0.1$ and 0.5 isosurfaces. Table 7.9 clearly reveals that the values of $A_{p,\tilde{c}}$ remain comparable to those of A_s for different mean inflow velocity cases. Turbulent burning velocities $S_T/S_{b(\phi_g=1)}$ for the $\tilde{c} = 0.1$ and 0.5 isosurfaces decrease with increasing a_d depending upon the decrease in S. Moreover, it can be seen from Table 7.9 that the turbulent burning velocity for droplet cases decreases with increasing mean inflow velocity and this behaviour arises due to increased probability of fuel-lean combustion with an increase in $u_{mean}/S_{b(\phi_g=1)}$ (see Figs. 7.12 and 7.15) . Furthermore, it can be seen that the gaseous premixed flame cases exhibit higher values of S_T than the droplet cases and an increase in the mean inflow velocity leads to a marginal decrease in turbulent burning velocity as a result of small changes in S values.

7.6 Summary of Key Findings

Three-dimensional carrier phase DNS of V-shaped n-heptane spray flames have been performed to investigate the influences of mean inflow velocity and droplet diameter on the burning rate and flame structure at different axial locations from the flame holder. The key outcomes are listed below:

- For the cases with $u_{mean}/S_{b(\phi_g=1)} = 5.0$, most of the small droplets are fully evaporated when they reach around halfway in the streamwise direction. Thus, the gaseous mixture composition in the unburned gas region can attain the stoichiometric value, whilst the gaseous equivalence ratio within the flame is found predominantly smaller than unity similar to the spherically expanding spray flame cases addressed in Chapter 4. However, in case of $u_{mean}/S_{b(\phi_g=1)} = 10.0$, shorter residence time prevents the completed evaporation of small droplets and this leads a leaner combustion for all droplet sizes. Furthermore, the mean values of gaseous equivalence ratio increases in the downstream direction and this behaviour strengths for large droplets.

- Greater residence time for the cases with $u_{mean}/S_{b(\phi_g=1)} = 5.0$, allows small droplets complete their evaporation before reaching the flame front. Thus, the extent of droplet-induced flame wrinkling is found to be significantly smaller than in the cases with high

mean inflow velocity. Moreover, the total flame surface is found to be comparable for droplet cases with $u_{mean}/S_{b(\phi_g=1)} = 5.0$, while it shows a considerable growth with increasing droplet diameter for the cases with $u_{mean}/S_{b(\phi_g=1)} = 10.0$.

- Increasing droplet diameter enhances the flame front thickness for the cases with higher mean inflow velocity due to the greater availability of fuel-lean gaseous mixture within the flame. However, the cases with $u_{mean}/S_{b(\phi_g=1)} = 5.0$ show an opposite tendency where the thickening of the flame front is suppressed by the reduced extent of flame wrinkling.

- The dependence of the mean behaviour of the reaction rate of reaction progress variable on droplet diameter is found similar in V-shaped spray flames to those in spherically expanding spray flames. However, the mean value of the reaction rate of reaction progress variable assumes comparable values at different axial locations for all droplet cases and it is insensitive to variations in the mean inflow velocity.

- The main part of heat release originates due to the premixed mode of combustion as it does in spherically expanding turbulent spray flames, but the role of non-premixed combustion combustion reaches considerable levels at higher mean inflow velocities particularly for large droplet cases and the increasing occurrence of droplet-flame interactions enhances the contribution of non-premixed combustion to the total heat release at the locations closer to the flame holder.

- The mean values of consumption speed show a decreasing trend with increasing droplet diameter regardless of the mean inflow velocity due to the leaner combustion in large droplet cases. The mean density weighted displacement speed in the cases with $u_{mean}/S_{b(\phi_g=1)} = 5.0$ exhibits comparable values for different droplet diameters whereas higher mean inflow velocity enhances the mean values of density weighted displacement speed for large droplet cases at all locations. Furthermore, for a given droplet diameter, the mean values of consumption speed and density-weighted displacement speed remain comparable at different axial distances from the flame holder for both mean inflow velocities.

Chapter 8

Conclusions and Future Work

8.1 Conclusions

In this thesis, three-dimensional compressible Direct Numerical Simulations (DNS) of spherically expanding n-heptane flames propagating into mono-sized fuel droplet-mists have been performed. Chemical reaction has been described using a modified single-step Arrhenius-type mechanism which allows to carry out an extensive parametric study with a reasonable computational cost. Flame behaviour has been investigated under different conditions including various droplet diameter a_d, turbulence intensity u' and overall (gaseous + liquid) equivalence ratio ϕ_{ov} to gain fundamental physical insight. In order to compare the spray flame statistics with a corresponding premixed flame case, additional spherically expanding premixed flame cases, with the same initial burned gas radius and statistically similar fluid flow conditions, have been considered.

The influences of turbulent intensity, droplet diameter and overall equivalence ratio on the reacting mixture composition, combustion characteristics and the evolution of flame surface area and burned gas volume have been analysed for spray kernel flames. It has been found that the flame-droplet interaction leads to flame wrinkling even under laminar conditions for spherically expanding flames propagating into the droplet-mists and the effects of droplet-induced wrinkling strengthen with increasing droplet diameter and overall equivalence ratio. This effect is partially eclipsed by the flow-induced flame wrinkling in turbulent droplet cases, but its imprint can be seen in the form of wider curvature PDFs for droplet cases in comparison to the corresponding statistically spherical premixed flame cases. The presence of droplets in the $\phi_{ov} = 0.8$ cases enhances the growth of flame surface area except for the cases with initial $a_d/\delta_{st} = 0.04$ under turbulent conditions. However, for $\phi_{ov} = 1.0$, only small droplets with initial $a_d/\delta_{st} = 0.04$ under a laminar flow field can grow faster than the corresponding laminar premixed flame and for $\phi_{ov} = 1.2$, this tendency is obvious only for the turbulent case.

The growth rate of flame surface area increases with increasing droplet diameter for $\phi_{ov} = 0.8$, whereas an opposite behaviour has been observed for $\phi_{ov} = 1.0$ and 1.2. Furthermore, turbulence enhances the flame surface area generation for both premixed and droplet cases. It has been observed that the gaseous phase mixture within the flame is predominantly fuel-lean in comparison to the overall equivalence ratio for droplet cases with $\phi_{ov} = 1.0$ and 1.2, and this tendency strengthens with increasing droplet diameter due to slow evaporation of large droplets. However, mixing of evaporated fuel from droplet sites gives rise to local availability of more reactive fuel–air mixtures than a homogeneous mixture corresponding to the overall equivalence ratio of $\phi_{ov} = 0.8$, and this tendency strengthens with increasing droplet diameter. Furthermore, high turbulence intensity promotes the availability of fuel-lean mixture. A major part of the overall heat release in droplet cases arises due to the premixed mode of combustion. However, the contribution of the non-premixed mode of combustion to the overall heat release rate increases with high turbulence intensity, overall fuel-rich mixture composition and large droplet sizes. A combination of predominant fuel-lean burning and extraction of latent heat from the gaseous phase in the droplet cases leads to local reduction of burned gas temperature in comparison to the adiabatic flame temperature of the stoichiometric mixture. The turbulent droplet cases have been shown to exhibit greater propensity of obtaining smaller magnitudes of the reaction progress variable gradient, dilatation rate, and product formation rate per unit flame surface area than in the corresponding stoichiometric turbulent premixed flames. These trends strengthen with increasing droplet size due to slow burning of predominant fuel-lean mixture arising from slow evaporation of large fuel droplets. Thus, an increase in initial droplet diameter and turbulence intensity adversely affects the evolution of burned gas volume and flame surface area for the droplet cases with $\phi_{ov} = 1.0$. The burned gas volume for the droplet cases with with $\phi_{ov} = 1.0$ grows slower than for the corresponding premixed flames. For $\phi_{ov} = 0.8$, large droplets with initial $a_d/\delta_{st} = 0.05$ and 0.06 the flames show greater growth rate of burned gas volume than with the corresponding premixed flame under laminar conditions. For $\phi_{ov} = 1.2$, the burned gas volume grows faster for small droplets with initial $a_d/\delta_{st} = 0.04$ than the corresponding premixed flame under laminar conditions. Turbulence increases the growth rate of burned gas volume for large droplets with $\phi_{ov} = 0.8$ and for small droplets with $\phi_{ov} = 1.0$ and 1.2. The increase of the burned gas mass for large (small) droplets for overall fuel-lean (fuel-rich) mixtures for flame propagation in droplet-laden mixtures is in qualitative agreement consistent with previous experimental findings by Hayashi et al. [118] and Lawes and Saat [119]. It has been shown that an increase in turbulence intensity leads to flame thinning for the premixed flames considered here, whereas for droplet cases, the flame becomes thicker under increasing turbulence intensity. Detailed physical explanations have been provided for the aforementioned observed behaviours. The statistical behaviours of

scalar gradient, flame index, and reaction rate in response to the variations of droplet diameter, overall equivalence ratio and turbulence intensity discussed in Chapter 4 and 5 will be valuable for the purpose of the modelling of combustion processes involving droplet-laden mixtures.

The statistical behaviours of the Surface Density Function (SDF) and the strain rates, which affect its evolution, have been analysed using DNS data for different turbulence intensities and droplet diameters for spherically expanding flames in droplet-laden mixtures with an overall equivalence ratio of unity. The predominance of fuel–lean combustion for large droplets and/or at high turbulence intensities acts to promote flame thickening. The increasing extent of fuel–lean combustion for the cases with large droplets and high turbulence intensities leads to a decreasing trend in the mean values of displacement speed, dilatation rate and normal strain rate. The relative magnitudes of dilatation rate and normal strain rate give rise to positive mean values of tangential strain rate a_T, and the mean value of a_T increases with increasing droplet size and turbulence intensity. The mean normal strain rate induced by flame propagation assumes predominantly negative values but the magnitude decreases with increasing turbulence intensity for all cases with an overall equivalence ratio of unity considered here. The mean tangential strain rate induced by flame propagation (alternatively curvature stretch rate) assumes negative values for the turbulent cases considered here. However, for the laminar case with small droplets the curvature stretch rate assumes predominantly positive values due to the reduced extent of flame deformation and relatively larger flame radius in comparison to the laminar cases with larger droplet sizes. The mean effective normal strain rate remains predominantly positive and increases with increasing turbulence intensity. By contrast, the mean effective tangential strain rate (alternatively stretch rate) remains mostly negative as the predominantly negative curvature stretch rate dominates over the mean positive fluid-dynamic tangential strain rate except for the laminar case with small droplets where the mean values of both fluid-dynamic tangential strain rate and curvature stretch rate are positive. The mean effective tangential strain rate (alternatively stretch rate) shows a decreasing trend with increasing droplet size, which gives rise to a smaller extent of flame surface area generation due to turbulence for larger droplets. The aforementioned statistics of the SDF and strain rates, which affect the SDF evolution, are of fundamental importance for the purpose of Flame Surface Density (FSD) and Scalar Dissipation Rate (SDR) based closures. Thus, the effects of droplet diameter and turbulence intensity should be explicitly accounted for in the FSD and SDR modelling of turbulent flames propagating into droplet-laden mixtures.

The simulation data has been utilised to analyse the flame surface topology and the statistical behaviours of different flame speeds under turbulent conditions for different droplet diameters and overall equivalence ratios. It has been found that droplets significantly affect the flame surface topology, as the presence of droplets leads to dimples on the flame surface

for large droplet diameters and large droplet number densities (i.e. overall equivalence ratio). However, turbulent gaseous premixed flames exhibit a smooth wrinkled flame surface and this behaviour may prevail for droplet cases with overall fuel-lean equivalence ratios due to the small number of droplets interacting with the flame. Besides dimples on the flame surface, the spray flames show increased probability of finding saddle topologies in comparison to the corresponding premixed gaseous flames. The mixture composition within the flame and droplet-induced flame wrinkling significantly affect the statistical behaviours of both displacement and consumption speeds. It has been found that the contribution of droplets on the density-weighted displacement speed statistics comes principally through the reaction rate of the mixture arising from mixing of evaporated fuel vapour with surrounding air, and the curvature distribution induced by flame-droplet interaction. The contributions of cross-scalar dissipation arising from mixture inhomogeneity and droplet evaporation remain weak in comparison to the reaction rate and molecular diffusion rate components of the density-weighted displacement speed. It has been found that the probability of finding negative displacement speed increases with increasing droplet diameter for $\phi_{ov} = 1.0$ and 1.2, whereas the consumption speed remains deterministically positive due to its sole dependence on reaction rate of reaction progress variable. It has been found that the consumption speed decreases with increasing droplet diameter for $\phi_{ov} = 1.0$ and 1.2 and its mean value remains smaller than that in the corresponding premixed gaseous flames. However, the mean consumption speed has been found to be greater for large droplet cases with $\phi_{ov} = 0.8$ than in the corresponding premixed gaseous flames. The mean value of consumption speed remains greater than the mean density-weighted displacement speed for all cases considered here. In addition to consumption and displacement speeds, two additional flame speeds have been considered, which are taken to represent the growth rates of flame surface area and burned gas volume, respectively. These flame speeds have been compared to the mean values of consumption speed and density-weighted displacement speed. The flame speed, which represents the growth rate of flame area, provides an approximate measure of the mean value of the consumption speed, whereas the flame speed representing the growth rate of burned gas volume provides an approximate measure of the mean density-weighted displacement speed for large droplet diameters for $\phi_{ov} = 1.0$ and 1.2.

Flame topologies associated with flame self-interaction events have been investigated for turbulent spherically expanding flames propagating into mono-sized droplet-mists with an overall equivalence ratio of unity. The flame self interaction (FSI) events have predominantly been found close to the burned gas side in turbulent premixed gaseous flames for all turbulence intensities, whereas this behaviour is observed for droplet cases only under small turbulence intensities. However, tunnel formation/tunnel closure topologies are prevalent for

the FSI events in turbulent gaseous premixed flames, whereas the unburned mixture pockets are predominantly obtained for droplet cases under small turbulence intensities. The frequency of obtaining the FSI events towards the preheat zone increases with increasing turbulence intensity. The FSI events associated with tunnel formation/tunnel closure exhibit a higher frequency than unburned mixture pockets/burned mixture pockets in all cases except for the droplet cases under low turbulence intensities, which show a considerable amount of unburned mixture pockets. The frequency of the FSI events increases with increasing u' and a_d . The differences in qualitative nature and distributions of the FSI events between turbulent droplet and gaseous premixed flames have important implications on the possible extension of flame surface based modelling methodology for turbulent droplet combustion. Previous simple chemistry DNS analyses [57–59, 73, 80–83] have been found to capture the flame propagation statistics extracted from detailed chemistry DNS data [84–89] for turbulent premixed flames, and this holds true in particular for curvature effects. Nevertheless, the present findings based on moderate turbulence intensity and simple chemical mechanism need to be validated further for higher values of turbulent Reynolds number (and consequently different Da/Ka) in the presence of detailed chemistry and transport.

The influences of droplet inertia on the reaction zone structure, flame surface area and volume of the burned gas have been investigated for spherically expanding flames propagating into mono-sized droplet-laden mixtures with $\phi_{ov} = 1.0$ using three-dimensional DNS. Simulations for different initial mono-disperse droplet sizes and turbulence intensities have been conducted for inertial and hypothetical inertialess droplets to isolate the effects of droplet inertia. It has been found that the cases with inertial droplets show a higher probability of obtaining stoichiometric mixture in the flame than those with inertialess droplets and the occurrence of locally fuel-rich pockets within the flame is either rare or absent altogether for inertialess droplets. This behaviour originates due to higher number density of droplets within the flame for the inertial droplet cases than in the corresponding inertialess droplet cases where the fluid velocity directed from the burned products to the unburned reactants carries the inertialess droplets away from the flame. The higher number density of inertial droplets within the flame induces greater extent of droplet-induced flame wrinkling than in the corresponding inertialess droplet cases, which leads to wider PDFs of flame curvature for inertial droplet cases. The flame front in the inertialess droplet cases has also been found to be thicker than in the corresponding inertial droplet cases. As diffusion flame is obtained at the stoichiometric mixture, the cases with inertialess droplets exhibit a smaller contribution of non-premixed combustion to the total heat release rate due to the reduced probability of obtaining stoichiometric mixture in the flame region. As the heat release rate is the highest for the stoichiometric mixture, the combination of reduced availability of stoichiometric mixture and higher probability of

obtaining fuel-lean mixture within the flame leads to reduced flame surface area and burned gas volume for the inertialess droplet cases in comparison to the corresponding cases with inertial droplets. This tendency strengthens further for high u' and the cases with large inertialess droplets under high u' exhibit tendencies of eventual flame extinction. Point source assumption is made for the droplets in this analysis, which limits the maximum droplet size that can be analysed in this framework. Furthermore, the resolution of reaction layers around individual droplets cannot be possible in the current numerical framework, and thus further analysis using DNS based on resolved droplets will be necessary.

The DNS database of spherically expanding flames propagating into mono-sized fuel-droplet mists for different overall equivalence ratios and droplet diameters has been considered to analyse flame–droplet interaction in terms of the source terms associated with two-phase coupling arising from droplet evaporation in various gaseous carrier phase transport equations. It has been found that the slip velocity is significantly affected by the droplet size, whereas the overall equivalence ratio does not have a significant impact on slip velocity. Temperature difference between liquid droplets and surrounding gaseous phase has been observed to increase towards the burned gas side because of the high gaseous phase temperature in the flame. Overall equivalence ratio, besides the droplet size, has been found to play an important role in flame–droplet interaction. Small droplets primarily evaporate in the preheat zone, especially for the case with an overall fuel-lean mixture composition. However, large droplets penetrate the flame structure and under some conditions escape through the flame and reach the burned gas before the completion of their evaporation. Some of these heated droplets are brought to the relatively cold gas due to turbulent motion and locally heat transfer takes place from the droplet to the surrounding gas in contrast to the heat transfer from the hot gas to the droplets which occurs predominantly on the unburned gas side of the flame. It has been found that the contributions of the coupling between the Eulerian and Lagrangian phases have significant influences on the mass, momentum, energy and mixture fraction conservation equations in the gaseous phase, but this influence is relatively weak for the reaction progress variable transport equation. Therefore, the source terms due to the coupling between the Eulerian and Lagrangian phases need to be explicitly modelled for mass, momentum, energy and mixture fraction evolutions in the context of Reynolds Averaged Navier-Stokes (RANS) and Large Eddy Simulations (LES). By contrast, the existing modelling techniques for averaged/filtered reaction progress variable evolution for turbulent-stratified flames are likely to be valid for spray flames driven by a predominantly premixed mode of combustion similar to the ones considered here. For these flames, the extra term arising from the coupling between the Eulerian and Lagrangian phases in the reaction progress variable conservation equation can be ignored without incurring any significant errors. The present analysis focuses only on the stat-

istical behaviours of the source terms due to two-phase coupling in the conservation equations of mass, momentum, energy and mixture fraction but their modelling is kept beyond the scope of the present analysis. Modelling of these terms in the context of RANS and LES will form the basis of future investigations.

V-shaped flames are often used as a laboratory scale experimental configuration for the analysis of turbulent flames [116, 117, 222–228, 233]. The advancements of computational resources have made it possible to carry out DNS of V-shaped flames [63, 64, 229–232, 246, 247] due to its geometrical simplicity. The V-shaped flame offers a convenient configuration for the evaluation of turbulent flame speed, flame brush thickness and Flame Surface Density (FSD) in turbulent premixed flames. However, most of the above-mentioned analyses have been conducted for turbulent premixed [222–227, 233] and stratified [116, 117] flames and this configuration received relatively limited experimental [228] and computational attention for turbulent spray flames despite the importance of flame propagation in droplet-laden mixtures in automotive engines, gas turbines and accidental explosions. Thus, the mode of combustion, droplet-induced flame wrinkling, mean behaviours of different terms of the reaction progress variable transport equation, and flame propagation statistics for V- shaped flames in a droplet-laden mixture of an overall equivalence ratio of unity have been investigated for different droplet diameters using three-dimensional DNS data. The spray flame behaviour has been compared with a turbulent gaseous stoichiometric premixed V-shaped flame under same flow conditions. It has been found that the flame brush thickness is affected by both droplet diameter and the axial distance from the flame holder and it increases with decreasing droplet diameter and with increasing axial distance. Furthermore, the flame brush has been found to be thicker in droplet cases than in the corresponding gaseous premixed flame case. The predominance of finding fuel-lean mixture within the flame decreases in the downstream direction due to evaporation of droplets and this effect is particularly strong for large droplets. The interaction of droplets with the flame surface gives rise to dimples on the reaction progress variable isosurfaces. However, droplet-induced flame wrinkling contributes to the widening of flame curvature PDFs, and also acts to increase the total flame surface area for large droplets. The mean values of the reaction rate of progress variable decrease with increasing droplet diameter. Furthermore, the mean value of the reaction rate of progress variable for a given droplet diameter shows similar magnitudes at different axial locations for all droplet cases. A similar qualitative trend has been observed for the axial distance dependences of the mean values of consumption speed and density- weighted displacement speed for a given value of droplet diameter. The mean values of consumption speed are found to decrease with increasing droplet diameter because of the greater likelihood of fuel-lean combustion in large droplet cases. By contrast, the mean density-weighted displacement speed remains comparable for

all the droplet sizes considered here. Recent DNS analyses in statistically planar flames [47] and spherically expanding flames (see Chapter 4) under both laminar and weakly turbulent conditions revealed significant differences in flame curvature, density-weighted displacement speed and consumption speed in response to droplet diameter, whereas the effects of droplet diameter are relatively weaker in V-flames than in statistically planar and spherically expanding flames. For the droplet cases with globally stoichiometric equivalence ratio, the mean values of density-weighted displacement speed were found to exhibit a mild increase with the increasing droplet diameter whereas the mean values of consumption speed showed a decreasing trend with the increasing droplet diameter. The statistically planar and spherically expanding flames interact with droplets at all stages of their propagation into the unburned gas but in turbulent V-spray flames, the droplets evaporate in the mean flow direction. Therefore, the frequency of flame-droplet interaction decreases and the mean value of gaseous phase equivalence ratio increases in the downstream direction in turbulent V-shaped spray flames. It has been demonstrated that in turbulent droplet-laden V-shaped flames, the enhancement of burning rate under turbulence cannot be equated to the enhancement of the flame surface area with respect to the corresponding quantities under laminar conditions. Moreover, the turbulent burning velocity has been found to decrease with increasing droplet diameter due to the reduction in the volume-integrated reaction rate of reaction progress variable as a result of the greater likelihood of finding fuel-lean gaseous mixture for larger droplets. The distance of the flame holder from the inlet can also potentially have an influence on the results, but the gaseous phase equivalence ratio remains small for the axial locations before the flame holder, and thus it can reasonably be expected that the qualitative nature of the results are unlikely to change with the variation of the distance of the flame holder from the inlet. However, further study in this respect will be necessary. The aforementioned challenges will form the basis of future investigations. Furthermore, V-shaped spray flame simulations have been carried out under various mean inflow velocity conditions for different droplet diameters for an overall equivalence ratio of unity. It has been found that reacting mixture composition in the flame becomes leaner due to the shorter residence time of droplets in the case of higher mean inflow velocity. Mean inflow velocity, alongside droplet diameter and the axial distance, affects the flame brush thickness. The flame front thickens with increasing droplet diameter for the cases with higher mean inflow velocity due to the predominance of fuel-lean gaseous mixture within the flame. However, an opposite behaviour has been observed for the cases with lower mean inflow velocity where the smaller extent of flame wrinkling dominates over the effects of the thickening of the flame front. Liquid droplets interact with the flame and lead to dimples on the flame surface. Under higher mean inflow velocity conditions, distribution of local curvature values broadens as a result of the occurrence of significantly increased droplet-induced flame

wrinkling. It has been demonstrated that the major part of total heat release arises from the premixed mode of combustion. However, the contribution of non-premixed combustion to the total heat release becomes stronger for larger droplets with higher mean inflow velocity and this trend is relatively strong at the locations closer to the flame holder due to the greater availability of droplets interacting with the flame. The mean values of the terms which govern the statistical characteristic of displacement speed exhibit comparable magnitudes for different mean inflow velocities irrespective of the distance from flame holder. The mean values of consumption speed diminish with increasing droplet diameters for both mean inflow velocities. Furthermore, under smaller mean inflow velocity conditions, the mean values of density-weighted displacement speed have been found to be comparable for different droplet diameters at all locations. This trend changes under higher mean inflow conditions and the mean values of density-weighted displacement speed increase for larger droplet cases at the locations close to the flame holder. The increased probability of fuel-lean combustion leads to a decrease in turbulent burning velocity with increasing mean inflow velocity. The present analysis has been conducted using a single step chemistry, and thus the investigation carried out in this thesis needs to be extended for detailed chemistry DNS for further validation of the current findings. Moreover, the physical mechanisms, which are responsible for the variations observed based on two mean inlet velocities in this analysis are unlikely to change for a different value of $u_{mean}/S_{b(\phi_g=1)}$, and thus, the qualitative trends in response to the changes in $u_{mean}/S_{b(\phi_g=1)}$ can be inferred from the results presented in this thesis. However, further analyses for different mean inflow velocities will be necessary for deeper physical understanding.

8.2 Future Work

The present thesis focused on providing a fundamental understanding on the behaviour of the spherically expanding flames propagating into droplet-laden mixtures using three-dimensional DNS based on a modified single-step Arrhenius chemical scheme. Although the results have been presented and discussed for a broad range of parameters, there are aspects which are kept beyond the current study and need to be addressed in the future studies. Some of the possible research aspects are described below for future work:

- Although several previous analyses revealed that the flame speed statistics for turbulent premixed flames obtained from simple chemistry [73, 81, 82] remain in good agreement with the corresponding results obtained from a detailed chemical mechanism [86, 98], further analyses in the presence of a detailed chemical mechanism will be necessary for confirming the current findings and obtaining more comprehensive physical understanding regarding the roles played by the intermediate species.

- In the current DNS analysis, mono-sized liquid droplets have been considered in order to identify the effects of droplet diameter on spray flame characteristics. However, atomisation process leads to a polydispersed spray environment in practical combustion systems. Further analyses involving the polydispersity of liquid fuel droplets will be required for the simulations close to realistic combustion applications.

- Simulations of spherically expanding and V-shaped flames propagating in droplet-mists have been performed for moderate Reynolds numbers and droplet diameters as it becomes extremely expensive in terms of computational cost to achieve high turbulence Reynolds numbers with small droplet diameters using DNS approach. Therefore, further assessment for gaining more extensive physical insight on the spray flame behaviour will be needed for high turbulence Reynolds numbers and small droplet diameters.

- The present study considers liquid fuel droplets to be point-source particles in the concept of the Lagrangian approach. In this context, the flow behaviour inside and vicinity of the liquid droplets has not been resolved. Simulations with a fully resolved dispersed phase description will provide valuable information to gain further insight on the spray combustion. However, conducting such a detailed parametric analysis based on DNS of fully resolved spray combustion requires vast amount of computational power.

- Numerical analysis of laboratory scale turbulent premixed flames based on DNS-like simulation techniques [231] has become available using the recent strategies for efficient algorithms. The rapid advancement in computational technologies is expected to make high-fidelity simulations of laboratory scale spray combustion possible. Thus, the fundamental flow aspects obtained in this study can be further assessed through DNS of laboratory scale spray flames.

References

[1] Ozel Erol, G., Hasslberger, J., Klein, M., and Chakraborty, N. A direct numerical simulation analysis of spherically expanding turbulent flames in fuel droplet-mists for an overall equivalence ratio of unity. *Physics of Fluids*, 30(8):086104, 2018.

[2] Ozel Erol, G., Hasslberger, J., Klein, M., and Chakraborty, N. A direct numerical simulation investigation of spherically expanding flames propagating in fuel droplet-mists for different droplet diameters and overall equivalence ratios. *Combustion Science and Technology*, 191(5-6):833–867, 2019.

[3] Ozel Erol, G., Hasslberger, J., Klein, M., and Chakraborty, N. Propagation of spherically expanding turbulent flames into fuel droplet-mists. *Flow, Turbulence and Combustion*, 103(4):913–941, 2019.

[4] Ozel Erol, G., Hasslberger, J., Klein, M., and Chakraborty, N. Surface density function evolution in spherically expanding flames in globally stoichiometric droplet-laden mixtures. *Combustion Science and Technology*, pages 1–21, 2019.

[5] Ozel Erol, G., Hasslberger, J., and Chakraborty, N. Statistics of two-phase coupling in turbulent spherically expanding flames in mono-sized fuel-droplet mists. *Combustion Science and Technology*, pages 1–18, 2020.

[6] Ozel Erol, G. and Chakraborty, N. Inertial effects on globally stoichiometric spherically expanding turbulent flames propagating in droplet-laden mixtures. *Proceedings of the Combustion Institute*, 38(2):3379–3387, 2021.

[7] Ozel Erol, G., Ahmed, U., and Chakraborty, N. Flame self-interactions in globally stoichiometric spherically expanding flames propagating into fuel droplet-mists. *Proceedings of the Combustion Institute*, 38(2):3351–3359, 2021.

[8] Ozel Erol, G., Hasslberger, J., Klein, M., and Chakraborty, N. A direct numerical simulation analysis of turbulent v-shaped flames propagating into droplet-laden mixtures. *International Journal of Multiphase Flow*, 133:103455, 2020.

[9] Ozel Erol, G. and Chakraborty, N. Effects of mean inflow velocity and droplet diameter on the propagation of turbulent shaped flames in droplet-laden mixtures. *Fluids*, 6(1):1, 2021.

[10] *World Energy Outlook 2019*. International Energy Agency, Paris, 2019.

[11] *BP Energy Outlook: 2019 edition*. BP p.l.c., 2019.

[12] Lefebvre, A. H. and Ballal, D. R. *Gas Turbine Combustion: Alternative Fuels and Emissions*. CRC press, 2010.

[13] Roy, G. D. Technical challenges and scientific approach for a sustainable energy efficient future. In *Novel Combustion Concepts for Sustainable Energy Development*, pages 9–22. Springer, 2014.

[14] Erazo Jr, J. A., Parthasarathy, R., and Gollahalli, S. Atomization and combustion of canola methyl ester biofuel spray. *Fuel*, 89(12):3735–3741, 2010.

[15] Chong, C. T. and Hochgreb, S. Spray flame structure of rapeseed biodiesel and Jet-A1 fuel. *Fuel*, 115:551–558, 2014.

[16] Bilger, R. W. The role of combustion technology in the 21st century. *Turbulent Combustion Modeling*, pages 3–18, 2011.

[17] Wendt, J. F. *Computational Fluid Dynamics: An Introduction*. Springer Science & Business Media, 2008.

[18] Chakraborty, N. and Lai, J. Direct numerical simulations of premixed turbulent combustion: Relevance and applications to engineering computational analyses. In *Modeling and Simulation of Turbulent Combustion*, pages 135–180. Springer, 2018.

[19] Lipatnikov, A. *Fundamentals of Premixed Turbulent Combustion*. CRC Press, 2012.

[20] De, S., Agarwal, A. K., Chaudhuri, S., and Sen, S. *Modeling and Simulation of Turbulent Combustion*. Springer, 2018.

[21] Pope, S. B. *Turbulent Flows*. Cambridge Univ. Press, Cambrigde, 2000.

[22] Chen, J. H. Petascale direct numerical simulation of turbulent combustion: Fundamental insights towards predictive models. *Proceedings of the Combustion Institute*, 33(1):99–123, 2011.

[23] Im, H. G. Direct numerical simulations for combustion science: Past, present, and future. In *Modeling and Simulation of Turbulent Combustion*, pages 99–132. Springer, 2018.

[24] Poinsot, T. and Veynante, D. *Theoretical and Numerical Combustion*. RT Edwards, Inc., 2005.

[25] Yoo, C. S. and Im, H. G. Characteristic boundary conditions for simulations of compressible reacting flows with multi-dimensional, viscous and reaction effects. *Combustion Theory and Modelling*, 11(2):259–286, 2007.

[26] Yoo, C. S., Wang, Y., Trouvé, A., and Im, H. G. Characteristic boundary conditions for direct simulations of turbulent counterflow flames. *Combustion Theory and Modelling*, 9(4):617–646, 2005.

[27] Sutherland, J. C. and Kennedy, C. A. Improved boundary conditions for viscous, reacting, compressible flows. *Journal of Computational Physics*, 191(2):502–524, 2003.

[28] Poinsot, T. J. and Lelef, S. K. Boundary conditions for direct simulations of compressible viscous flows. *Journal of Computational Physics*, 101(1):104–129, 1992.

[29] Jiang, X., Siamas, G. A., Jagus, K., and Karayiannis, T. G. Physical modelling and advanced simulations of gas–liquid two-phase jet flows in atomization and sprays. *Progress in Energy and Combustion Science*, 36(2):131–167, 2010.

[30] Jenny, P., Roekaerts, D., and Beishuizen, N. Modeling of turbulent dilute spray combustion. *Progress in Energy and Combustion Science*, 38(6):846–887, 2012.

[31] Mathew, J. and Chakravorty, S. Large-eddy simulation of nonpremixed flames by explicit filtering. In *Modeling and Simulation of Turbulent Combustion*, pages 429–445. Springer, 2018.

[32] Echekki, T. and Mastorakos, E. Turbulent combustion: Concepts, governing equations and modeling strategies. In *Turbulent Combustion Modeling*, pages 19–39. Springer, 2011.

[33] Gicquel, L. Y. M., Staffelbach, G., and Poinsot, T. Large eddy simulations of gaseous flames in gas turbine combustion chambers. *Progress in Energy and Combustion Science*, 38(6):782–817, 2012.

[34] Jones, W. P. and Launder, B. E. The prediction of laminarization with a two-equation model of turbulence. *International Journal of Heat and Mass Transfer*, 15(2):301–314, 1972.

[35] Libby, P. A. and Bray, K. N. C. Countergradient diffusion in premixed turbulent flames. *AIAA journal*, 19(2):205–213, 1981.

[36] Clavin, P. and Williams, F. A. Theory of premixed-flame propagation in large-scale turbulence. *Journal of Fluid Mechanics*, 90(3):589–604, 1979.

[37] Veynante, D., Trouvé, A., Bray, K. N. C., and Mantel, T. Gradient and counter-gradient scalar transport in turbulent premixed flames. *Journal of Fluid Mechanics*, 332(263-293):66, 1997.

[38] Chakraborty, N. and Cant, R. S. Effects of Lewis number on turbulent scalar transport and its modelling in turbulent premixed flames. *Combustion and Flame*, 156(7):1427–1444, 2009.

[39] Chakraborty, N. and Cant, R. S. Effects of Lewis number on scalar transport in turbulent premixed flames. *Physics of Fluids*, 21(3):035110, 2009.

[40] Chakraborty, N. and Cant, R. S. Physical insight and modelling for Lewis number effects on turbulent heat and mass transport in turbulent premixed flames. *Numerical Heat Transfer, Part A: Applications*, 55(8):762–779, 2009.

[41] Luo, K., Pitsch, H., Pai, M. G., and Desjardins, O. Direct numerical simulations and analysis of three-dimensional n-heptane spray flames in a model swirl combustor. *Proceedings of the Combustion Institute*, 33(2):2143–2152, 2011.

[42] Schroll, P., Wandel, A. P., Cant, R. S., and Mastorakos, E. Direct numerical simulations of autoignition in turbulent two-phase flows. *Proceedings of the Combustion Institute*, 32(2):2275–2282, 2009.

[43] Wandel, A. P., Chakraborty, N., and Mastorakos, E. Direct numerical simulations of turbulent flame expansion in fine sprays. *Proceedings of the Combustion Institute*, 32(2):2283–2290, 2009.

[44] Wandel, A. P. Influence of scalar dissipation on flame success in turbulent sprays with spark ignition. *Combustion and Flame*, 161(10):2579–2600, 2014.

[45] Neophytou, A., Mastorakos, E., and Cant, R. S. DNS of spark ignition and edge flame propagation in turbulent droplet-laden mixing layers. *Combustion and Flame*, 157(6):1071–1086, 2010.

[46] Neophytou, A., Mastorakos, E., and Cant, R. S. The internal structure of igniting turbulent sprays as revealed by complex chemistry DNS. *Combustion and Flame*, 159(2):641–664, 2012.

[47] Wacks, D. H., Chakraborty, N., and Mastorakos, E. Statistical analysis of turbulent flame-droplet interaction: A direct numerical simulation study. *Flow, Turbulence and Combustion*, 96(2):573–607, 2016.

[48] Wacks, D. H. and Chakraborty, N. Flame structure and propagation in turbulent flame-droplet interaction: A direct numerical simulation analysis. *Flow, Turbulence and Combustion*, 96(4):1053–1081, 2016.

[49] Miller, R. S. and Bellan, J. Direct numerical simulation of a confined three-dimensional gas mixing layer with one evaporating hydrocarbon-droplet laden stream. *Journal of Fluid Mechanics*, 1998.

[50] Reveillon, J. and Vervisch, L. Spray vaporization in nonpremixed turbulent combustion modeling: A single droplet model. *Combustion and Flame*, 121(1-2):75–90, 2000.

[51] Reveillon, J. and Vervisch, L. Analysis of weakly turbulent dilute-spray flames and spray combustion regimes. *Journal of Fluid Mechanics*, 537:317–347, 2005.

[52] Nakamura, M., Akamatsu, F., Kurose, R., and Katsuki, M. Combustion mechanism of liquid fuel spray in a gaseous flame. *Physics of Fluids*, 17(12):123301, 2005.

[53] Reveillon, J. and Demoulin, F. X. Evaporating droplets in turbulent reacting flows. *Proceedings of the Combustion Institute*, 31(2):2319–2326, 2007.

[54] Sreedhara, S. and Huh, K. Y. Conditional statistics of nonreacting and reacting sprays in turbulent flows by direct numerical simulation. *Proceedings of the Combustion Institute*, 31(2):2335–2342, 2007.

[55] Xia, J. and Luo, K. H. Direct numerical simulation of inert droplet effects on scalar dissipation rate in turbulent reacting and non-reacting shear layers. *Flow, Turbulence and Combustion*, 84(3):397–422, 2010.

[56] Fujita, A., Watanabe, H., Kurose, R., and Komori, S. Two-dimensional direct numerical simulation of spray flames-Part 1: Effects of equivalence ratio, fuel droplet size and radiation, and validity of flamelet model. *Fuel*, 104:515–525, 2013.

[57] Klein, M., Chakraborty, N., Jenkins, K. W., and Cant, R. S. Effects of initial radius on the propagation of premixed flame kernels in a turbulent environment. *Physics of Fluids*, 18(5):055102, 2006.

[58] Klein, M., Chakraborty, N., and Cant, R. S. Effects of turbulence on self-sustained combustion in premixed flame kernels: A direct numerical simulation (DNS) study. *Flow, Turbulence and Combustion*, 81(4):583–607, 2008.

[59] Chakraborty, N., Klein, M., and Cant, R. S. Stretch rate effects on displacement speed in turbulent premixed flame kernels in the thin reaction zones regime. *Proceedings of the Combustion Institute*, 31(1):1385–1392, 2007.

[60] Chakraborty, N. and Klein, M. Effects of global flame curvature on surface density function transport in turbulent premixed flame kernels in the thin reaction zones regime. *Proceedings of the Combustion Institute*, 32(1):1435–1443, 2009.

[61] Chakraborty, N., Rogerson, J. W., and Swaminathan, N. The scalar gradient alignment statistics of flame kernels and its modelling implications for turbulent premixed combustion. *Flow, Turbulence and Combustion*, 85(1):25–55, 2010.

[62] Mizutani, Y. and Nakajima, A. Combustion of fuel vapor-drop-air systems: Part II spherical flames in a vessel. *Combustion and Flame*, 20(3):351–357, 1973.

[63] Dunstan, T. D., Swaminathan, N., Bray, K. N. C, and Cant, R. S. Geometrical properties and turbulent flame speed measurements in stationary premixed V-flames using direct numerical simulation. *Flow, Turbulence and Combustion*, 87(2-3):237–259, 2011.

[64] Dunstan, T. D., Swaminathan, N., and Bray, K. N. C. Influence of flame geometry on turbulent premixed flame propagation: A DNS investigation. *Journal of Fluid Mechanics*, 709:191, 2012.

[65] Sirignano, W. A. *Fluid Dynamics and Transport of Droplets and Sprays*. Cambridge University Press, 2010.

[66] Crowe, C. T., Schwarzkopf, J. D., Sommerfeld, M., and Tsuji, Y. *Multiphase Flows with Droplets and Particles*. CRC press, 2011.

[67] Wang, Y. and Rutland, C. J. Effects of temperature and equivalence ratio on the ignition of n-heptane fuel spray in turbulent flow. *Proceedings of the Combustion Institute*, 30(1):893–900, 2005.

[68] Watanabe, H., Kurose, R., Hwang, S., and Akamatsu, F. Characteristics of flamelets in spray flames formed in a laminar counterflow. *Combustion and Flame*, 148(4):234–248, 2007.

[69] Watanabe, H., Kurose, R., Komori, S., and Pitsch, H. Effects of radiation on spray flame characteristics and soot formation. *Combustion and Flame*, 152(1-2):2–13, 2008.

[70] Baba, Y. and Kurose, R. Analysis and flamelet modelling for spray combustion. *Journal of Fluid Mechanics*, 612:45–79, 2008.

[71] Malkeson, S. *Fundamental understanding and modelling of turbulent combustion in stratified mixtures using Direct Numerical Simulations (DNS)*. PhD thesis, University of Liverpool, 2011.

[72] Thompson, K. W. Time dependent boundary conditions for hyperbolic systems. *Journal of Computational Physics*, 68(1):1–24, 1987.

[73] Chakraborty, N. and Cant, S. Unsteady effects of strain rate and curvature on turbulent premixed flames in an inflow–outflow configuration. *Combustion and Flame*, 137(1-2):129–147, 2004.

[74] Rudy, D. H. and Strikwerda, J. C. A nonreflecting outflow boundary condition for subsonic Navier-Stokes calculations. *Journal of Computational Physics*, 36(1):55–70, 1980.

[75] Fernández-Tarrazo, E., Sánchez, A. L., Linan, A., and Williams, F. A. A simple one-step chemistry model for partially premixed hydrocarbon combustion. *Combustion and Flame*, 147(1-2):32–38, 2006.

[76] Swaminathan, N. and Bray, K. N. C. *Turbulent Premixed Flames*. Cambridge University Press, 2011.

[77] Malkeson, S. P. and Chakraborty, N. Statistical analysis of displacement speed in turbulent stratified flames: A direct numerical simulation study. *Combustion Science and Technology*, 182(11-12):1841–1883, 2010.

[78] Kumar, K., Freeh, J. E., Sung, C. J., and Huang, Y. Laminar flame speeds of preheated iso-octane/O2/N2 and n-heptane/O2/N2 mixtures. *Journal of Propulsion and Power*, 23(2):428–436, 2007.

[79] Chaos, M., Kazakov, A., Zhao, Z., and Dryer, F. L. A high-temperature chemical kinetic model for primary reference fuels. *International Journal of Chemical Kinetics*, 39(7):399–414, 2007.

[80] Jenkins, K. W., Klein, M., Chakraborty, N., and Cant, R. S. Effects of strain rate and curvature on the propagation of a spherical flame kernel in the thin-reaction-zones regime. *Combustion and Flame*, 145(1-2):415–434, 2006.

[81] Chakraborty, N. and Cant, R. S. Influence of Lewis number on curvature effects in turbulent premixed flame propagation in the thin reaction zones regime. *Physics of Fluids*, 17(10):105105, 2005.

[82] Chakraborty, N. Comparison of displacement speed statistics of turbulent premixed flames in the regimes representing combustion in corrugated flamelets and thin reaction zones. *Physics of Fluids*, 19(10):105109, 2007.

[83] Han, I. and Huh, K. Y. Roles of displacement speed on evolution of flame surface density for different turbulent intensities and Lewis numbers in turbulent premixed combustion. *Combustion and Flame*, 152(1-2):194–205, 2008.

[84] Echekki, T. and Chen, J. H. Unsteady strain rate and curvature effects in turbulent premixed methane-air flames. *Combustion and Flame*, 106(1-2):184–202, 1996.

[85] Chen, J. H. and Im, H. G. Correlation of flame speed with stretch in turbulent premixed methane/air flames. 27(1):819–826, 1998.

[86] Echekki, T. and Chen, J. H. Analysis of the contribution of curvature to premixed flame propagation. *Combustion and Flame*, 118(1-2), 1999.

[87] Hawkes, E. R. and Chen, J. H. Direct numerical simulation of hydrogen-enriched lean premixed methane–air flames. *Combustion and Flame*, 138(3):242–258, 2004.

[88] Hawkes, E. R. and Chen, J. H. Evaluation of models for flame stretch due to curvature in the thin reaction zones regime. *Proceedings of the Combustion Institute*, 30(1):647–655, 2005.

[89] Chakraborty, N., Hawkes, E. R., Chen, J. H., and Cant, R. S. The effects of strain rate and curvature on surface density function transport in turbulent premixed methane–air and hydrogen–air flames: A comparative study. *Combustion and Flame*, 154(1-2):259–280, 2008.

[90] Domingo, P., Vervisch, L., and Réveillon, J. DNS analysis of partially premixed combustion in spray and gaseous turbulent flame-bases stabilized in hot air. *Combustion and Flame*, 140(3):172–195, 2005.

[91] Bilger, R. W., Pope, S. B., Bray, K. N. C., and Driscoll, J. F. Paradigms in turbulent combustion research. *Proceedings of the Combustion Institute*, 30(1):21–42, 2005.

[92] Kuo, K. K. and Acharya, R. *Fundamentals of Turbulent and Multiphase Combustion*. John Wiley & Sons, 2012.

[93] Peters, N. *Turbulent Combustion*. IOP Publishing, 2001.

[94] Yamashita, H., Shimada, M., and Takeno, T. A numerical study on flame stability at the transition point of jet diffusion flames. *Proceedings of the Combustion Institute*, 26(1):27–34, 1996.

[95] Rosenberg, D. A., Allison, P. M., and Driscoll, J. F. Flame index and its statistical properties measured to understand partially premixed turbulent combustion. *Combustion and Flame*, 162(7):2808–2822, 2015.

[96] Dinesh, K. K. J. R., Jiang, X., and Van Oijen, J. A. Hydrogen-enriched non-premixed jet flames: Analysis of the flame surface, flame normal, flame index and Wobbe index. *International Journal of Hydrogen Energy*, 39(12):6753–6763, 2014.

[97] Gibson, C. H. Fine structure of scalar fields mixed by turbulence. I. zero-gradient points and minimal gradient surfaces. *The Physics of Fluids*, 11(11):2305–2315, 1968.

[98] Peters, N., Terhoeven, P., Chen, J. H., and Echekki, T. Statistics of flame displacement speeds from computations of 2-D unsteady methane-air flames. *Proceedings of the Combustion Institute*, 27(1):833–839, 1998.

[99] Wacks, D. H. and Chakraborty, N. Statistical analysis of the reaction progress variable and mixture fraction gradients in flames propagating into droplet mist: A direct numerical simulation analysis. *Combustion Science and Technology*, 188(11-12):2149–2177, 2016.

[100] Wacks, D. H., Malkeson, S. P., and Chakraborty, N. Statistical behavior of fuel mass fraction variance transport in turbulent flame–droplet interaction: A direct numerical simulation analysis. *Numerical Heat Transfer, Part A: Applications*, 70(10):1087–1100, 2016.

[101] Wray, A. A. Minimal storage time advanced schemes for spectral methods. *NASA Ames Research Centre*, 1990.

[102] Cant, S. *Initial Conditions for Direct Numerical Simulation of Turbulence*. University of Cambridge, Department of Engineering, 2012.

[103] Rogallo, R. S. *Numerical Experiments in Homogeneous Turbulence*, volume 81315. National Aeronautics and Space Administration, 1981.

[104] Batchelor, G. K. and Townsend, A. A. Decay of turbulence in the final period. *Proceedings of the Royal Society of London. Series A. Mathematical and Physical Sciences*, 194(1039):527–543, 1948.

[105] Govindaraju, P. B., Jaravel, T., and Ihme, M. Coupling of turbulence on the ignition of multicomponent sprays. *Proceedings of the Combustion Institute*, 37(3):3295–3302, 2019.

[106] Zhou, T., Ye, T., Zhu, M., Zhao, M., and Chen, J. Effect of droplet diameter and global equivalence ratio on n-heptane spray auto-ignition. *Fuel*, 187:137–145, 2017.

[107] Duret, B., Luret, G., Reveillon, J., Ménard, T., Berlemont, A., and Demoulin, F. DNS analysis of turbulent mixing in two-phase flows. *International Journal of Multiphase Flow*, 40:93–105, 2012.

[108] Orszag, S. A. Numerical methods for the simulation of turbulence. *The Physics of Fluids*, 12(12):II–250, 1969.

[109] Papapostolou, V., Ozel Erol, G., Turquand dÀuzay, C., and Chakraborty, N. A numerical investigation of the minimum ignition energy requirement for forced ignition of turbulent droplet-laden mixtures. *Combustion Science and Technology*, 193(2):307–340, 2021.

[110] Turquand dâAuzay, C., Papapostolou, V., Ahmed, S. F., and Chakraborty, N. On the minimum ignition energy and its transition in the localised forced ignition of turbulent homogeneous mixtures. *Combustion and Flame*, 201:104–117, 2019.

[111] Trivedi, S., Nivarti, G. V., and Cant, R. S. Flame self-interactions with increasing turbulence intensity. *Proceedings of the Combustion Institute*, 37(2):2443–2449, 2019.

[112] Mastorakos, E. Forced ignition of turbulent spray flames. *Proceedings of the Combustion Institute*, 36(2):2367–2383, 2017.

[113] Haworth, D. C. and Poinsot, T. J. Numerical simulations of Lewis number effects in turbulent premixed flames. *Journal of Fluid Mechanics*, 244:405–436, 1992.

[114] Rotexo Software. Cosilab, 2011.

[115] Neophytou, A. and Mastorakos, E. Simulations of laminar flame propagation in droplet mists. *Combustion and Flame*, 156(8):1627–1640, 2009.

[116] Vena, P. C., Deschamps, B., Smallwood, G. J., and Johnson, M. R. Equivalence ratio gradient effects on flame front topology in a stratified iso-octane/air turbulent V-flame. *Proceedings of the Combustion Institute*, 33(1):1551–1558, 2011.

[117] Vena, P. C., Deschamps, B., Guo, H., Smallwood, G. J., and Johnson, M. R. Heat release rate variations in a globally stoichiometric, stratified iso-octane/air turbulent V-flame. *Combustion and Flame*, 162(4):944–959, 2015.

[118] Hayashi, S., Kumagai, S., and Sakai, T. Propagation velocity and structure of flames in droplet-vapor-air mixtures. *Combustion Science and Technology*, 15(5-6):169–177, 1977.

[119] Lawes, M. and Saat, A. Burning rates of turbulent iso-octane aerosol mixtures in spherical flame explosions. *Proceedings of the Combustion Institute*, 33(2):2047–2054, 2011.

[120] Zhao, S., Bouali, Z., and Mura, A. Computational investigation of weakly turbulent flame kernel growths in iso-octane droplet clouds in CVC conditions. *Flow, Turbulence and Combustion*, 104(1):139–177, 2020.

[121] Alqallaf, A., Klein, M., and Chakraborty, N. Effects of Lewis number on the evolution of curvature in spherically expanding turbulent premixed flames. *Fluids*, 4(1):12, 2019.

[122] Haruki, Y., Pillai, A. L., Kitano, T., and Kurose, R. Numerical investigation of flame propagation in fuel droplet arrays. *Atomization and Sprays*, 28(4), 2018.

[123] De Chaisemartin, S., Fréret, L., Kah, D., Laurent, F., Fox, R. O., Reveillon, J., and Massot, M. Eulerian models for turbulent spray combustion with polydispersity and droplet crossing. *Comptes Rendus Mécanique*, 337(6-7):438–448, 2009.

[124] Lefebvre, A. H. and McDonell, V. G. *Atomization and Sprays*. CRC press, 2017.

[125] Navarro-Martinez, S. Large eddy simulation of spray atomization with a probability density function method. *International Journal of Multiphase Flow*, 63:11–22, 2014.

[126] Lee, S., Moiz, A. A., and Cung, K. D. Turbulent spray combustion. In *Droplets and Sprays*, pages 277–312. Springer, 2018.

[127] Masri, A. R., Kourmatzis, A., O'Loughlin, W., and Gounder, J. D. From dilute to dense turbulent sprays: Combustion, auto-ignition and atomization. *Experiments and Numerical Simulations of Turbulent Combustion of Diluted Sprays*, pages 1–29, 2014.

[128] Masri, A. R. and Gounder, J. D. Details and complexities of boundary conditions in turbulent piloted dilute spray jets and flames. *Experiments and Numerical Simulations of Diluted Spray Turbulent Combustion*, pages 41–68, 2011.

[129] Gutheil, E. Issues in computational studies of turbulent spray combustion. *Experiments and Numerical Simulations of Diluted Spray Turbulent Combustion*, pages 1–39, 2011.

[130] Balachandar, S. and Eaton, J. K. Turbulent dispersed multiphase flow. *Annual Review of Fluid Mechanics*, 42:111–133, 2010.

[131] Bagchi, P. and Balachandar, S. Response of the wake of an isolated particle to an isotropic turbulent flow. *Journal of Fluid Mechanics*, 518:95–123, 2004.

[132] Faeth, G. M. Mixing, transport and combustion in sprays. *Progress in Energy and Combustion Science*, 13(4):293–345, 1987.

[133] Eaton, J. K. and Fessler, J. R. Preferential concentration of particles by turbulence. *International Journal of Multiphase Flow*, 20:169–209, 1994.

[134] Law, C. K. Recent advances in droplet vaporization and combustion. *Progress in Energy and Combustion Science*, 8(3):171–201, 1982.

[135] Wang, Z. G. *Internal Combustion Processes of Liquid Rocket Engines: Modeling and Numerical Simulations*. John Wiley & Sons, 2016.

[136] Godsave, G. A. E. Studies of the combustion of drops in a fuel spray: The burning of single drops of fuel. *Proceedings of the Combustion Institute*, 4(1):818–830, 1953.

[137] Williams, A. Combustion of droplets of liquid fuels: A review. *Combustion and Flame*, 21(1):1–31, 1973.

[138] Faeth, G. M. Current status of droplet and liquid combustion. *Energy and Combustion Science*, 3(4):149–182, 1979.

[139] Spalding, D. B. Combustion of liquid fuels. *Proceedings of the Combustion Institute*, 4:847–864, 1953.

[140] Cant, R. S. and Mastorakos, E. *An Introduction to Turbulent Reacting Flows*. Imperial College Press, 2008.

[141] Cant, R. S. and Bray, K. N. C. Strained laminar flamelet calculations of premixed turbulent combustion in a closed vessel. *Proceedings of the Combustion Institute*, 22(1):791–799, 1989.

[142] Borghi, R. On the structure and morphology of turbulent premixed flames. *Recent Advances in the Aerospace Sciences*, pages 117–138, 1985.

[143] Peters, N. The turbulent burning velocity for large-scale and small-scale turbulence. *Journal of Fluid Mechanics*, 384:107–132, 1999.

[144] Chiu, H. H. and Liu, T. M. Group combustion of liquid droplets. *Combustion Science and Technology*, 17(3-4):127–142, 1977.

[145] Chiu, H. H., Kim, H. Y., and Croke, E. J. Internal group combustion of liquid droplets. *Proceedings of the Combustion Institute*, 19(1):971–980, 1982.

[146] Reveillon, J., Bray, K., and Vervisch, L. DNS study of spray vaporization and turbulent micro-mixing. *36th AIAA Aerospace Sciences Meeting and Exhibit*, page 1028, 1998.

[147] Borghi, R. Background on droplets and sprays. In *Combustion and Turbulence in Two-Phase Flows. Lecture series 1996-02.*, pages 1–28, 1996.

[148] Borghi, R. The links between turbulent combustion and spray combustion and their modelling. In *8th International Symposium on Transport Phenomena in Combustion*, pages 1–18, 1996.

[149] Burgoyne, J. H. and Cohen, L. The effect of drop size on flame propagation in liquid aerosols. *Proceedings of the Royal Society of London. Series A. Mathematical and Physical Sciences*, 225(1162):375–392, 1954.

[150] Mizutani, Y. and Nishjmoto, T. Turbulent flame velocities in premixed sprays: Part I experimental study. *Combustion Science and Technology*, 6(1-2):1–10, 1972.

[151] Ballal, D. R. and Lefebvre, A. H. Flame propagation in heterogeneous mixtures of fuel droplets, fuel vapor and air. *Proceedings of the Combustion Institute*, 18(1):321–328, 1981.

[152] Aggarwal, S. K. and Sirignano, W. A. Unsteady spray flame propagation in a closed volume. *Combustion and Flame*, 62(1):69–84, 1985.

[153] Szekely Jr, G. A. and Faeth, G. M. Effects of envelope flames on drop gasification rates in turbulent diffusion flames. *Combustion and Flame*, 49(1-3):255–259, 1983.

[154] Nomura, H., Koyama, M., Miyamoto, H., Ujiie, Y., Sato, J., Kono, M., and Yoda, S. Microgravity experiments of flame propagation in ethanol droplet-vapor-air mixture. *Proceedings of the Combustion Institute*, 28(1):999–1005, 2000.

[155] Polymeropoulos, C. E. Flame propagation in aerosols of fuel droplets, fuel vapor and air. *Combustion Science and Technology*, 40(5-6):217–232, 1984.

[156] Greenberg, J. B., Silverman, I., and Tambour, Y. On droplet enhancement of the burning velocity of laminar premixed spray flames. *Combustion and Flame*, 113(1-2):271–273, 1998.

[157] Silverman, I., Greenberg, J. B., and Tambour, Y. Stoichiometry and polydisperse effects in premixed spray flames. *Combustion and Flame*, 93(1-2):97–118, 1993.

[158] Greenberg, J. B. and Kalma, A. A study of stretch in premixed spray flames. *Combustion and Flame*, 123(3):421–429, 2000.

[159] Greenberg, J. B. Finite-rate evaporation and droplet drag effects in spherical flame front propagation through a liquid fuel mist. *Combustion and Flame*, 148(4):187–197, 2007.

[160] Chung, S. H. Stabilization, propagation and instability of tribrachial triple flames. *Proceedings of the Combustion Institute*, 31(1):877–892, 2007.

[161] Domingo, P. and Vervisch, L. Triple flames and partially premixed combustion in autoignition of non-premixed turbulent mixtures. *Proceedings of the Combustion Institute*, 26(1):233–240, 1996.

[162] Amantini, G., Frank, J. H., Bennett, B. A. V., Smooke, M. D., and Gomez, A. Comprehensive study of the evolution of an annular edge flame during extinction and reignition of a counterflow diffusion flame perturbed by vortices. *Combustion and Flame*, 150(4):292–319, 2007.

[163] Hesse, H., Chakraborty, N., and Mastorakos, E. The effects of the Lewis number of the fuel on the displacement speed of edge flames in igniting turbulent mixing layers. *Proceedings of the Combustion Institute*, 32(1):1399–1407, 2009.

[164] Papapostolou, V., Turquand dÀuzay, C., Ozel Erol, G., and Chakraborty, N. Edge flame propagation statistics in igniting monodisperse droplet-laden mixtures. *Physics of Fluids*, 31(10):105108, 2019.

[165] Bradley, D., Hicks, R. A., Lawes, M., Sheppard, C. G. W., and Woolley, R. The measurement of laminar burning velocities and markstein numbers for iso-octane–air and iso-octane–n-heptane–air mixtures at elevated temperatures and pressures in an explosion bomb. *Combustion and Flame*, 115(1-2):126–144, 1998.

[166] Abdel-Gayed, R. G. and Bradley, D. Criteria for turbulent propagation limits of premixed flames. *Combustion and Flame*, 62(1):61–68, 1985.

[167] Renou, B., Boukhalfa, A., Puechberty, D., and Trinité, M. Local scalar flame properties of freely propagating premixed turbulent flames at various Lewis numbers. *Combustion and Flame*, 123(4):507–521, 2000.

[168] Haq, M. Z., Sheppard, C. G. W., Woolley, R., Greenhalgh, D. A., and Lockett, R. D. Wrinkling and curvature of laminar and turbulent premixed flames. *Combustion and Flame*, 131(1-2):1–15, 2002.

[169] Thevenin, D., Gicquel, O., De Charentenay, J., Hilbert, R., and Veynante, D. Two- versus three-dimensional direct simulations of turbulent methane flame kernels using realistic chemistry. *Proceedings of the Combustion Institute*, 29(2):2031–2039, 2002.

[170] Jenkins, K. W. and Cant, R. S. Curvature effects on flame kernels in a turbulent environment. *Proceedings of the Combustion Institute*, 29(2):2023–2029, 2002.

[171] Van Oijen, J. A., Groot, G. R. A., Bastiaans, R. J. M., and De Goey, L. P. H. A flamelet analysis of the burning velocity of premixed turbulent expanding flames. *Proceedings of the Combustion Institute*, 30(1):657–664, 2005.

[172] Thévenin, D. Three-dimensional direct simulations and structure of expanding turbulent methane flames. *Proceedings of the Combustion Institute*, 30(1):629–637, 2005.

[173] Hult, J., Gashi, S., Chakraborty, N., Klein, M., Jenkins, K. W., Cant, S., and Kaminski, C. F. Measurement of flame surface density for turbulent premixed flames using PLIF and DNS. *Proceedings of the Combustion Institute*, 31(1):1319–1326, 2007.

[174] Gashi, S., Hult, J., Jenkins, K. W., Chakraborty, N., Cant, S., and Kaminski, C. F. Curvature and wrinkling of premixed flame kernels comparisons of OH PLIF and DNS data. *Proceedings of the Combustion Institute*, 30(1):809–817, 2005.

[175] Echekki, T. and Kolera-Gokula, H. A regime diagram for premixed flame kernel-vortex interactions. *Physics of Fluids*, 19(4):043604, 2007.

[176] Dunstan, T. D. and Jenkins, K. W. Flame surface density distribution in turbulent flame kernels during the early stages of growth. *Proceedings of the Combustion Institute*, 32(1):1427–1434, 2009.

[177] Ahmed, I. and Swaminathan, N. Simulation of spherically expanding turbulent premixed flames. *Combustion Science and Technology*, 185(10):1509–1540, 2013.

[178] Chakraborty, N., Klein, M., and Cant, R. S. Effects of turbulent Reynolds number on the displacement speed statistics in the thin reaction zones regime of turbulent premixed combustion. *Journal of Combustion*, 2011, 2011.

[179] Sandeep, A., Proch, F., Kempf, A. M., and Chakraborty, N. Statistics of strain rates and surface density function in a flame-resolved high-fidelity simulation of a turbulent premixed bluff body burner. *Physics of Fluids*, 30(6):065101, 2018.

[180] Chakraborty, N., Klein, M., Alwazzan, D., and Im, H. G. Surface density function statistics in hydrogen-air flames for different turbulent premixed combustion regimes. *Combustion Science and Technology*, 190(11):1988–2002, 2018.

[181] Vervisch, L., Bidaux, E., Bray, K. N. C., and Kollmann, W. Surface density function in premixed turbulent combustion modeling, similarities between probability density function and flame surface approaches. *Physics of Fluids*, 7(10):2496–2503, 1995.

[182] Kollmann, W. and Chen, J. H. Pocket formation and the flame surface density equation. *Proceedings of the Combustion Institute*, 27(1):927–934, 1998.

[183] Pope, S. B. The evolution of surfaces in turbulence. *International Journal of Engineering Science*, 26(5):445–469, 1988.

[184] Candel, S. M. and Poinsot, T. J. Flame stretch and the balance equation for the flame area. *Combustion Science and Technology*, 70(1-3):1–15, 1990.

[185] Chakraborty, N. and Cant, R. S. Effects of strain rate and curvature on surface density function transport in turbulent premixed flames in the thin reaction zones regime. *Physics of Fluids*, 17(6):065108, 2005.

[186] Dopazo, C., Cifuentes, L., Martin, J., and Jimenez, C. Strain rates normal to approaching iso-scalar surfaces in a turbulent premixed flame. *Combustion and Flame*, 162(5):1729–1736, 2015.

[187] Dopazo, C., Cifuentes, L., Hierro, J., and Martin, J. Micro-scale mixing in turbulent constant density reacting flows and premixed combustion. *Flow, Turbulence and Combustion*, 96(2):547–571, 2016.

[188] Dopazo, C. and Cifuentes, L. The physics of scalar gradients in turbulent premixed combustion and its relevance to modeling. *Combustion Science and Technology*, 188(9):1376–1397, 2016.

[189] Dopazo, C., Cifuentes, L., Alwazzan, D., and Chakraborty, N. Influence of the Lewis number on effective strain rates in weakly turbulent premixed combustion. *Combustion Science and Technology*, 190(4):591–614, 2018.

[190] Klein, M., Alwazzan, D., and Chakraborty, N. A direct numerical simulation analysis of pressure variation in turbulent premixed bunsen burner flames-Part 1: Scalar gradient and strain rate statistics. *Computers & Fluids*, 173:178–188, 2018.

[191] Boger, M., Veynante, D., Boughanem, H., and Trouvé, A. Direct numerical simulation analysis of flame surface density concept for large eddy simulation of turbulent premixed combustion. *Proceedings of the Combustion Institute*, 27(1):917–925, 1998.

[192] Chakraborty, N., Champion, M., Mura, A., and Swaminathan, N. Scalar dissipation rate approach. In *Turbulent Premixed Flame*. Cambridge University Press, 2011.

[193] Sankaran, R., Hawkes, E. R., Chen, J. H., Lu, T., and Law, C. K. Structure of a spatially developing turbulent lean methane–air bunsen flame. *Proceedings of the Combustion Institute*, 31(1):1291–1298, 2007.

[194] Chakraborty, N. and Swaminathan, N. Influence of the Damköhler number on turbulence-scalar interaction in premixed flames. I. physical insight. *Physics of Fluids*, 19(4):045103, 2007.

[195] Kim, S. H. and Pitsch, H. Scalar gradient and small-scale structure in turbulent premixed combustion. *Physics of Fluids*, 19(11):115104, 2007.

[196] Chakraborty, N. and Klein, M. Influence of Lewis number on the surface density function transport in the thin reaction zone regime for turbulent premixed flames. *Physics of Fluids*, 20(6):065102, 2008.

[197] Wang, H., Hawkes, E. R., Chen, J. H., Zhou, B., Li, Z., and Aldén, M. Direct numerical simulations of a high Karlovitz number laboratory premixed jet flame–An analysis of flame stretch and flame thickening. *Journal of Fluid Mechanics*, 815(SAND-2017-0646J), 2017.

[198] Moffatt, H. K. The topology of scalar fields in 2D and 3D turbulence. In *IUTAM symposium on geometry and statistics of turbulence*, pages 13–22. Springer, 2001.

[199] Dopazo, C., Martín, J., and Hierro, J. Local geometry of isoscalar surfaces. *Physical Review E*, 76(5):056316, 2007.

[200] Cant, R. S., Rutland, C. J., and Trouvé, A. Statistics for laminar flamelet modeling. In *Proceedings of the summer program*, page 271. Center for Turbulence Research Stanford, 1990.

[201] Chakraborty, N. and Cant, R. S. Statistical behavior and modeling of the flame normal vector in turbulent premixed flames. *Numerical Heat Transfer, Part A*, 50(7):623–643, 2006.

[202] Griffiths, R. A. C., Chen, J. H., Kolla, H., Cant, R. S., and Kollmann, W. Three-dimensional topology of turbulent premixed flame interaction. *Proceedings of the Combustion Institute*, 35(2):1341–1348, 2015.

[203] Trivedi, S., Griffiths, R., Kolla, H., Chen, J. H., and Cant, R. S. Topology of pocket formation in turbulent premixed flames. *Proceedings of the Combustion Institute*, 37(2):2619–2626, 2019.

[204] Dunstan, T. D., Swaminathan, N., Bray, K. N. C., and Kingsbury, N. G. Flame interactions in turbulent premixed twin V-flames. *Combustion Science and Technology*, 185(1):134–159, 2013.

[205] Dunstan, T. D., Swaminathan, N., Bray, K. N. C., and Kingsbury, N. G. The effects of non-unity Lewis numbers on turbulent premixed flame interactions in a twin V-flame configuration. *Combustion Science and Technology*, 185(6):874–897, 2013.

[206] Minamoto, Y., Yenerdag, B., and Tanahashi, M. Morphology and structure of hydrogen-air turbulent premixed flames. *Combustion and Flame*, 192:369–383, 2018.

[207] Doan, N. A. K., Swaminathan, N., and Minamoto, Y. DNS of mild combustion with mixture fraction variations. *Combustion and Flame*, 189:173–189, 2018.

[208] Tyagi, A., Boxx, I., Peluso, S., and O'Connor, J. The role of flow interaction in flame–flame interaction events in a dual burner experiment. *Proceedings of the Combustion Institute*, 37(2):2485–2491, 2019.

[209] Marble, F. E. and Broadwell, J. E. The coherent flame model of non-premixed turbulent combustion. *Project Squid TRW-9-PU, Project Squid Headquarters, Chaffee Hall, Purdue University*, 1977.

[210] Poinsot, T., Echekki, T., and Mungal, M. G. A study of the laminar flame tip and implications for premixed turbulent combustion. *Combustion Science and Technology*, 81(1-3):45–73, 1992.

[211] Rutland, C. J. and Trouvé, A. Direct simulations of premixed turbulent flames with nonunity Lewis numbers. *Combustion and Flame*, 94(1-2):41–57, 1993.

[212] Fries, D., Ochs, B. A., Saha, A., Ranjan, D., and Menon, S. Flame speed characteristics of turbulent expanding flames in a rectangular channel. *Combustion and Flame*, 199:1–13, 2019.

[213] Sahafzadeh, M., Dworkin, S. B., and Kostiuk, L. W. Predicting the consumption speed of a premixed flame subjected to unsteady stretch rates. *Combustion and Flame*, 196:237–248, 2018.

[214] Nwagwe, I. K., Weller, H. G., Tabor, G. R., Gosman, A. D., Lawes, M., Sheppard, C. G. W., and Wooley, R. Measurements and large eddy simulations of turbulent premixed flame kernel growth. *Proceedings of the Combustion Institute*, 28(1):59–65, 2000.

[215] Brequigny, P., Endouard, C., Mounaïm-Rousselle, C., and Foucher, F. An experimental study on turbulent premixed expanding flames using simultaneously Schlieren and tomography techniques. *Experimental Thermal and Fluid Science*, 95:11–17, 2018.

[216] Thimothée, R., Chauveau, C., Halter, F., and Gökalp, I. Characterization of cellular instabilities of a flame propagating in an aerosol. 56697:V04BT04A063, 2015.

[217] Jog, M. A., Ayyaswamy, P. S., and Cohen, I. M. Evaporation and combustion of a slowly moving liquid fuel droplet: Higher-order theory. *Journal of Fluid Mechanics*, 307:135–165, 1996.

[218] Atzler, F., Demoulin, F. X., Lawes, M., and Lee, Y. Oscillations in the flame speed of globally homogeneous two phase mixtures. In *18th International Colloquium on the Dynamics of Explosions and Reactive Systems*, volume 29, page 191, 2001.

[219] Atzler, F., Demoulin, F. X., Lawes, M., Lee, Y., and Marquez, N. Burning rates and flame oscillations in globally homogeneous two-phase mixtures (flame speed oscillations in droplet cloud flames). *Combustion Science and Technology*, 178(12):2177–2198, 2006.

[220] Reveillon, J., Péra, C., Massot, M., and Knikker, R. Eulerian analysis of the dispersion of evaporating polydispersed sprays in a statistically stationary turbulent flow. *Journal of Turbulence*, 5(1):1–4, 2004.

[221] Smith, K. and Gouldin, F. Experimental investigation of flow turbulence effects on premixed methane-air flames. In *15th Aerospace Sciences Meeting*, page 183, 1978.

[222] Veynante, D., Duclos, J. M., and Piana, J. Experimental analysis of flamelet models for premixed turbulent combustion. *Proceedings of the Combustion Institute*, 25(1):1249–1256, 1994.

[223] Veynante, D., Piana, J., Duclos, J. M., and Martel, C. Experimental analysis of flame surface density models for premixed turbulent combustion. *Proceedings of the Combustion Institute*, 26(1):413–420, 1996.

[224] Gouldin, F. C. Combustion intensity and burning rate integral of premixed flames. *Proceedings of the Combustion Institute*, 26(1):381–388, 1996.

[225] Shepherd, I. G. Flame surface density and burning rate in premixed turbulent flames. *Proceedings of the Combustion Institute*, 26(1):373–379, 1996.

[226] Sattler, S .S., Knaus, D. A., and Gouldin, F. C. Determination of three-dimensional flamelet orientation distributions in turbulent v-flames from two-dimensional image data. *Proceedings of the Combustion Institute*, 29(2):1785–1792, 2002.

[227] Sponfeldner, T., Boxx, I., Beyrau, F., Hardalupas, Y., Meier, W., and Taylor, A. M. K. P. On the alignment of fluid-dynamic principal strain-rates with the 3D flamelet-normal

in a premixed turbulent V-flame. *Proceedings of the Combustion Institute*, 35(2):1269–1276, 2015.

[228] Letty, C., Renou, B., Reveillon, J., Saengkaew, S., and Gréhan, G. Experimental study of droplet temperature in a two-phase heptane/air V-flame. *Combustion and Flame*, 160(9):1803–1811, 2013.

[229] Alshaalan, T. M. and Rutland, C. J. Turbulence, scalar transport, and reaction rates in flame-wall interaction. *Proceedings of the Combustion Institute*, 27(1):793–799, 1998.

[230] Domingo, P., Vervisch, L., Payet, S., and Hauguel, R. DNS of a premixed turbulent V-flame and les of a ducted flame using a FSD-PDF subgrid scale closure with FPI-tabulated chemistry. *Combustion and Flame*, 143(4):566–586, 2005.

[231] Bell, J. B., Day, M. S., Shepherd, I. G., Johnson, M. R., Cheng, R. K., Grcar, J. F., Beckner, V. E., and Lijewski, M. J. Numerical simulation of a laboratory-scale turbulent V-flame. *Proceedings of the National Academy of Sciences*, 102(29):10006–10011, 2005.

[232] Wu, Y. Y., Chan, C. K., and Zhou, L. X. Large eddy simulation of an ethylene–air turbulent premixed V-flame. *Journal of Computational and Applied Mathematics*, 235(13):3768–3774, 2011.

[233] Kheirkhah, S. and Gülder, O. Topology and brush thickness of turbulent premixed V-shaped flames. *Flow, Turbulence and Combustion*, 93(3):439–459, 2014.

[234] Hélie, J. and Trouvé, A. Turbulent flame propagation in partially premixed combustion. *Proceedings of the Combustion Institute*, 27(1):891–898, 1998.

[235] Bray, K. N. C. *Turbulent Flows with Premixed Reactants, in Turbulent Reacting Flows*. Springer Verlag, Berlin Heidelburg, 1980.

[236] Langevin, P. Sur la théorie du mouvement brownien. *Compt. Rendus*, 146:530–533, 1908.

[237] Taylor, G. I. Diffusion by continuous movements. *Proceedings of the London Mathematical Society*, 2(1):196–212, 1922.

[238] Meneveau, C. and Poinsot, T. Stretching and quenching of flamelets in premixed turbulent combustion. *Combustion and Flame*, 86(4):311–332, 1991.

[239] Trouvé, A. and Poinsot, T. The evolution equation for the flame surface density in turbulent premixed combustion. *Journal of Fluid Mechanics*, 278:1–31, 1994.

[240] Aspden, A. J., Day, M. S., and Bell, J. B. Turbulence–flame interactions in lean premixed hydrogen: Transition to the distributed burning regime. *Journal of Fluid mechanics*, 680:287–320, 2011.

[241] Nivarti, G. and Cant, S. Direct numerical simulation of the bending effect in turbulent premixed flames. *Proceedings of the Combustion Institute*, 36(2):1903–1910, 2017.

[242] Ahmed, U., Chakraborty, N., and Klein, M. Insights into the bending effect in premixed turbulent combustion using the flame surface density transport. *Combustion Science and Technology*, 191(5-6):898–920, 2019.

[243] Damköhler, G. The influence of turbulence on the flame speed in gas mixtures. *Zeitschrift für Electrochemistry and Applied Physical Chemistry*, 46(11):601–626, 1940.

[244] Chakraborty, N., Alwazzan, D., Klein, M., and Cant, R. S. On the validity of Damköhler's first hypothesis in turbulent bunsen burner flames: A computational analysis. *Proceedings of the Combustion Institute*, 37(2):2231–2239, 2019.

[245] Lipatnikov, A. N. and Chomiak, J. Turbulent flame speed and thickness: Phenomenology, evaluation, and application in multi-dimensional simulations. *Progress in Energy and Combustion Science*, 28(1):1–74, 2002.

[246] Lai, J., Chakraborty, N., Zhao, P., and Wang, L. Heat flux and flow topology statistics in oblique and head-on quenching of turbulent premixed flames by isothermal inert walls. *Combustion Science and Technology*, 191(2):353–381, 2019.

[247] Ahmed, U., Chakraborty, N., and Klein, M. Scalar gradient and strain rate statistics in oblique premixed flame–wall interaction within turbulent channel flows. *Flow, Turbulence and Combustion*, 106(2):701–732, 2021.